POST-TRANSCRIPTIONAL AND POST-TRANSLATIONAL REGULATION OF CANCER METABOLISM

EDITED BY: Qinong Ye, Changliang Shan, Binghui Li, Pei Wang and Bin Yuan

PUBLISHED IN: Frontiers in Cell and Developmental Biology

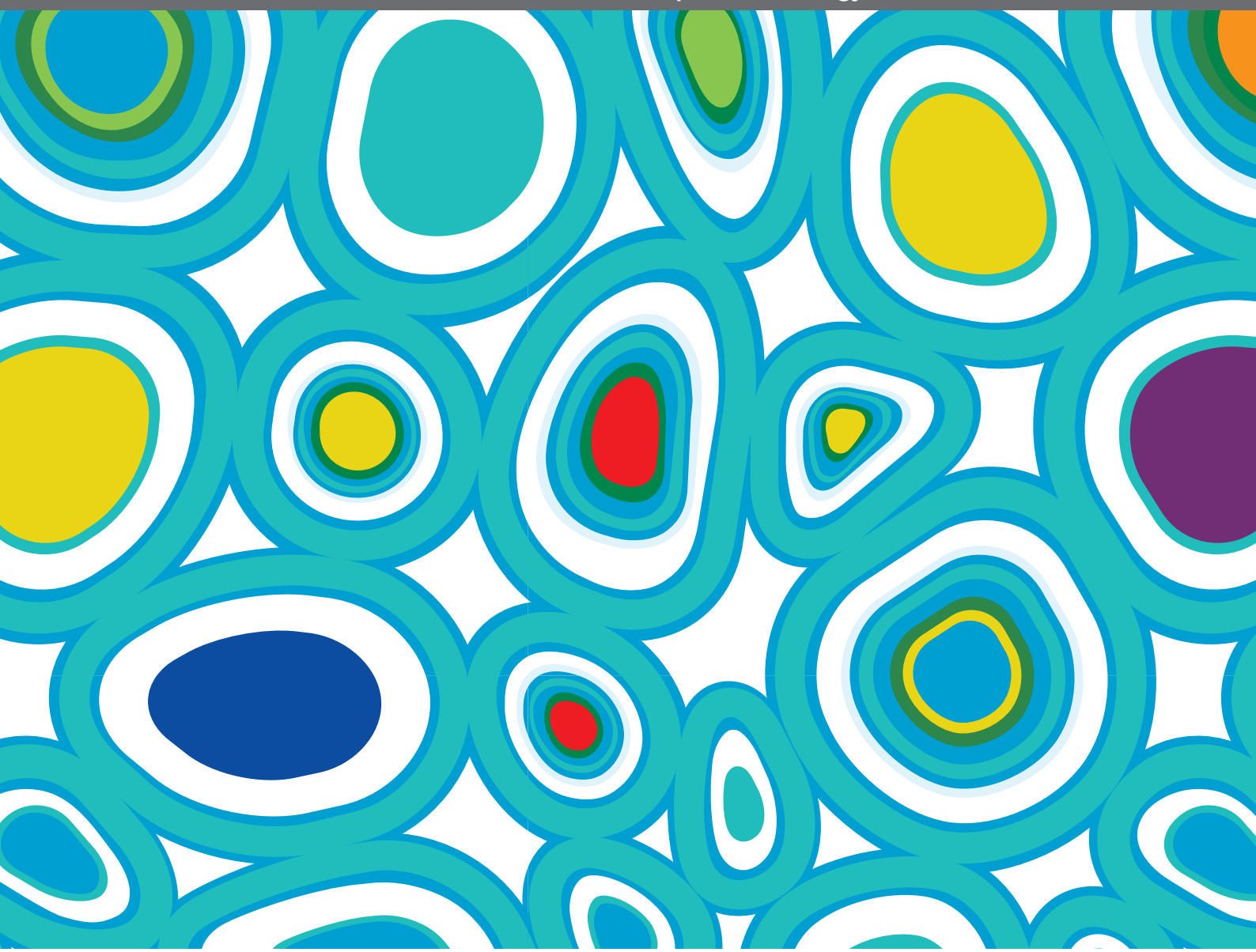

frontiers Research Topics

frontiers

ISSN 1664-8714
ISBN 978-2-88974-004-8
DOI 10.3389/978-2-88974-004-8

About Frontiers

Frontiers is more than just an open-access publisher of scholarly articles: it is a pioneering approach to the world of academia, radically improving the way scholarly research is managed. The grand vision of Frontiers is a world where all people have an equal opportunity to seek, share and generate knowledge. Frontiers provides immediate and permanent online open access to all its publications, but this alone is not enough to realize our grand goals.

Frontiers Journal Series

The Frontiers Journal Series is a multi-tier and interdisciplinary set of open-access, online journals, promising a paradigm shift from the current review, selection and dissemination processes in academic publishing. All Frontiers journals are driven by researchers for researchers; therefore, they constitute a service to the scholarly community. At the same time, the Frontiers Journal Series operates on a revolutionary invention, the tiered publishing system, initially addressing specific communities of scholars, and gradually climbing up to broader public understanding, thus serving the interests of the lay society, too.

Dedication to Quality

Each Frontiers article is a landmark of the highest quality, thanks to genuinely collaborative interactions between authors and review editors, who include some of the world's best academicians. Research must be certified by peers before entering a stream of knowledge that may eventually reach the public - and shape society; therefore, Frontiers only applies the most rigorous and unbiased reviews.
Frontiers revolutionizes research publishing by freely delivering the most outstanding research, evaluated with no bias from both the academic and social point of view. By applying the most advanced information technologies, Frontiers is catapulting scholarly publishing into a new generation.

What are Frontiers Research Topics?

Frontiers Research Topics are very popular trademarks of the Frontiers Journals Series: they are collections of at least ten articles, all centered on a particular subject. With their unique mix of varied contributions from Original Research to Review Articles, Frontiers Research Topics unify the most influential researchers, the latest key findings and historical advances in a hot research area! Find out more on how to host your own Frontiers Research Topic or contribute to one as an author by contacting the Frontiers Editorial Office: frontiersin.org/about/contact

POST-TRANSCRIPTIONAL AND POST-TRANSLATIONAL REGULATION OF CANCER METABOLISM

Topic Editors:
Qinong Ye, Institute of Biotechnology (CAAS), China
Changliang Shan, Nankai University, China
Binghui Li, Capital Medical University, China
Pei Wang, The University of Texas Health Science Center at San Antonio, United States
Bin Yuan, Anhui Medical University, China

Citation: Ye, Q., Shan, C., Li, B., Wang, P., Yuan, B., eds. (2021). Post-Transcriptional and Post-Translational Regulation of Cancer Metabolism. Lausanne: Frontiers Media SA. doi: 10.3389/978-2-88974-004-8

Table of Contents

frontiers in Cell and Developmental Biology

EDITORIAL
published: 17 November 2021
doi: 10.3389/fcell.2021.779157

Editorial: Post-transcriptional and Post-translational Regulation of Cancer Metabolism

Bin Yuan[1]* *and Qinong Ye*[2]*

[1] Department of Pharmacology, School of Basic Medical Sciences, Anhui Medical University, Hefei, China, [2] Department of Medical Molecular Biology, Beijing Institute of Biotechnology, Beijing, China

Keywords: cancer metabolism, regulation, microRNA, transcription, metabolic reprograming

Editorial on the Research Topic

Post-Transcriptional and Post-Translational Regulation of Cancer Metabolism

The metabolic reprogramming of cancer cells is required for cancer cell growth, migration, and invasion. The common phenomenon of this altered metabolism, also termed the Warburg effect or aerobic glycolysis, is elevated glucose uptake and lactate production, as well as utilization of amino acids and lipids (Koppenol et al., 2011; Liberti and Locasale, 2016; Li et al., 2018). Metabolic reprogramming is a well-recognized hallmark of cancer biology (Hanahan and Weinberg, 2011). The metabolic regulation of cancer cells is controlled by intrinsic genetic mutations and/or external responses to the tumor microenvironment (TME) (Cairns et al., 2011). Expression of metabolism-related genes can be regulated at multiple levels, including transcriptional, post-transcriptional, and post-translational levels. However, knowledge on the regulation of cancer metabolism at the post-transcriptional and post-translational levels is limited. This Research Topic "Post-Transcriptional and Post-Translational Regulation of Cancer Metabolism" provides articles on the fast-growing field of cancer metabolism, where 10 research articles and one review are presented, although most articles focus on transcriptional regulation of cancer metabolism.

Transcription factors, such as the oncoproteins c-Myc (Kim et al., 2004) and HIF-1α (Denko, 2008), have been shown to regulate cancer metabolism by directly binding promoters of metabolism-related genes and controlling the expression of metabolism-related genes. In this topic, Yang et al. (a) shows that c-MYC increases cholesterol biosynthesis and enhances cancer cell proliferation through transcriptional upregulation of SQLE, a rate-limiting enzyme in the cholesterol synthesis pathway. Similarly, Che et al. discovered that the MYC family members c-MYC/MYCN are involved in Keratin 6A-mediated upregulation of glucose-6-phosphate dehydrogenase (G6PD), the rate-limiting enzyme of the pentose phosphate pathway (PPP), leading to enhanced PPP flux in lung cancer cells. The authors of these two articles each present novel mechanistic insights into the c-Myc regulation of cancer cell metabolism, and provide potential targets or approaches for selectively targeting c-Myc-driven metabolic reprogramming in cancer cells. The study by Yang et al. (b) discusses how the F-box protein JFK is a novel transcriptional target of HIF-1α and mediates HIF-1α-induced glycolysis in breast cancer. JFK promotes mammary tumor initiation and progression in the MMTV-PyMT murine spontaneous mammary tumor model. Reactive oxygen species (ROS) are a crucial determinant of cancer metabolism phenotype, and glutathione (GSH) biosynthesis is required for cellular redox homeostasis, which provides energy support for cancer cell growth. As illustrated in the study by Zhao et al., the transcription factors CREB1 and ATF1 negatively regulate GSH biosynthesis by suppressing the transcription and expression of glutamate-cysteine ligase modifier subunit (GCLM) and glutathione synthase (GSS), and thereby dampen the cellular ability to

OPEN ACCESS

Edited and reviewed by:
Ramani Ramchandran, Medical College of Wisconsin, United States

***Correspondence:**
Bin Yuan
yuanbin@ahmu.edu.cn
Qinong Ye
yeqn66@yahoo.com

Specialty section:
This article was submitted to Molecular and Cellular Pathology, a section of the journal Frontiers in Cell and Developmental Biology

Received: *18 September 2021*
Accepted: *11 October 2021*
Published: *17 November 2021*

Citation:
Yuan B and Ye Q (2021) Editorial: Post-transcriptional and Post-translational Regulation of Cancer Metabolism. Front. Cell Dev. Biol. 9:779157. doi: 10.3389/fcell.2021.779157

scavenge ROS, resulting in sensitizing cancer cells to oxidative stress. Dong et al. identified recombination activating genes 1 (Rag1) and Rag2 as novel Notch1 transcriptional targets in acute T-cell lymphoblastic leukemia (T-ALL) cells. Dimeric Notch1 transcriptional complexes stimulate Rag1 and Rag2 expression via a novel cis-element harboring a sequence-paired site. Although Notch1 was shown to be involved in cancer glycolysis, it remains unclear whether Rag1 and Rag2 regulate glycolysis in T-ALL cells.

Metabolic reprogramming not only results from the dysregulated expression of diverse genes but also the altered expression of non-coding RNAs (ncRNAs), including microRNAs (miRNAs). miRNAs are involved in several metabolic and tumorigenic pathways through their post-transcriptional regulatory mechanisms. Ye et al. showed that miR-16-1-3p inhibits expression of PGK1 (Phosphoglycerate kinase 1), the first adenosine triphosphate (ATP)-generating glycolytic enzyme in the aerobic glycolysis pathway, by directly targeting PGK1 3'-untranslated region, resulting in decreased glucose uptake, lactate, and ATP production, and extracellular acidification rate, and increased oxygen consumption rate. Aerobic glycolysis modulated by the miR-16-1-3p/PGK1 axis is important for controlling breast cancer cell proliferation, migration, invasion, and metastasis.

Post-translational modifications of key metabolic enzymes, such as phosphorylation, acetylation, ubiquitination, and sumoylation, are also implicated in cancer metabolic reprogramming by changing the activity and/or stability of the enzymes. Li et al. analyzed the expression of 15 SUMOylation regulators in glioblastoma and found that single-nucleotide variant mutations exist in 10 SUMOylation regulators (SENP7, SENP3, SENP5, PIAS3, RANBP2, USPL1, SENP1, PIAS2, SENP2, and PIAS1). The SUMOylation regulator-related molecules (ATF7IP, CCNB1IP1, and LBH) had a strong predictive ability for the overall survival of patients with glioblastoma. However, whether these SUMOylation regulators and SUMOylation of their substrates regulate cancer metabolism remains to be investigated in glioblastoma.

In addition to the regulation of cancer metabolism by altered metabolic enzymes and their upstream regulators, alterations in downstream metabolites are also important for metabolic reprogramming in cancer. Bai et al. analyzed serum metabolites by targeted metabolomics and screened urea, a by-product of ammonia metabolism, as a potential biomarker for HCC. Sepsis may occur in some patients with cancer. Li et al. performed a comprehensive analysis with plasma metabolic profiling of pediatric sepsis, especially identifying a panel of metabolites alteration associated with pediatric sepsis. The authors also discussed energy and carbohydrate metabolism may contribute to sepsis progression. However, these two articles lack molecular mechanisms by which altered metabolites are regulated.

Importantly, the metabolic phenotype of a given tumor is largely influenced not only by the tumor cells themselves but also by the tumor microenvironment. Zhang et al. screened prostaglandin-endoperoxide synthase 2 (PTGS2) as a potential therapeutic target from TCGA-UVM (uveal melanoma) dataset. Decreased tumor cell proliferation and increased apoptosis was observed with the treatment of PTGS2 inhibitor, celecoxib. In an extensive review, Wang et al. focus on the inhibitory effects of cancer-associated fibroblasts (CAFs) and on cancer development, including heterogenous CAFs metabolism.

The current collection mainly focuses on the genetic changes that alter cancer cell metabolism and lack research articles on the abnormal TME, which play an important role in determining the metabolic reprogramming of cancer cells. On the other hand, the current collection does not cover all the topics proposed in the open call for submissions and still lacks a deeper understanding of post-transcriptional and post-translational regulation of cancer metabolism. For instance, it remains unclear how RNA binding proteins and ncRNAs regulate mRNA stability of metabolic enzymes, and how metabolic enzymes, at least some metabolic enzymes, are post-translationally modified, thus regulating cancer metabolism. However, the insights gathered in the present Research Topic nevertheless strengthen understanding of the regulation of cancer metabolism as an important area in cancer biology research.

AUTHOR CONTRIBUTIONS

All authors listed have made a substantial, direct and intellectual contribution to the work, and approved it for publication.

ACKNOWLEDGMENTS

We thank all authors who submitted work to this Research Topic as well as the invaluable help of reviewers in manuscript evaluation and the support of the editorial staff at Frontiers.

REFERENCES

Cairns, R. A., Harris, I. S., and Mak, T. W. (2011). Regulation of cancer cell metabolism. *Nat. Rev. Cancer* 11, 85–95. doi: 10.1038/nrc2981

Denko, N. C. (2008). Hypoxia, HIF1 and glucose metabolism in the solid tumour. *Nat. Rev. Cancer* 8, 705–713. doi: 10.1038/nrc2468

Hanahan, D., and Weinberg, R. A. (2011). Hallmarks of cancer: the next generation. *Cell* 144, 646–674. doi: 10.1016/j.cell.2011.02.013

Kim, J. W., Zeller, K. I., Wang, Y., Jegga, A. G., Aronow, B. J., O'Donnell, K. A., et al. (2004). Evaluation of myc E-box phylogenetic footprints in glycolytic genes by chromatin immunoprecipitation assays. *Mol. Cell. Biol.* 24, 5923–5936. doi: 10.1128/MCB.24.13.5923-5936.2004

Koppenol, W. H., Bounds, P. L., and Dang, C. V. (2011). Otto Warburg's contributions to current concepts of cancer metabolism. *Nat. Rev. Cancer* 11, 325–337. doi: 10.1038/nrc3038

Li, L., Liang, Y., Kang, L., Liu, Y., Gao, S., Chen, S., et al. (2018). Transcriptional regulation of the Warburg effect in cancer by SIX1. *Cancer Cell* 33, 368–385 e367. doi: 10.1016/j.ccell.2018.01.010

Liberti, M. V., and Locasale, J. W. (2016). The Warburg effect: how does it benefit cancer cells? *Trends Biochem. Sci.* 41, 211–218. doi: 10.1016/j.tibs.2015.12.001

Conflict of Interest: The authors declare that the research was conducted in the absence of any commercial or financial relationships that could be construed as a potential conflict of interest.

Publisher's Note: All claims expressed in this article are solely those of the authors and do not necessarily represent those of their affiliated organizations, or those of the publisher, the editors and the reviewers. Any product that may be evaluated in this article, or claim that may be made by its manufacturer, is not guaranteed or endorsed by the publisher.

frontiers in Cell and Developmental Biology

ORIGINAL RESEARCH
published: 03 December 2020
doi: 10.3389/fcell.2020.615154

MicroRNA-16-1-3p Represses Breast Tumor Growth and Metastasis by Inhibiting PGK1-Mediated Warburg Effect

*Tianxing Ye[1,2], Yingchun Liang[2], Deyu Zhang[2] and Xuewu Zhang[1]**

[1] College of Medicine, Yanbian University, Yanji, China, [2] Department of Medical Molecular Biology, Beijing Institute of Biotechnology, Collaborative Innovation Center for Cancer Medicine, Beijing, China

The Warburg effect (aerobic glycolysis) is a hallmark of cancer and is becoming a promising target for diagnosis and therapy. Phosphoglycerate kinase 1 (PGK1) is the first adenosine triphosphate (ATP)-generating glycolytic enzyme in the aerobic glycolysis pathway and plays an important role in cancer development and progression. However, how microRNAs (miRNAs) regulate PGK1-mediated aerobic glycolysis remains unknown. Here, we show that miR-16-1-3p inhibits PGK1 expression by directly targeting its 3′-untranslated region. Through inhibition of PGK1, miR-16-1-3p suppressed aerobic glycolysis by decreasing glucose uptake, lactate and ATP production, and extracellular acidification rate, and increasing oxygen consumption rate in breast cancer cells. Aerobic glycolysis regulated by the miR-16-1-3p/PGK1 axis is critical for modulating breast cancer cell proliferation, migration, invasion and metastasis *in vitro* and *in vivo*. In breast cancer patients, miR-16-1-3p expression is negatively correlated with PGK1 expression and breast cancer lung metastasis. Our findings provide clues regarding the role of miR-16-1-3p as a tumor suppressor in breast cancer through PGK1 suppression. Targeting PGK1 through miR-16-1-3p could be a promising strategy for breast cancer therapy.

Keywords: the Warburg effect, PGK1, miR-16-1-3p, cell proliferation, metastasis

OPEN ACCESS

Edited by:
Bin Yuan,
George Washington University, United States

Reviewed by:
Zhihong Yang,
Indiana University, United States
Chi Zhu,
University of California, Berkeley, United States

****Correspondence:***
Xuewu Zhang
zhangxuewu@ybu.edu.cn;
zhangxuewu18@163.com

Specialty section:
This article was submitted to Molecular Medicine, a section of the journal Frontiers in Cell and Developmental Biology

Received: *08 October 2020*
Accepted: *09 November 2020*
Published: *03 December 2020*

Citation:
Ye T, Liang Y, Zhang D and Zhang X (2020) MicroRNA-16-1-3p Represses Breast Tumor Growth and Metastasis by Inhibiting PGK1-Mediated Warburg Effect. Front. Cell Dev. Biol. 8:615154. doi: 10.3389/fcell.2020.615154

INTRODUCTION

The Warburg effect (also known as aerobic glycolysis) is a phenomenon predominantly observed in tumor cells which give priority to glycolysis to provide energy even when oxygen is sufficient (Schwartz et al., 2017; Tekade and Sun, 2017; Lu, 2019; Pereira-Nunes et al., 2020). Under aerobic condition, more glucose is consumed by tumor cells compared to normal cells, and a large amount of lactate is produced as a metabolite, providing an acidic environment suitable for tumor growth and metastasis. Targeting the Warburg effect is becoming a new strategy for cancer therapy. Phosphoglycerate kinase 1 (PGK1) is one of the key enzymes in the Warburg effect (He et al., 2019; Qian et al., 2019). During glycolysis, PGK1 catalyzes the reversible transfer of the high-energy phosphate group from 1,3-bisphosphoglycerate (1,3-BPG) to ADP, producing 3-phosphoglycerate (3-PG) and adenosine triphosphate (ATP). At the same time, PGK1 promotes glucose uptake and lactate production in cancer cells. Many studies show that PGK1 is highly expressed in various

cancers, such as breast cancer, liver cancer, and colon cancer (Ahmad et al., 2013; Hu et al., 2017; Fu et al., 2018). High expression of PGK1 is associated with poor prognosis of cancer patients. PGK1 expression is affected by some transcription factors, such as hypoxia-inducible factor 1α (HIF1α) and sine oculis homeobox 1 (SIX1; Meijer et al., 2012; Li et al., 2018; Nagao et al., 2019). Moreover, phosphorylation and acetylation of PGK1 also regulate tumorigenesis (Hu et al., 2017; Zhang Y. et al., 2018). Thus, PGK1 inhibition with small interfering RNAs (siRNAs) or other approaches may provide a new strategy for cancer treatment.

MicroRNAs (miRNAs) are small, non-coding RNA, typically 18–25 bases in length (Dykxhoorn, 2010; Mulrane et al., 2013; Shen and Hung, 2015; Adams et al., 2017). MicroRNAs usually bind to the 3′-untranslated region (UTR) of mRNA to silence its expression at the post-transcriptional level. Many studies have shown that miRNAs are involved in cancer cell proliferation, invasion and metastasis. Recently, miRNA-450b-3p, miRNA-548c-5p, miRNA-215-5p, and miRNA-6869-5p have been shown to directly target PGK1 3′-UTR and inhibit PGK1 expression (Chen et al., 2019, 2020; Ge et al., 2019; Wang et al., 2020). These miRNAs can regulate cancer cell proliferation, migration and/or invasion. However, whether these miRNAs regulates the Warburg effect via PGK1 remains unclear.

MiRNA-16-1-3p has been reported to act as a tumor suppressor in osteosarcoma (Maximov et al., 2019), non-small cell lung cancer (NSCLC; Feng et al., 2018) and gastric cancer (Wang et al., 2017). However, the function of miRNA-16-1-3p in breast cancer remains unclear. In this study, we show that miRNA-16-1-3p represses aerobic glycolysis in breast cancer cells, leading to inhibition of cancer cell proliferation, migration, invasion, and metastasis *in vitro* and *in vivo*. Mechanistically, miR-16-1-3p inhibits PGK1 expression by directly targeting its 3′-UTR, and represses breast cancer cell growth and metastasis by inhibiting PGK1-mediated Warburg effect.

MATERIALS AND METHODS

Cell Lines, Plasmids, Lentivirus, and Reagents

The human breast cancer cell lines ZR75-1 and MDA-MB-231 and the human embryonic kidney cell line HEK293T were purchased from the American Type Culture Collection. Firefly luciferase-labeled MDA-MB-231 cells were a gift from Professor Yongfeng Shang of Peking University (China). These cell lines were testified without mycoplasma contamination. The PCR amplified fragment was inserted into pcDNA3.0 (Invitrogen) to obtain a PGK1 expression vector. The primers for PGK1 were 5′-CGGGATCCATGTCGCTTTCTAACAAGCTG AC-3′ (forward) and 5′-GCTCTAGACTAAATATTGCTGAGAG CATCC-3′ (reverse) (The underlined part represents the restriction sites). The wild type and mutated miR-16-1-3p putative targets on PGK1 3′-UTR were cloned into pmir-GLO dual luciferase miRNA target expression vector (Promega). Recombinant PCR was performed to generate mutations. The lentiviral vectors that express PGK1 short hairpin RNA (shRNA) were made by cloning PCR-amplified PGK1 shRNA fragment into pSIH-H1-Puro (System Biosciences). The target sequence of PGK1 shRNA was 5′-GUCCAAAGCUGAAGAAUTT-3′. Lentiviruses were produced by cotransfection of HEK293T cells with recombinant lentivirus vectors and pPACK Packaging Plasmid Mix (System Biosciences) using Megatran reagent (Origene), and were used to infect breast cancer cells according to the manufacturers′ instructions. The successfully infected cells were selected with 1 μg/ml puromycin to generate stably cell lines. MiR-16-1-3p mimics and miR-16-1-3p inhibitor were purchased from GenePharma (Jiangsu, China). The sequence of the miR-16-1-3p inhibitor is 5′-UCAG CAGCACAGUUAAUACUGG-3′. The reagents for transfection of plasmids and miRNAs were Lipofectamine 3000 reagent and Lipofectamine RNAiMAX (Invitrogen), respectively. Cells were transfected according to the manufacturers' protocols. Anti-PGK1 antibody was purchased from Proteintech and anti-α-tubulin antibody was purchased from Santa Cruz Biotechnology.

Luciferase Reporter Gene Activity

Luciferase reporter assays were carried out according to the manufacturer's instructions (Promega). Briefly, cells were seeded in 24-well plates. After 24 h, cells were transfected with the wild-type or mutated PGK1 3′-UTR reporter and miR-16-1-3p mimics using Lipofectamine 3000. Twenty four hours after transfection, the cells were harvested and analyzed for luciferase activities according to the manufacture's instruction (Promega).

Revere Transcription-Quantitative Polymerase Chain Reaction (RT-qPCR)

Total RNA, including miRNAs, was extracted from cultured cells using the miRcute miRNA Isolation Kit (Tiangen). The miRcute miRNA First-Strand cDNA Synthesis Kit (Tiangen) was used to reverse transcribe the target miRNA into cDNA. For real-time PCR analysis, the primers for PGK1 were 5′-ATGTCGCTTTCTAACAAGCTGA-3′ (forward) and 5′-GCGGAGGTTCTCCAGCA-3′ (reverse). The control primers (α-tubulin) for PGK1 were 5′-CCAAGCTGGAGTTCTCTA-3′ (forward) and 5′-CAATCAGAGTGCTCCAGG-3′ (reverse). The primers for miR-16-1-3p were 5′-GGGGCCAGTATTAACTGT-3′ (forward) and 5′-TGCGTGTCGTGGAGTC-3′ (reverse). The control primers (U6) for miRNAs were 5′-CGCGCTTCGGCA GCACATATACT-3′ (forward) and 5′-ACGCTTCACGAATT TGCGTGTC-3′ (reverse). The relative fold expression of the target, normalized to the corresponding control, was calculated by the comparative Ct methods.

Cell Proliferation, Migration, and Invasion

Cell proliferation was examined by a CCK-8 Kit according to the manufacturer's instructions (Dojindo). Cell migration was determined by wound healing assays. Briefly, transfected cells grown to 90% in six-well plates were scratched via a 200 μl pipette tip to create the wound followed by washing detached cells with PBS. The cells were cultured for 16 h to allow wound healing. The wound healing rates were calculated, and compared to the

width at 0 h. Cell invasion assay was carried out with Matrigel Invasion Chambers according to the manufacturer's instructions (BD Biosciences). Briefly, transfected cells were placed on the upper surface of the transwell insert. After 16 h, the invasive cells were fixed with 4% paraformaldehyde and stained with 0.5% crystal violet. The number of invasive cells were counted in five randomly selected microscope visions and photographed.

Assays of Glucose Uptake and Production of Lactate and ATP

Glucose Uptake Colorimetric Assay Kit, Lactate Assay Kit II and ATP Colorimetric Assay Kit were used to measure glucose uptake and production of lactate and ATP according to the manufacturer's instructions (Biovision). For glucose uptake colorimetric assay, cells were seeded at a density of 1500 cells per well in a 96-well plate. The cells were starved for glucose by preincubating with 100 μl Krebs-Ringer-Phosphate-HEPES (KRPH) buffer containing 2% BSA for 40 min. Ten microliters of 10 mM 2-DG was added and the cells incubated for 20 min. For lactate and ATP assays, one million cells were homogenized in 100 μl corresponding assay buffer provided by the kits. The homogenized cells were centrifuged, and the soluble fraction was analyzed.

Assays of Extracellular Acidification Rate and Oxygen Consumption Rate

The extracellular acidification rate (ECAR) and cellular oxygen consumption rate (OCR) were assessed using the Seahorse XFe 96 Extracellular Flux Analyzer (Seahorse Bioscience) according to the manufacturer's instructions. ECAR and OCR were determined using Seahorse XFe Glycolysis Stress Test Kit and Seahorse XF Cell Mito Stress Test Kit, respectively. Briefly, 1×10^4 cells per well were seeded into a Seahorse XFe 96 cell culture microplate. After baseline measurements, for ECAR, glucose, the oxidative phosphorylation inhibitor oligomycin, and the glycolytic inhibitor 2-DG were sequentially injected into each well at indicated time points; and for OCR, oligomycin, the reversible inhibitor of oxidative phosphorylation FCCP (p-trifluoromethoxy carbonyl cyanide phenylhydrazone), and the mitochondrial complex I inhibitor rotenone plus the mitochondrial complex III inhibitor antimycin A (Rote/AA) were sequentially injected. Data were analyzed by Seahorse XFe 96 Wave software. OCR is indicated in pmols/minute and ECAR in mpH/minute.

Analysis of Tumor Growth and Metastasis in Nude Mice

We performed animal experiments with the approval of the Institutional Animal Care Committee of the Beijing Institute of Biotechnology. A total of 1×10^7 MDA-MB-231 cells harboring different constructs were subcutaneously inoculated into second mammary fat pad on the right side of nude mice. Tumor size was examined at a specified time using a caliper. The tumor volume is calculated according to the following formula: volume = (longest diameter $\times$ shortest diameter^2)/2. The mice were euthanized at the designated time. Excised tumors were frozen in liquid nitrogen for further study.

For lung metastasis analysis, 1×10^7 MDA-MB-231 cells stably expressing PGK1 shRNA or control shRNA with firefly luciferase labels were treated for three days with antagomiR-16-1-3p (miR-16-1-3p inhibitor) (1 μmol) or antagomiR-NC (scramble) (1 μmol), a negative control. The treated cells were collected and 1×10^6 cells were injected into the lateral tail vein of each BALB/c female mouse. After the indicated times, the mice were imaged using the IVIS200 imaging system (Xenogen Corporation, Alameda, CA, United States). After euthanasia, all lungs were excised for metastatic foci assessment.

Clinical Samples, MiRNA *in situ* Hybridization and Immunohistochemical Staining

Ninety one human breast cancer samples were obtained from the Chinese PLA General Hospital, with the informed consent of patients and with approval for experiments from the hospital. None of the breast cancer patients had received any chemotherapy prior to surgery. All patients were female with 31-74 years of age (mean age: 51.9 years).

For examination of miR-16-1-3p expression levels in breast cancer samples, miRNA *in situ* hybridization (MISH) was performed. Slides were hybridized with 200 nM of 5′-digoxigenin (DIG) LNA-modified- miR-16-1-3p (GenePharma, China), and then incubated with anti-DIG-horse reddish peroxidase (HRP) (Zhongshan Biotech). The miRNA signal was amplified by TSA Plus Cyanine 3 system (Perkin Elmer). The sequences complementary to miR-16-1-3p were 5′-TCAGCAGCACAGT TAATACTGG-3′. A U6 probe 5′-GAACGCTTCACGAATT TGCGTGTCATCCTTGCGCA-3′ was used as a positive control. A scramble probe 5′-GTGTAACACGTCTATACGCCCA-3′ was used as a negative control. To detect miR-16-1-3p expression, immunohistochemical staining (IHC) of formalin-fixed paraffin-embedded breast cancer samples was performed as described previously (Zhang et al., 2005). Rabbit anti-PGK1 was used at dilutions of 1:200 as primary antibodies for IHC. The expression of miR-16-1-3p and PGK1 was assessed by H score method. H score was generated by multiplying the percentage of stained cells (0–100%) by the intensity of the staining (low, 1+; medium, 2+; strong, 3+).

Statistics Analysis

All *in vitro* experiments were performed in triplicate and repeated three times unless otherwise indicated. Statistical significance in cell line experiments was determined by two-tailed Student's *t*-test (two groups) or the ANOVA-Dunnett test (more than two groups). Estimation of disease-free survival was performed using the Kaplan–Meier method, and differences between survival curves were determined with the log-rank test. Statistical analysis was performed using SPSS 17.0 statistical software package. The correlation between the expression of miR-16-1-3p and PGK1 was calculated by Spearman rank correlation analysis using GraphPad Prism 7. *P* values of less than 0.05 were considered statistically significant.

RESULTS

Identification of MiR-16-1-3p as a Direct Upstream Regulator of PGK1

Since PGK1 is the first ATP-generating enzyme in the glycolysis pathway and plays an important role in the development and progression of cancer, we identified potential miRNAs regulating PGK1 by using two target prediction programs, miRanda[1] and TargetScan.[2] Our analysis predicted several potential PGK1-targeting miRNAs, among which only miR-16-1-3p inhibited PGK1 protein expression in human embryonic kidney HEK293T cells and two breast cancer cell lines, ZR75-1 and MDA-MB-231 (**Figure 1A** and **Supplementary Figure 1A**). We further performed experiments by increasing or reducing mi-16-1-3p expression in ZR75-1 and MDA-MB-231. As expected, miR-16-1-3p mimics reduced PGK1 protein expression in these cells (**Figure 1B**), whereas miR-16-1-3p inhibitor (anti-miR-16-1-3p) increased PGK1 protein expression (**Figure 1C**). Moreover, miR-16-1-3p mimics suppressed PGK1 mRNA expression, while miR-16-1-3p inhibitor enhanced PGK1 mRNA expression (**Figure 1D**).

To investigate whether the inhibitory effect of miR-16-1-3p on PGK1 was mediated through direct binding of PGK1 3′-UTR, ZR75-1 and MDA-MB-231 cells were transfected with wild-type PGK1 3′-UTR or mutated PGK1 3′-UTR luciferase reporter and miR-16-1-3p mimics. Overexpression of miR-16-1-3p decreased the wild-type 3′-UTR luciferase activity, but not the reporter activity of mutated 3′-UTR (**Figure 1E**). Taken together, these results suggest that miR-16-1-3p inhibits PGK1 expression by targeting PGK1 3′-UTR.

The MiR-16-1-3p/PGK1 Axis Regulates Glycolysis in Breast Cancer Cells

The glycolytic pathway is the main metabolic pathway for tumor cells to perform energy metabolism. In this process, every molecule of glucose taken by cancer cells can quickly generate 2 molecules of ATP to meet their own energy needs. Regardless of whether oxygen is sufficient, the final product of tumor glycolysis is lactate. As PGK1 is a key enzyme in the glycolytic pathway and miR-16-1-3p is an upstream regulator of PGK1, we examined the effect of the miR-16-1-3p/PGK1 axis on aerobic glycolysis. MiR-16-1-3p mimics decreased glucose uptake and production of lactate and ATP in MDA-MB-231 cells (**Figure 2A**). Reexpression of PGK1 in the miR-16-1-3p-transfected cells reversed these effects. Conversely, anti- miR-16-1-3p increased glucose uptake and production of lactate and ATP (**Figure 2B**). PGK1 knockdown had opposite effects. Importantly, PGK1 knockdown abolished the ability of anti-miR-16-1-3p to increase glucose uptake and production of lactate and ATP, suggesting that miR-16-1-3p regulates glucose uptake and production of lactate and ATP through PGK1. Moreover, in MDA-MB-231 cells, overexpression of miR-16-1-3p led to a decrease in ECAR, which reflects overall glycolytic flux, and an increase in OCR, an indicator of mitochondrial respiration (**Figure 2C**). Reexpression of PGK1 in the miR-16-1-3p-transfected cells rescued these effects. In contrast, anti-miR-16-1-3p increased ECAR and decreased OCR in MDA-MB-231 cells (**Figure 2D**). PGK1 knockdown had opposite effects. Importantly, PGK1 knockdown abrogated the ability of anti-miR-16-1-3p to increase ECAR and decrease OCR, suggesting that miR-16-1-3p regulates ECAR and OCR through PGK1. Similar results were observed in ZR75-1 cells (**Supplementary Figures 1B–E**). Taken together, these data suggest that miR-16-1-3p regulates glycolysis via PGK1.

Aerobic Glycolysis Is Responsible for MiR-16-1-3p Modulation of Breast Cancer Cell Proliferation

Since aerobic glycolysis is a hallmark of cancer and the biological function of miR-16-1-3p in breast cancer is unknown, we investigated whether miR-16-1-3p regulates breast cancer cell proliferation and whether aerobic glycolysis plays a role in miR-16-1-3p -mediated regulation of breast cancer cell proliferation. As expected, the glycolytic inhibitor 2-deoxy-D-glucose (2-DG) inhibited proliferation of ZR75-1 and MDA-MB-231 breast cancer cells (**Figure 3**). Intriguingly, the miR-16-1-3p inhibitor (anti-miR-16-1-3p) promoted breast cancer cell proliferation. 2-DG almost abrogated the ability of anti-miR-16-1-3p to promote breast cancer cell proliferation, suggesting that aerobic glycolysis is responsible for breast cancer cell proliferation regulated by miR-16-1-3p.

The MiR-16-1-3p/PGK1 Axis Regulates Breast Cancer Cell Proliferation, Migration, and Invasion

Next, we examined whether miR-16-1-3p inhibits proliferation, migration and invasion by repressing PGK1 expression in breast cancer cells. Cell proliferation experiments showed that overexpression of miR-16-1-3p suppressed the proliferation of MDA-MB-231 and ZR75-1 cells (**Figure 4A** and **Supplementary Figure 2A**). These effects were reversed by PGK1 reexpression in the miR-16-1-3p-transfected cell lines. Overexpression of miR-16-1-3p also revealed reduced migration and invasion ability (**Figures 4B,C** and **Supplementary Figures 2B,C**). Again, PGK1 reexpression in the miR-16-1-3p-transfected cells reversed these effects. Conversely, anti-miR-16-1-3p increased breast cancer cell proliferation, migration, and invasion in MDA-MB-231 and ZR75-1 cells (**Figures 4D–F** and **Supplementary Figures 2D–F**). PGK1 knockdown had opposite effects. Importantly, PGK1 knockdown abolished the ability of anti-miR-16-1-3p to increase breast cancer cell proliferation, migration, and invasion. Moreover, miR-16-1-3p mimics increased expression of E-cadherin, an epithelial marker, and decreased that of Vimentin, a mesenchymal marker (**Figure 4G**), while anti-16-1-3p had opposite effects (**Figure 4H**), suggesting that miR-16-1-3p may regulate epithelial-mesenchymal transition (EMT), a process critical for cancer cell migration and invasion. Taken together, these results suggest that miR-16-1-3p inhibits breast

[1]http://www.microrna.org/

[2]http://www.targetscan.org/

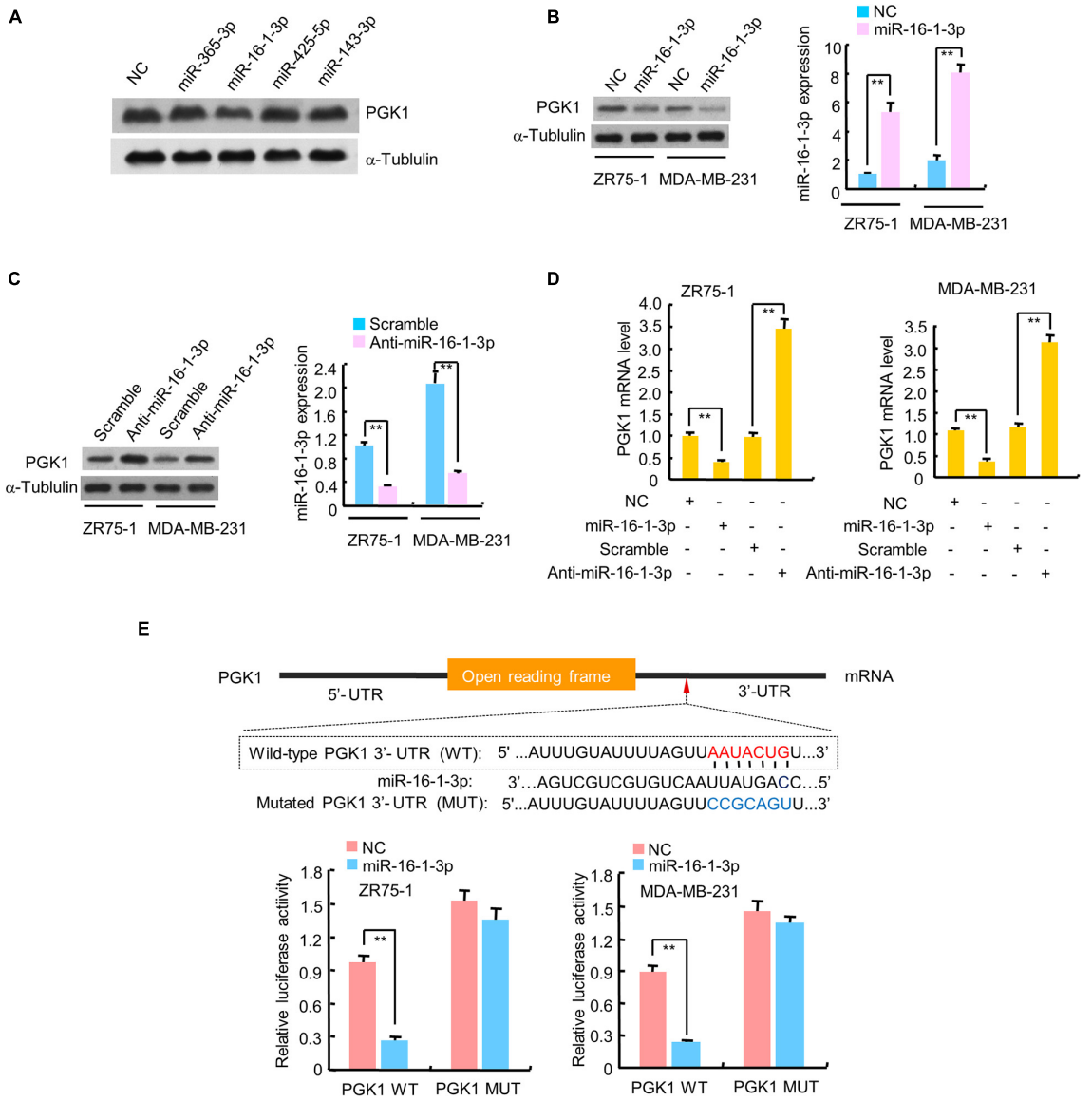

FIGURE 1 | miR-16-1-3p suppresses PGK1 expression by directly targeting its 3′-UTR in breast cancer cells. **(A)** HEK293T cells were transfected with negative control (NC) for miRNAs or mimics of candidate miRNAs as indicated. The representative immunoblot shows PGK1 expression. α-Tubulin was used as a loading control. **(B,C)** Immunoblot analysis of PGK1 expression in ZR75-1 and MDA-MB-231 breast cancer cells transfected with **(B)** NC or miR-16-1-3p mimics, or **(C)** scramble for miRNA inhibitors or miR-16-1-3p inhibitor (anti-miR-16-1-3p). Right histograms indicate relative miR-16-1-3p expression by RT-qPCR. **(D)** RT-qPCR analysis of PGK1 mRNA expression in ZR75-1 and MDA-MB-231 cells transfected as in panels **(B,C)**. **(E)** miRNA luciferase reporter assays of ZR75-1 and MDA-MB-231 cells transfected with wild-type (WT) or mutated (MUT) PGK1 reporter plus miR-16-1-3p mimics. The top panel indicates WT and MUT forms of putative miR-16-1-3p target sequences of PGK1 3′-UTR. Red font indicates the putative miR-16-1-3p binding sites within human PGK1 3′-UTR. Blue font shows the mutations introduced into the PGK1 3′-UTR. Data shown are mean ± SD of triplicate measurements that were repeated three times with similar results. $^{**}P < 0.01$.

cancer cell proliferation, migration and invasion by repressing PGK1 expression.

The MiR-16-1-3p/PGK1 Axis Regulates Tumor Glycolysis, Growth and Metastasis in Nude Mice

To investigate the effect of the miR-16-1-3p/PGK1 axis on breast tumor growth *in vivo*, we used MDA-MB-231 cells harboring anti-miR-16-1-3p or PGK1 shRNA or anti-miR-16-1-3p plus PGK1 shRNA to inject the mammary fat pads of BALB/c nude mice. The results showed that tumor growth was significantly slower in the PGK1 shRNA group and faster in the anti-miR-16-1-3p group than that in the control group (**Figure 5A**). Moreover, the ability of anti-miR-16-1-3p to promote tumor growth was compromised by PGK1 knockdown. After analyzing lactate production and PGK1 expression of representative tumor tissues, we found that PGK1 expression

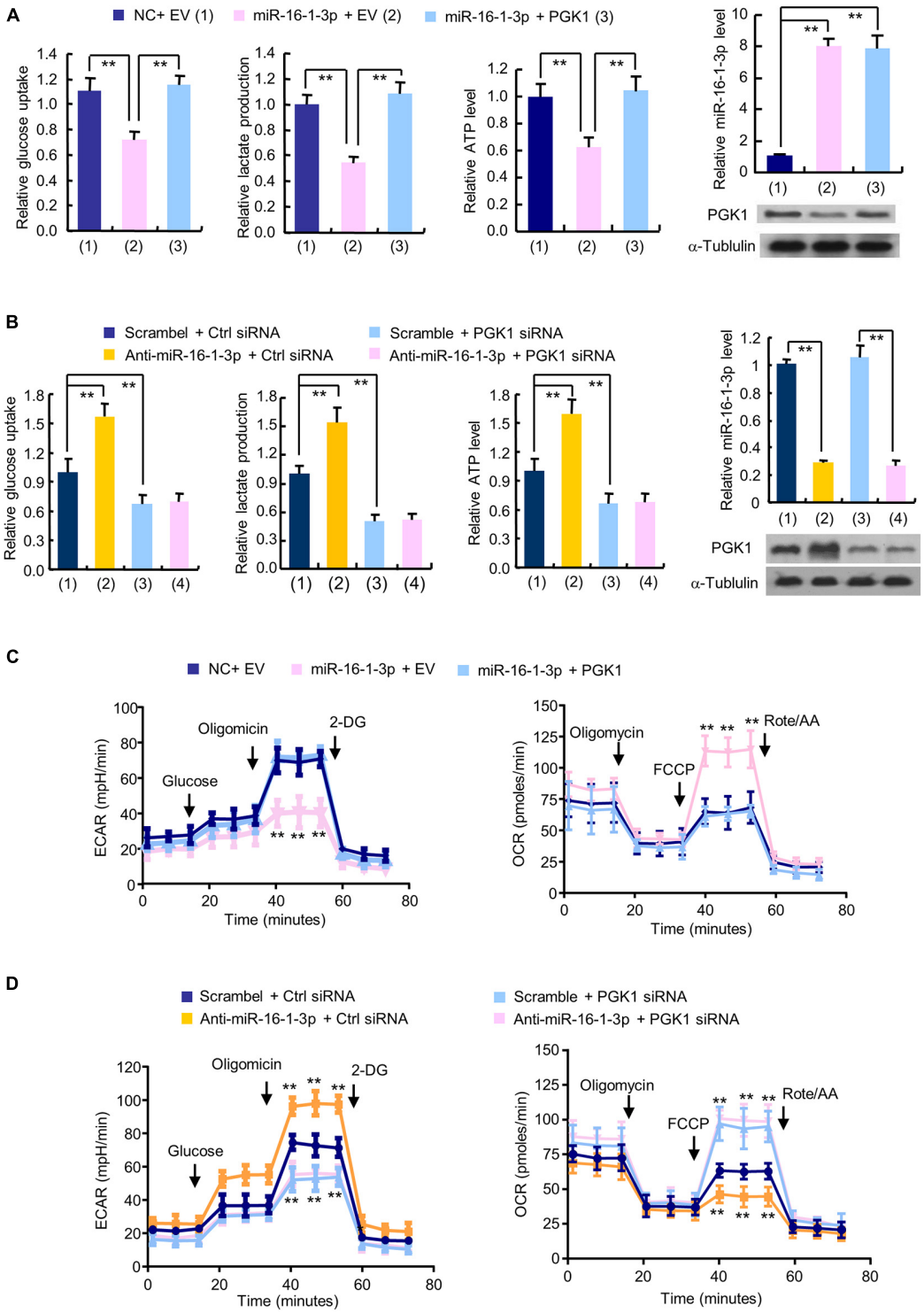

FIGURE 2 | The miR-16-1-3p/PGK1 axis modulates aerobic glycolysis in breast cancer cells. **(A)** Glucose uptake and the production of lactate and ATP were examined in MDA-MB-231 cells transfected with miR-16-1-3p or miR-16-1-3p plus PGK1 expression vector as indicated. EV, empty vector. **(B)** Glucose uptake and the production of lactate and ATP were examined in MDA-MB-231 cells transfected with anti-miR-16-1-3p, PGK1 siRNA or anti-miR-16-1-3p plus PGK1 siRNA. Ctrl siRNA, control siRNA. Representative immunoblot shows PGK1 expression, and RT-qPCR analysis indicates miR-16-1-3p expression **(A,B)**. **(C)** ECAR and OCR assays of MDA-MB-231 cells transfected as in panel **(A)**. **(D)** ECAR and OCR assays of MDA-MB-231 cells transfected as in panel **(B)**. Data shown are mean ± SD of quintuplicate measurements that were repeated three times with similar results [panels **(A,B)** for glucose uptake and the production of lactate and ATP]. Data shown are mean ± SD of triplicate measurements that were repeated three times with similar results (A and B for RT-qPCR analysis). $^{**}P < 0.01$ **(A,B)**. Data shown are mean ± SD of quintuplicate measurements that were repeated 3 times with similar results **(C,D)**. $^{**}P < 0.01$ vs NC plus EV or Scramble plus Ctrl shRNA **(C,D)**.

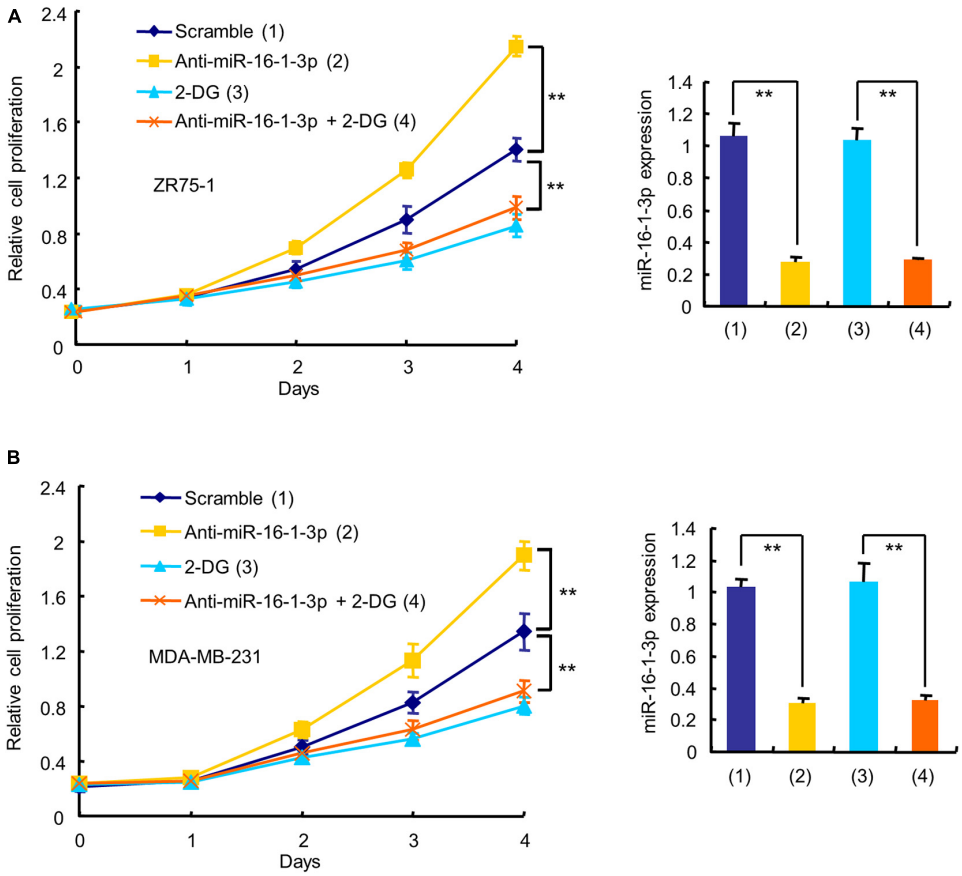

FIGURE 3 | Aerobic glycolysis is responsible for miR-16-1-3p modulation of breast cancer cell proliferation. The proliferation curve shows ZR75-1 **(A)** and MDA-MB-231 **(B)** cells transfected with anti-miR-16-1-3p or scramble and treated with 2.5 mM 2-DG as indicated. RT-qPCR reveals miR-16-1-3p expression. Data shown are mean ± SD of triplicate measurements that were repeated three times with similar results. $^{**}P < 0.01$.

was stimulated by anti-miR-16-1-3p, and anti-miR-16-1-3p promoted lactate production via PGK1 (**Figure 5A**). These results suggest that miR-16-1-3p inhibits tumor growth via PGK1-mediated glycolysis.

Next, we explored whether the miR-16-1-3p/PGK1 axis regulates breast cancer metastasis. The results showed that the luminescence signal in the lung region of mice in the anti-miR-16-1-3p group and the PGK1 shRNA group was significantly stronger or weaker, respectively, than that in the control group (**Figure 5B**). Similar results were observed with the number of nodules in the lung region of mice in the anti-miR-16-1-3p group and the PGK1 shRNA group (**Figure 5C**). Importantly, the anti-miR-16-1-3p's stimulatory effect on breast tumor lung metastasis was abolished by PGK1 knockdown (**Figures 5B,C**). These results suggest that miR-16-1-3p suppresses breast tumor lung metastasis via PGK1.

Association of MiR-16-1-3p With PGK1 Expression and Metatstasis in Human Breast Cancer Patients

Since miR-16-1-3p inhibits PGK1 expression and suppresses breast cancer lung metastasis, we evaluated the expression of miR-16-1-3p and PGK1 by MISH and IHC, respectively, in 91 human breast cancer samples. Consistent with miR-16-1-3p inhibition of PGK1 *in vitro* and in mice, there was a negative correlation between miR-16-1-3p and PGK1 expression in breast cancer patients (**Figure 6A**). Moreover, miR-16-1-3p expression negatively correlated with breast cancer lung metatstasis, and PGK1 expression positively associated with breast cancer lung metatstasis (**Figure 6B**). The specificity of the anti-PGK1 antibody and the miR-16-1-3p probe used was confirmed (**Supplementary Figure 3**). In addition, miR-16-1-3p negatively correlated with tumor size, nodal status, and grade (**Supplementary Table 1**), and PGK1 positively correlated with tumor size, nodal status, and grade (**Supplementary Table 2**). Breast cancer patients with decreased miR-16-1-3p expression had shorter disease-free survival (**Supplementary Figure 4A**), and breast cancer patients with decreased PGK1 expression had longer disease-free survival (**Supplementary Figure 4B**). Taken together, these data suggest that the miR-16-1-3p/PGK1 axis plays an important pathological role in human breast cancer.

On the other hand, we compared miR-16-1-3p expression between breast cancer tissues and matched normal tissues from TCGA (The Cancer Genome Atlas) dataset. Surprisingly, miR-16-1-3p expression was upregulated in breast cancer tissues

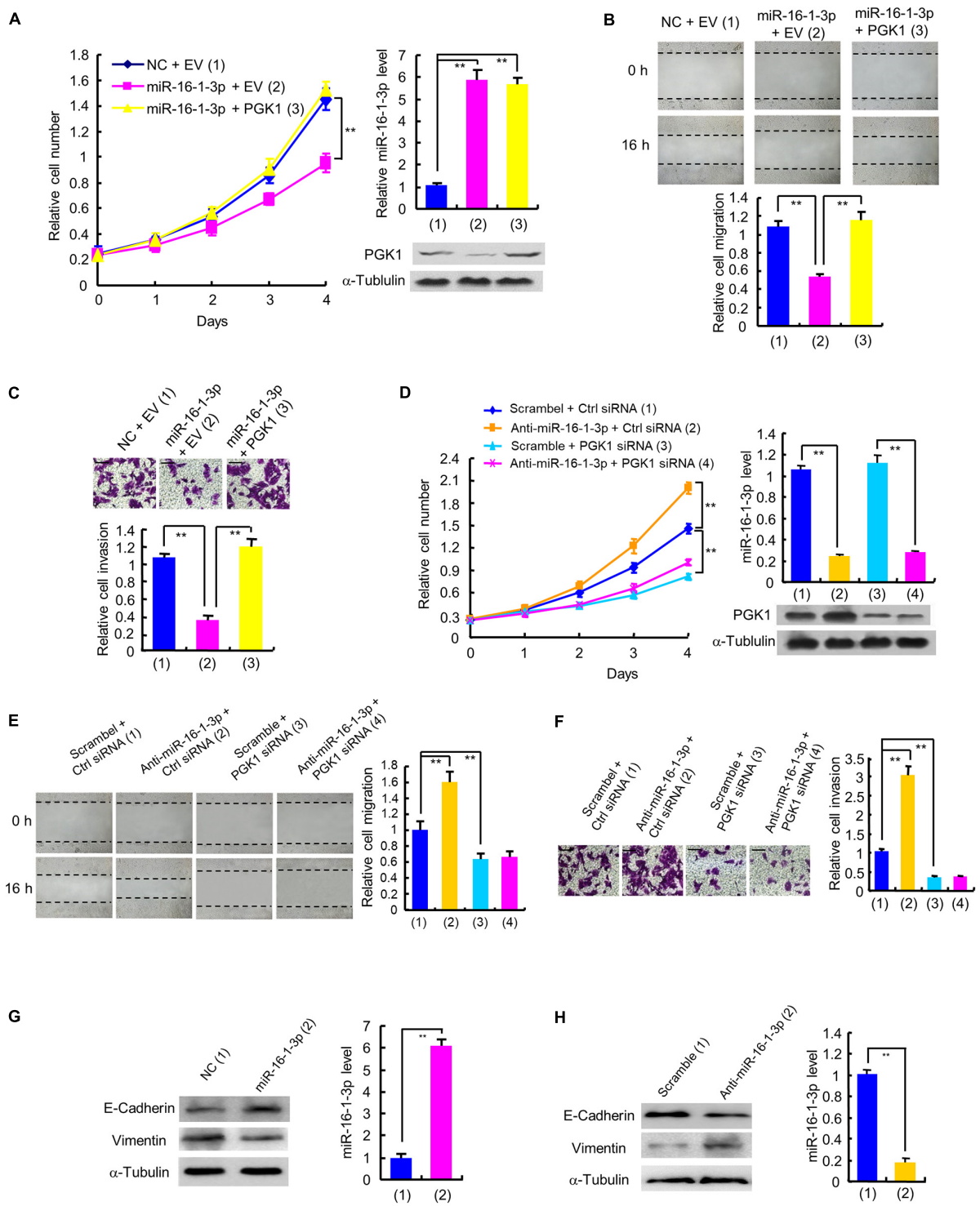

FIGURE 4 | miR-16-1-3p inhibits proliferation, migration and invasion by inhibiting PGK1 expression in breast cancer cells. **(A)** The proliferation curve of MDA-MB-231 cells transfected with miR-16-1-3p mimics or miR-16-1-3p mimics plus PGK1 expression plasmid as indicated. Immunoblot analysis shows PGK1 expression. RT-qPCR indicates miR-16-1-3p expression. **(B,C)** Wound healing **(B)** and invasion **(C)** assays of MDA-MB-231 cells transfected as in panel **(A)**. Histograms denote relative cell migration **(B)** and invasion **(C)**. **(D)** The proliferation curve of MDA-MB-231 cells transfected with anti-miR-16-1-3p, PGK1 siRNA or anti-miR-16-1-3p plus PGK1 siRNA as indicated. Immunoblot analysis shows PGK1 expression. RT-qPCR indicates miR-16-1-3p expression. **(E,F)** Wound healing **(E)** and invasion **(F)** assays of MDA-MB-231 cells transfected as in panel **(D)**. Histograms show relative cell migration **(E)** and invasion **(F)**. All values shown are mean ± SD of triplicate measurements that were repeated three times with similar results. **(G)** Immunoblot analysis of E-Cadherin and Vimentin expression in MDA-MB-231 cells transfected with NC or miR-16-1-3p mimics. **(H)** Immunoblot analysis of E-Cadherin and Vimentin expression in MDA-MB-231 cells transfected with scramble or miR-16-1-3p inhibitor. $^{**}P < 0.01$.

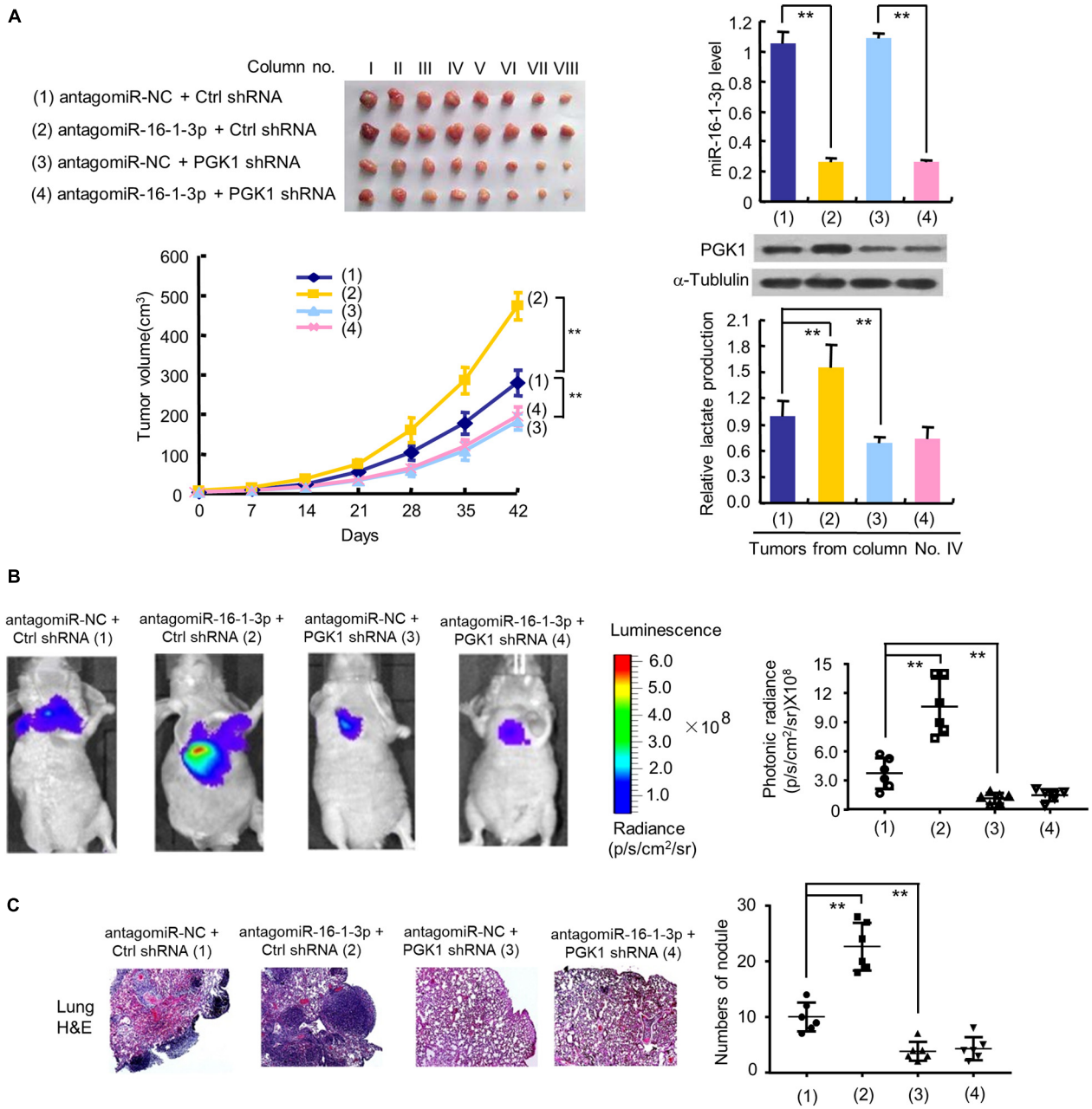

FIGURE 5 | The miR-16-1-3p/PGK1 axis regulates breast tumor growth and metastasis in nude mice. **(A)** MDA-MB-231 cells stably infected with lentivirus harboring PGK1 shRNA or control shRNA (Ctrl shRNA) were treated with antagomiR-16-1-3p or antagomiR-NC and injected into nude mice as indicated. After 42 days, mice were euthanized to harvest tumors. Images of all xenograft tumors excised at day 42 are shown. The tumor growth curves were plotted. Lactate production of representative tumor tissues was measured. miR-16-1-3p and PGK1 expression of representative tumor tissues was determined by RT-qPCR and immunoblot, respectively. Tumor volumes are presented as means ± SD (n = 8). $^{**}P < 0.01$ at day 42. Data shown are mean ± SD of quintuplicate measurements for lactate production that were repeated 3 times with similar results. $^{**}P < 0.01$. **(B)** Representative bioluminescence images at 30 days of nude mice injected by tail vein with MDA-MB-231 cells expressing firefly luciferase and the indicated constructs (n = 6). The luminescence signal is represented by an overlaid false-color image with the signal intensity indicated by the scale **(right panel)**. **(C)** Representative H&E-stained sections of the lung tissues from **(B)**. The number of tumor nodules are shown **(right panel)**. $^{**}P < 0.01$ **(B,C)**.

(**Supplementary Figure 4C**). However, miR-16-1-3p expression was downregulated in plasma of breast cancer patients from GSE58606 dataset (**Supplementary Figure 4D**). Thus, the clinical significance of miR-16-1-3p in breast cancer needs further validation. Furthermore, there was no correlation between miR-16-1-3p expression and PGK1 mRNA expression in 764 cases of infiltrating ductal carcinoma from TCGA dataset (**Supplementary Figure 4E**). The discrepancy in the correlation

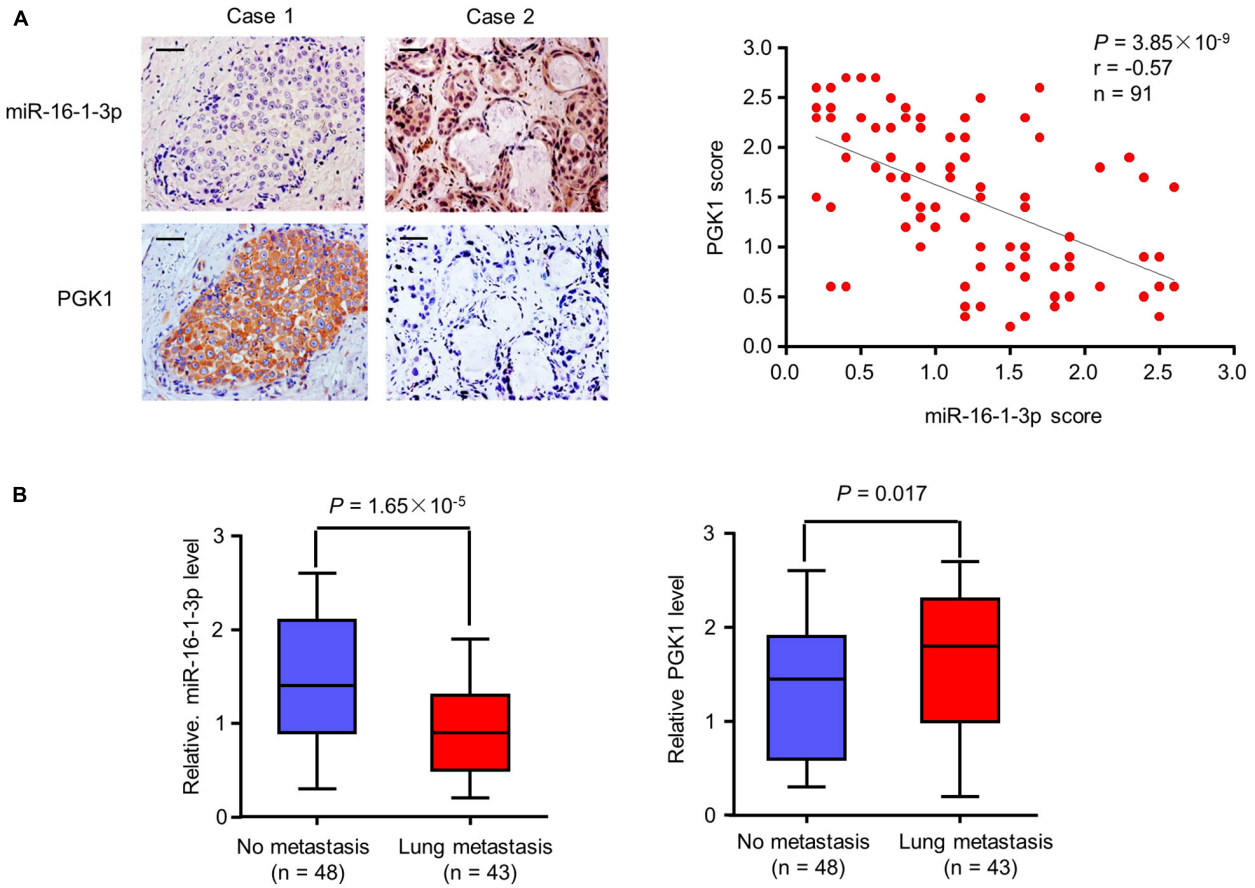

FIGURE 6 | Correlation of miR-16-1-3p expression with PGK1 expression and metastasis in breast cancer patients. **(A)** Correlation between miR-16-1-3p and PGK1 expression in 91 breast cancer patients. miR-16-1-3p and PGK1 expression was assessed by MISH and IHC, respectively. Scale bar: 100 μm. The *P* value was generated using Spearman's Rank Correlation test. **(B)** Association of miR-16-1-3p expression with metastasis. The *P* value was generated using independent *t* test.

between results of our study and those from the TCGA dataset may be that PGK1 expression was examined in this study at the protein level but not at the mRNA level shown in the TCGA dataset, and only ductal breast carcinoma was detected in the TCGA dataset, while besides ductal breast carcinoma, other breast cancer types such as lobular breast carcinoma were also examined in this study.

DISCUSSION

In recent years, the relationship between tumor glucose metabolism and anti-tumor therapy has become a research hotspot. One of the salient features of tumor metabolism is reprogramming of energy metabolism, which is manifested by abnormal glucose metabolism. Even when oxygen is sufficient, tumor cells still tend to undergo glycolysis and metabolize glucose to lactic acid. The aerobic glycolytic capacity of tumor cells is 20–30 times that of normal cells, which provides a lot of energy and intermediate products for tumor metabolism. Thus, targeting metabolic enzymes in abnormal metabolic pathways such as glycolytic pathway has become the focus of anti-tumor therapy (Gill et al., 2016; Abdel-Wahab et al., 2019; Kim, 2019; Weiss, 2020). Researchers are exploring the abnormal regulation of glucose metabolism in tumors and the inhibitors targeting related metabolic responses so as to facilitate better treatment and prognosis for tumor patients by inhibiting tumor glycolysis or switching to normal metabolic pathways.

Phosphoglycerate kinase 1 is one of the key enzymes in tumor glucose metabolism. High PGK1 expression was shown in various human cancers and correlated with poor prognosis of cancer patients (Ahmad et al., 2013; Hu et al., 2017; Fu et al., 2018). Phosphoglycerate kinase 1 promotes cancer cell proliferation, invasion and metastasis (Zhang et al., 2019, 2020; Fu and Yu, 2020). Because of this, scientists are working hard to explore PGK1 inhibitors. Very recently, miRNA-450b-3p, miR-548c-5p, miRNA-215-5p, and miR-6869-5p have been reported to directly target PGK1 3′-UTR and repress PGK1 expression (Chen et al., 2019, 2020; Ge et al., 2019; Wang et al., 2020). However, it remains unknown whether these miRNAs regulate the Warburg effect and whether the Warburg effect is responsible for cancer cell growth by these miRNAs. In this study, we discovered for the first time that miR-16-1-3p is another PGK1 inhibitor, and can modulate cancer cell growth and metatstasis by a variety of biological

function tests. Importantly, we revealed that in human breast cancer, miR-16-1-3p can inhibit tumor glycolysis by repressing glucose uptake and lactate production, with decreased ECAR and increased OCR. MiR-16-1-3p plays an important role in regulation of PGK1-mediated Warburg effect and breast cancer cell proliferation, migration, invasion, and metastasis. In breast cancer specimens, miR-16-1-3p expression is inversely correlated with PGK1 expression. Therefore, miR-16-1-3p activation may have a positive effect on the treatment of breast cancer patients with PGK1 overexpression.

MiRNAs have been shown to play an important role in cancer development and progression. However, the biological functions of miR-16-1-3p in cancer are largely unknown. MiR-16-1-3p was shown to act as a tumor suppressor (Wang et al., 2017). MiR-16-1-3p negatively regulates transcription factor Twist1 to inhibit NSCLC cell migration and invasion (Feng et al., 2018). MiR-16-1-3p has powerful tumor suppressive and anti-metastatic properties in osteosarcoma (Maximov et al., 2019). Except for gastric cancer, osteosarcoma and lung cancer, the biological function of miR-16-1-3p in other cancers remains unclear. In this study, we showed that miR-16-1-3p represses breast cancer cell proliferation, migration, invasion, and metastasis. MiR-16-1-3p expression was downregulated in breast cancer samples we collected. Cancer cells inhibit miRNA expression via various factors, such as methylation of CpG islands in miRNA promoters, transcription factors, long non-coding RNAs (lncRNAs), etc. For example, CpG islands of miR-137 promoter are hypermethylated in endometrial cancers (Zhang W. et al., 2018), resulting in lower miR-137 expression. The transcription factor c-Myc represses miR-129-5p expression in hepatocellular carcinoma (Han et al., 2016). Overexpression of lncRNA CASC11 promotes bladder cancer cell proliferation via inhibition of miR-150 expression (Luo et al., 2019). The mechanisms by which miR-16-1-3p is repressed in breast cancer require to be investigated. Moreover, we also used *in vitro* and *in vivo* experiments to tightly combine the Warburg effect with cancer cell proliferation, migration and invasion regulated by miR-16-1-3p, enriching the theory of tumor glycolysis at the molecular level.

CONCLUSION

Our study revealed for the first time that miR-16-1-3p inhibits tumor glycolysis by targeting PGK1 both *in vitro* and *in vivo*, thereby repressing breast cancer cell proliferation, migration, invasion, and metastasis. In breast cancer patients, the abundance of miR-16-1-3p is inversely related to PGK1 expression. Therefore, up-regulating miR-16-1-3p may provide new treatment ideas for cancer patients, especially breast cancer patients with PGK1 overexpression.

DATA AVAILABILITY STATEMENT

The raw data supporting the conclusions of this article will be made available by the authors, without undue reservation.

ETHICS STATEMENT

The studies involving human participants were reviewed and approved by the Ethics Committee of the Chinese PLA General Hospital. The patients/participants provided their written informed consent to participate in this study. The animal study was reviewed and approved by the Institutional Animal Care and Use Committee of Beijing Institute of Biotechnology.

AUTHOR CONTRIBUTIONS

XZ conceived the project, designed the study, and analyzed the data. TY designed and performed the experiments and analyzed the data, aided by YL and DZ. TY and XZ wrote the manuscript. All authors contributed to the interpretation of the data and approved the content of the manuscript.

FUNDING

This work was supported by National Natural Science Foundation of China (81760728 and 81802756).

ACKNOWLEDGMENTS

We thank Jing Lin (the Chinese PLA General Hospital, Beijing, China) for providing the clinical samples.

SUPPLEMENTARY MATERIAL

The Supplementary Material for this article can be found online at: https://www.frontiersin.org/articles/10.3389/fcell.2020.615154/full#supplementary-material

REFERENCES

Abdel-Wahab, A. F., Mahmoud, W., and Al-Harizy, R. M. (2019). Targeting glucose metabolism to suppress cancer progression: prospective of anti-glycolytic cancer therapy. *Pharmacol. Res.* 150:104511. doi: 10.1016/j.phrs.2019.104511

Adams, B. D., Parsons, C., Walker, L., Zhang, W. C., and Slack, F. J. (2017). Targeting noncoding RNAs in disease. *J. Clin. Invest.* 127, 761–771.

Ahmad, S. S., Glatzle, J., Bajaeifer, K., Bühler, S., Lehmann, T., Königsrainer, I., et al. (2013). Phosphoglycerate kinase 1 as a promoter of metastasis in colon cancer. *Int. J. Oncol.* 43, 586–590. doi: 10.3892/ijo.2013.1971

Chen, J. Y., Xu, L. F., Hu, H. L., Wen, Y. Q., Chen, D., and Liu, W. H. (2020). MiRNA-215-5p alleviates the metastasis of prostate cancer by targeting PGK1. *Eur. Rev. Med. Pharmacol. Sci.* 24, 639–646.

Chen, Z., Zhuang, W., Wang, Z., Xiao, W., Don, W., Li, X., et al. (2019). MicroRNA-450b-3p inhibits cell growth by targeting phosphoglycerate kinase 1 in hepatocellular carcinoma. *J. Cell. Biochem.* 120, 18805–18815. doi: 10.1002/jcb.29196

Dykxhoorn, D. M. (2010). MicroRNAs and metastasis: little RNAs go a long way. *Cancer Res.* 70, 6401–6406. doi: 10.1158/0008-5472.can-10-1346

Feng, Q. Q., Dong, Z. Q., Zhou, Y., Zhang, H., and Long, C. (2018). miR-16-1-3p targets TWIST1 to inhibit cell proliferation and invasion in NSCLC. *Bratisl Lek Listy* 119, 60–65. doi: 10.4149/bll_2018_012

Fu, D., He, C., Wei, J., Zhang, Z., Luo, Y., Tan, H., et al. (2018). PGK1 is a potential survival biomarker and invasion promoter by regulating the HIF-1α-Mediated epithelial-mesenchymal transition process in Breast Cancer. *Cell. Physiol. Biochem.* 51, 2434–2444. doi: 10.1159/000495900

Fu, Q., and Yu, Z. (2020). Phosphoglycerate kinase 1 (PGK1) in cancer: a promising target for diagnosis and therapy. *Life Sci.* 256:117863. doi: 10.1016/j.lfs.2020.117863

Ge, J., Li, J., Na, S., Wang, P., Zhao, G., and Zhang, X. (2019). miR-548c-5p inhibits colorectal cancer cell proliferation by targeting PGK1. *J. Cell. Physiol.* 234, 18872–18878. doi: 10.1002/jcp.28525

Gill, K. S., Fernandes, P., O'Donovan, T. R., McKenna, S. L., Doddakula, K. K., Power, D. G., et al. (2016). Glycolysis inhibition as a cancer treatment and its role in an anti-tumour immune response. *Biochim. Biophys. Acta* 1866, 87–105. doi: 10.1016/j.bbcan.2016.06.005

Han, H., Li, W., Shen, H., Zhang, J., Zhu, Y., and Li, Y. (2016). microRNA-129-5p, a c-Myc negative target, affects hepatocellular carcinoma progression by blocking the Warburg effect. *J Mol Cell Biol.* 8, 400–410. doi: 10.1093/jmcb/mjw010

He, Y., Luo, Y., Zhang, D., Wang, X., Zhang, P., Li, H., et al. (2019). PGK1-mediated cancer progression and drug resistance. *Am. J. Cancer Res.* 9, 2280–2302.

Hu, H., Zhu, W., Qin, J., Chen, M., Gong, L., Li, L., et al. (2017). Acetylation of PGK1 promotes liver cancer cell proliferation and tumorigenesis. *Hepatology* 65, 515–528. doi: 10.1002/hep.28887

Kim, S. Y. (2019). Targeting cancer energy metabolism: a potential systemic cure for cancer. *Arch. Pharm. Res.* 42, 140–149. doi: 10.1007/s12272-019-01115-2

Li, L., Liang, Y., Kang, L., Liu, Y., Gao, S., Chen, S., et al. (2018). Transcriptional regulation of the Warburg effect in Cancer by SIX1. *Cancer Cell* 33, 368–385. doi: 10.1016/j.ccell.2018.01.010

Lu, J. (2019). The Warburg metabolism fuels tumor metastasis. *Cancer Metastasis Rev.* 38, 157–164. doi: 10.1007/s10555-019-09794-5

Luo, H., Xu, C., Le, W., Ge, B., and Wang, T. (2019). lncRNA CASC11 promotes cancer cell proliferation in bladder cancer through miRNA-150. *J. Cell Biochem.* 120, 13487–13493. doi: 10.1002/jcb.28622

Maximov, V. V., Akkawi, R., Khawaled, S., Salah, Z., Jaber, L., Barhoum, A., et al. (2019). MiR-16-1-3p and miR-16-2-3p possess strong tumor suppressive and antimetastatic properties in osteosarcoma. *Int. J. Cancer* 145, 3052–3063. doi: 10.1002/ijc.32368

Meijer, T. W., Kaanders, J. H., Span, P. N., and Bussink, J. (2012). Targeting hypoxia, HIF-1, and tumor glucose metabolism to improve radiotherapy efficacy. *Clin. Cancer Res.* 18, 5585–5594. doi: 10.1158/1078-0432.ccr-12-0858

Mulrane, L., McGee, S. F., Gallagher, W. M., and O'Connor, D. P. (2013). miRNA dysregulation in breast cancer. *Cancer Res.* 73, 6554–6562. doi: 10.1158/0008-5472.can-13-1841

Nagao, A., Kobayashi, M., Koyasu, S., Chow, C. C. T., and Harada, H. (2019). HIF-1-dependent reprogramming of glucose metabolic pathway of cancer cells and its therapeutic significance. *Int. J. Mol. Sci.* 20:238. doi: 10.3390/ijms20020238

Pereira-Nunes, A., Afonso, J., Granja, S., and Baltazar, F. (2020). Lactate and lactate transporters as key players in the maintenance of the Warburg effect. *Adv. Exp. Med. Biol.* 1219, 51–74. doi: 10.1007/978-3-030-34025-4_3

Qian, X., Li, X., Shi, Z., Xia, Y., Cai, Q., Xu, D., et al. (2019). PTEN Suppresses glycolysis by dephosphorylating and inhibiting autophosphorylated PGK1. *Mol. Cell* 76, 516–527. doi: 10.1016/j.molcel.2019.08.006

Schwartz, L., Supuran, C. T., and Alfarouk, K. O. (2017). The Warburg effect and the hallmarks of Cancer. *Anticancer Agents Med. Chem.* 17, 164–170. doi: 10.2174/1871520616666161031143301

Shen, J., and Hung, M. C. (2015). Signaling-mediated regulation of MicroRNA processing. *Cancer Res.* 75, 783–791. doi: 10.1158/0008-5472.can-14-2568

Tekade, R. K., and Sun, X. (2017). The Warburg effect and glucose-derived cancer theranostics. *Drug Discov. Today* 22, 1637–1653. doi: 10.1016/j.drudis.2017.08.003

Wang, F., Zhang, H., Liu, B., Liu, W., and Zhang, Z. (2020). miR-6869-5p inhibits glioma cell proliferation and invasion via targeting PGK1. *Mediators Inflamm.* 2020:9752372.

Wang, T., Hou, J., Li, Z., Zheng, Z., Wei, J., Song, D., et al. (2017). miR-15a-3p and miR-16-1-3p negatively regulate twist1 to repress gastric cancer cell invasion and metastasis. *Int. J. Biol. Sci.* 13, 122–134. doi: 10.7150/ijbs.14770

Weiss, J. M. (2020). The promise and peril of targeting cell metabolism for cancer therapy. *Cancer Immunol. Immunother.* 69, 255–261. doi: 10.1007/s00262-019-02432-7

Zhang, H., Xie, X., Zhu, X., Zhu, J., Hao, C., Lu, Q., et al. (2005). Stimulatory cross-talk between NFAT3 and estrogen receptor in breast cancer cells. *J. Biol. Chem.* 280, 43188–43197. doi: 10.1074/jbc.m506598200

Zhang, J., Zhang, J., Wei, Y., Li, Q., and Wang, Q. (2019). ACTL6A regulates follicle-stimulating hormone-driven glycolysis in ovarian cancer cells via PGK1. *Cell Death Dis.* 10:811.

Zhang, W., Chen, J. H., Shan, T., Aguilera-Barrantes, I., Wang, L. S., Huang, T. H., et al. (2018). miR-137 is a tumor suppressor in endometrial cancer and is repressed by DNA hypermethylation. *Lab Invest.* 98, 1397–1407. doi: 10.1038/s41374-018-0092-x

Zhang, Y., Yu, G., Chu, H., Wang, X., Xiong, L., Cai, G., et al. (2018). Macrophage-Associated PGK1 phosphorylation promotes aerobic glycolysis and tumorigenesis. *Mol. Cell* 71, 201–215. doi: 10.1016/j.molcel.2018.06.023

Zhang, Y., Cai, H., Liao, Y., Zhu, Y., Wang, F., and Hou, J. (2020). Activation of PGK1 under hypoxic conditions promotes glycolysis and increases stem cell-like properties and the epithelial-mesenchymal transition in oral squamous cell carcinoma cells via the AKT signalling pathway. *Int. J. Oncol.* 57, 743–755. doi: 10.3892/ijo.2020.5083

Conflict of Interest: The authors declare that the research was conducted in the absence of any commercial or financial relationships that could be construed as a potential conflict of interest.

frontiers in Cell and Developmental Biology

CORRECTION
published: 21 January 2021
doi: 10.3389/fcell.2021.649787

Corrigendum: MicroRNA-16-1-3p Represses Breast Tumor Growth and Metastasis by Inhibiting PGK1-Mediated Warburg Effect

Tianxing Ye[1,2], *Yingchun Liang*[2], *Deyu Zhang*[2] *and Xuewu Zhang*[1]*

[1] College of Medicine, Yanbian University, Yanji, China, [2] Department of Medical Molecular Biology, Beijing Institute of Biotechnology, Collaborative Innovation Center for Cancer Medicine, Beijing, China

Keywords: the Warburg effect, PGK1, miR-16-1-3p, cell proliferation, metastasis

OPEN ACCESS

Approved by:
Frontiers Editorial Office, Frontiers Media SA, Switzerland

***Correspondence:**
Xuewu Zhang
zhangxuewu@ybu.edu.cn; zhangxuewu18@163.com

Specialty section:
This article was submitted to Molecular Medicine, a section of the journal Frontiers in Cell and Developmental Biology

Received: *05 January 2021*
Accepted: *06 January 2021*
Published: *21 January 2021*

Citation:
Ye T, Liang Y, Zhang D and Zhang X (2021) Corrigendum: MicroRNA-16-1-3p Represses Breast Tumor Growth and Metastasis by Inhibiting PGK1-Mediated Warburg Effect. Front. Cell Dev. Biol. 9:649787. doi: 10.3389/fcell.2021.649787

A Corrigendum on

MicroRNA-16-1-3p Represses Breast Tumor Growth and Metastasis by Inhibiting PGK1-Mediated Warburg Effect

by Ye, T., Liang, Y., Zhang, D., and Zhang, X. (2020) Front. Cell Dev. Biol. 8:615154. doi: 10.3389/fcell.2020.615154

An author name was incorrectly spelled as **Tianxin Ye**. The correct spelling is **Tianxing Ye**.

The authors apologize for this error and state that this does not change the scientific conclusions of the article in any way. The original article has been updated.

frontiers in Cell and Developmental Biology

REVIEW
published: 04 February 2021
doi: 10.3389/fcell.2021.613534

Cancer-Associated Fibroblasts Suppress Cancer Development: The Other Side of the Coin

Zhanhuai Wang[1], Qi Yang[2], Yinuo Tan[3], Yang Tang[1], Jun Ye[4], Bin Yuan[5] and Wei Yu[6]**

[1] Department of Colorectal Surgery and Oncology, Key Laboratory of Cancer Prevention and Intervention, Ministry of Education, The Second Affiliated Hospital, Zhejiang University School of Medicine, Hangzhou, China, [2] Department of Pathology, The Second Affiliated Hospital, Zhejiang University School of Medicine, Hangzhou, China, [3] Department of Medical Oncology, Key Laboratory of Cancer Prevention and Intervention, Ministry of Education, The Second Affiliated Hospital, Zhejiang University School of Medicine, Hangzhou, China, [4] Department of Gastroenterology, The Second Affiliated Hospital, Zhejiang University School of Medicine, Hangzhou, China, [5] Department of Biochemistry and Molecular Medicine, School of Medicine and Health Sciences, The George Washington University, Washington, DC, United States, [6] Department of Radiation Oncology, Key Laboratory of Cancer Prevention and Intervention, Ministry of Education, The Second Affiliated Hospital, Zhejiang University School of Medicine, Hangzhou, China

OPEN ACCESS

Edited by:
Alexander D. Borowsky, University of California, Davis, United States

Reviewed by:
Michele Bernasconi, University Children's Hospital Bern, Switzerland
Huarong Chen, The Chinese University of Hong Kong, China
Ruth Birbe, Cooper Medical School of Rowan University, United States

***Correspondence:**
Wei Yu
Wei-yu@zju.edu.cn
Bin Yuan
yuanbin@gwu.edu

Specialty section:
This article was submitted to Molecular Medicine, a section of the journal Frontiers in Cell and Developmental Biology

Received: *02 October 2020*
Accepted: *15 January 2021*
Published: *04 February 2021*

Citation:
Wang Z, Yang Q, Tan Y, Tang Y, Ye J, Yuan B and Yu W (2021) Cancer-Associated Fibroblasts Suppress Cancer Development: The Other Side of the Coin. Front. Cell Dev. Biol. 9:613534. doi: 10.3389/fcell.2021.613534

Cancer-associated fibroblasts (CAFs) are the main stromal components of cancer, representing a group of heterogeneous cells. Many studies indicate that CAFs promote tumor development. Besides, evidence of the tumor suppression effects of CAFs keeps on merging. In the tumor microenvironment, multiple stimuli can activate fibroblasts. Notably, this does not necessarily mean the activated CAFs become strong tumor promoters immediately. The varying degree of CAFs activation makes quiescent CAFs, tumor-restraining CAFs, and tumor-promoting CAFs. Quiescent CAFs and tumor-restraining CAFs are more present in early-stage cancer, while comparatively, more tumor-promoting CAFs present in advanced-stage cancer. The underlying mechanism that balances tumor promotion or tumor inhibition effects of CAFs is mostly unknown. This review focus on the inhibitory effects of CAFs on cancer development. We describe the heterogeneous origin, markers, and metabolism in the CAFs population. Transgenetic mouse models that deplete CAFs or deplete CAFs activation signaling in the tumor stroma present direct evidence of CAFs protective effects against cancer. Moreover, we outline CAFs subpopulation and CAFs derived soluble factors that act as a tumor suppressor. Single-cell RNA-sequencing on CAFs population provides us new insight to classify CAFs subsets. Understanding the full picture of CAFs will help translate CAFs biology from bench to bedside and develop new strategies to improve precision cancer therapy.

Keywords: cancer-associated fibroblasts, neoplasms, tumor microenvironment, biomarker, Humans

Abbreviations: CAFs, cancer-associated fibroblasts; CAC, colitis associated-colon cancer; DNMT1, DNA (cytosine-5)-methyltransferase 1; Evs, extracellular vesicles; HCC, hepatocellular carcinoma; HGF, hepatocyte growth factor; HR, hormone receptor; IHC, Immunohistochemistry; ISH, *in situ* hybridization; NFs, normal fibroblasts; OSCC, oral squamous cell carcinoma; PDAC, pancreatic ductal adenocarcinoma; TNBC, triple-negative breast cancer.

INTRODUCTION

Fibroblasts are one of the significant stromal components in many organs, e.g., the gastrointestinal tract. They participate in adjacent tissue components' function through paracrine signaling and juxtacrine signaling (Biswas et al., 2015; Kalluri, 2016). One of their most crucial tasks is regulating ECM synthesis. When tissue injury happens, fibroblasts are getting ready to respond. They actively act to restrain the injury place and reconstruct the wound tissue framework. The classic description of cancer is "wounds that never heal." Could fibroblasts act as potential defenders against cancer progression? Numerous studies are being carried out to answer this question, but the results are unclear or sometimes contradicting. Generally, fibroblasts observed within and adjacent to the cancer are termed as cancer-associated fibroblasts (CAFs). In practice, the criteria to define CAFs are (1) mesenchymal cell isolated from a tumor; (2) negative markers for epithelial cells, endothelial cells and leukocyte markers; (3) elongated morphology; and (4) exclude the mutations of cancer cells (Sahai et al., 2020). CAFs are a group of heterogeneous cells and are the most prevalent stromal components of the tumor microenvironment. Previous studies have focused on tumor cells, yet now, it is increasingly recognized that the stromal components of the tumor microenvironment play critical roles in cancer progression (Hanahan and Weinberg, 2011). Importantly, CAFs play diverse parts in the interaction between different components in the tumor microenvironment. Thus, in cancer biology, understanding the functional evolution of CAFs during cancer development becomes a fundamental question to answer.

In the tumor microenvironment, potential stimuli that activate fibroblasts include bone morphogenetic protein (BMP), interleukin-1, interleukin-6, platelet-derived growth factor (PDGF), sonic hedgehog (SHH), reactive oxygen species (ROS), transforming growth factor-β (TGF-β), as well as TNF. These stimuli are released by tumor cells and multiple stromal components, including CAFs themselves (Theiss et al., 2005; Erez et al., 2010; Kalluri, 2016). The activated fibroblasts specifically express α smooth muscle actin (α-SMA), fibroblast activation protein (FAP), fibroblast-specific protein 1 (FSP1), PDGF receptor-β (PDGFRβ), and some other myofibroblasts markers. α-SMA, a cytoskeleton protein, functions as a cell contraction regulator, is most commonly used as an activated fibroblast marker (Ohlund et al., 2014; Kalluri, 2016; Sahai et al., 2020). Cell morphology is a reliable way to distinguish activated CAFs within the quiescent fibroblasts. Activated CAFs undergo morphological changes from spindle-shaped into cruciform or stellate shaped. They become more proliferative, migrative, and metabolically active, with the enhanced acquisition of ECM production and synthetic phenotype. They have different epigenetic expression pattern compared to quiescent fibroblasts (Albrengues et al., 2015; Zhang et al., 2015; Kalluri, 2016). Notably, the activation of fibroblasts by stimuli in the tumor microenvironment does not necessarily mean these activated CAFs become strong cancer promoters immediately. Indeed, the varying degree of CAFs activation patterns produce quiescent CAFs, tumor-restraining CAFs, and tumor-promoting CAFs (Sugimoto et al., 2006; Kobayashi et al., 2019). Quiescent CAFs and tumor-restraining CAFs are frequently present in early-stage cancer, while comparatively, more tumor-promoting CAFs are predominantly present in advanced-stage disease. The chronic activation of CAFs requires continuous cross-talk between CAFs and cancer cells. This permanent cross-talk educates CAFs to accquire the pro-tumorigenic ability. Meanwhile, the stimuli that promote CAFs activation are essential factors that enhance tumor niche formation (Roberts et al., 2017). The co-evolution of CAFs and cancer cells continues throughout all the cancer progression stages (**Figures 1**, **2**).

The tumor microenvironment plays a key part in fostering tumor progression through the collaboration of multiple components. Besides, evidence of the tumor inhibition effects of individual cancer stromal component keeps on merging. The underlying mechanism that balances tumor promotion or tumor inhibition effects of the tumor microenvironment is mostly unknown. Most studies that explore CAFs functions show that CAFs support tumor growth. Naturally, the reverse side evidence of this is much less. If the tumor stroma inhibiting effect continuously exists, the tumor can not necessarily develop. Failure to educate quiescent fibroblasts to acquire pro-tumorigenic ability means tumor cells might not survive (Mueller and Fusenig, 2004; Proia and Kuperwasser, 2005). In the very beginning of tumorigenesis, tumor cells conduct a dedicated education system to reprogram CAFs and other tumor stroma cells. In the later stage, tumor cells deliver messages to distant healthy organs stroma to build a pre-metastatic stromal niche (Hanahan and Weinberg, 2011). Recently, tumor associated-extracellular vesicles (EVs) have been identified as an important cellular interchange mechanism between tumor cells and CAFs (Becker et al., 2016; Maacha et al., 2019). EVs isolated from tumor cells and CAFs are implicated in multi-steps of CAFs evolution, such as normal fibroblasts (NFs) differentiation into CAFs, CAF-like state maintenance, and CAFs' function support (Luga et al., 2012; Webber et al., 2015; Richards et al., 2017; Giusti et al., 2018).

Understanding the time point when CAFs shift from tumor defender into tumor supporter is critically essential. Thus, preventing CAFs functional change from a tumor-supportive phenotype will be potentially promising in anti-tumor therapy. This review focus on the inhibitory effects of CAFs on cancer development. We describe the heterogeneous origin, markers, and metabolism in the CAFs population. Transgenetic mouse models that deplete CAFs or deplete CAFs activation signaling in the tumor stroma present direct evidence of CAFs' protective effects against cancer. Moreover, we outline CAFs subpopulation and CAFs derived soluble factors that act as a tumor suppressor. Single-cell RNA-sequencing on CAFs population provides us new insight to classify CAFs subsets. The main findings concerning the tumor inhibitory effects of CAFs are list in **Table 1**.

THE HETEROGENEITY OF CAFS POPULATION

Heterogenous CAFs Origin

Despite the highly organized NFs, the CAFs population is highly heterogeneous. The origin of CAFs is still contested. The direct correlation between CAFs subtype function and CAFs subtype

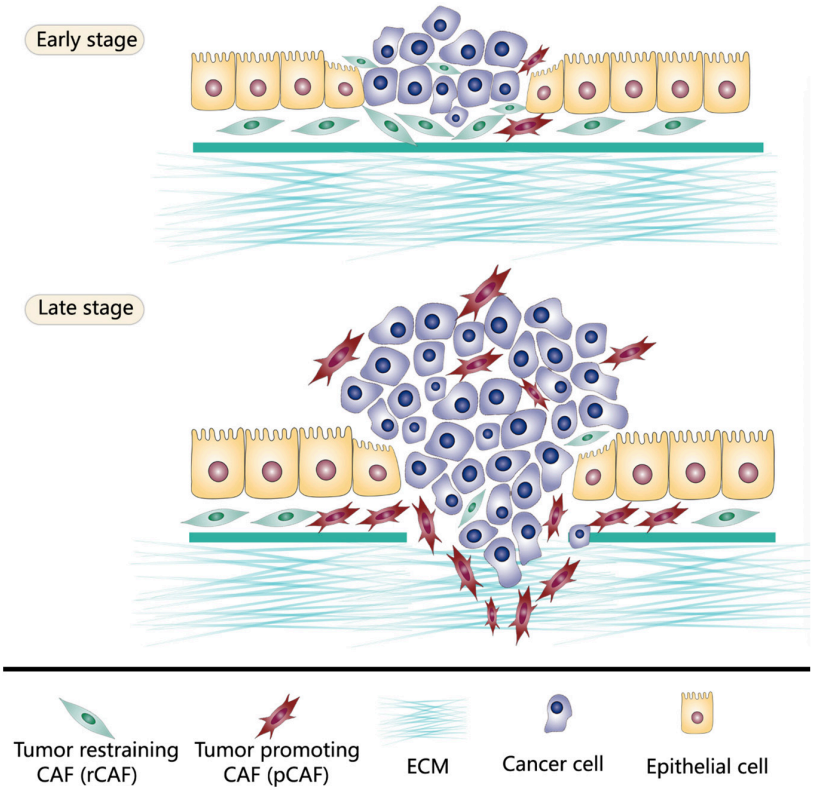

FIGURE 1 | Tumor-restraining CAFs (rCAFs) and tumor-promoting CAFs (pCAFs) both exist in the tumor microenvironment. rCAFs are frequently present in early-stage cancer which protect normal tissue against cancer invasiveness. However, in advanced-stage disease, tumor cells reprogram CAFs through continuous messages exchange to build cancer supporting stromal niche. Thus, pCAFs are predominantly present in late-stage cancer.

cellular origin is not clearly illustrated. However, it is convincing that CAFs originated from different cell lineages might have distinct functional phenotypes (Ishii et al., 2015; Sahai et al., 2020). In general, CAFs have four main sources of cellular origin. The primary source is normal local fibroblasts, which are activated by stimuli from the tumor microenvironment. Mesenchymal stem cells (MSCs) and other mesenchymal precursor cells are other sources. They are recruited to the TME to become CAFs-state cells by cytokines and chemokines, including TGF-β and CXC-chemokine ligand 12 (CXCL12; Koliaraki et al., 2017). Endothelial cells and epithelial cells do not belong to the fibroblast lineage, but they could transdifferentiate into CAFs-state cells. Finally, a self-renewable CAFs-stem cell population might exist in the hierarchical organization, and these cells share similar characteristics as MSCs. They differentiate into progeny CAFs including cancer-promoting CAFs and cancer-restraining CAFs (Worthley et al., 2015).

Heterogenous CAFs Marker

Studies to identify CAF subsets are still in their infancy. In the experiment, CAFs are isolated through flow cytometry-based cell sorting by using a series of combined markers. The markers that CAFs lack expression of are CD31 (an endothelial marker), CD45 (a hematopoietic cell marker), desmin (a smooth muscle cell marker), and EPCAM (epithelial cell adhesion molecule, an epithelial cell marker). These markers are combined with a representative CAFs marker (e.g., FAP) for CAFs sorting (Feig et al., 2013; Calon et al., 2015; Costa et al., 2018). The most commonly used CAFs markers include but are not limited to α-SMA, Collegen1A1, FAP, FSP1, PDGFRα and PDGFRβ, Podoplanin, and vimentin. However, all of these markers are not CAFs specific and can be expressed in other cell types in cancer or normal tissues (Kalluri, 2016). α-SMA is unable to identify all CAFs in the TME, and it is expressed in smooth muscle in normal gastrointestinal and vascular (Koliaraki et al., 2017; Ohlund et al., 2017). FAP combined with CD45 is used to label a subgroup of cancer-associated macrophages (Arnold et al., 2014). FSP1 also corresponds to epithelial cells experiencing epithelial-to-mesenchymal transition (EMT; Rhim et al., 2012; Fischer et al., 2015). In a liver fibrosis model, FSP1 distinguishes inflammatory macrophage subpopulation (Osterreicher et al., 2011). The different origins of CAFs add to the complexity of CAFs definitions. A sole CAFs marker is impossible to find theoretically. Depending on different markers used, different results regarding CAFs pro-tumorigenic function (pCAFs) or CAFs tumor-restain (rCAFs) function can be obtained (Kobayashi et al., 2019). One of the most urgent works required in CAFs biology is to explore the different markers of subtype CAFs based on biology and function.

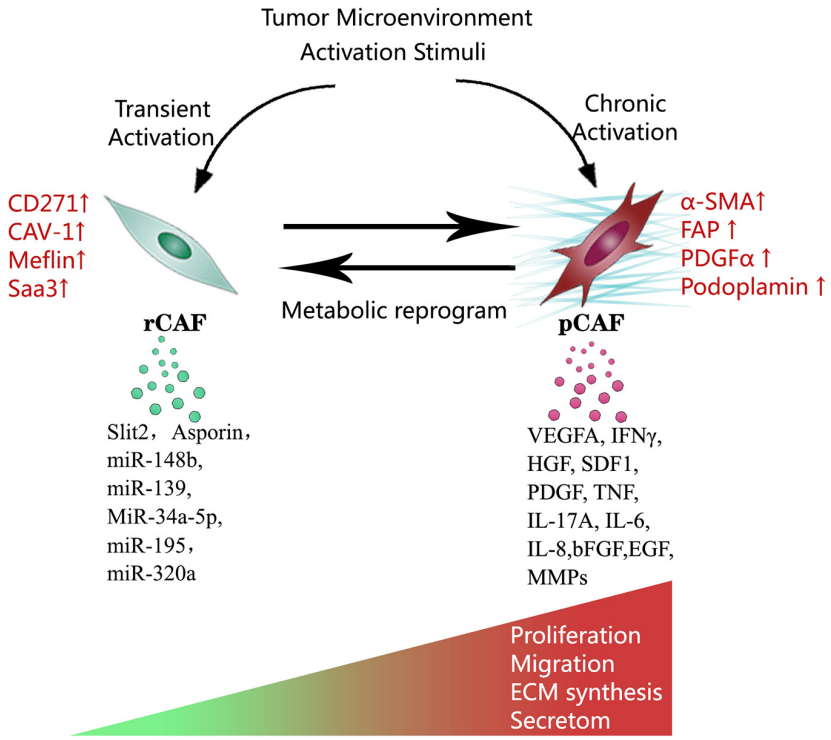

FIGURE 2 | Multiple stimuli in the tumor microenvironment activate CAFs. Notably, this activation process does not necessarily mean the activated CAFs become strong cancer promoters immediately. Depending on the degree of activation, CAFs can be functionally divided into tumor-restraining CAFs, and tumor-promoting CAFs. Transient activation makes tumor-restraining CAFs and chronic activation makes tumor-promoting CAFs. Tumor-restraining CAFs are morphologically similar to quiescent fibroblasts. Tumor-promoting CAFs undergo morphological changes from spindle-shaped into cruciform or stellate shaped. Two types of CAFs show the main difference in cellular markers, metabolic status, proliferation, migration, ECM synthesis, and secretory phenotype.

Heterogenous CAFs Metabolism

Traditionally, the glycolytic pathway has been considered the main metabolic pathway in cancer. Recent studies revealed that cancers are highly organized tissues and are categorized with heterogeneous metabolism in different components (Wallace, 2012). Even in the CAFs population, the heterogeneous metabolic status also exists. Compared to quiescent fibroblasts, parts of activated CAFs undergo metabolic changes and become catabolic CAFs. Biomarkers of this catabolic CAFs phenotype including down-regulated caveolin-1 (Cav-1; Martinez-Outschoorn et al., 2011) and up-regulated monocarboxylate transporter 4 (MCT4; Whitaker-Menezes et al., 2011). Cav-1 is abundantly expressed in NFs. Loss of Cav-1 expression is an autophagy marker, indicating decreased mitochondrial metabolisms, such as oxidative phosphorylation (OXPHOS), increasing glycolysis and oxidative stress (Sotgia et al., 2011). MCT4, with its expression controlled by HIF-1, is the main cellular lactate exporter (Ullah et al., 2006). Recent studies demonstrate the collaboration of catabolic fibroblasts and anabolic cancer cells, which is the so-called metabolic coupling. This metabolic coupling exists in many different human malignancies, such as breast cancer, head and neck cancer, and prostate cancer (Giatromanolaki et al., 2012; Witkiewicz et al., 2012; Curry et al., 2013). The driving pathway of catabolic CAFs are HIF1-α, NFκB signaling, and TGF-β signaling, promoting autophagy, glycolysis, oxidative stress, and senescence (Martinez-Outschoorn et al., 2014). These catabolic CAFs generate local mitochondrial fuels, such as fatty acids, glutamine, ketone bodies, lactate, to support the cancer microenvironment (Martinez-Outschoorn et al., 2014). Noticed that not all the CAFs become catabolic CAFs, the catabolic CAFs and the anabolic CAFs both exist. The catabolic changes of CAFs could be reversed upon anti-oxidants treatments (Yang et al., 2016; Monti et al., 2017; Zhang et al., 2018). Does the transformation from tumor-restraining CAFs into tumor-promoting CAFs accompany with catabolic phenotype changes? The answer is still not clear. Explore the heterogeneity in CAFs metabolism will help us to classify CAFs in a critical functional aspect.

THE PROTECTIVE ACTION OF CAFS AGAINST CANCER: EVIDENCE FROM TRANSGENIC MICE

Depletion of CAFs Enhances Tumor Development

The transgenic mouse model allows us to deplete CAFs through germline mutation or organ-specifically in mature tissue. Such a model helps to investigate roles that CAFs

TABLE 1 | Studies focus on the tumor inhibitory effects of CAFs.

Author	Cancer type	Main findings
Dai et al., 2019	Mice pancreatic cancer	1 In RAMP3-/- mice, spleen injection of PAN02 murine pancreatic cancer cells showed reduced liver metastasis. 2 RAMP3-/- mice metastatic tumor showed decreased podoplanin positive or α-SMA positive CAFs. 3 Primary RAMP3-/- CAFs inhibited proliferation, migration, and metastasis in co-cultures with PAN02 murine pancreatic cancer cells.
Mizutani et al., 2019	Mice Pancreatic ductal adenocarcinoma (PDAC)	1 Meflin is expressed in CAFs originate from pancreatic stellate cells 2 Meflin positive CAFs showed decreased a-SMA expression and stromal collagen regulating 3 Meflin negative CAFs showed more aggressive pro-tumorigenic functions 4 Meflin knockout mice showed a poorly differentiated tumor with more a-SMA + CAFs compared to Meflin wild type mice
Djurec et al., 2018	Mice PDAC	1 PDGFRα + Saa3 + CAFs stimulated mice PDAC growth, but PDGFRα + Saa3- CAFs inhibited tumor growth. 2 The PDGFRα + Saa3- CAFs inhibited tumor growth by overexpression Mpp6
Gerling et al., 2016	Mice colitis associated-colon cancer (CAC)	1 Downstream Hh signaling is restricted to the tumor stroma particularly in CAFs 2 Hh signaling deletion in CAFs promoted tumorigenesis, whereas Hh activation inhibited tumor progression 3 Hh signaling in CAFs suppressed tumor by regulating BMP activity and inhibting colonic stem cell signature
Maris et al., 2015	Breast cancer	1 Asporin suppressed TGF-β1-mediated SMAD2 phosphorylation, EMT, and cancer stem cell signature. 2 Asporin overexpression CAFs reduce tumor growth in the mice xenograft TNBC model
Koliaraki et al., 2015	Mice CAC	Genetic deletion of IKKβ in COLVI + CAFs caused decreased tumor growth and inflammation in the CAC mice model. The effect is mainly due to the down-regulated IL-6 release in IKKβ-deficient CAFs compared to control
Pallangyo et al., 2015	Mice CAC	1 Genetic deletion of IKKβ in COL1A2 + CAFs in mice colon cancer accelerated tumor growth 2 IKKβ-deficient COL1A2 + CAFs showed enhanced secretion of HGF, which promoted tumor growth through HGF–Met signaling
Ozdemir et al., 2014	Mice PDAC	1 Effects of genetic a-SMA + myofibroblast depletion were test in both early and late stage PDAC 2 a-SMA + myofibroblast depletion tumor showed more invasive, undifferentiated, and necrotic characteristics with a poor survival compared to control.
Rhim et al., 2014	Mice PDAC	1 SHH-deficient PDAC showed decreased a-SMA-positive myofibroblasts compared to the control tumor. 2 SHH-deficient PDAC exhibited undifferentiated histology, increased proliferation, vascularity, and reduced survival time.
Zhang et al., 2013	Mice skin fibrosarcoma	1 FSP1 was predominantly expressed in procollagen I + fibroblasts in mice skin 2 Genetic deletion of FSP1 + CAFs enhanced mice skin fibrosarcoma formation
Chang et al., 2012	Breast cancer	1 CAFs derived Slit2 conducted its tumor inhibition effects by bind to Robo1 receptor expressed in cancer cells.

Abbreviations: *CAC, colitis associated-colon cancer; Evs, extracellular vesicles; HGF, hepatocyte growth factor; HR, hormone receptor; OSCC, Oral squamous cell carcinoma; PDAC, Pancreatic ductal adenocarcinoma; and TNBC, triple-negative breast cancer.*

play in different stages of carcinogenesis. What happens if CAFs are diminished in certain types of tumors? Results of recent studies strikingly indicated that CAFs depletion causes rapid tumor progression rather than tumor suppression. a-SMA is one of the most commonly used CAFs markers, distinguishing activated fibroblasts from the quiescent fibroblasts in tumor microenvironments (Kalluri, 2016). Ozdemir et al., applied a genetic approach to deplete a-SMA + myofibroblasts in mice selectively. They aimed to examine the function of a-SMA + myofibroblasts in early-stage, as well as late-stage pancreatic ductal adenocarcinoma (PDAC). They crossed a-SMA- thymidine kinase (TK) transgenic mice that allowed target depletion of a-SMA + myofibroblasts and the mice that developed spontaneous PDAC. By crossed two type of mice, a-SMA + myofibroblasts could be selectively depleted in PDAC tissue. The effects of a-SMA + myofibroblasts depletion were analyzed in both early-stage and late-stage PDAC. Compared to control, a-SMA + myofibroblast depletion tumor was significantly more invasive, undifferentiated, and necrotic. Mice bearing a-SMA + myofibroblast depletion tumor ended up with multiple adverse outcomes. The author also suggested that a-SMA + myofibroblast produced collagen I and the associated fibrosis protected the host against tumorigenesis at both early and late stages of PDAC (Ozdemir et al., 2014). Zhang et al. tested the hypothesis of whether depletion FSP1 fibroblasts impair skin fibrosarcoma formation. The author applied FSP-TK transgenic mice, which allowed FSP1 + cells to be selectively depleted upon administration of ganciclovir (GCV; Salomon et al., 1995; Iwano et al., 2001). Zhang et al. found that FSP1 was predominantly expressed in procollagen I + fibroblasts in mice skin. Thus, FSP1 + depletion in stromal cells mainly caused CAFs depletion. Mice model of skin fibrosarcoma was induced via carcinogen methylcholanthrene (MCA) subcutaneous injection. A Ablation of FSP1 + cells enhanced tumor formation and altered skin fibrosarcoma morphology. Interestingly, these skin tumors showed epithelial phenotype instead of fibroblastoid. The author also showed that degrading collagen produced by fibroblasts promoted tumor formation in the long-term "tumor-free" mice. These findings indicated that FSP1 + CAFs and collagens exert a critical protective role against chemical induced fibrosarcoma in the skin (Zhang et al., 2013).

Depletion of Activation Signaling in CAFs Enhances Tumor Progression

Cancer-associated fibroblasts activation signaling relies on various stimuli from the TME, and SHH is one of these. SHH, a soluble ligand of hedgehog signaling, is frequently overexpressed by neoplastic cells, which stimulates CAFs to form a fibroblast-rich desmoplastic stroma (Valenti et al., 2017). Earlier studies indicated that over activation of hedgehog-signaling accelerated tumorigenesis in the pancreatic epithelium

(Mao et al., 2006; Pasca Di Magliano et al., 2006; Morton et al., 2007). Since the deletion of SHH expression might impair CAFs activation signaling, what is the impact on malignant progression if SHH expression is removed from cancer cells? Rhim et al used the transgenic mice to delete SHH in the PDAC model. The SHH-deficient tumor showed decreased stromal content, especially a-SMA-positive myofibroblasts, compared to the control tumor. These tumors exhibited more aggressive features with undifferentiated histology, increased proliferation, and vascularity. SHH deletion also caused more frequent acinar-to-ductal metaplasia (ADM) and pancreatic intraepithelial neoplasia (PanIN) at a younger age. Thus, SHH deletion lead to rapid death in mice. SHH deletion in pancreatic cancer showed increased Zeb1 and Slug expression consistent with EMTs and increased metastasis (Rhim et al., 2014). Similar results were reported in a mouse model of colitis-associated colonic tumorigenesis. In that study, Gerling et al applied hedgehog (Hh) signaling reporter mice. They demonstrated that Hh signaling deletion promoted tumorigenesis, whereas stroma-specific Hh activation significantly attenuated tumor progression. Activated Hh signaling in CAFs suppressed tumor growth through regulating BMP activity and inhibiting colonic stem cell gene expression (Gerling et al., 2016). The IKKβ-dependent NF-κB signaling activation is considered as a key to connect inflammation and carcinogenesis (Greten et al., 2004). CAFs from the cervical, mammary, pancreatic, and skin tumors exhibit a proinflammatory signature regulated by NF-κB signaling (Erez et al., 2010). Two separate studies probed the effects of IKKβ on CAFs during tumor development. The first study used Tg (CollagenVI-Cre) mice, which allowed tracing of the distribution of collagen type VI positive (COLVI +) fibroblasts in the mice intestine. Tg (CollagenVI-Cre) mice were crossed with $Ikk\beta^{F/F}$ mice to generate IKKβ deficient COLVI + fibroblasts. These transgenic mice were further applied with AOM/DSS to form colitis-associated cancer (CAC). IKKβ deficiency in COLVI + CAFs caused decreased tumor growth and inflammation in the CAC mice model. The effect is mainly due to the down-regulated IL-6 release in IKKβ-deficient CAFs compared to control (Koliaraki et al., 2015). The second study, however, showed the tumor-restraining function of IKKβ/NF-κB in CAFs. Koliaraki et al used a different Cre, collagen type a2 Cre (Col1a2-creER), to trace fibroblasts. And IkkβF/F mice were crossed with Col1a2-creER mice. COL1A2 + fibroblasts represent a larger population than COLVI + fibroblasts. The genetic deletion of IKKβ in COL1A2 + CAFs in the similar CAC model unexpectedly accelerated tumor growth. The Ikkβ deficient CAFs showed impaired Smad7 and Smurf1, which were both TGF-β pathway negative regulators. Thus, the upregulation of TGF-β signaling was observed in Ikkβ deficient CAFs. Moreover, these CAFs showed enhanced secretion of hepatocyte growth factor (HGF), which promoted tumor growth through HGF–Met signaling (Pallangyo et al., 2015). Since COL1A2 targets nearly 80% of PDGFRα + fibroblasts, COL1A2 + fibroblasts comprised a much larger fibroblasts population than COLVI + fibroblasts. The possible explanation of conflict results is that different fibroblast subpopulations may exhibit distinct IKKβ/NF-κB signaling functions. Meanwhile, CAFs display different activation status could display different NF-κB signaling status.

CAFS SUBPOPULATION INHIBIT TUMOR PROGRESSION

Despite numerous results indicating CAFs' pro-tumorigenic effects, here, we provide shreds of evidence that CAFs subsets restrain tumor progression. Djurec et al., showed that PDGFRα + CAFs derived from a PDAC mouse model promoted tumor cell growth, and that normal pancreatic fibroblasts inhibited tumor growth. When PDGFRα + CAFs were subdivided by the expression of Saa3, a protein belonging to the acute-phase serum amyloid A (SAA) apolipoprotein family, PDGFRα + Saa3- CAFs and PDGFRα + Saa3 + CAF showed different properties. PDGFRα + Saa3 + CAFs stimulated mice PDAC growth in both the orthotopic model and organoid cultures; however, PDGFRα + Saa3- CAFs inhibited tumor growth. The PDGFRα + Saa3- CAFs exerted their tumor inhibition effects by overexpressing membrane palmitoylated protein 6 (Mpp6). This study sheds light on the future direction of target therapy through the management of Mpp6 expression (Djurec et al., 2018). Dai et al found that RAMP3 deficient CAFs inhibited tumor growth and metastasis. RAMPs, receptor-activity-modifying proteins, are modulators of G-protein-coupled receptors, which function as tumor angiogenesis regulator and prognostic marker (Mclatchie et al., 1998; Fang et al., 2018; Mackie et al., 2019). In RAMP3-/- mice, spleen injection of PAN02 murine pancreatic cancer cells showed significantly reduced liver metastasis. Compared to wild-type mice, liver metastatic lesion in RAMP3-/- mice showed decreased podoplanin positive or α-SMA positive CAFs. Moreover, primary cultured RAMP3-/- CAFs inhibited proliferation, migration, and metastasis in co-cultures with PAN02 murine pancreatic cancer cells *in vitro* and *in vivo* (Dai et al., 2019). Meflin is a mesenchymal stromal/stem cell marker and indicates their undifferentiated state. In pancreatic cancer, Meflin is expressed in CAFs originate from pancreatic stellate cells. Meflin positive CAFs showed decreased a-SMA expression and stromal collagen regulation, while Meflin negative CAFs showed more aggressive pro-tumorigenic functions. In the mouse PDAC model, Meflin knockout mice showed a poorly differentiated tumor with more a-SMA + CAFs compared to Meflin wild type mice. Results suggested Meflin served as a tumor-restraining CAFs marker in PDAC (Mizutani et al., 2019).

CAFS DERIVED SOLUBLE FACTORS SUPPRESS TUMOR PROGRESSION

Cancer-associated fibroblasts support cancer progression by secreting various soluble factors, whereas CAFs can also derive tumor restraining factors. In breast cancer, CAFs derived Slit2 acted as a tumor inhibitor. Slit2 exerted tumor suppression effects by binding to Robo1 receptor expressed in cancer cells. Stable Robo1-depletion in breast cancer cells abolished the CAFs tumor

suppression effect in the orthotopic mouse model. Meanwhile, ectopic Robo1 overexpression in breast cancer cells enhanced CAFs related tumor suppression effect. The active Slit2/Robo1 signaling prevented β-catenin translocation into nuclei, which resulted in c-myc and cyclin D1 downregulation through the PI3K/Akt pathway (Chang et al., 2012). Asporin, a stromal secreted extracellular matrix protein, inhibited canonical TGF-β/Smad signaling by binding to TGF-β1 (Kizawa et al., 2005). The expression of asporin in CAFs increased when exposed to gastric cancer cells. CAFs-derived asporin activated CD44-Rac1 pathway in cancer cells and coordinated the co-invasion of these two types of cells (Satoyoshi et al., 2015). Interestingly, asporin functional studies in breast cancer is another story. Triple-negative breast cancer (TNBC) cells suppressed CAFs' asporin expression by secreting IL-1β, while hormone receptor (HR) positive breast cancer induced CAFs asporin expression. *In vitro* studies on breast cancer cells indicated asporin suppressed TGF-β1-mediated SMAD2 phosphorylation, EMT, and cancer stem cell signature. In the murine model of TNBC, asporin overexpression CAFs could significantly reduce tumor growth. The results of the two studies seem to conflict with each other. TGF-β signaling has both tumor suppression and tumor promotion effects depending on the cancer type and cancer stage (Seoane and Gomis, 2017). Asporin is a TGF-β1 natural inhibitor, which might also have various services in different cancer types.

MicroRNAs are known as small molecular RNA, which bind to their target mRNAs and negatively modulate gene expression at the post-transcriptional level. MicroRNAs transferred by exosomes are a common way of communication connecting CAFs and tumor cells (Li et al., 2018). Recently studies investigated the microRNA changes and their function in CAFs derived exosomes. Our previous review illustrates CAFs-derived microRNAs promote cancer development through a variety of approaches (Wang et al., 2017). During tumor progression, CAFs secreted tumor-promoting microRNAs show increased expression and CAFs secreted tumor-suppressing microRNAs are inhibited (Wang et al., 2017). Several studies indicated that tumor-suppressing microRNAs could strongly inhibit tumor development when they were re-expressed in CAFs. These CAFs derived tumor suppressor microRNAs include miR-195 in cholangiocarcinoma (Li L. et al., 2017), MiR-34a-5p in oral squamous cell carcinoma (OSCC; Li et al., 2018), miR-148b in endometrial cancer (Li et al., 2019), miR-139 in gastric cancer (Xu et al., 2019), and miR-320 in hepatocellular carcinoma (HCC; Zhang et al., 2017; **Table 2**).

TABLE 2 | CAFs derived tumor suppression microRNAs.

Author	Cancer type	Main findings
Li et al., 2019	Endometrial cancer	1 MiR-148b decreased in CAFs and CAFs-derived exosomes compared to NFs 2 CAFs derived miR-148b transferred to endometrial cancer cells by exosomes 3 MiR-148b overexpression in CAFs suppressed endometrial cancer metastasis *in vitro* and *in vivo* by directly binding to DNMT1
Xu et al., 2019	Gastric cancer	1 MiR-139 level was down-regulated in tumors compared with adjcent normal tissues 2 Exosomal miR-139 in CAFs was reduced compared to NFs 3 Exosomes shuttled miR-139 from fibroblasts to cancer cells 4 MiR-139 overexpression in CAFs suppressed cancer cells growth and metastasis by inhibiting the expression of MMP11
Li et al., 2018	OSCC	1 MiR-34a-5p in CAF-derived exosomes was reduced compared to NFs 2 Fibroblasts derived exosomal miR-34a-5p could transfer to OSCC cells 3 miR-34a-5p overexpression in CAFs inhibited OSCC cells proliferation and metastasis by binding to AXL in cancer cells
Li L. et al., 2017	Cholangiocarcinoma	1 Cholangiocarcinoma cells and the adjoining CAFs showed down-regulated miR-195 2 EVs shuttled miR-195 from fibroblasts to cancer cells 3 miR-195 overexpression in fibroblasts suppressed growth and invasion of cholangiocarcinoma cells 4 miR-195 loaded EVs inhibit tumor and improve survival of in a rat model of cholangiocarcinoma.
Zhang et al., 2017	HCC	1 miR-320a level was reduced in CAFs-derived exosomes compared to NFs 2 Fibroblasts derived exosomal miR-320a could transfer to HCC cells 3 Exosomal miR-320a binded to PBX3 in HCC cells and inhibited their proliferation and metastasis. 4 MiR-320a-PBX3 axis suppressed tumor progression by inhibiting MAPK pathway acitivation

Abbreviations: *DNMT1, DNA (cytosine-5)-methyltransferase 1; Evs, extracellular vesicles; HCC, hepatocellular carcinoma; HGF, hepatocyte growth factor; HR, hormone receptor; OSCC, Oral squamous cell carcinoma; and TNBC, triple-negative breast cancer.*

CAFS RELATED PROTEIN PROVIDE FAVORABLE CLINICAL OUTCOMES

Many studies have addressed the clinical prognostic value of CAFs markers and CAFs derived factors. These findings include but are not limited to FAP expression in CAFs being related to reduced survival time in non-small cell lung cancer (NSCLC; Liao et al., 2013), podoplanin expression in CAFs related to reduced recurrence-free survival in NSCLC (Ito et al., 2012; Ono et al., 2013), PDGFRβ expression in CAFs related to reduced cancer-specific survival in breast cancer patients (Paulsson et al., 2009). The correlation between particular CAFs related molecular and cancer prognosis, to some extent, reflect the education process of CAFs during tumor progression. Importantly, tumor-restraining CAFs also have particular markers and derived factors, and the increased expression of such molecules in patient samples indicates a better prognosis (**Table 3**). The membrane protein CAV-1 is associated with cell metabolism, modulating autophagy, cholesterol distribution, fatty acid metabolism, glycolysis, glutaminolysis, and mitochondrial bioenergetics. In CAFs, CAV-1 acts as a tumor suppression protein. CAFs that lose

TABLE 3 | CAFs related protein provide favorable clinical outcomes: main findings.

References	Gene	Human cancer type	Methods and patient number	Histopathological findings
Rhim et al., 2014	Meflin	Pancreatic cancer	ISH (*n* = 71)	1 Aproximately 10% of a-SMA + CAFs show positive Meflin mRNA expression in ISH assay. 2 Meflin-high (≥20% Meflin + stromal cells) group showe prognosis and a more differentiated histology than Meflin-low (<20% Meflin + stromal cells) group
Zhang et al., 2017	Asporin	Breast cancer	IHC (*n* = 60) mRNA (*n* = 375)	1 Asporin is low expressed in TNBC and HER2 + tumors, compared with HR + tumor 2 Low asporin express indicated to poor outcome, high asporin expression indicated a favorable outcome
Ono et al., 2013	CD271	Pancreatic cancer	IHC (*n* = 105)	1 CD271 + stromal expression was mostly detected on the tumor edge and was mainly in CAFs 2 CD271 + CAFs predominantly exist in the areas with strong a-SMA expression in the tumor 3 Stromal high CD271 expression represented a better prognosis.
Wang et al., 2017	Cav-1	Breast cancer	IHC (*n* = 358)	1 Cav-1 was predominantly expressed in CAFs in breast cancer 2 Cav-1-positive breast cancer patients showed increased cancer-specific survival compared Cav-1-negative group 3 Cav-1-deficient CAFs enhanced the invasiveness of breast cancer cells.

Abbreviations: *HR, hormone receptor; IHC, Immunohistochemistry; ISH, In situ hybridization; and TNBC, triple-negative breast cancer.*

the expression of Cav-1 undergo a series of metabolic changes and autophagy. The process of autophagy in CAFs stimulates mitochondrial activity in adjacent tumor cells by providing a critical source of energy-rich glutamine (Nwosu et al., 2016). In a retrospective study regarding breast cancer patients, the Cav-1-positive group showed 72 months of cancer-specific survival, whereas the survival time of the Cav-1-negative group was 29.5 months (Simpkins et al., 2012). Cav-1 negative tumors show increased tumor progression, metastasis, and estrogen receptor-negative genotype compared to Cav-1 positive breast cancer (Sloan et al., 2009; Witkiewicz et al., 2009; Qian et al., 2011; Simpkins et al., 2012). Asporin is another tumor inhibitor protein expressed by CAFs in breast cancer. A histopathological study on human breast cancer (*n* = 180) indicated that asporin has low expression in TNBC and HER2 + tumors, which are both aggressive breast cancer types. Survival analysis suggested that low asporin status is an independent risk factor correlated to poor outcome, whereas high asporin expression indicated a favorable outcome (Maris et al., 2015). CD271, a neurotrophin receptor, is also named as the nerve growth factor receptor (NGFR; Liang et al., 2018; Nielsen et al., 2018). The prognostic value of stromal CD271 was assessed in 31 normal pancreases and 105 pancreatic cancer (PDACs) by an IHC assay. Stromal CD271 was express mainly in CAFs, and its high expression represented a better prognosis. Results suggested CD271 + CAFs acts to restrain cancer progression. Interestingly, CD271 + CAFs predominantly existed in the areas with strong a-SMA expression in the tumor, which suggested CD271 + CAFs was a subpopulation of SMA + CAFs. Yet, how SMA + CAFs differentiated into CD271 + CAFs and CD271- CAFs is unknown, and in pancreatic cancer, the functional role of CD271 + CAFs remains to be explored (Fujiwara et al., 2012). In another PDACs related study, approximately 10% of a-SMA + CAFs showed positive Meflin mRNA expression in *In situ* hybridization (ISH) assay. The PDACs tissue samples were divided into Meflin-high (≥20% Meflin + stromal cells) and Meflinlow (<20% Meflin + stromal cells) groups. The Meflin-high group exhibited better prognosis and more differentiated histology than the Meflin-low group, which indicated that Meflin expression in CAFs correlates with a favorable outcome of human patients with PDAC (Mizutani et al., 2019).

SINGLE-CELL RNA-SEQUENCING: A NEW STRATEGY TO CLASSIFY CAFS SUBPOPULATION

The coexistence of tumor restraining and tumor-promoting abilities within the CAFs population seems to be puzzling. These contradictory results can be explained by the existence of CAFs subpopulations with opposing functions. Therefore, it is essential to classify CAFs by combining a couple of different markers to identify their biological characteristics, thereby improving their therapeutic relevance. Using Single-cell RNA-sequencing, we can examine the transcriptome of single cells to distinguish cell subpopulations inferred by the same transcriptional programs. Single-cell RNA-sequencing allows us to recognize fibroblasts subsets within CAFs by restricting analytical cell numbers (Bartoschek et al., 2018). Li H et al analyzed CAFs from human CRC by single-cell RNA sequencing. Based on TGFβ signaling gene expression, CAFs in colorectal cancer were divided into two major subtypes: CAF-As and CAF-Bs. The CAF-As showed a high expression of matrix collagen type I α2 (COL1A2), decorin, metalloproteinase 2 (MMP2). At the same time, CAF-Bs exhibited high expression of myofibroblastic markers such as αSMA, transgelin, and PDGF-α (Li H. et al., 2017). Another study applied single-cell RNA sequencing to explore CAFs from the pancreatic cancer sample. Results verified the existence of previously reported myCAF and iCAF subpopulations (Ohlund et al., 2017) and mapped the gene signatures of these CAFs subsets. Notably, in this study, a new subpopulation of CAFs named "antigen-presenting CAFs" (apCAF) was identified. This subtype CAFs expressed MHC class II (MHCII)–related genes and presented antigens to CD4 + T cells, which regulating immune response (Elyada et al., 2019). The above studies provide evidence that single-cell RNA-sequencing helps to map the gene signature and function of CAFs subpopulations. However, we are still in the beginning to take

advantage of this technique to explain the origin, maker, function, and intratumoral heterogeneity in CAFs.

DISCUSSION

This review summarizes the primary evidence of CAFs' protective role against cancer. Although the hypotheses of a guarding stroma against cancer are not novel, we now possess a more robust picture of CAFs possible tumor restraining reactions. The surprising results that CAFs' depletion in transgenic mice models accelerate tumor progression raise the cautionof non-specific CAFs depletion target therapy. Theoretically, patients can benefit from a successful anti-CAFs therapy as: (1) targeting pCAFs or the pCAFs-releasing factors; (2) normalize pCAFs to NFs; and (3) reprogramming of pCAFs to rCAFs phenotype (Sahai et al., 2020). A good example of normalizing CAFs is targeting the vitamin D receptor in pancreatic cancer. Vitamin D receptor ligand calcipotriol treatment reverted CAFs activation state into a quiescent state. This lead to an increased intratumoral gemcitabine concentration and prolonged survival time (Sherman et al., 2014). Given the reversible CAFs functions and subtypes, targeting pCAFs or reprogramming of pCAFs to rCAFs remains a challenge for the field. It is critically important to identify the individual fibroblast's state in the CAFs population and pre-existing "lineage-restricted" effects that control CAFs phynotypes (Sahai et al., 2020).

Recently, the interaction between CAFs and immune cells in the TME has been increasingly recognized. Many studies in this field conclude that CAFs inhibit host anti-tumor immunity by shaping the immune cells, such as monocytes or neutrophils, into an immunosuppressive phenotype. By contrast, limited results are showing CAFs suppress tumor progression by enhancing host immunity (Ziani et al., 2018). Based on the above evidence of CAFs' tumor inhibition effects, we believe that a particular CAFs subtype, which can strengthen host anti-tumor immunity might exist in the early cancer stage. A more delicate co-culture system needs to established and explore the cross-talk between tumor cells, CAFs subtype, and immune cells.

Fundamentally, CAFs biology will be best understood through subtyping by biology and by function. Single-cell sequencing provides a new insight to map the functional role of distinct CAFs types. To examine the functional associations among the diverse CAFs subpopulation, we now urgently require generating computational tools for cross-platform comparison. Notably, the CAFs' tumor-promoting or tumor-restraining status can convert to each other depending on different tumor stages. CAFs population lineage tracing provides a useful approach to demonstrate the evolution between different CAFs subset. Accordingly, we need to figure out which factors from cancer cells or other stromal cells determine the signaling pathways of pCAFs and rCAFs and maintain their phenotype. Despite the vital research value of CAFs, our development of CAFs-oriented cancer management approaches is still in the elemental stage. Shortly, we will have a deeper understanding of the genetic events and signaling changes in the evolution of CAFs. The emergence of a broadly accepted CAF molecular subtyping will better recognize CAFs' biological behaviors in particular contexts. These novel insights will help translate CAFs biology from bench to bedside and develop new strategies to improve precision cancer therapy.

AUTHOR CONTRIBUTIONS

WY and BY made substantial contributions to conception and determined the final version. ZW drafted the manuscript or revised it critically for important intellectual content. YaT, YiT, and JY contributed to table editing, figure drawing, and manuscript drafting. QY contributed to revising the manuscript by literature reviewing and drafting new parts of the manuscript. All authors read and approved the final manuscript.

FUNDING

This work was supported by grants from Zhejiang Provincial Natural Science Foundation of China (Natural Science Foundation of Zhejiang Province LY20H180015 to ZW). The sponsors of the study had no role in study design, data collection, data analysis, results in interpretation, writing the manuscript, and the decision to submit the manuscript for publication.

ACKNOWLEDGMENTS

We thank Dr. Weidong Chai from the Geroge Washington University for his essential work in English language editing.

REFERENCES

Albrengues, J., Bertero, T., Grasset, E., Bonan, S., Maiel, M., Bourget, I., et al. (2015). Epigenetic switch drives the conversion of fibroblasts into proinvasive cancer-associated fibroblasts. *Nat. Commun.* 6:10204.

Arnold, J. N., Magiera, L., Kraman, M., and Fearon, D. T. (2014). Tumoral immune suppression by macrophages expressing fibroblast activation protein-alpha and heme oxygenase-1. *Cancer Immunol. Res.* 2, 121–126. doi: 10.1158/2326-6066.cir-13-0150

Bartoschek, M., Oskolkov, N., Bocci, M., Lovrot, J., Larsson, C., Sommarin, M., et al. (2018). Spatially and functionally distinct subclasses of breast cancer-associated fibroblasts revealed by single cell RNA sequencing. *Nat. Commun.* 9:5150.

Becker, A., Thakur, B. K., Weiss, J. M., Kim, H. S., Peinado, H., and Lyden, D. (2016). Extracellular vesicles in cancer: cell-to-cell mediators of metastasis. *Cancer Cell* 30, 836–848. doi: 10.1016/j.ccell.2016.10.009

Biswas, S., Davis, H., Irshad, S., Sandberg, T., Worthley, D., and Leedham, S. (2015). Microenvironmental control of stem cell fate in intestinal homeostasis and disease. *J. Pathol.* 237, 135–145. doi: 10.1002/path.4563

Calon, A., Lonardo, E., Berenguer-Llergo, A., Espinet, E., Hernando-Momblona, X., Iglesias, M., et al. (2015). Stromal gene expression defines poor-prognosis subtypes in colorectal cancer. *Nat. Genet.* 47, 320–329. doi: 10.1038/ng.3225

Chang, P. H., Hwang-Verslues, W. W., Chang, Y. C., Chen, C. C., Hsiao, M., Jeng, Y. M., et al. (2012). Activation of robo1 signaling of breast cancer cells by Slit2 from stromal fibroblast restrains tumorigenesis via blocking PI3K/Akt/beta-catenin pathway. *Cancer Res.* 72, 4652–4661.

Costa, A., Kieffer, Y., Scholer-Dahirel, A., Pelon, F., Bourachot, B., Cardon, M., et al. (2018). Fibroblast heterogeneity and immunosuppressive environment in human breast Cancer. *Cancer Cell* 33, 463–479.e10.

Curry, J. M., Tuluc, M., Whitaker-Menezes, D., Ames, J. A., Anantharaman, A., Butera, A., et al. (2013). Cancer metabolism, stemness and tumor recurrence: MCT1 and MCT4 are functional biomarkers of metabolic symbiosis in head and neck cancer. *Cell Cycle* 12, 1371–1384. doi: 10.4161/cc.24092

Dai, K., Tanaka, M., Kamiyoshi, A., Sakurai, T., Ichikawa-Shindo, Y., Kawate, H., et al. (2019). Deficiency of the adrenomedullin-RAMP3 system suppresses metastasis through the modification of cancer-associated fibroblasts. *Oncogene* 39, 1914–1930. doi: 10.1038/s41388-019-1112-z

Djurec, M., Grana, O., Lee, A., Troule, K., Espinet, E., Cabras, L., et al. (2018). Saa3 is a key mediator of the protumorigenic properties of cancer-associated fibroblasts in pancreatic tumors. *Proc. Natl. Acad. Sci. U.S.A.* 115, E1147–E1156.

Elyada, E., Bolisetty, M., Laise, P., Flynn, W. F., Courtois, E. T., Burkhart, R. A., et al. (2019). Cross-species single-cell analysis of pancreatic ductal adenocarcinoma reveals antigen-presenting cancer-associated fibroblasts. *Cancer Discov.* 9, 1102–1123. doi: 10.1158/2159-8290.cd-19-0094

Erez, N., Truitt, M., Olson, P., Arron, S. T., and Hanahan, D. (2010). Cancer-associated fibroblasts are activated in incipient neoplasia to orchestrate tumor-promoting inflammation in an NF-kappaB-dependent manner. *Cancer Cell* 17, 135–147. doi: 10.1016/j.ccr.2009.12.041

Fang, A., Zhou, S., Su, X., Liu, C., Chen, X., Wan, Y., et al. (2018). RAMP3 is a prognostic indicator of liver cancer and might reduce the adverse effect of TP53 mutation on survival. *Future Oncol.* 14, 2615–2625. doi: 10.2217/fon-2018-0296

Feig, C., Jones, J. O., Kraman, M., Wells, R. J., Deonarine, A., Chan, D. S., et al. (2013). Targeting CXCL12 from FAP-expressing carcinoma-associated fibroblasts synergizes with anti-PD-L1 immunotherapy in pancreatic cancer. *Proc. Natl. Acad. Sci. U.S.A.* 110, 20212–20217. doi: 10.1073/pnas.1320318110

Fischer, K. R., Durrans, A., Lee, S., Sheng, J., Li, F., Wong, S. T., et al. (2015). Epithelial-to-mesenchymal transition is not required for lung metastasis but contributes to chemoresistance. *Nature* 527, 472–476. doi: 10.1038/nature15748

Fujiwara, K., Ohuchida, K., Mizumoto, K., Shindo, K., Eguchi, D., Kozono, S., et al. (2012). CD271(+) subpopulation of pancreatic stellate cells correlates with prognosis of pancreatic cancer and is regulated by interaction with cancer cells. *PLoS One* 7:e52682. doi: 10.1371/journal.pone.0052682

Gerling, M., Buller, N. V., Kirn, L. M., Joost, S., Frings, O., Englert, B., et al. (2016). Stromal hedgehog signalling is downregulated in colon cancer and its restoration restrains tumour growth. *Nat. Commun.* 7:12321.

Giatromanolaki, A., Koukourakis, M. I., Koutsopoulos, A., Mendrinos, S., and Sivridis, E. (2012). The metabolic interactions between tumor cells and tumor-associated stroma (TAS) in prostatic cancer. *Cancer Biol. Ther.* 13, 1284–1289. doi: 10.4161/cbt.21785

Giusti, I., Di Francesco, M., D'ascenzo, S., Palmerini, M. G., Macchiarelli, G., Carta, G., et al. (2018). Ovarian cancer-derived extracellular vesicles affect normal human fibroblast behavior. *Cancer Biol. Ther.* 19, 722–734.

Greten, F. R., Eckmann, L., Greten, T. F., Park, J. M., Li, Z. W., Egan, L. J., et al. (2004). IKKbeta links inflammation and tumorigenesis in a mouse model of colitis-associated cancer. *Cell* 118, 285–296. doi: 10.1016/j.cell.2004.07.013

Hanahan, D., and Weinberg, R. A. (2011). Hallmarks of cancer: the next generation. *Cell* 144, 646–674. doi: 10.1016/j.cell.2011.02.013

Ishii, G., Ochiai, A., and Neri, S. (2015). Phenotypic and functional heterogeneity of cancer-associated fibroblast within the tumor microenvironment. *Adv. Drug Deliv. Rev.* 99, 186–196. doi: 10.1016/j.addr.2015.07.007

Ito, M., Ishii, G., Nagai, K., Maeda, R., Nakano, Y., and Ochiai, A. (2012). Prognostic impact of cancer-associated stromal cells in patients with stage I lung adenocarcinoma. *Chest* 142, 151–158. doi: 10.1378/chest.11-2458

Iwano, M., Fischer, A., Okada, H., Plieth, D., Xue, C., Danoff, T. M., et al. (2001). Conditional abatement of tissue fibrosis using nucleoside analogs to selectively corrupt DNA replication in transgenic fibroblasts. *Mol. Ther.* 3, 149–159. doi: 10.1006/mthe.2000.0251

Kalluri, R. (2016). The biology and function of fibroblasts in cancer. *Nat. Rev. Cancer* 16, 582–598. doi: 10.1038/nrc.2016.73

Kizawa, H., Kou, I., Iida, A., Sudo, A., Miyamoto, Y., Fukuda, A., et al. (2005). An aspartic acid repeat polymorphism in asporin inhibits chondrogenesis and increases susceptibility to osteoarthritis. *Nat. Genet.* 37, 138–144. doi: 10.1038/ng1496

Kobayashi, H., Enomoto, A., Woods, S. L., Burt, A. D., Takahashi, M., and Worthley, D. L. (2019). Cancer-associated fibroblasts in gastrointestinal cancer. *Nat. Rev. Gastroenterol. Hepatol.* 16, 282–295. doi: 10.1038/s41575-019-0115-0

Koliaraki, V., Pallangyo, C. K., Greten, F. R., and Kollias, G. (2017). Mesenchymal cells in colon cancer. *Gastroenterology* 152, 964–979.

Koliaraki, V., Pasparakis, M., and Kollias, G. (2015). IKKbeta in intestinal mesenchymal cells promotes initiation of colitis-associated cancer. *J. Exp. Med.* 212, 2235–2251. doi: 10.1084/jem.20150542

Li, B. L., Lu, W., Qu, J. J., Ye, L., Du, G. Q., and Wan, X. P. (2019). Loss of exosomal miR-148b from cancer-associated fibroblasts promotes endometrial cancer cell invasion and cancer metastasis. *J. Cell Physiol.* 234, 2943–2953. doi: 10.1002/jcp.27111

Li, H., Courtois, E. T., Sengupta, D., Tan, Y., Chen, K. H., Goh, J. J. L., et al. (2017). Reference component analysis of single-cell transcriptomes elucidates cellular heterogeneity in human colorectal tumors. *Nat. Genet.* 49, 708–718. doi: 10.1038/ng.3818

Li, L., Piontek, K., Ishida, M., Fausther, M., Dranoff, J. A., Fu, R., et al. (2017). Extracellular vesicles carry microRNA-195 to intrahepatic cholangiocarcinoma and improve survival in a rat model. *Hepatology* 65, 501–514. doi: 10.1002/hep.28735

Li, Y. Y., Tao, Y. W., Gao, S., Li, P., Zheng, J. M., Zhang, S. E., et al. (2018). Cancer-associated fibroblasts contribute to oral cancer cells proliferation and metastasis via exosome-mediated paracrine miR-34a-5p. *EBioMedicine* 36, 209–220. doi: 10.1016/j.ebiom.2018.09.006

Liang, L., Coudiere-Morrison, L., Tatari, N., Stromecki, M., Fresnoza, A., Porter, C. J., et al. (2018). CD271(+) cells are diagnostic and prognostic and exhibit elevated MAPK activity in SHH medulloblastoma. *Cancer Res.* 78, 4745–4759. doi: 10.1158/0008-5472.can-18-0027

Liao, Y., Ni, Y., He, R., Liu, W., and Du, J. (2013). Clinical implications of fibroblast activation protein-alpha in non-small cell lung cancer after curative resection: a new predictor for prognosis. *J. Cancer Res. Clin. Oncol.* 139, 1523–1528. doi: 10.1007/s00432-013-1471-8

Luga, V., Zhang, L., Viloria-Petit, A. M., Ogunjimi, A. A., Inanlou, M. R., Chiu, E., et al. (2012). Exosomes mediate stromal mobilization of autocrine Wnt-PCP signaling in breast cancer cell migration. *Cell* 151, 1542–1556. doi: 10.1016/j.cell.2012.11.024

Maacha, S., Bhat, A. A., Jimenez, L., Raza, A., Haris, M., Uddin, S., et al. (2019). Extracellular vesicles-mediated intercellular communication: roles in the tumor microenvironment and anti-cancer drug resistance. *Mol. Cancer* 18:55.

Mackie, D. I., Nielsen, N. R., Harris, M., Singh, S., Davis, R. B., Dy, D., et al. (2019). RAMP3 determines rapid recycling of atypical chemokine receptor-3 for guided angiogenesis. *Proc. Natl. Acad. Sci. U.S.A.* 116, 24093–24099. doi: 10.1073/pnas.1905561116

Mao, J., Ligon, K. L., Rakhlin, E. Y., Thayer, S. P., Bronson, R. T., Rowitch, D., et al. (2006). A novel somatic mouse model to survey tumorigenic potential applied to the hedgehog pathway. *Cancer Res.* 66, 10171–10178. doi: 10.1158/0008-5472.can-06-0657

Maris, P., Blomme, A., Palacios, A. P., Costanza, B., Bellahcene, A., Bianchi, E., et al. (2015). Asporin is a fibroblast-derived TGF-beta1 inhibitor and a tumor suppressor associated with good prognosis in breast cancer. *PLoS Med.* 12:e1001871. doi: 10.1371/journal.pmed.1001871

Martinez-Outschoorn, U. E., Lisanti, M. P., and Sotgia, F. (2014). Catabolic cancer-associated fibroblasts transfer energy and biomass to anabolic cancer cells, fueling tumor growth. *Semin. Cancer Biol.* 25, 47–60. doi: 10.1016/j.semcancer.2014.01.005

Martinez-Outschoorn, U. E., Whitaker-Menezes, D., Lin, Z., Flomenberg, N., Howell, A., Pestell, R. G., et al. (2011). Cytokine production and inflammation drive autophagy in the tumor microenvironment: role of stromal caveolin-1 as a key regulator. *Cell Cycle* 10, 1784–1793. doi: 10.4161/cc.10.11.15674

Mclatchie, L. M., Fraser, N. J., Main, M. J., Wise, A., Brown, J., Thompson, N., et al. (1998). RAMPs regulate the transport and ligand specificity of the calcitonin-receptor-like receptor. *Nature* 393, 333–339. doi: 10.1038/30666

Mizutani, Y., Kobayashi, H., Iida, T., Asai, N., Masamune, A., Hara, A., et al. (2019). Meflin-positive cancer-associated fibroblasts inhibit pancreatic carcinogenesis. *Cancer Res.* 79, 5367–5381. doi: 10.1158/0008-5472.can-19-0454

Monti, D., Sotgia, F., Whitaker-Menezes, D., Tuluc, M., Birbe, R., Berger, A., et al. (2017). Pilot study demonstrating metabolic and anti-proliferative effects of in vivo anti-oxidant supplementation with N-acetylcysteine in breast cancer. *Semin. Oncol.* 44, 226–232. doi: 10.1053/j.seminoncol.2017.10.001

Morton, J. P., Mongeau, M. E., Klimstra, D. S., Morris, J. P., Lee, Y. C., Kawaguchi, Y., et al. (2007). Sonic hedgehog acts at multiple stages during pancreatic tumorigenesis. *Proc. Natl. Acad. Sci. U.S.A.* 104, 5103–5108. doi: 10.1073/pnas.0701158104

Mueller, M. M., and Fusenig, N. E. (2004). Friends or foes – bipolar effects of the tumour stroma in cancer. *Nat. Rev. Cancer* 4, 839–849. doi: 10.1038/nrc1477

Nielsen, P. S., Riber-Hansen, R., and Steiniche, T. (2018). Immunohistochemical CD271 expression correlates with melanoma progress in a case-control study. *Pathology* 50, 402–410. doi: 10.1016/j.pathol.2017.12.340

Nwosu, Z. C., Ebert, M. P., Dooley, S., and Meyer, C. (2016). Caveolin-1 in the regulation of cell metabolism: a cancer perspective. *Mol. Cancer* 15:71.

Ohlund, D., Elyada, E., and Tuveson, D. (2014). Fibroblast heterogeneity in the cancer wound. *J. Exp. Med.* 211, 1503–1523. doi: 10.1084/jem.20140692

Ohlund, D., Handly-Santana, A., Biffi, G., Elyada, E., Almeida, A. S., Ponz-Sarvise, M., et al. (2017). Distinct populations of inflammatory fibroblasts and myofibroblasts in pancreatic cancer. *J. Exp. Med.* 214, 579–596. doi: 10.1084/jem.20162024

Ono, S., Ishii, G., Nagai, K., Takuwa, T., Yoshida, J., Nishimura, M., et al. (2013). Podoplanin-positive cancer-associated fibroblasts could have prognostic value independent of cancer cell phenotype in stage I lung squamous cell carcinoma: usefulness of combining analysis of both cancer cell phenotype and cancer-associated fibroblast phenotype. *Chest* 143, 963–970. doi: 10.1378/chest.12-0913

Osterreicher, C. H., Penz-Osterreicher, M., Grivennikov, S. I., Guma, M., Koltsova, E. K., Datz, C., et al. (2011). Fibroblast-specific protein 1 identifies an inflammatory subpopulation of macrophages in the liver. *Proc. Natl. Acad. Sci. U.S.A.* 108, 308–313. doi: 10.1073/pnas.1017547108

Ozdemir, B. C., Pentcheva-Hoang, T., Carstens, J. L., Zheng, X., Wu, C. C., Simpson, T. R., et al. (2014). Depletion of carcinoma-associated fibroblasts and fibrosis induces immunosuppression and accelerates pancreas cancer with reduced survival. *Cancer Cell* 25, 719–734. doi: 10.1016/j.ccr.2014.04.005

Pallangyo, C. K., Ziegler, P. K., and Greten, F. R. (2015). IKKbeta acts as a tumor suppressor in cancer-associated fibroblasts during intestinal tumorigenesis. *J. Exp. Med.* 212, 2253–2266. doi: 10.1084/jem.20150576

Pasca Di Magliano, M., Sekine, S., Ermilov, A., Ferris, J., Dlugosz, A. A., and Hebrok, M. (2006). Hedgehog/Ras interactions regulate early stages of pancreatic cancer. *Genes Dev.* 20, 3161–3173. doi: 10.1101/gad.1470806

Paulsson, J., Sjoblom, T., Micke, P., Ponten, F., Landberg, G., Heldin, C. H., et al. (2009). Prognostic significance of stromal platelet-derived growth factor beta-receptor expression in human breast cancer. *Am. J. Pathol.* 175, 334–341. doi: 10.2353/ajpath.2009.081030

Proia, D. A., and Kuperwasser, C. (2005). Stroma: tumor agonist or antagonist. *Cell Cycle* 4, 1022–1025. doi: 10.4161/cc.4.8.1903

Qian, N., Ueno, T., Kawaguchi-Sakita, N., Kawashima, M., Yoshida, N., Mikami, Y., et al. (2011). Prognostic significance of tumor/stromal caveolin-1 expression in breast cancer patients. *Cancer Sci.* 102, 1590–1596. doi: 10.1111/j.1349-7006.2011.01985.x

Rhim, A. D., Mirek, E. T., Aiello, N. M., Maitra, A., Bailey, J. M., Mcallister, F., et al. (2012). EMT and dissemination precede pancreatic tumor formation. *Cell* 148, 349–361. doi: 10.1016/j.cell.2011.11.025

Rhim, A. D., Oberstein, P. E., Thomas, D. H., Mirek, E. T., Palermo, C. F., Sastra, S. A., et al. (2014). Stromal elements act to restrain, rather than support, pancreatic ductal adenocarcinoma. *Cancer Cell* 25, 735–747. doi: 10.1016/j.ccr.2014.04.021

Richards, K. E., Zeleniak, A. E., Fishel, M. L., Wu, J., Littlepage, L. E., and Hill, R. (2017). Cancer-associated fibroblast exosomes regulate survival and proliferation of pancreatic cancer cells. *Oncogene* 36, 1770–1778. doi: 10.1038/onc.2016.353

Roberts, K. J., Kershner, A. M., and Beachy, P. A. (2017). The stromal niche for epithelial stem cells: a template for regeneration and a brake on malignancy. *Cancer Cell* 32, 404–410. doi: 10.1016/j.ccell.2017.08.007

Sahai, E., Astsaturov, I., Cukierman, E., Denardo, D. G., Egeblad, M., Evans, R. M., et al. (2020). A framework for advancing our understanding of cancer-associated fibroblasts. *Nat. Rev. Cancer* 20, 174–186. doi: 10.1038/s41568-019-0238-1

Salomon, B., Maury, S., Loubiere, L., Caruso, M., Onclercq, R., and Klatzmann, D. (1995). A truncated herpes simplex virus thymidine kinase phosphorylates thymidine and nucleoside analogs and does not cause sterility in transgenic mice. *Mol. Cell Biol.* 15, 5322–5328. doi: 10.1128/mcb.15.10.5322

Satoyoshi, R., Kuriyama, S., Aiba, N., Yashiro, M., and Tanaka, M. (2015). Asporin activates coordinated invasion of scirrhous gastric cancer and cancer-associated fibroblasts. *Oncogene* 34, 650–660. doi: 10.1038/onc.2013.584

Seoane, J., and Gomis, R. R. (2017). TGF-beta family signaling in tumor suppression and cancer progression. *Cold Spring Harb. Perspect. Biol.* 9:a022277. doi: 10.1101/cshperspect.a022277

Sherman, M. H., Yu, R. T., Engle, D. D., Ding, N., Atkins, A. R., Tiriac, H., et al. (2014). Vitamin D receptor-mediated stromal reprogramming suppresses pancreatitis and enhances pancreatic cancer therapy. *Cell* 159, 80–93. doi: 10.1016/j.cell.2014.08.007

Simpkins, S. A., Hanby, A. M., Holliday, D. L., and Speirs, V. (2012). Clinical and functional significance of loss of caveolin-1 expression in breast cancer-associated fibroblasts. *J. Pathol.* 227, 490–498. doi: 10.1002/path.4034

Sloan, E. K., Ciocca, D. R., Pouliot, N., Natoli, A., Restall, C., Henderson, M. A., et al. (2009). Stromal cell expression of caveolin-1 predicts outcome in breast cancer. *Am. J. Pathol.* 174, 2035–2043. doi: 10.2353/ajpath.2009.080924

Sotgia, F., Martinez-Outschoorn, U. E., Pavlides, S., Howell, A., Pestell, R. G., and Lisanti, M. P. (2011). Understanding the Warburg effect and the prognostic value of stromal caveolin-1 as a marker of a lethal tumor microenvironment. *Breast Cancer Res.* 13:213.

Sugimoto, H., Mundel, T. M., Kieran, M. W., and Kalluri, R. (2006). Identification of fibroblast heterogeneity in the tumor microenvironment. *Cancer Biol. Ther.* 5, 1640–1646. doi: 10.4161/cbt.5.12.3354

Theiss, A. L., Simmons, J. G., Jobin, C., and Lund, P. K. (2005). Tumor necrosis factor (TNF) alpha increases collagen accumulation and proliferation in intestinal myofibroblasts via TNF receptor 2. *J. Biol. Chem.* 280, 36099–36109. doi: 10.1074/jbc.m505291200

Ullah, M. S., Davies, A. J., and Halestrap, A. P. (2006). The plasma membrane lactate transporter MCT4, but not MCT1, is up-regulated by hypoxia through a HIF-1alpha-dependent mechanism. *J. Biol. Chem.* 281, 9030–9037. doi: 10.1074/jbc.m511397200

Valenti, G., Quinn, H. M., Heynen, G., Lan, L., Holland, J. D., Vogel, R., et al. (2017). Cancer stem cells regulate cancer-associated fibroblasts via activation of hedgehog signaling in mammary gland tumors. *Cancer Res.* 77, 2134–2147. doi: 10.1158/0008-5472.can-15-3490

Wallace, D. C. (2012). Mitochondria and cancer. *Nat. Rev. Cancer* 12, 685–698. doi: 10.1038/nrc3365

Wang, Z., Tan, Y., Yu, W., Zheng, S., Zhang, S., Sun, L., et al. (2017). Small role with big impact: miRNAs as communicators in the cross-talk between cancer-associated fibroblasts and cancer cells. *Int. J. Biol. Sci.* 13, 339–348. doi: 10.7150/ijbs.17680

Webber, J. P., Spary, L. K., Sanders, A. J., Chowdhury, R., Jiang, W. G., Steadman, R., et al. (2015). Differentiation of tumour-promoting stromal myofibroblasts by cancer exosomes. *Oncogene* 34, 290–302. doi: 10.1038/onc.2013.560

Whitaker-Menezes, D., Martinez-Outschoorn, U. E., Lin, Z., Ertel, A., Flomenberg, N., Witkiewicz, A. K., et al. (2011). Evidence for a stromal-epithelial "lactate shuttle" in human tumors: MCT4 is a marker of oxidative stress in cancer-associated fibroblasts. *Cell Cycle* 10, 1772–1783. doi: 10.4161/cc.10.11.15659

Witkiewicz, A. K., Dasgupta, A., Sotgia, F., Mercier, I., Pestell, R. G., Sabel, M., et al. (2009). An absence of stromal caveolin-1 expression predicts early tumor recurrence and poor clinical outcome in human breast cancers. *Am. J. Pathol.* 174, 2023–2034.

Witkiewicz, A. K., Whitaker-Menezes, D., Dasgupta, A., Philp, N. J., Lin, Z., Gandara, R., et al. (2012). Using the "reverse Warburg effect" to identify high-risk breast cancer patients: stromal MCT4 predicts poor clinical outcome in triple-negative breast cancers. *Cell Cycle* 11, 1108–1117. doi: 10.4161/cc.11.6.19530

Worthley, D. L., Churchill, M., Compton, J. T., Tailor, Y., Rao, M., Si, Y., et al. (2015). Gremlin 1 identifies a skeletal stem cell with bone, cartilage, and reticular stromal potential. *Cell* 160, 269–284. doi: 10.1016/j.cell.2014.11.042

Xu, G., Zhang, B., Ye, J., Cao, S., Shi, J., Zhao, Y., et al. (2019). Exosomal miRNA-139 in cancer-associated fibroblasts inhibits gastric cancer progression

by repressing MMP11 expression. *Int. J. Biol. Sci*. 15, 2320–2329. doi: 10.7150/ijbs.33750

Yang, L., Achreja, A., Yeung, T. L., Mangala, L. S., Jiang, D., Han, C., et al. (2016). Targeting stromal glutamine synthetase in tumors disrupts tumor microenvironment-regulated cancer cell growth. *Cell Metab*. 24, 685–700. doi: 10.1016/j.cmet.2016.10.011

Zhang, D., Wang, Y., Shi, Z., Liu, J., Sun, P., Hou, X., et al. (2015). Metabolic reprogramming of cancer-associated fibroblasts by IDH3alpha downregulation. *Cell Rep*. 10, 1335–1348. doi: 10.1016/j.celrep.2015.02.006

Zhang, J., Chen, L., Liu, X., Kammertoens, T., Blankenstein, T., and Qin, Z. (2013). Fibroblast-specific protein 1/S100A4-positive cells prevent carcinoma through collagen production and encapsulation of carcinogens. *Cancer Res*. 73, 2770–2781. doi: 10.1158/0008-5472.CAN-12-3022

Zhang, Y., Wei, J., Xu, J., Leong, W. S., Liu, G., Ji, T., et al. (2018). Suppression of tumor energy supply by liposomal nanoparticle-mediated inhibition of aerobic glycolysis. *ACS Appl. Mater. Interfaces* 10, 2347–2353. doi: 10.1021/acsami.7b16685

Zhang, Z., Li, X., Sun, W., Yue, S., Yang, J., Li, J., et al. (2017). Loss of exosomal miR-320a from cancer-associated fibroblasts contributes to HCC proliferation and metastasis. *Cancer Lett*. 397, 33–42. doi: 10.1016/j.canlet.2017.03.004

Ziani, L., Chouaib, S., and Thiery, J. (2018). Alteration of the antitumor immune response by cancer-associated fibroblasts. *Front. Immunol*. 9:414. doi: 10.3389/fimmu.2018.00414

Conflict of Interest: The authors declare that the research was conducted in the absence of any commercial or financial relationships that could be construed as a potential conflict of interest.

frontiers in Cell and Developmental Biology

ORIGINAL RESEARCH
published: 15 February 2021
doi: 10.3389/fcell.2021.643979

Plasma Metabolic Profiling of Pediatric Sepsis in a Chinese Cohort

Guo-Bang Li[1†], Hong-Rong Hu[1,3†], Wen-Feng Pan[1†], Bo Li[1], Zhi-Ying Ou[4], Hui-Ying Liang[4*] and Cong Li[4,2*]*

[1] Department of Biochemistry, Zhongshan School of Medicine, Sun Yat-sen University, Guangzhou, China, [2] Central Laboratory, Affiliated Dongguan People's Hospital, Southern Medical University, Guangzhou, China, [3] Department of Neurosurgery/Neuro-oncology, Sun Yat-sen University Cancer Center, State Key Laboratory of Oncology in South China, Collaborative Innovation Center for Cancer Medicine, Guangzhou, China, [4] Affiliated Guangzhou Women and Children's Hospital, Zhongshan School of Medicine, Sun Yat-sen University, Guangzhou, China

OPEN ACCESS

Edited by:
Binghui Li,
Capital Medical University, China

Reviewed by:
Zeping Hu,
Tsinghua University, China
Wenjing Du,
Chinese Academy of Medical Sciences and Peking Union Medical College, China

***Correspondence:**
Cong Li
licong28@hotmail.com
Hui-Ying Liang
lianghuiying@hotmail.com
Zhi-Ying Ou
252833558@qq.com

[†] These authors have contributed equally to this work

Specialty section:
This article was submitted to Molecular Medicine, a section of the journal Frontiers in Cell and Developmental Biology

Received: *19 December 2020*
Accepted: *15 January 2021*
Published: *15 February 2021*

Citation:
Li G-B, Hu H-R, Pan W-F, Li B, Ou Z-Y, Liang H-Y and Li C (2021) Plasma Metabolic Profiling of Pediatric Sepsis in a Chinese Cohort. Front. Cell Dev. Biol. 9:643979. doi: 10.3389/fcell.2021.643979

Sepsis represents one of the most pressing problems in pediatrics, characterized by pathogenic bacteria invading the blood, growing and multiplying in the blood circulation, and ultimately causing severe infections. Most children with sepsis have a rapid disease onset and frequently exhibit sudden high fever or first chills. Here we performed comprehensive metabolomic profiling of plasma samples collected from pediatric sepsis patients to identify specific metabolic alterations associated with these patients (n = 84, designated as case subjects) as compared to healthy cohorts (n = 59, designated as control subjects). Diagnostic models were constructed using MetaboAnalyst, R packages, and multiple statistical methods, such as orthogonal partial least squares-discriminant analysis, principal component analysis, volcano plotting, and one-way ANOVA. Our study revealed a panel of metabolites responsible for the discrimination between case and control subjects with a high predictive value of prognosis. Moreover, significantly altered metabolites in sepsis survivors versus deceased patients (non-survivors) were identified as those involved in amino acids, fatty acids, and carbohydrates metabolism. Nine metabolites including organic acids and fatty acids were also identified with significantly higher abundance in sepsis patients with related microbes, implicating greater potentials to distinguish bacterial species using metabolomic analysis than blood culture. Pathway enrichment analysis further revealed that fatty acid metabolism might play an important role in the pathogenesis of sepsis.

Keywords: sepsis, metabolomics, amino acids, fatty acids, carbohydrates

INTRODUCTION

Sepsis is a complication of infectious processes associated with substantial morbidity and mortality, especially in childhood patients (Kaukonen et al., 2014). The incidence of sepsis varies by different social-economic regions, and it remains a global health concern. There are more than 18 million severe sepsis cases worldwide each year (Kumar et al., 2011; Fleischmann-Struzek et al., 2018). In the United States, sepsis and septic shock affect up to 300 patients per 100,000 people per year, and the annual number is increasing at a rate of 1.5 to 8.0% (Torio and Moore, 2006). According to epidemiological surveys, sepsis is one of the leading causes of death in the intensive care unit (ICU), and there is an urgent need to improve the diagnosis and treatment of severe

sepsis patients (Angus and Van der Poll, 2013). Sepsis is defined as patients who are acutely infected and demonstrate two or more systemic inflammatory response syndromes (SIRS), including temperature >38°C or <36°C, heart rate >90/min, respiratory rate >20/min or $PaCO_2$ <32 mm Hg (4.3 kPa), and white blood cell count >12,000/mm^3 or < 4000/mm^3 or >10% immature bands (Singer et al., 2016). The key pathological components to develop sepsis is the runaway inflammatory responses to infection, and it is postulated that sepsis could be triggered by numerous metabolic products, such as proinflammatory mediators responsive to infectious agents, alien products generated by invading bacteria, and those released by damaged cells (Bosmann and Ward, 2013; Drosatos et al., 2015). It is noted that sepsis is caused by infection, but sepsis itself is not contagious; therefore, by nature, sepsis is the body's response to infectious factors.

Blood culture is the gold standard for sepsis diagnosis. However, only one-third case is commonly tested positive by blood culture, and approximately 30% sepsis samples from multiple sites of one individual patient are tested negative (Opal et al., 2003; Ranieri et al., 2012). Patients with sepsis have a certain disturbance of whole-body metabolism during the early stage of infection, and the dynamic changes of the metabolic network can be detected by metabolomic analysis to provide specific diagnostic markers, microbiota classification, and prognosis prediction (Langley et al., 2013; Fischer et al., 2014; Wang et al., 2016). According to recent research data, energy metabolism, including glycolysis, gluconeogenesis, and lipid metabolism, is elevated in patient serum with sepsis. However, there is no clear serum biomarker for distinguishing different sources of infection (such as Gram-negative or Gram-positive bacteria). In terms of prognostic judgment, it mainly depends on clinical indicators, which do not always reflect disease severity. Therefore, identifying metabolic biomarkers with great predictive power will be of great significance for the diagnosis and treatment of patients with sepsis.

Metabolomics is a technique quantitatively analyzing all metabolites involved in certain pathological processes, and the resultant metabolic landscape can be used to improve the understanding of disease pathogenesis including sepsis (Guo et al., 2015). In this study, we aim to characterize the plasma metabolic signatures in sepsis survivors, non-survivors, and control subjects, by employing high-performance liquid chromatography and mass spectroscopy (HPLC-MS)-based metabolomics. These data set a solid foundation for constructing an accurate metabolic model for predicting sepsis patient outcome.

MATERIALS AND METHODS

Clinical Subjects

The peripheral blood samples of all participants in this retrospective study were collected from Guangzhou Women and Children's Medical Center in China. Eighty-four pediatric sepsis patients including 52 males and 32 females were admitted to the ICU from 2015 to 2016, and inclusion of the patients was determined by a consensus panel of pediatric and ICU physicians according to the presentation of inflammation and infection, plus hyperthermia or hypothermia (Singer et al., 2016). The extent of infection and infectious origin was adjudicated by polymerase chain reaction after blood culture (Patel et al., 2011; Kirn and Weinstein, 2013). Non-infected controls were healthy children undergoing physical examination in the Guangzhou Women and Children's Medical Center, with matched age and geographical birthplace. The local ethics committees have approved this study, and parental informed consent was obtained from every participant.

Statistical Analysis

Continuous clinical variables were presented as the mean ± standard deviation. Metabolic intensities were log2-transformed to normalize non-normal distributions before further analysis. We assessed metabolic profiles of serum samples from sepsis survivors, sepsis non-survivors, and healthy controls by ANOVA and logistic regression by including covariates of sex and age of admittance. MetaboAnalyst and R packages were employed to construct statistical plots, including principal components analysis (PCA) and orthogonal partial least squares-discriminant analysis (OPLS-DA) (Pang et al., 2020). The variable importance in the projection (VIP) value of each variable in the OPLS-DA model was calculated to indicate its contribution to the classification. Metabolites with the VIP value > 1 were further applied to Student's *t*-test at the univariate level to measure the significance of each metabolite; *q*-values were calculated for multiple testing, with the criteria of VIP > 1 and *p*-value less < 0.05 (**Table 2**).

Metabolomic Profiling

High-performance liquid chromatography and mass spectroscopy was performed as described previously (Lawton et al., 2008). Briefly, 10 microliters were taken out from each plasma sample, evenly mixed to generate 20 quality control samples. The mobile phase of positive mode consisted of 0.1% formic acid in water (solvent A) and 0.1% formic acid in acetonitrile (solvent B), and the mobile phase of negative mode consisted of 0.5 mM ammonium acetate in water (solvent A) and 100% acetonitrile (solvent B). Raw MS data were first converted to.mzxml files, then the individual data for each participant were grouped together and processed for further analysis. mzxml files were imported to MetAnalyzer for peak detection, and the peak areas of positive and negative ions were measured according to corresponding internal standard ions. MetDNA was employed to confirm the metabolite identification in untargeted metabolomics (Shen et al., 2019). Quantifications were performed using the weighted linear least squares regression analysis based on fortified calibration standards as prepared before each run. This integrated platform enabled the high-throughput collection and relative quantitative analysis of analytical data and identified a large number and broad spectrum of molecules with high confidence. In this study, a total of 514 small molecules were measured and annotated as metabolites

in the positive (281) and negative (233) mode (Wishart et al., 2009).

RESULTS

Clinical Characteristics of the Subjects

The general and clinical characteristics of the subjects participating in the study were shown in **Table 1**. We selected a total of 84 sepsis cases after admission to the ICU with the month of onset ranging from 15 days after birth to 13 years old, and the average onset month was 25.59 ± 35.3. Sepsis cases with any known risk of alternative lethality were excluded. In addition, 59 children with an average age of 3.48 ± 2.43 were recruited from physical examination center as controls. All participants included in our analysis were of Southern Chinese Han origin as reported by their guardian. Sepsis cases could be categorized into two groups based on their final outcome at day 28: sepsis survivors (n = 74, 88.1%) and sepsis non-survivors (n = 10, 11.9%).

Metabolomic Profiling of Plasma Samples

We carried out metabolic profiling in collected serum samples (separated from peripheral blood specimen) to investigate whether metabolic changes correlate with the severity and prognosis of pediatric sepsis. PCA results showed an ideal aggregation of quality control samples, indicating a stable performance of the metabolomic platform, and the metabolomic profile was obtained with high reproducibility. The orthogonal partial least squares discrimination analysis (OPLS-DA) implicated that the case and control samples were well distinguished by the metabolomic data (**Figures 1A,B**). The volcano plot highlighted the potential metabolic biomarkers with fold change >1.5 or <0.67, P-value < 0.05, and VIP > 1 (**Figure 1C**). Metabolites with differential abundance were demonstrated by a heatmap plot, as those with increased levels in cases lie in the class of amino acids and carbohydrates, and the decreased panel includes lipids and their derivatives (**Figure 1D**). In particular, phosphatidylcholine, phosphatidylinositol, and phosphoglyceride were found to be significantly less in cases relative to the control group, and serum levels of several amino acids and carbohydrates were elevated in sepsis serum by over 100% (**Figures 1E,F** and **Table 2**).

An array of metabolites has been implicated in sepsis-related mortality after logistic regression, with significantly altered abundance between sepsis survivors and non-survivors. Notably, Harmane, Genistein, Metronidazole, Quinolinate, and Cortisone were excluded from further analysis, because these biochemicals were considered to be either drug molecules or products from drug metabolism. The top five decreased metabolites in non-survivors are all lipid species, and the increased level of amino acids and their derivatives was found to be highly correlated with sepsis-related death, including adenine, indolelactic acid, lps(18:1/0:0), Ile-Tyr, and kynurenine (**Figures 2A–D**).

Differences in Plasma Metabolites According to Sepsis-Causing Pathogens

As the most commonly seen infectious microbes in sepsis cases, *S. aureus, S. pneumoniae,* and *E. coli* contribute to most sepsis cases, especially in children. In our study cohort, only one blood sample was confirmed to be infected by *E. coli*, and the sample was from a 4-year-old girl, cured 63 days after admittance to the hospital. *P. aeruginosa* was the major infective origin (n = 10), followed by *C. albicans* (n = 6) and *S. aureus* (n = 5). We sought to identify differentially expressed metabolites in cases infected by different pathogens. A one-way ANOVA identified nine metabolites including 1-oleoyl-L-alpha-lysophosphatidic acid, cholic acid, hypoxanthine, indoxyl sulfate, isovalerylglycine, histidine, PC(P-16:0/18:1), PI(16:0/18:3), and pregnenolone sulfate with significantly altered abundance in sepsis survivors, non-survivors, and the control group. The serum levels of cholic acid, isovalerylglycine, and histidine were increased in sepsis survivors infected by *S. aureus* versus other microbes (**Figures 3A–C**).

Correlations Between the Plasma Metabolic Profile and Blood Gas Analysis in Sepsis Patients

The MS values of 514 annotated metabolites were log-transformed and normalized. Pearson correlation coefficients between the blood gas index and metabolites were then calculated, grouped by the hierarchical clustering, and presented in a heatmap form (**Figure 4A**). Given that lactate and bicarbonate are great prognostic values for sepsis patients, we performed enrichment analysis of those metabolites significantly related to these two clinical values. As a result, oxidation of very long chain and branched-chain fatty acids was highly enriched pathways correlated with lactate, whereas the metabolism of methionine and linoleic acids was enriched for bicarbonate. Another lipid-related pathway that warrants attention was fatty acid elongation in mitochondria (**Figures 4B,C**), demonstrating that the amounts of plasma lipid species are critical for the prognosis of sepsis patients.

TABLE 1 | General clinical variables of the sepsis case control cohort.

Characteristics	Sepsis survivors (n = 74)	Sepsis death (n = 10)	Control (n = 59)
Gender (male/female)	39/35	5/5	32/27
Onset month	23.22 ± 35.47	43.1 ± 37.20	NA
Temperature	37.1 ± 0.9	36.8 ± 0.4	NA

Onset month (mean ± SD): age (month) of onset for sepsis cases.

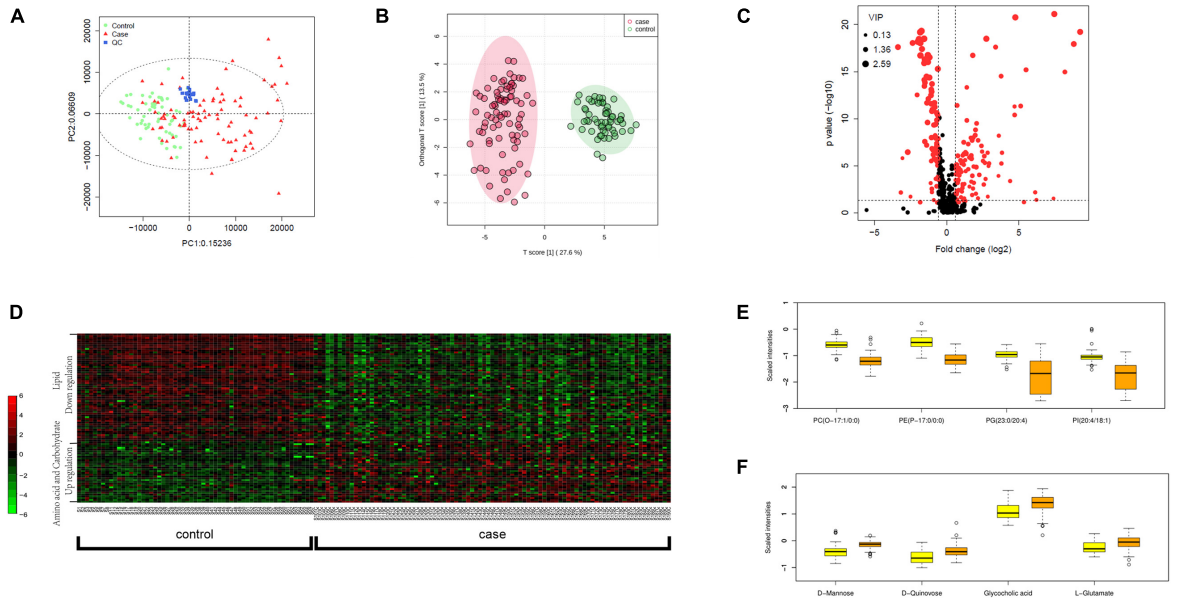

FIGURE 1 | Metabolomic profiling of plasma samples from sepsis cases and control group. **(A)** PCA plot based on the metabolomic analysis. Note that all quality control (QC) samples are clustered. **(B)** OPLS-DA score scatter plots for metabolic profiling of sepsis case (red dots) and control (green dots) group. Discriminations between case and control groups were clearly shown. **(C)** Volcano plot showing significantly altered metabolites in sepsis cases versus controls. Red dots represented metabolites above the thresholds (VIP > 1, *t*-test *P*-value < 0.05, and fold change > 1.5 or < 0.67). **(D)** 521 log-transformed annotated serum metabolites were visualized by a heatmap. Mean intensity was used to indicate the level of differences between case and control samples. **(E)** The four decreased metabolites in sepsis serum presented by scaled intensities in the boxplot (*t*-test $P < 0.05$). **(F)** The four increased metabolites presented by scaled intensities in the boxplot (*t*-test $P < 0.05$).

TABLE 2 | Metabolites associated with sepsis survivors versus controls, ranked by foldchange.

Metabolites	Class	VIP	Q_value	Foldchange
PE(P-17:0/0:0)	lipid	1.925585	9.14E-19	0.194985
PI(20:4/18:1)	Lipid	1.193777	3.00E-13	0.242166
PC(O-17:1/0:0)	Lipid	2.075808	7.09E-19	0.249678
PA(18:2/7:0)	Lipid	2.165168	4.00E-18	0.30559
Thr-Gly	Oligopeptide	1.48506	6.54E-08	0.382259
PG(23:0/20:4)	Lipid	1.730259	2.12E-12	0.387358
Indoxyl sulfate	Phenol	1.786883	2.56E-10	0.399003
L-Fucose-1-phosphate	Sugar	1.772869	7.94E-13	0.414575
Riboflavin (Vitamin B2)	Acid	0.793711	4.18E-07	14.1998
LPS(20:4/0:0)	Lipid	1.212115	1.56E-09	3.988089
Quinovose	Ketone	1.589411	1.89E-17	3.493425
Glycocholic acid	Acid	1.208684	8.23E-07	3.249042
Mannose	Sugar	1.22824	3.93E-12	1.645824
Glutamate	Amino acid	1.16144	8.17E-05	1.580853

Q values and VIP are results for the association with sepsis; logistic regression was performed for adjustment of onset month, gender, and liver and kidney diseases status.

DISCUSSION

The primary goal of this study is to identify appropriate metabolites, or an effective combination of metabolites, to predict the prognosis of pediatric sepsis. We performed LC-MS-based metabolomic analyses on serum samples harvested from sepsis patients and age-matched controls with detailed clinical information, and significant differences in an array of metabolites were identified during the very early stage of the disease course (from the day of admittance) between survivors and non-survivors. The data mining results indicated that most biomarkers associated with sepsis-related death were lipid molecules, especially phospholipid, and metabolites involved in energy and carbohydrate metabolism may also contribute to disease progression.

The crucial role of metabolic alterations in pathogenesis has been increasingly recognized by the field, and a vast number of research activities are devoted to the identification of

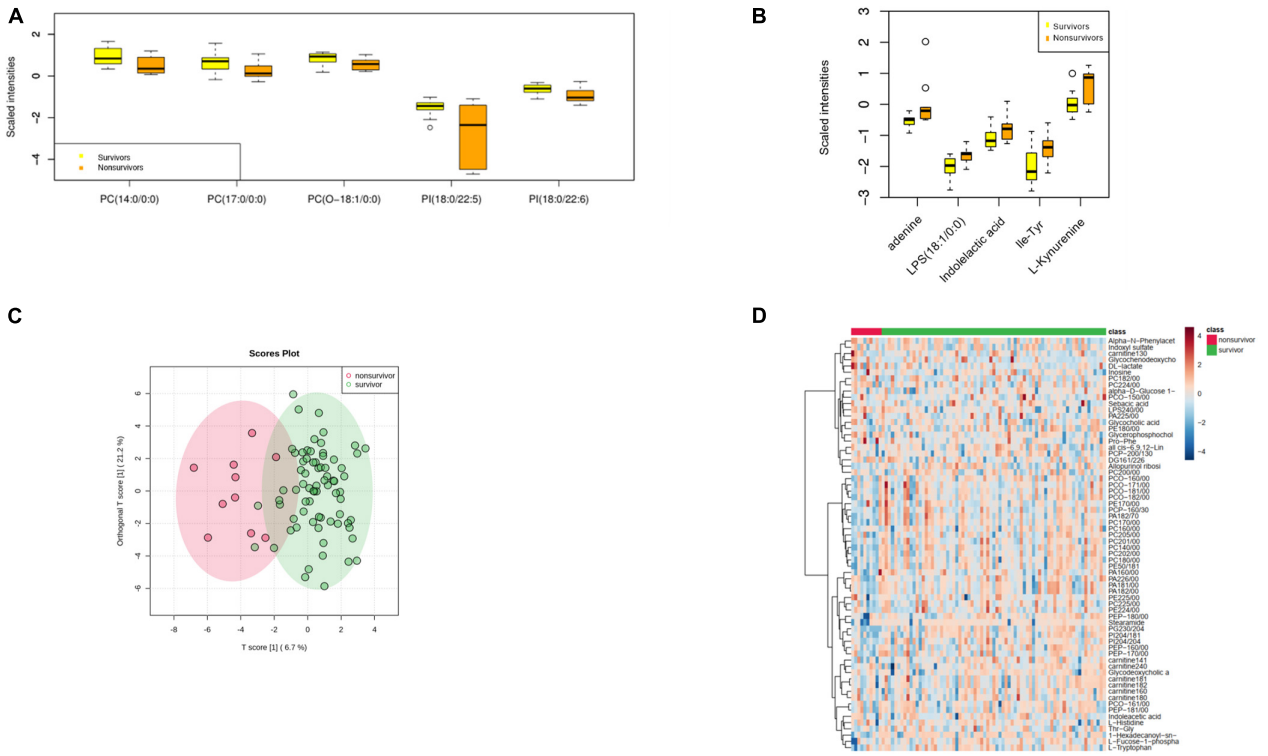

FIGURE 2 | Metabolomic profiling of plasma samples from sepsis survivors and non-survivors. **(A)** The top five decreasing metabolites presented in sepsis non-survivors compared to survivors. The *x*-axis represents specific metabolites, and the *y*-axis shows the normalized scaled intensity. **(B)** The top five increased metabolites in sepsis non-survivors. **(C)** OPLS-DA plot showing the metabolic discrimination between the non-survivor and survivor groups. **(D)** Hierarchical clustering analysis was performed to depict the metabolites that were altered significantly across the non-survivor and survivor groups.

metabolic biomarkers. Specifically, anti-inflammatory responses were found to be impacted by metabolism, and selective metabolites that change significantly in sepsis, SIRS, and endotoxemia were identified (Kamisoglu et al., 2015). Plenty of evidences have suggested the involvement of lipid synthesis in sepsis (Green et al., 2016), and one of the elucidated mechanisms was that lipid synthesis in macrophages can be inhibited by the deprivation of mitochondrial uncoupling protein-2 (UCP2), which was later distinguished as a potential therapeutic target for sepsis through *in vivo* and *in vitro* studies (Moon et al., 2015).

In our study, the PCA results proved that quality control samples were very well clustered, and the OPLS-DA score plot showed a perfect clustering between two examined groups, indicating effective separation and stable performance were both achieved through our analysis. Moreover, metabolic profiling revealed intriguing alterations in sepsis cases infected by different bacterial strains. Notably, different bacteria can lead to variable forms of sepsis, an urgent challenge put forward by precise management of this disease. In our analysis, we focused on the metabolites highly correlated with three major bacterial species and identified nine significantly altered metabolites, most of which belong to steroids and phospholipids. Specifically, increased levels of cholic acid, isovalerylglycine, and histidine were discovered in patients infected with *S. aureus* versus those with *P. aeruginosa* and *C. albicans*, suggesting that these metabolites may originate from immune responses in patients infected with *S. aureus*. Another possibility is that these metabolites are the secondary metabolic products of corresponding bacteria. It can be speculated that metabolic biomarkers could be utilized, together with clinical variables, to assist clinicians to distinguish bacterial species in a faster process than the traditional blood culture method.

By comparing metabolic profiles in sepsis survivors, non-survivors, and the control group, we identified 14 metabolites with elevated levels in sepsis cases versus controls, the majority of which include amino acids and carbohydrates. With respect to the differences between sepsis survivors and non-survivors, previous studies revealed that levels of metabolites related to the citric acid cycle, glycolysis, and gluconeogenic amino acids were decreased in sepsis survivors (Langley et al., 2013). In our study, we also evaluated amino acid catabolites, carnitine esters, nucleic acid catabolites, free fatty acids, glycerophosphocholines, GPC and GPE esters, glycolysis and citric acid cycle intermediates, and when sepsis survivors and non-survivors were compared, we found that two carnitine esters (palmitoylcarnitine and acetylcarnitine) and amino acids including glutamate, tyrosine, tryptophan, methionine, and proline were elevated in the non-survivor group. In addition, acetylneuraminate and N2,N2-dimethylguanosine were identified by our metabolomics platform and found

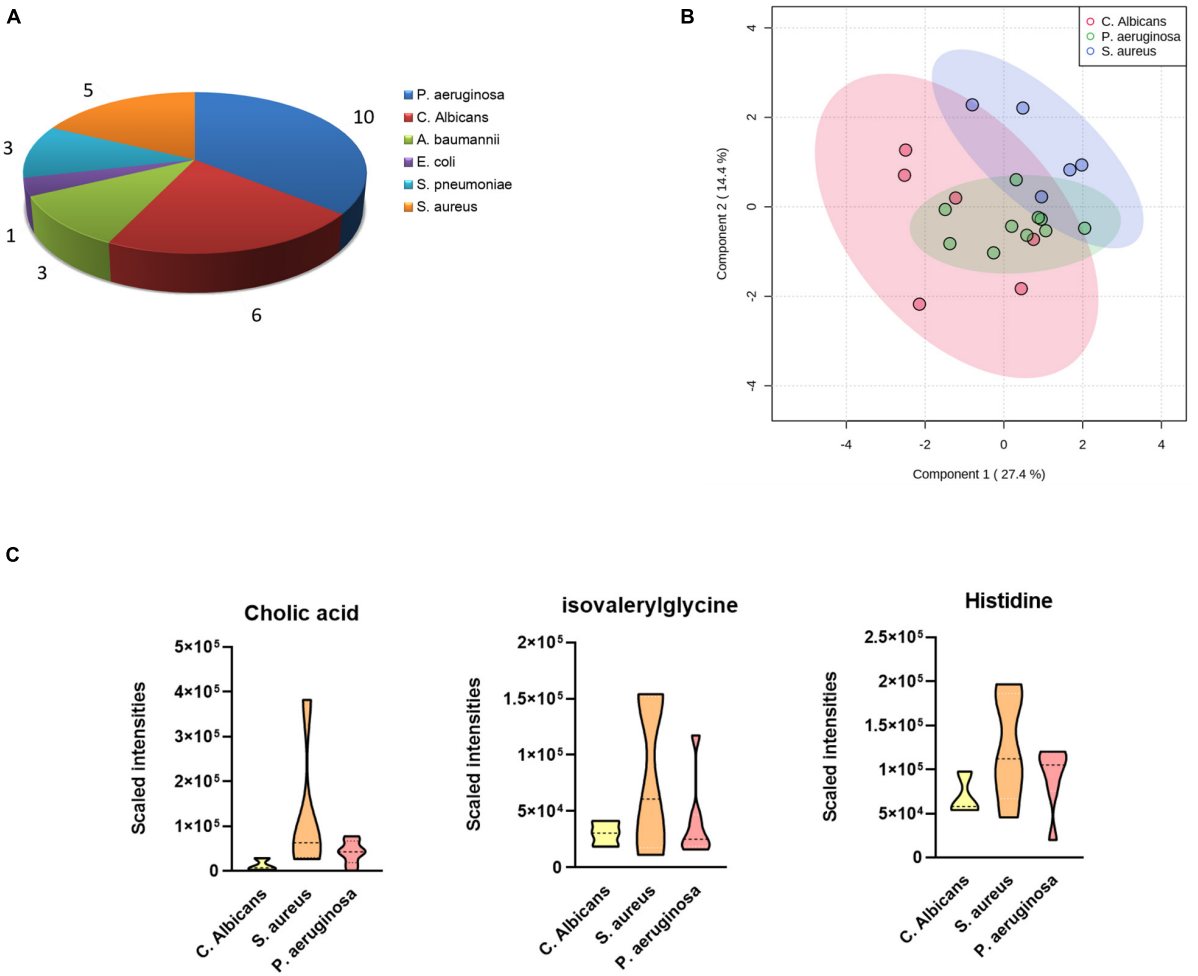

FIGURE 3 | Differences in plasma metabolites according to sepsis-causing pathogens. **(A)** Confirmed sepsis cases infected by different microbes. **(B)** OPLS-DA analysis showing the metabolic discrimination of cases infected by three major microbes: *P. aeruginosa*, *C. albicans*, and *S. aureus*. **(C)** Relative serum levels of cholic acid, isovalerylglycine, and histidine were represented in sepsis survivors infected by *S. aureus*, *P. aeruginosa*, and *C. albicans*.

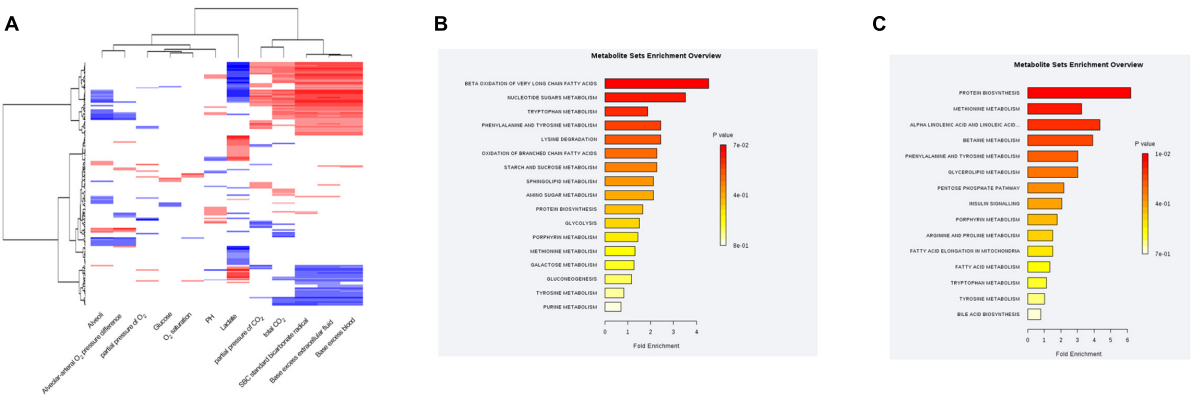

FIGURE 4 | Correlations between the plasma metabolic profile and blood gas analysis in sepsis patients. **(A)** Hierarchical clustering heatmap depicting correlations between metabolomic data and blood gas indices. **(B)** Pathway enrichment analysis highlighting metabolic pathways correlated with the plasma lactate level in sepsis patients. **(C)** Pathway-enrichment analysis highlighting metabolic pathways correlated with the plasma bicarbonate level in sepsis patients.

increased in non-survivors; these changes were consistent with previous studies (Drobnik et al., 2003; Langley et al., 2013).

We identified a number of additional metabolites with reduced levels in sepsis survivors, implicating that other metabolic pathways may contribute to sepsis progression, especially in the Chinese population (**Figure 2B**). Lactate has been widely considered as a sepsis severity marker, and the level of lactate was significantly elevated in patients with worse prognosis, such as organ failure or death. We identified a series of fatty acids associated with the alteration of lactate in examined cases, including the oxidation of very long chain and branched-chain fatty acids. Therefore, the oxidative stress of fatty acids may be involved in the pathogenesis of sepsis, at least in the severe subgroup.

CONCLUSION

In summary, we analyzed the global metabolomic information in a collected cohort of Chinese pediatric sepsis patients. Our study demonstrated the predictive value using the combination of metabolic biomarkers to distinguish individuals with or without sepsis, or patients with different pathogens and severities, which may lead to the development of personalized therapies against sepsis with higher accuracy.

DATA AVAILABILITY STATEMENT

The datasets generated and analyzed during the current study are available from the corresponding author on reasonable request.

ETHICS STATEMENT

The studies involving human participants were reviewed and approved by the Ethics Committee on Human Research at Zhongshan School of Medicine, Sun Yat-sen University. Written informed consent to participate in this study was provided by the participants' legal guardian/next of kin.

AUTHOR CONTRIBUTIONS

BL, Z-YO, H-YL, and CL conceived and designed the experiments. G-BL, H-RH, W-FP, BL, and CL contributed to the sample collection and metabolic analysis. G-BL, H-RH, and W-FP performed the experiments. G-BL, BL, and CL interpreted the data and wrote the manuscript. BL, Z-YO, H-YL, and CL contributed to the funding acquisition and supervision. All authors contributed to the article and approved the submitted version.

FUNDING

This study was supported by the National Natural Science Foundation of China (82073074 to BL).

ACKNOWLEDGMENTS

We would like to thank the study participants for their important support of this research.

REFERENCES

Angus, D. C., and Van der Poll, T. J. (2013). Severe sepsis and septic shock. *N. Engl. J. Med.* 369, 840–851.

Bosmann, M., and Ward, P. A. (2013). The inflammatory response in sepsis. *Trends Immunol.* 34, 129–136. doi: 10.1016/j.it.2012.09.004

Drobnik, W., Liebisch, G., Audebert, F.-X., Fröhlich, D., Glück, T., Vogel, P., et al. (2003). Plasma ceramide and lysophosphatidylcholine inversely correlate with mortality in sepsis patients. *J. Lipid Res.* 44, 754–761. doi: 10.1194/jlr.m200401-jlr200

Drosatos, K., Lymperopoulos, A., Kennel, P. J., Pollak, N., Schulze, P. C., and Goldberg, I. J. J. (2015). Pathophysiology of sepsis-related cardiac dysfunction: driven by inflammation, energy mismanagement, or both? *Curr. Heart Fail. Rep.* 12, 130–140. doi: 10.1007/s11897-014-0247-z

Fischer, K., Kettunen, J., Würtz, P., Haller, T., Havulinna, A. S., Kangas, A. J., et al. (2014). Biomarker profiling by nuclear magnetic resonance spectroscopy for the prediction of all-cause mortality: an observational study of 17,345 persons. *PLoS Med.* 11:e1001606. doi: 10.1371/journal.pmed.1001606

Fleischmann-Struzek, C., Goldfarb, D. M., Schlattmann, P., Schlapbach, L. J., Reinhart, K., and Kissoon, N. J. T. (2018). The global burden of paediatric and neonatal sepsis: a systematic review. *Lancet Respir. Med.* 6, 223–230. doi: 10.1016/s2213-2600(18)30063-8

Green, P., Theilla, M., and Singer, P. J. (2016). Lipid metabolism in critical illness. *Curr. Opin. Clin. Nutr. Metab. Care* 19, 111–115. doi: 10.1097/mco.0000000000000253

Guo, L., Milburn, M. V., Ryals, J. A., Lonergan, S. C., Mitchell, M. W., Wulff, J. E., et al. (2015). Serum metabolomic profiles enhance precision medicine for volunteers of normal health. *Proc. Natl. Acad. Sci. U.S.A.* 112, E4901–E4910.

Kamisoglu, K., Haimovich, B., Calvano, S. E., Coyle, S. M., Corbett, S. A., Langley, R. J., et al. (2015). Human metabolic response to systemic inflammation: assessment of the concordance between experimental endotoxemia and clinical cases of sepsis/SIRS. *Crit. Care* 19:71. doi: 10.1186/s13054-015-0783-2

Kaukonen, K. M., Bailey, M., Suzuki, S., Pilcher, D., and Bellomo, R. (2014). Mortality related to severe sepsis and septic shock among critically ill patients in Australia and New Zealand, 2000-2012. *JAMA* 311, 1308–1316. doi: 10.1001/jama.2014.2637

Kirn, T., and Weinstein, M. J. (2013). Update on blood cultures: how to obtain, process, report, and interpret. *Clin. Microbiol. Infect.* 19, 513–520. doi: 10.1111/1469-0691.12180

Kumar, G., Kumar, N., Taneja, A., Kaleekal, T., Tarima, S., McGinley, E., et al. (2011). Nationwide trends of severe sepsis in the 21st century (2000–2007). *Chest* 140, 1223–1231. doi: 10.1378/chest.11-0352

Langley, R. J., Tsalik, E. L., Van Velkinburgh, J. C., Glickman, S. W., Rice, B. J., Wang, C., et al. (2013). An integrated clinico-metabolomic model improves prediction of death in sepsis. *Sci. Transl. Med.* 5, 195 ra195.

Lawton, K. A., Berger, A., Mitchell, M., Milgram, K. E., Evans, A. M., Guo, L., et al. (2008). Analysis of the adult human serum metabolome. *Pharmacogenomics* 9, 383–397.

Moon, J.-S., Lee, S., Park, M.-A., Siempos, I. I., Haslip, M., Lee, P. J., et al. (2015). UCP2-induced fatty acid synthase promotes NLRP3 inflammasome activation during sepsis. *J. Clin. Invest.* 125, 665–680. doi: 10.1172/jci78253

Opal, S. M., Garber, G. E., LaRosa, S. P., Maki, D. G., Freebairn, R. C., Kinasewitz, G. T., et al. (2003). Systemic host responses in severe sepsis analyzed by causative microorganism and treatment effects of drotrecogin alfa (activated). *Clin. Infect. Dis.* 37, 50–58. doi: 10.1086/375593

Pang, Z., Chong, J., Li, S., and Xia, J. J. M. (2020). MetaboAnalystR 3.0: Toward an Optimized Workflow for Global Metabolomics. *Metabolites* 10:186. doi: 10.3390/metabo10050186

Patel, R., Vetter, E. A., Harmsen, W. S., Schleck, C. D., Fadel, H. J., and Cockerill, F. R. III (2011). Optimized pathogen detection with 30-compared to 20-milliliter blood culture draws. *J. Clin. Microbiol.* 49, 4047–4051. doi: 10.1128/jcm.01314-11

Ranieri, V. M., Thompson, B. T., Barie, P. S., Dhainaut, J.-F., Douglas, I. S., Finfer, S., et al. (2012). Drotrecogin alfa (activated) in adults with septic shock. *N. Engl. J. Med.* 366, 2055–2064.

Shen, X., Wang, R., Xiong, X., Yin, Y., Cai, Y., Ma, Z., et al. (2019). Metabolic reaction network-based recursive metabolite annotation for untargeted metabolomics. *Nat. Commun.* 10:1516. doi: 10.1038/s41467-019-09550-x

Singer, M., Deutschman, C. S., Seymour, C. W., Shankar-Hari, M., Annane, D., Bauer, M., et al. (2016). The third international consensus definitions for sepsis and septic shock (sepsis-3). *JAMA* 315, 801–810. doi: 10.1001/jama.2016.0287

Torio, C. M., and Moore, B. J. (2006). "National inpatient hospital costs: the most expensive conditions by payer, 2013: statistical brief# 204," in *Healthcare Cost and Utilization Project (HCUP) Statistical Briefs*, (Rockville, MD: Agency for Healthcare Research and Quality), 2006–2016. Available online at: https://europepmc.org/books/n/hcupsb/sb231/?extid=29578669&src=med

Wang, A., Huen, S. C., Luan, H. H., Yu, S., Zhang, C., Gallezot, J.-D., et al. (2016). Opposing effects of fasting metabolism on tissue tolerance in bacterial and viral inflammation. *Cell* 166:1512–1525.e12. doi: 10.1016/j.cell.2016.07.026

Wishart, D. S., Knox, C., Guo, A. C., Eisner, R., Young, N., Gautam, B., et al. (2009). HMDB: a knowledgebase for the human metabolome. *Nucleic Acids Res.* 37(suppl. 1), D603–D610.

Conflict of Interest: The authors declare that the research was conducted in the absence of any commercial or financial relationships that could be construed as a potential conflict of interest.

frontiers in Cell and Developmental Biology

ORIGINAL RESEARCH
published: 01 April 2021
doi: 10.3389/fcell.2021.650748

Urea as a By-Product of Ammonia Metabolism Can Be a Potential Serum Biomarker of Hepatocellular Carcinoma

Changsen Bai[1†], Hailong Wang[2†], Dong Dong[1], Tong Li[3], Zhi Yu[4], Junfei Guo[5], Wei Zhou[1], Ding Li[1], Ruochen Yan[6], Liyan Wang[6], Zhaosong Wang[7], Yueguo Li[1] and Li Ren[1]**

[1] Department of Laboratory, Tianjin Medical University Cancer Institute and Hospital, National Clinical Research Center for Cancer, Key Laboratory of Cancer Prevention and Therapy, Tianjin's Clinical Research Center for Cancer, Tianjin, China, [2] Department of Cancer Cell Biology, Tianjin Medical University Cancer Institute and Hospital, National Clinical Research Center for Cancer, Key Laboratory of Cancer Prevention and Therapy, Tianjin's Clinical Research Center for Cancer, Tianjin, China, [3] Department of Laboratory, Second Affiliated Hospital of Tianjin University of TCM, Tianjin, China, [4] Department of Laboratory, First Affiliated Hospital of Shaoyang University, Shaoyang, China, [5] Department of Laboratory, Guangdong Women and Children Hospital, Guangzhou, China, [6] School of Medical Laboratory, Tianjin Medical University, Tianjin, China, [7] Department of Public Laboratory, Tianjin Medical University Cancer Institute and Hospital, National Clinical Research Center for Cancer, Key Laboratory of Cancer, Prevention and Therapy, Tianjin's Clinical Research Center for Cancer, Tianjin, China

OPEN ACCESS

Edited by:
Changliang Shan,
Nankai University, China

Reviewed by:
Xue Gao,
University of Chicago, United States
Yan Chen,
Jinan University, China

***Correspondence:**
Yueguo Li
kesaqi@163.com
Li Ren
lirentmu@163.com

† These authors have contributed equally to this work

Specialty section:
This article was submitted to Molecular Medicine, a section of the journal Frontiers in Cell and Developmental Biology

Received: 07 January 2021
Accepted: 05 March 2021
Published: 01 April 2021

Citation:
Bai C, Wang H, Dong D, Li T, Yu Z, Guo J, Zhou W, Li D, Yan R, Wang L, Wang Z, Li Y and Ren L (2021) Urea as a By-Product of Ammonia Metabolism Can Be a Potential Serum Biomarker of Hepatocellular Carcinoma. Front. Cell Dev. Biol. 9:650748. doi: 10.3389/fcell.2021.650748

Hepatocellular carcinoma (HCC) is highly malignant; nearly half of the new cases and deaths are in China. The poor prognosis of HCC is mainly due to late diagnosis; many new biomarkers have been developed for HCC diagnosis. However, few markers are quickly translated into clinical practice; early and differential diagnosis of HCC from cirrhosis and/or hepatitis is still a clinical challenge. Metabolomics and biochemical methods were used to reveal specific serum biomarkers of HCC. Most of the elevated metabolites in HCC and HBV patients were overlapped compared with controls. Urea was the specifically elevated serum biomarker of HCC patients. Moreover, urea combined with AFP and CEA can improve the sensitivity of HCC diagnosis. The plasma ammonia of HCC patients was significantly higher than healthy controls. Co-culture cell model revealed normal liver cells cooperated with cancer cells to metabolize ammonia into urea. The urea metabolism in cancer cells marginally depended on the expression of CPS1. However, the expression of CPS1 did not change with ammonium chloride, which might regulate the urea cycle through enzyme activity. The urea cycle could detoxify high concentrations of ammonia to promote cancer cell proliferation. Therefore, urea was a by-product of ammonia metabolism and could be a potential serum biomarker for HCC. The combined application of metabolomics and biochemical methods can discover new biomarkers for the early diagnosis of HCC and be quickly applied to clinical diagnosis.

Keywords: metabolomics, hepatocellular carcinoma, urea, ammonia, CPS1, biomarker

INTRODUCTION

According to annual forecasts, the World Health Organization estimates that more than 1 million patients will die of liver cancer by 2030. New cases and deaths related to liver cancer in China account for about 50% of the world (Torre et al., 2015; Fu and Wang, 2018). Hepatocellular carcinoma (HCC) is highly malignant and usually diagnosed at an advanced stage, accounting for over 80% of primary liver cancers (Forner et al., 2018). Early diagnosis and a better understanding of the molecular mechanisms leading to HCC occurrence and progression are clinically urgent. At present, despite tremendous efforts have been made to discover new biomarkers for early diagnosis of HCC, the diagnosis of HCC still depends on imaging (ultrasound B, CT or MRI) and alpha-fetoprotein (AFP) in clinical practice (Montal et al., 2019; Timo Alexander et al., 2020; Zech et al., 2020). However, their sensitivity and/or specificity are not satisfactory.

Metabolic reprogramming is a recognized hallmark of cancer (Hanahan and Weinberg, 2011). Metabolites can regulate gene and protein expressions, and metabolic proteins and/or metabolites are potential diagnostic and prognostic biomarkers (DeBerardinis and Chandel, 2016; Pavlova and Thompson, 2016; Wolpaw and Chi, 2018). Reliable results have been obtained using certain metabolites, such as lactate and amino acid, and their changes in serum reflect the metabolic changes in tumor tissue (De Matteis et al., 2018; Fujiwara et al., 2018). Many studies were devoted to discovering serum biomarkers of HCC diagnosis from the aspect of metabolism. Ping Luo et al. (Luo and Yin, 2018) defined a group of biomarkers of serum metabolites, including phenylalanyl-tryptophan and glycine cholate. This panel has a higher diagnostic performance than AFP in distinguishing HCC from high-risk cirrhosis populations, with the area under the receiver-operating characteristic curve (ROC) of 0.807 for the panel versus 0.650 for AFP in the validation set. Tomoyoshi Soga et al. (2011) revealed that c-glutamyl dipeptides are new biomarkers for liver disease and can distinguish different liver disease forms. These studies may reflect various metabolic aspects of HCC. Still, the limited study cohort or lack of sufficient validation restricts further clinic applications of these biomarkers, because most laboratories do not have mass spectrometers for detecting metabolites, especially in developing countries. Moreover, they failed to elucidate the underlying molecular mechanism.

Second to glucose, cancer cells are highly dependent on glutamine for survival and proliferation. Glutamine catabolism is accompanied by the secretion of alanine and ammonia, leading to most of the amino groups of glutamine are lost from the cell instead of being incorporated into other molecules (DeBerardinis et al., 2007). Together with other amino acid metabolism, they lead to the accumulation of ammonia in the tumor microenvironment. Interestingly, ammonia metabolism plays different roles in cancers. Most researchers believe ammonia is a toxic cellular by-product of glutamine metabolism (Khan et al., 2019; Li et al., 2019) and needs to be metabolized into a non-toxic form, such as urea, to be excluded from the body. But Jessica B et al. prove that breast cancer cells can recycle glutamine amide to support biosynthesis (Spinelli and Yoon, 2017). Therefore, the role of ammonia in cancer cells remains to be determined.

The liver represents a perfect metabolic model that governs body energy metabolism through different metabolites' physiological regulation, including sugars, lipids, amino acids, and the urea cycle. Therefore, our research uses quantitative targeted metabolomics to screen for specific metabolites of HCC and in-depth verification using biochemical analysis methods. We found that urea was a potential biomarker of HCC, and combining it with AFP and CEA could improve the detection efficiency of HCC. Normal liver cells and cancer cells cooperated to metabolize ammonia into urea, leading to the elevated serum urea in HCC patients. The urea cycle could detoxify high concentration of ammonia to promote cancer cell proliferation.

MATERIALS AND METHODS

Study Design and Participants

In this study, we collected 10 serum samples of healthy controls, 10 HBV without cirrhosis and 10 HBV positive HCC patients evolved from cirrhosis with similar sex and age. Hence, the data was comparable between both groups. The metabolites of the serum were analyzed by quantitative targeted metabolomics for differential analysis to find specific potential markers of HCC patients. The biochemical analysis method was used for in-depth analysis and verification. The serum of 115 cases of healthy controls, 69 cases of HBV, 108 cases of HBV positive cirrhosis, 95 cases of HCV, 294 cases of HBV positive HCC patients, and 77 cases of metastatic HCC patients (other cancers metastasize to the liver) were preliminary verified as the training set. Next, the serum of 118 normal healthy controls, 142 cases of lung cancer patients, 150 cases of breast cancer patients, 140 cases of colorectal cancer patients, and 165 cases of HBV positive HCC patients were analyzed as the validation set. All tumor patients were at the early stage, without treatment and metastasis to other sites (except for metastatic HCC). The groups' age and gender in the training set and validation set were similar, except for the breast cancer group (**Supplementary Tables 1, 2**). All serum samples were collected on the first day after hospitalization, before surgery or treatment, and quick-freeze at −80°C until use. The exclusion criteria for healthy controls were abnormal liver and kidney function, with a history of liver disease or other systemic diseases. All tumor types were diagnosed by pathology. This study was approved by the Ethics Committee of Tianjin Medical University Cancer Hospital, and all patients signed informed consent.

Targeted Metabolomics

The frozen serum samples were thawed at 4°C. Take 100 μL of serum to a 1.5 mL Ep tube and add 4 volumes of extract made of MeOH/Acetonitrile (ACN) = (1/1, v/v), containing 0.05 mM DL-Methionine sulfone as an internal standard. After shaking and mixing well, place the protein precipitate at −20°C for 2 h. Centrifuge at 20,000 *g* at 4°C for 10 min, and transfer the upper layer to a new 1.5 mL Ep tube. Spin to dry *in vacuo* by Eppendorf Concentrator 5301, add 100 μL ACN/H_2O (1/1,

v/v), and reconstitute by shaking. Filter with a 0.22 μm filter membrane, and transfer the sample to the sample bottle for testing. The sample injection volume was 10 μL/time, separated by Agilent 1260 Infinity HPLC/PRF/5 liquid phase system, and detected by Agilent 6460 QQQ at Aksomics (Shanghai, China). The analysis was performed on an Amide column (3.5 μm, 2.1 * 150 mm, Waters) with a column temperature of 40°C. Mobile phase A is an aqueous solution containing 25 mM NH_4OAc, 25 mM NH_3H_2O, and liquid B is an acetonitrile solution. The column is equilibrated with 90% liquid B. The sample is loaded onto the chromatographic column by the auto-sampler and then separated by the chromatographic column at a flow rate of 0.4 mL/min. Mass spectrometry detection mode and metabolite detection condition settings: Multiple reaction monitoring (MRM) mode detections, select the detection polarity corresponding to the specific metabolite, retention time, and optimized ion pair for detection. Metabolite detection data is quantified using QuantAnalysis software. Perform differential analysis on the quantitative results to obtain corresponding differentially expressed metabolites.

Biochemical Analyses

Serum and plasma samples were stored at −80°C until further analysis. Urea, creatinine (Cr), and uric acid were detected using an automatic biochemical analyzer AU5800 (Beckman Coulter, United States). Urea was detected as previously described (Wang et al., 2019). Briefly, urea is hydrolyzed by urease to produce ammonia and carbon dioxide. Ammonia and a-ketoglutarate are converted to glutamate under the catalysis of GDH. At the same time, a molar equivalent of reduced NADH is oxidized. For each molecule of urea to be hydrolyzed, two NADH molecules are oxidized. Due to the disappearance of NADH, the absorbance at 340 nm is proportional to the urea concentration in the sample. Cr was measured by enzyme colorimetry. Briefly, creatinine is catalyzed by creatininase to generate creatine, and creatine is catalyzed by creatase to generate sarcosine and urea, and then sarcosine is oxidized to generate glycine and hydrogen peroxide; the red intensity of the produced quinoneimine is proportional to the concentration of Cr, and the intensity can be determined by measuring the increase in absorbance. Uric acid was determined by enzymatic colorimetry. Uricase breaks down uric acid to produce allantoin and hydrogen peroxide. In the presence of peroxidase, 4-aminopyrine generates quinoneimine dye from hydrogen peroxide. The red intensity of the produced quinoneimine is proportional to the concentration of uric acid.

Ammonia was detected by VITROS 5600 Integrated System (Ortho Clinical Diagnostics, United States) as previously described (Wang et al., 2019). Briefly, a drop of sample is deposited on the slide and then evenly distributed to the underlying layers. Water and non-protein components travel to the underlying buffered reagent layer, and ammonium ions are converted into gaseous ammonia. The semi-permeable membrane only allows ammonia gas to pass through and prevents buffer or hydroxide ions from reaching the indicator layer. After a period of time, the white background of the extended layer is used as a diffuse reflector to measure the reflection density of the dye.

Cell Culture

The human HL-7702 hepatocyte cell line and human HCC cell line MHCC97H were obtained from the Liver Cancer Institute, Zhongshan Hospital, Fudan University, Shanghai, China. HepG2, PLC/PRF/5, Hep3B, A549, MCF-7, NCM460, HCT116, HCT8 cells were obtained from ATCC. HLE cell line was from the Health Science Research Resources Bank (Osaka, Japan). All the cells were maintained in high glucose DMEM supplemented with 10% fetal bovine serum (BioInd, Israel) and 50 IU penicillin/streptomycin (Invitrogen, United States) in a humidified atmosphere with 5% CO2 at 37°C. All cell lines were free of mycoplasma contamination and cultured for no more than 2 months.

Co-Culture Cell Models

200,000 HL-7702 and 100,000 MHCC97H + 100,000 HL-7702 cells were seeded in triplicate in 6-well plates. The next day the medium was changed by fresh DMEM with 10% dialysis fetal bovine serum, 25 mM glucose, and 2 mM glutamine. After 48 h, the medium was collected for urea detection. Falcon embedded cell culture chamber (PET track-etched membrane, 6 well formats, 0.4 μm, Corning, Cat#353090) was used for the co-culture model. 200,000 HL-7702, MHCC97H or PLC/PRF/5 were seeded in triplicate in 6-well plates (lower layer). 100,000 HL-7702 for each cell line were seeded in triplicate in the chamber (upper layer) on new 6-well plates. The next day the medium in 6-well plates and the chamber were changed by fresh DMEM with 10% dialysis fetal bovine serum, 25 mM glucose, and 2 mM glutamine, respectively. Then transfer the chamber to the six-well plate inoculated with HL-7702, MHCC97H or PLC/PRF/5 for culture. After 48 h, medium was collected for urea and ammonia detection.

Ammonia and Urea Excretion

200,000 cells were seeded in triplicate in 12-well plates. The next day the medium was changed by fresh DMEM with 10% dialysis fetal bovine serum, 25 mM glucose and 2 mM glutamine. After 8 h the medium was collected for ammonia detection. 100,000 cells were seeded in triplicate in 12-well plates. The next day the medium was changed by fresh DMEM with 10% dialysis fetal bovine serum, 25 mM glucose, and 2 mM glutamine. After 48 h, the medium was collected for urea detection. The medium without cells under the same conditions was used to measure the concentration of metabolites as the background control. Values for ammonia and urea in the experimental conditions were subtracted from the respective control media values.

Proliferation Assays

20,000 cells were seeded in triplicate in 24-well plates, and changed to the conditioned medium the next day. After 3 days, wells were washed twice with PBS buffer to remove dead cells, and then the cells were trypsinized; cell number was determined using a hemocytometer. For each well, the fold change in cell number relative to Day_0 was calculated.

Colony Formation Assay

Colony formation assays were performed to assess the effects of NH_4Cl on cell proliferation. 1000 cells were seeded in triplicate in 12-well plates, change to 2 ml of culture medium containing 0–20 mM of NH_4Cl the next day. After incubating at 37°C for 2 weeks, cells were stained with 0.5% crystal violet for 5 min, and colonies were counted with Image J.

Western Blot

After desired treatments as specified as indicated, cells were washed twice with PBS and lysed in buffer on ice (20 mM Tris–HCl, pH 7.5, 150mM NaCl, 1 mM EDTA, 1% Triton X-100, 2.5 mM sodium pyrophosphate, 1mM β-glycer-ophosphate, 1mM sodium vanadate, 1mgml-1 leupeptin, 1mM phenylmethyl-sulfonylfluoride). Equal amounts of protein (30 μg) were loaded onto 10% SDS–PAGE gels. Western detection was carried out using a Li-Cor Odyssey image reader (Li-Cor, United States). The goat anti-rabbit IgG (Cat#C30502-01) and goat anti-mouse IgG (Cat#C30509-01) secondary antibodies were obtained from Li-Cor (United States). The final concentration of the secondary antibodies used was 0.1 μg/ml (1:10000 dilution). The primary antibodies against β-Actin (Cat#60008-1, 1:5000 dilution), GAPDH (Cat#60004-1-Ig, 1:5000 dilution), FLAG Tag (Cat#80010-1-RR, 1:3000 dilution), α-Tubulin (Cat#11224-1-AP, 1:5000 dilution), CPS1 (Cat#18703-1-AP, 1:1000 dilution), OTC (Cat#26470-1-AP, 1:1000 dilution), ARG1 (Cat#16001-1-AP, 1:1000), GDH1 (Cat#14299-1-AP, 1:1000 dilution), and GS (Cat#11037-2-AP, 1:1000 dilution) were purchased from Proteintech (United States), The primary antibodies against CAD (Cat#sc-376072, Santa Cruz, United States) and p-CAD (Ser1859) (Cat#70307, Cell Signaling Technology, United States) were used with a dilution of 1:1000.

Gene Construction and Lentivirus Production

The pLKO.1 lentiviral RNAi expression system was used to construct lentiviral shRNA for genes. The sequences of shRNA used in this study included the following: shScramble: CCTAAGGTTAAGTCGCCCTCG, shCPS1-#1: CCAGAAATTAAGAACGTCGTA, shCPS1-#2: CGTACTTCAATCAATGTTGTT. pCDH-FLAG-CPS1 plasmid was kindly gifted by Professor Peng Jiang at Tsinghua University. Viral packaging was done according to the protocol: expression plasmids pCDH-CMV-cDNA, pCMV-dR8.91, and pCMV-VSV-G were co-transfected into 293T cells using the Polyethylenimine (PEI) coprecipitation at 20:10:10 μg (for a 10-cm dish). After incubation for 6 h, the medium containing PEI and plasmid mixture was replaced with complete fresh medium. Media containing virus was collected 48 h after transfection and then filter the culture medium with a 0.2 μm filter (Merck Millipore Ltd., IRELAND). The culture medium with the virus was stored at −80°C for use. Cancer cells were infected with the viruses in the presence of polybrene (10 μgml^{-1}) for 8 h, the medium was replaced with complete fresh medium for 40 h, and then cells were selected with puromycin, generating stable CPS1 knockdown or over-expression cell lines.

Statistical Analysis

Quantitative data was expressed as data plots; non-normally distributed data was expressed as median (25% Percentile, 75% Percentile), and normally distributed data was expressed as mean ± SD. Differences between two independent groups were compared with the Mann-Whitney U test. One-way ANOVA followed by Tukey's multiple comparison tests were used for multi comparisons. The two-tailed value of $P < 0.05$ is statistically significant. GraphPad Prism 8.0 software was adopted to analyze the above data. MedCalc software was used to draw ROC curves of different indicators. The 95% confidence interval for comparing the Area Under Curve (AUC) and *P*-values of related ROC curves were obtained by the method described by DeLong et al. (1988).

RESULTS

Screening for Differential Serum Metabolites of HCC by Targeted Metabolomics

To screen for specific serum metabolites of HCC patients can be verified by biochemical methods, we quantitatively detected 135 metabolites, including glycolysis, tricarboxylic acid (TCA) cycle, amino acids, nucleotides, CoA, etc., in the serum of normal people, HBV and HCC patients through targeted metabolomics. Cluster analysis was performed on the 67 different metabolites detected ($P < 0.05$) (**Figure 1A**). Compared with healthy controls, 11 serum metabolites of HCC significantly increased, including lactate, glycolic acid, cis-Aconitic acid, fumarate, malate, urea, glutamate, aspartate, choline, uric acid, and 3-Hydroxybutyric acid, and 8 decreased, consist of cystine, arginine, lysine, tryptophan, cAMP, guanine, guanosine and inosine (**Figure 1B** and **Table 1**). Compared with healthy controls, 11 serum metabolites of HBV significantly increased, including lactate, phenylalanine, fumarate, uric acid, malate, glutamate, methionine, cystathionine, aspartate, glycolic acid, and cis-Aconitic acid, and 4 decreased, consist of guanosine, cAMP, inosine and creatine (**Figure 1C** and **Table 1**). To find the specific serum metabolites of HCC patients, we used a Venn diagram to analyze three groups of different metabolites. Most of the elevated metabolites (including lactate, fumarate, malate, and glutamate et al) in HCC and HBV patients were overlapped; urea was the specifically elevated biomarker of HCC patients, arginine, lysine and guanine were the specifically decreased markers of HCC (**Figure 1D**). MetaboAnalyst was used for KEGG pathway analysis of differential metabolites (Chong et al., 2018). Compared with healthy controls, HCC and HBV patients were both enriched in arginine biosynthesis, alanine, aspartate and glutamate metabolism, D-glutamine and D-glutamate metabolism, pyruvate metabolism, citrate cycle (TCA cycle), cysteine and methionine metabolism, and arginine and proline metabolism pathways (**Supplementary Figures 1A,B**). Purine metabolism was a differential metabolic pathway in patients with HCC compared with HBV patients (**Supplementary Figures 1A,B**).

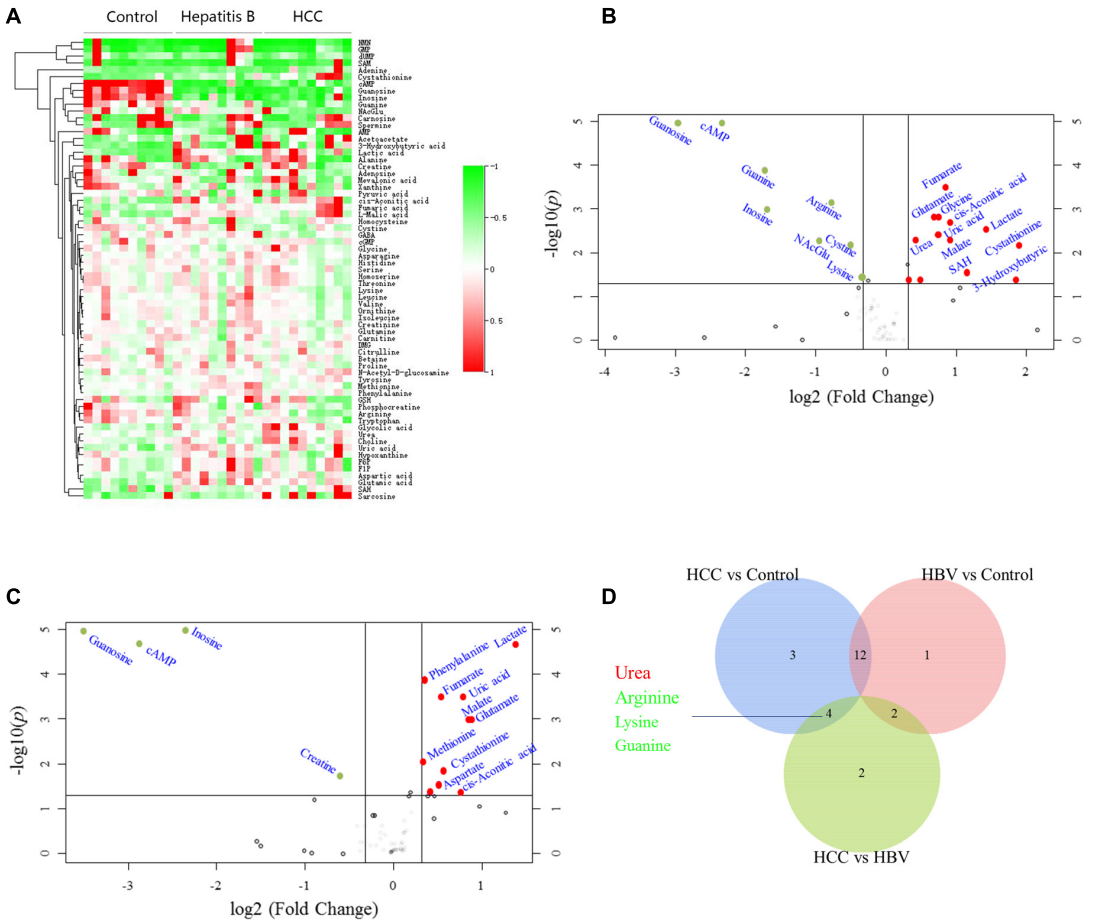

FIGURE 1 | Screening for differential serum metabolites of HCC by targeted metabolomics. **(A)** Heatmap clustering analysis of differential metabolites in serum of 10 normal controls, 10 HBV and 10 HBV positive HCC patients. **(B)** Metabolites volcano map of HCC vs control. Compared with the control group, the significantly increased metabolites were shown in red, and the significantly decreased metabolites were shown in green. **(C)** Metabolites volcano map of HBV vs control. Compared with the control group, the significantly increased metabolites were shown in red, and the significantly decreased metabolites were shown in green. **(D)** Venn diagram was used to characterize different metabolites of HCC vs control, HBV vs control and HCC vs HBV.

Serum Urea Was a Potential Biomarker for HCC

To verify the results of metabolomics, we used biochemical methods to detect metabolites. First of all, to find specific markers in the transition from HBV to HCC, serums of normal people, HBV, HBV positive cirrhosis, HCV, HBV positive HCC, and metastatic HCC patients were collected for verification. Our results showed serum urea in HCC and metastatic HCC patients were significantly higher than healthy controls in the training set (**Figure 2A**). Moreover, serum urea of HCC was much higher than HBV, Cirrhosis, and HCV patients (**Figure 2A**), indicating urea can distinguish HCC from other liver diseases. The liver is the metabolic center of the body; many metabolic enzymes are specifically expressed in the liver, we wander to know if other cancers are different from HCC. Therefore, serum samples of patients with HCC, colorectal cancer, lung cancer and breast cancer were collected for multi-tumor analysis. We found serum urea in patients with lung cancer, gastric cancer, colorectal cancer, breast cancer, and HCC were significantly higher than healthy controls in the validation set (**Figure 2B**), which revealed that elevated serum urea in cancer patients might be a common phenomenon. Next, we asked whether the glomerular filtration and renal tubular reabsorption in cancer patients lead to increased serum urea. We tested creatinine and uric acid to evaluate glomerular filtration and renal tubular reabsorption, respectively. The serum creatinine level in HCC and metastatic HCC patients did not increase significantly compared with healthy controls, HBV, Cirrhosis, and HCV patients (**Figure 2C**). The serum creatinine of patients with lung cancer and breast cancer was even lower than that of healthy controls (**Figure 2D**). Metabolomics results showed uric acid in patients with HCC and HBV were significantly higher than those in healthy controls. However, we detected serum uric acid in patients with HCC and various tumors did not increase in the training set and validation set (**Figures 2E,F**). Taken together, these data demonstrated it was not the abnormal renal function in cancer patients leading to the elevated urea; urea might be a biomarker for HCC.

TABLE 1 | The main differential metabolites of HCC, hepatitis B patients and healthy controls by targeted metabolomics.

Metabolites (g/L)	Control (NC)	Hepatitis B (HBV)	HCC	*P*-value (HCC/NC)	Fold change (HCC/NC)	*P*-value (HBV/NC)	Fold change (HBV/NC)	*P*-value (HCC/HBV)	Fold change (HCC/HBV)
Lactate	4.50 ± 1.38	11.69 ± 6.07	12.13 ± 9.35	0.0200	2.7	0.0018	2.6	0.9034	1.04
Glycolic acid	0.10 ± 0.02	0.13 ± 0.03	0.16 ± 0.07	0.0072	1.68	0.0267	1.31	0.1415	1.28
cis-Aconitic acid	0.05 ± 0.02	0.08 ± 0.04	0.09 ± 0.03	0.0028	1.9	0.0203	1.7	0.5490	1.12
Fumarate	0.01 ± 0.00	0.02 ± 0.00	0.03 ± 0.01	0.0063	1.8	0.0003	1.45	0.1868	1.25
L-Malate	0.69 ± 0.00	1.25 ± 0.12	1.30 ± 0.78	0.0355	1.88	0.0001	1.81	0.8465	1.04
Cystine	1.27 ± 0.24	1.19 ± 0.44	0.90 ± 0.26	0.0035	0.7	0.6096	0.94	0.0837	0.75
Arginine	95.96 ± 21.10	81.52 ± 24.13	56.16 ± 20.74	0.0005	0.59	0.1712	0.85	0.0214	0.69
Urea	25.93 ± 4.27	28.24 ± 5.25	34.61 ± 6.77	0.0030	1.33	0.2966	1.09	0.0303	1.23
GABA	0.12 ± 0.03	0.13 ± 0.04	0.09 ± 0.02	0.0289	0.76	0.7805	1.04	0.0246	0.74
Glutamate	7.53 ± 2.19	13.89 ± 4.23	12.13 ± 2.62	0.0005	1.61	0.0005	1.84	0.2765	0.87
Histidine	374.06 ± 41.81	378.28 ± 70.96	313.19 ± 62.85	0.0201	0.84	0.8731	1.01	0.0435	0.83
Aspartate	1.06 ± 0.16	1.51 ± 0.44	1.33 ± 0.32	0.0282	1.25	0.0074	1.42	0.3075	0.88
Lysine	29.96 ± 6.22	31.80 ± 7.41	23.71 ± 5.68	0.0306	0.79	0.5551	1.06	0.0135	0.75
Tiyptophan	800.96 ± 190.34	691.64 ± 139.92	607.54 ± 205.72	0.0426	0.76	0.1606	0.86	0.2992	0.88
Choline	96.59 ± 17.93	103.30 ± 32.86	135.92 ± 44.61	0.0186	1.41	0.5777	1.07	0.0791	1.32
Sarcosine	0.12 ± 0.10	0.10 ± 0.02	0.23 ± 0.15	0.0729	1.94	0.5657	0.83	0.0152	2.33
cAMP	0.17 ± 0.04	0.02 ± 0.03	0.03 ± 0.02	0.0000	0.2	0.0000	0.14	0.3479	1.46
Guanine	0.09 ± 0.07	0.05 ± 0.02	0.03 ± 0.01	0.0151	0.3	0.0964	0.54	0.0084	0.56
Guanosine	15.76 ± 9.04	1.38 ± 0.74	2.02 ± 1.57	0.0002	0.13	0.0001	0.09	0.2593	1.46
Inosine	115.85 ± 46.88	22.61 ± 21.65	35.81 ± 59.90	0.0037	0.31	0.0000	0.2	0.5206	1.58
Uric acid	0.05 ± 0.02	0.09 ± 0.02	0.09 ± 0.03	0.0054	1.67	0.0001	1.73	0.7918	0.97
3-Hydroxybutyric acid	0.11 ± 0.04	0.27 ± 0.20	0.40 ± 0.40	0.0347	3.61	0.0283	2.41	0.3611	1.5

Serum Urea Combined With AFP and CEA Can Improve the Diagnostic Efficiency of HCC

AFP is closely related to the occurrence and development of liver cancer and a variety of tumors, mainly used as a serum marker for the diagnosis of primary liver cancer in clinical practice (Ahn et al., 2020; Su et al., 2020). Carcinoembryonic antigen (CEA) is a broad-spectrum tumor marker, which plays an important role in the differential diagnosis, disease monitoring, and efficacy evaluation of malignant tumors (Cheong et al., 2020; Chi et al., 2020). Performances of urea, AFP, and CEA as individual and combined HCC biomarkers were evaluated by the ROC curves. These three markers individually showed unsatisfactory performance for HCC diagnosis in the training set (AUC_{urea} = 0.766, AUC_{AFP} = 0.789, AUC_{CEA} = 0.736), the validation set (AUC_{urea} = 0.730, AUC_{AFP} = 0.834, AUC_{CEA} = 0.727), and the whole set (AUC_{urea} = 0.748, AUC_{AFP} = 0.812, AUC_{CEA} = 0.731). Nevertheless, combining the three indicators as a panel could significantly improve the diagnostic efficiency, with the $AUC_{AFP+CEA+urea}$ = 0.918 in the training set, $AUC_{AFP+CEA+urea}$ = 0.872 in the validation set, $AUC_{AFP+CEA+urea}$ = 0.917 in the whole set ($P < 0.05$) (**Figures 3A–C** and **Table 2**).

TABLE 2 | Performances of biomarkers for the diagnosis of HCC.

	AUC (95% CI)	Sensitivity (%)	Specificity (%)
Training set			
AFP	0.789 (0.735 to 0.836)	58.13	97.39
CEA	0.736 (0.678 to 0.787)	66.05	72.17
Urea	0.766 (0.713 to 0.817)	65.38	75.65
AFP + CEA + Urea	0.918 (0.879 to 0.948)*	73.20	99.13
Validation set			
AFP	0.834 (0.785 to 0.876)	60.98	100.00
CEA	0.727 (0.670 to 0.779)	75.00	57.38
Urea	0.730 (0.674 to 0.782)	61.64	75.00
AFP + CEA + Urea	0.872 (0.827 to 0.909)*	67.92	99.18
Whole set			
AFP	0.812 (0.777 to 0.844)	60.49	96.62
CEA	0.731 (0.692 to 0.768)	63.19	71.31
Urea	0.748 (0.709 to 0.784)	63.49	75.32
AFP + CEA + Urea	0.917 (0.891 to 0.939)*	74.68	99.13

**P < 0.05 in comparison with AFP, CEA or Urea, AUC, area under the curve; CI, confidence interval.*

The Key Enzymes of the Urea Cycle Were Often Low Expressed in HCC Patients

Next, we investigated the mechanism of elevated serum urea in cancer patients. Serum urea in patients with various tumors was significantly increased, we asked whether the ammonia released by the vigorous amino acid metabolism in cancer cells was detoxified to urea and excreted from the cells. However, by querying the UALCAN database (Chandrashekar et al., 2017), it was found to be inconsistent with our speculations. The key enzymes of the urea cycle, Carbamoyl-phosphate synthase 1 (CPS1), Ornithine carbamoyl-transferase (OTC), and Arginase (ARG1) were highly expressed in the liver, but normal tissues were significantly higher than cancer tissues in most cases (**Figure 4A** and **Supplementary Figures 2A, 3A**).

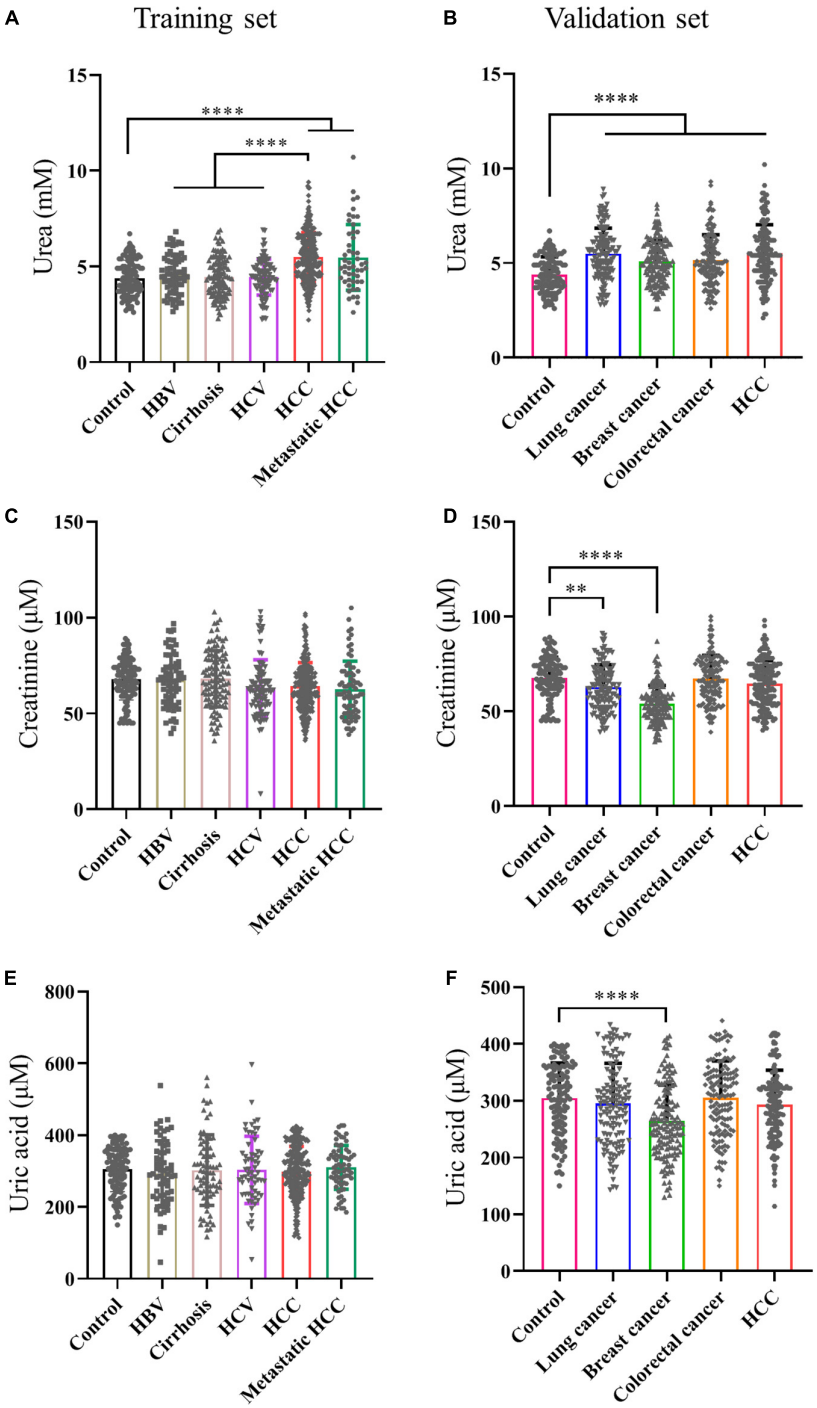

FIGURE 2 | Serum urea was a potential biomarker for HCC. **(A,C,E)** Scatter plots with bar of urea, creatinine and uric acid of control, HBV, Cirrhosis, HCV, HCC and metastatic HCC patients in training set. **(B,D,F)** Scatter plots with bar of urea, creatinine and uric acid of control, lung cancer, breast cancer, colorectal cancer and HCC patients in validation set. *$p < 0.05$; **$p < 0.01$, ***$p < 0.001$, ****$p < 0.0001$.

Immunohistochemistry results from The Human Protein Atlas (Uhlén et al., 2015) showed that CPS1, OTC, and ARG1 were often low expressed in HCC tissue compared with normal liver tissue (**Figure 4B** and **Supplementary Figures 2B, 3B**). Moreover, as the tumor progressed, the expression of key enzymes of the urea cycle tended to gradually decrease in HCC (**Figure 4C** and **Supplementary Figures 2C, 3C**). Meanwhile, we collected 14 pairs of HCC and adjacent tissues to detect the expression of CPS1, OTC and ARG1. Our results showed that the expression of CPS1, OTC and ARG1 in most HCC

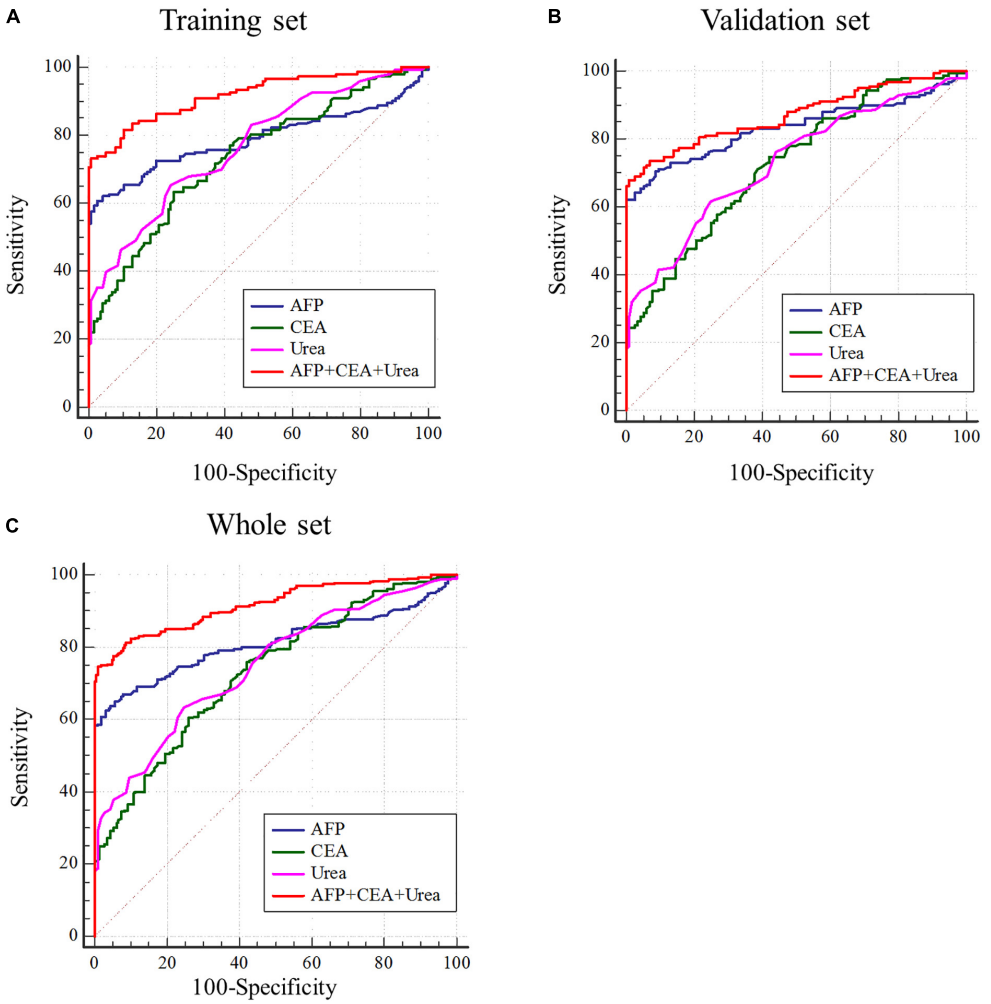

FIGURE 3 | Performance of urea, AFP, and CEA in the diagnosis of HCC. **(A–C)** Receiver operating characteristic curves of urea, AFP, CEA and AFP + CEA + urea to distinguish HCC from healthy controls in training set, validation set and whole set.

tissues were lower than that in normal liver tissues. Surprisingly, CPS1 was not expressed in more than half of tested HCC tissues (**Figure 4D**). By querying the GEPIA and Kaplan-Meier Plotter database (Tang et al., 2017; Menyhárt et al., 2018), we found HCC patients with high expression of CPS1, OTC, and ARG1 had higher overall survival rate (**Figures 4E,F** and **Supplementary Figures 2D,E, 3D,E**), which might be due to the low expression of CPS1 in patients with advanced HCC. However, the mechanism of elevated urea remained to be determined.

Ammonia Is Metabolized by Normal Liver and Cancer Cells Into Urea

The urea cycle plays an important role in the protection against excess ammonia. The physiological concentration of ammonia in the plasma of healthy people ranges from 0–50 μM (Dasarathy et al., 2017). Super-physiological concentration of ammonia is toxic to neurons, and most studies believe that it is also toxic to cancer cells (Braissant, 2010; Kappler et al., 2017). Until Jessica B. et al. revealed that breast cancer cells could recycle ammonia for biosynthesis (Spinelli et al., 2017), but the fate of ammonia in other tumors has not been fully studied, we draw a schematic diagram of the urea cycle (**Figure 5A**). We speculated it might be HCC and other cancer cells release ammonia into the blood or microenvironment. Then normal liver cells metabolized it into urea and secreted to the blood.

To test this hypothesis, we collected plasma and serum samples from HCC patients and normal controls to detect ammonia and urea levels. Consistent with our speculation, the levels of ammonia and urea in HCC patients were significantly higher than healthy controls (**Figures 5B,C**), indicating ammonia in the microenvironment of HCC could be detoxified by urea. CCLE analysis (Ghandi et al., 2019) showed that CPS1 mRNA was expressed in some cancer cell lines, but most cancer cells did not express OTC and ARG1, implying the urea cycle was down-regulated in cancer cells (**Supplementary Figure 4A**). Next, we used normal and cancer cell lines for protein level verification, including normal liver cell HL-7702, HBV + HCC cell line

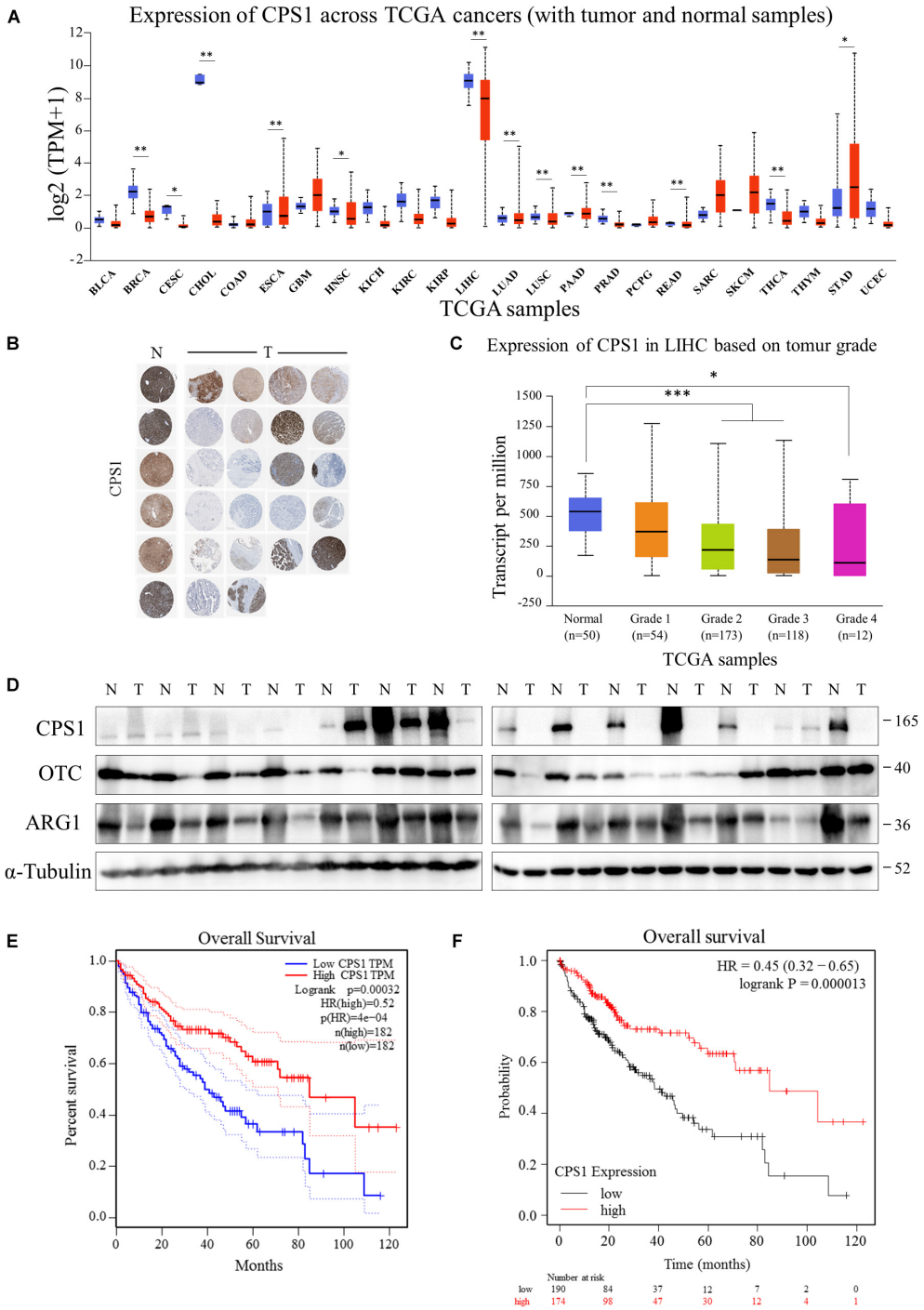

FIGURE 4 | The key enzymes of the urea cycle were often low expressed in HCC patients. **(A)** UALCAN portal analysis of cancer samples from the TCGA database (http://ualcan.path.uab.edu/). A comparison of CPS1 expression between normal and multiple cancer samples. Tumor tissues were shown in red, and normal tissues were shown in blue. BLCA, Bladder urothelial carcinoma; BRCA, Breast invasive carcinoma; CESC, Cervical squamous cell carcinoma; CHOL, Cholangiocarcinoma; COAD, Colon adenocarcinoma; ESCA, Esophageal carcinoma; GBM, Glioblastoma multiforme; HNSC, Head and Neck squamous cell carcinoma; KICH, Kidney Chromophobe; KIRC, Kidney renal clear cell carcinoma; KIRP, Kidney renal papillary cell carcinoma; LIHC, Liver hepatocellular carcinoma; LUAD, Lung adenocarcinoma; LUSC, Lung squamous cell carcinoma; PAAD, Pancreatic adenocarcinoma; PRAD, Prostate adenocarcinoma; PCPG, Pheochromocytoma and Paraganglioma; READ, Rectum adenocarcinoma; SARC, Sarcoma; SKCM, Skin Cutaneous Melanoma; THYM, Thymoma; STAD, Stomach adenocarcinoma; UCEC, Uterine Corpus Endometrial Carcinoma. **(B)** Expression of CPS1 of normal liver (N) and HCC (T) samples from The Human Protein Atlas (Human Protein Atlas available from http://www.proteinatlas.org). **(C)** UALCAN portal analysis of CPS1 expression between normal and different grade HCC samples from the TCGA database. **(D)** Western blot to detect the expression of CPS1, OTC, ARG1 and GAPDH from 14 pairs of cancer and adjacent tissues of HCC. **(E,F)** Survival probability between HCC patients with high and low CPS1 expression. The GEPIA database (http://gepia.cancer-pku.cn/) and Kaplan-Meier Plotter (http://kmplot.com/analysis/) were used to conduct survival analyses based on core gene expression. *$p < 0.05$; **$p < 0.01$, ***$p < 0.001$, ****$p < 0.0001$.

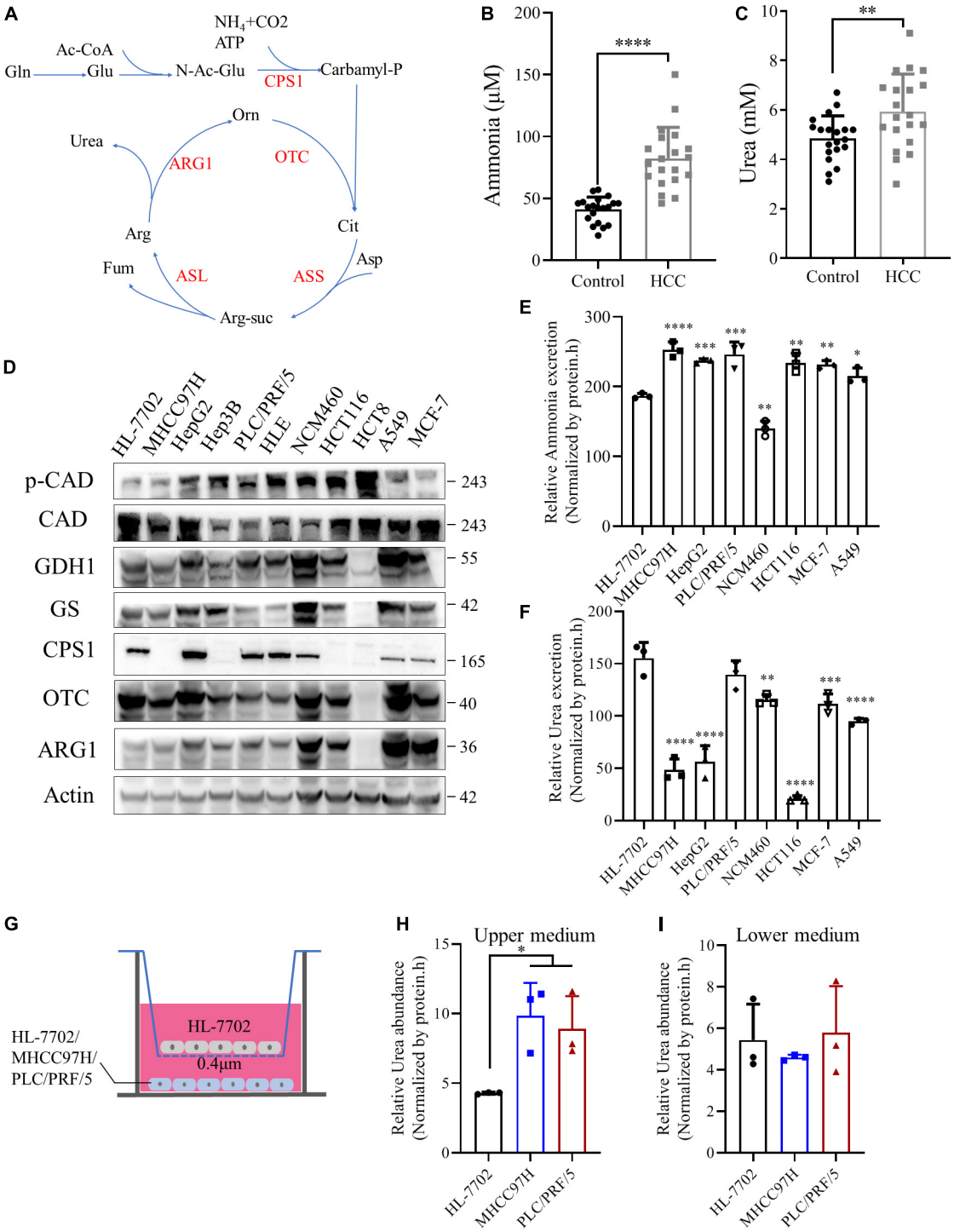

FIGURE 5 | Ammonia is metabolized by normal liver and cancer cells into urea**. (A)** A schematic to show the metabolism of urea cycle. **(B)** Scatter plots with bar of plasma ammonia of 20 age and sex matched control and HCC patients. **(C)** Scatter plots with bar of serum urea of 20 age and sex matched control and HCC patients. **(D)** Western blot of lysates from HL-7702, MHCC97H, HepG2, Hep3B, PLC/PRF/5, HLE, NCM460, HCT116, HCT8, MCF-7 and A549 cells. **(E)** Excretion of ammonia to medium from HL-7702, MHCC97H, HepG2, PLC/PRF/5, NCM460, HCT116, MCF-7 and A549 cells. **(F)** Excretion of urea to medium from HL-7702, MHCC97H, HepG2, PLC/PRF/5, NCM460, HCT116, MCF-7 and A549 cells. **(G)** Schematic diagram of co-culture cell model. HL-7702, MHCC97H or PLC/PRF/5 were cultured in the lower layer respectively, and the upper layer was HL-7702. **(H)** Relative urea abundance in the upper medium of the cell lines as indicated. **(I)** Relative urea abundance in the lower medium of the cell lines as indicated. Values are the means ± SD of three independent experiments. $^{*}p < 0.05$; $^{**}p < 0.01$, $^{***}p < 0.001$, $^{****}p < 0.0001$.

PLC/PRF/5, Hep3B, HBV- HCC cell line HepG2, MHCC97H, and HLE, breast cancer cell MCF-7, lung cancer cell A549, normal colon cell line NCM460, colorectal cancer cell HCT116 and HCT8. Our results showed that except for HL-7702, some cancer cells also express CPS1, which in PLC/PRF/5, HepG2 and HLE were even higher than HL-7702 (**Figure 5D**). The CPS1 expression of normal colon cell line NCM460 is higher than the colon cancer cell lines HCT116 and HCT8 (**Figure 5D**), consistent with the tissue level data (**Figure 4A**). To our surprise, OTC and ARG1 were expressed in most cancer cells. Coupled with HCC and adjacent tissues data, ARG1 and OTC1 were also expressed in most HCC tissues (**Figure 4D**), suggesting that the synthesis of urea might marginally depend on the expression of CPS1 (**Figure 5D**). Besides, we detected the expression of two other enzymes involved in ammonia assimilation, glutamate dehydrogenase 1 (GDH1), and glutamine synthetase (GS), which were expressed in most cancer cells, except for colon cancer cell line HCT8, but the level of phosphorylated CAD was higher in HCT8 than other cells. CAD can also catalyze glutamine to carbamyl-phosphate, and be activated by phosphorylation (Robitaille et al., 2013). Furthermore, the excretion of ammonia and urea was detected in these cells. We found that normal liver cell HL-7702 released lower ammonia (**Figure 5E**) but excreted more urea than other cancer cells (**Figure 5F**). Besides, normal colon cell NCM460 released lower ammonia (**Figure 5E**) but excreted more urea than colorectal cancer cell HCT116. PLC/PRF/5, MCF-7, and A549 with CPS1 expression excreted more urea than MHCC97H and HCT116 (**Figure 5F**). However, it was strange that HepG2, with the highest expression of CPS1, did not secrete much urea, suggesting ammonia-derived carbamyl-phosphate catalyzed by CPS1 might support anabolism in HepG2 cells, such as pyrimidine or polyamine biosynthesis.

Enzymes involved in ammonia assimilation were generally low expressed in HCC tissues (**Figure 4D** and **Supplementary Figure 4B**), implying that the ammonia assimilation capacity of HCC tissue was lower than normal liver tissue. In order to further validate the mechanism, we cultured normal liver cell line HL-7702 and a mixture of normal liver cells and HCC cell line MHCC97H with the same total number under the same conditions (**Supplementary Figure 4C**). Our results showed that the urea in the mixed culture medium was higher than the normal liver cells (**Supplementary Figure 4D**). Next, we established a co-culture model of normal liver and HCC cells, using a small chamber with a pore size of 0.4 μm. Cells in this small chamber could not pass, but metabolites could exchange. We cultured HL-7702, MHCC97H and PLC/PRF/5 in the lower layer, and the same amount of HL-7702 in the upper chamber, then collected the upper and lower media (**Figure 5G**). Our data revealed that the urea in the upper medium of MHCC97H and PLC/PRF/5 were higher than HL-7702, but there was no difference in the lower medium (**Figures 5H,I**). Besides, there was no difference in ammonia levels in both the upper and lower medium (**Supplementary Figures 4E,F**). Furthermore, in order to explore the metabolic phenomenon *in vivo*, we detected urea and ammonia in HCC and adjacent tissues. Our results showed that urea in HCC tissue was lower than adjacent tissues, while ammonia in HCC tissues was higher than that in adjacent tissues (**Supplementary Figures 4G,H**). These data demonstrating the extra ammonia released by HCC cells could indeed be metabolized by normal liver cells into urea. Taken together, these data indicate that the ability to metabolize ammonia into urea in cancer cells marginally depends on the expression of CPS1. Normal liver and cancer cells cooperate to metabolize ammonia into urea: excessive ammonia from cancer cells can be metabolized into urea by normal liver cells and secreted into medium (blood), leading to the elevated serum urea in HCC patients.

The Relationship of Urea Cycle With Ammonia Metabolism in Cancer Cells

To further investigate this interesting phenomenon, we treated cells with ammonium chloride (NH_4Cl) and detected the expression of enzymes involved in ammonia assimilation. To our disappointment, the expression of CPS1, GDH1, and GS was not enhanced under various concentrations of ammonia in HL-7702 (**Figure 6A**). Because 10 mM NH_4Cl does not significantly affect the pH of the culture medium (Spinelli et al., 2017), we treated cancer cells with 10 mM NH_4Cl, the expression of enzymes involved in ammonia assimilation was not significantly increased either (**Figure 6B**). Jessica B. et al. (Spinelli et al., 2017) reported ammonia enhances GDH activity to support biosynthesis, Hakvoort et al. showed the detoxification of stepwise increments of intravenously infused ammonia depends on GS activity (Hakvoort et al., 2017), suggesting ammonia might affect the activity of CPS1, GDH1 and GS. Next, we treated normal liver cell HL-7702 and HCC cell line PLC/PRF/5 with different concentrations of NH_4Cl and detect urea secretion. Our results showed that ammonia induced concentration-dependent urea excretion in HL-7702 and PLC/PRF/5 cells (**Figures 6C,D**). Then we knocked down the CPS1 in HCC cell lines PLC/PRF/5 and HepG2(**Figure 6E** and **Supplementary Figure 5A**). Knockdown of CPS1 increased the release of ammonia and suppressed the excretion of urea in PLC/PRF/5 and HepG2 cells (**Figures 6F,G** and **Supplementary Figures 5B,C**). Furthermore, we over-expressed CPS1 in MHCC97H and HCT116. MHCC97H and HCT116 cells with CPS1 over-expression secreted more urea but less ammonia (**Figures 6H–J** and **Supplementary Figures 5D–F**). The above results indicate that urea cycle can detoxify high concentrations of ammonia.

Urea Cycle Protects Cancer Cells From the High Concentration of Ammonia

To investigate whether ammonia was metabolized into urea or contributed to biosynthesis, we observed the effect of different concentrations of NH_4Cl on cancer cell colony formation. The number of colonies of MHCC 97H and HCT116 cells with low expression of CPS1 decreased significantly at the concentration of 0.75 mM NH_4Cl, but the number of colonies of cells with high expression of CPS1 begun to decline at 1mM. Cells with high CPS1 expression formed more colonies than cells with low expression of CPS1 under high concentrations of NH_4Cl (5-10 mM) (**Figures 7A–E** and **Supplementary Figures 6A–D**). The number of clones formed by MCF-7 even begun to decrease

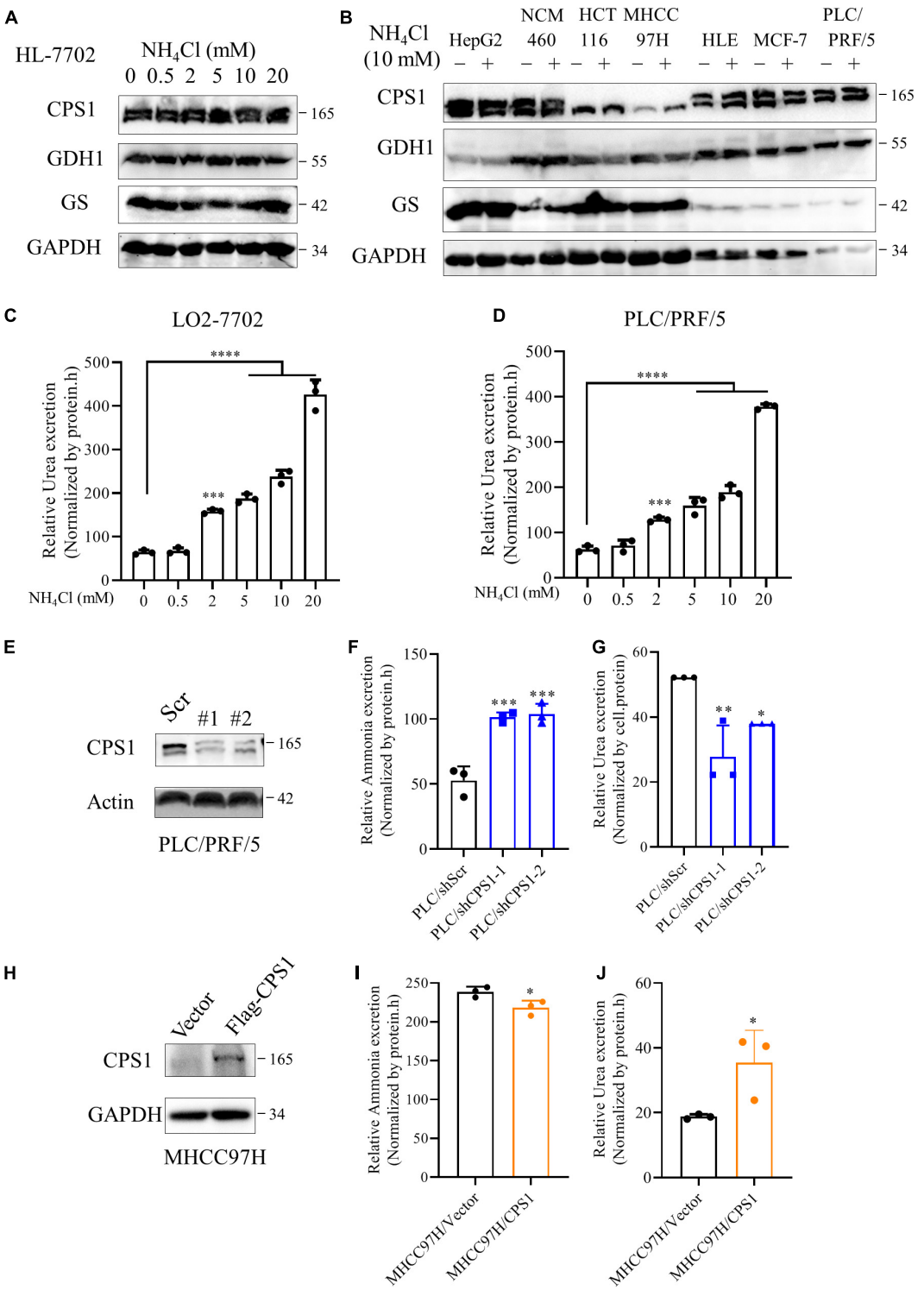

FIGURE 6 | The relationship of urea cycle with ammonia metabolism in cancer cells. **(A)** Western blot of lysates from HL-7702 cells cultured under 0, 0.5, 2, 5, 10 or 20 mM NH_4Cl for 8 h. **(B)** Western blot of lysates from HepG2, NCM460, HCT116, MHCC97H, HLE, MCF-7, PLC/PRF/5 cells cultured under 0 or 10 mM NH_4Cl for 8 h. **(C,D)** Relative urea excretion from HL-7702 and PLC/PRF/5 cells cultured under 0, 0.5, 2, 5, 10 or 20 mM NH_4Cl for 48 h. **(E)** Western blot confirmed the knockdown of CPS1 in PLC/PRF/5 cells. **(F)** Relative ammonia excretion in PLC/PRF/5/shScramble, PLC/PRF/5/shCPS1 for 8 hours. **(G)** Relative urea excretion in PLC/shScr, PLC/shCPS1 for 48 h. **(H)** Western blot confirmed the over-expression of CPS1 in MHCC97H cells. **(I)** Relative ammonia excretion in MHCC97H/Vector, MHCC97H/CPS1 for 8 h. **(J)** Relative urea excretion in MHCC97H/Vector, MHCC97H/CPS1 for 48 h. Values are the means ± SD of three independent experiments. $^*p < 0.05$; $^{**}p < 0.01$, $^{***}p < 0.001$, $^{****}p < 0.0001$.

until 5mM NH_4Cl treatment (**Supplementary Figures 6A,D**), might mainly because breast cancer cells can recycle ammonia through GDH (Spinelli et al., 2017). Then we treated PLC/PRF/5 and HepG2 cells with high concentrations of NH_4Cl and detected the proliferation. 5 mM NH_4Cl could inhibit the proliferation of PLC/PRF/5, but HepG2 could even tolerate ultra-high concentration of ammonia (20 mM) without significantly affecting its proliferation (**Supplementary Figures 7A,B**). This might be due to the high expression of CPS1 in HepG2, but its urea excretion was not high (**Figure 5F**), indicating ammonia might have other metabolic fate in HepG2 cells. Study also showed that ammonia via urea cycle contributes to polyamine biosynthesis and promotes tumor growth (Li et al., 2019). Next, we used 10 mM NH_4Cl to treat PLC/PRF/5 and HepG2 cells with CPS1 down-regulation to observe the role of urea cycle in proliferation. Our results showed that knockdown of CPS1 does not significantly inhibit cancer cell proliferation, but can make cancer cells more sensitive to ammonia toxicity (**Figures 7F,G**). Moreover, knockdown of CPS1 did not affect cell colony formation under normal condition, but suppressed the ability of clone formation of cancer cells under 10 mM of NH_4Cl (**Supplementary Figures 7A–C**). Furthermore, MHCC97H and HCT116 cells with CPS1 over-expression could tolerate higher ammonia toxicity than controls (**Figures 7H,I** and **Supplementary Figures 7D–F**). Taken together, these results suggest that in addition to biosynthesis, cancer cells metabolized a part of ammonia into a non-toxic form and secreted out of cells, and released excess ammonia out of cells into the blood, which was finally metabolized into urea by normal liver cells.

DISCUSSION

The work presented here was undertaken to investigate new serum biomarkers for HCC by targeted quantitative metabolomics and automated biochemical analyzer. Our results revealed that urea was a potential serum biomarker for HCC, and could be used to distinguish HCC from other liver diseases. Urea combined with AFP and CEA can significantly improve the diagnostic efficiency of HCC. But the key enzymes of the urea cycle, especially CPS1, were often low expressed in HCC and other cancer tissues. Strikingly, we found the plasma ammonia in HCC patients was significantly higher than normal people. Moreover, cell experiments showed that normal liver cells released lower ammonia but excreted more urea than cancer cells. The urea metabolism in cancer cells might marginally depend on the expression of CPS1. Our co-culture cell models further revealed that excess ammonia from HCC cells can be metabolized into urea by normal liver cells. But the expression of CPS1 was not enhanced with the concentration of NH_4Cl; it might regulate the urea cycle through enzyme activity. Furthermore, the urea cycle could detoxify high concentrations of ammonia to promote cancer cell proliferation. This study demonstrated the role of urea cycle in cancer cells and the possibility of urea as a serum biomarker for HCC.

Identifying accurate non-invasive biomarkers that can be widely used remains a challenge. To date, many plasma/serum metabolic biomarkers have been reported for the early diagnosis of HCC (Banales et al., 2019; Han et al., 2020). However, few biomarkers have been used in the clinical diagnosis of HCC, mainly because most clinical laboratories cannot detect them. In our study, we found that serum urea, a common clinical indicator, was significantly higher in HCC patients than healthy controls and other liver diseases. Moreover, the serum urea of patients with lung cancer, breast cancer, and colorectal cancer were also significantly higher. Serum AFP is widely recognized and used for HCC diagnosis (Montal et al., 2019). However, it is difficult to characterize HCC with a single biomarker, since it is a complex disease caused by various risk factors with multiple pathogenic mechanisms (Galle and Foerster, 2019). Our data showed the sensitivity of AFP for HCC diagnosis is unsatisfactory (60.49%). But combined AFP with urea and CEA as a panel can significantly improve the diagnostic performance, leading to more early diagnosis of HCC.

The urea cycle can eliminate excess nitrogen and ammonia produced by protein decomposition or nitrogen compound synthesis in the human body (Caldwell et al., 2018; Lee et al., 2018). Urea cycle enzymes also contribute to anabolism, such as nucleotide biosynthesis in certain tumor types (Kim et al., 2017; Rom et al., 2018). However, the urea cycle dysregulation is a common feature of tumors (Lee et al., 2018). And the expression of key enzymes CPS1, OTC, ARG1 in the urea cycle were lower than normal tissue in HCC and other cancers. The HCC microenvironment is composed of stromal cells, hepatic stellate cells, endothelial cells and immune cells (Biswas et al., 2013). Crosstalk between cancer cells and their surrounding microenvironment is necessary to maintain HCC development by promoting angiogenesis, EMT or regulating the polarization of immune cells (Hernandez-Gea et al., 2013). From this, we speculate that it may be the metabolic process of HCC and other cancer cells release ammonia into the blood and/or microenvironment; normal liver cells detoxify ammonia into urea and secrete it into the serum to avoid the accumulation of ammonia in cancer cells. Because ammonia entry was regulated by diffusion, and ammonia can diffuse across the plasma membrane (Spinelli et al., 2017). Consistent with our speculation, the plasma ammonia in HCC patients was significantly higher than normal controls. Although we found cancer cells also excrete urea, most cancer cells excreted much less urea than normal liver cells. Besides, KEGG analysis of metabolomics revealed that the purine metabolism pathway in HCC patients was enriched. Skeletal muscle, myocardium, liver, and brain may all be deaminated by purine nucleotide cycles. Experiments have shown that 50% of the ammonia in brain tissue is produced by purine nucleotide cycles (Schultz and Lowenstein, 1978). Although some breast cancer cells can recycle ammonia for biosynthesis (Spinelli et al., 2017), our previous study proved that the reuse of ammonia by cancer cells is not universal: cancer cells excrete dihydroorotate out of the cells to avoid ammonia accumulation under hypoxia (Wang et al., 2019). Moreover, we found urea excretion marginally depended on the expression of CPS1 in cancer cells. Although the expression of CPS1 in

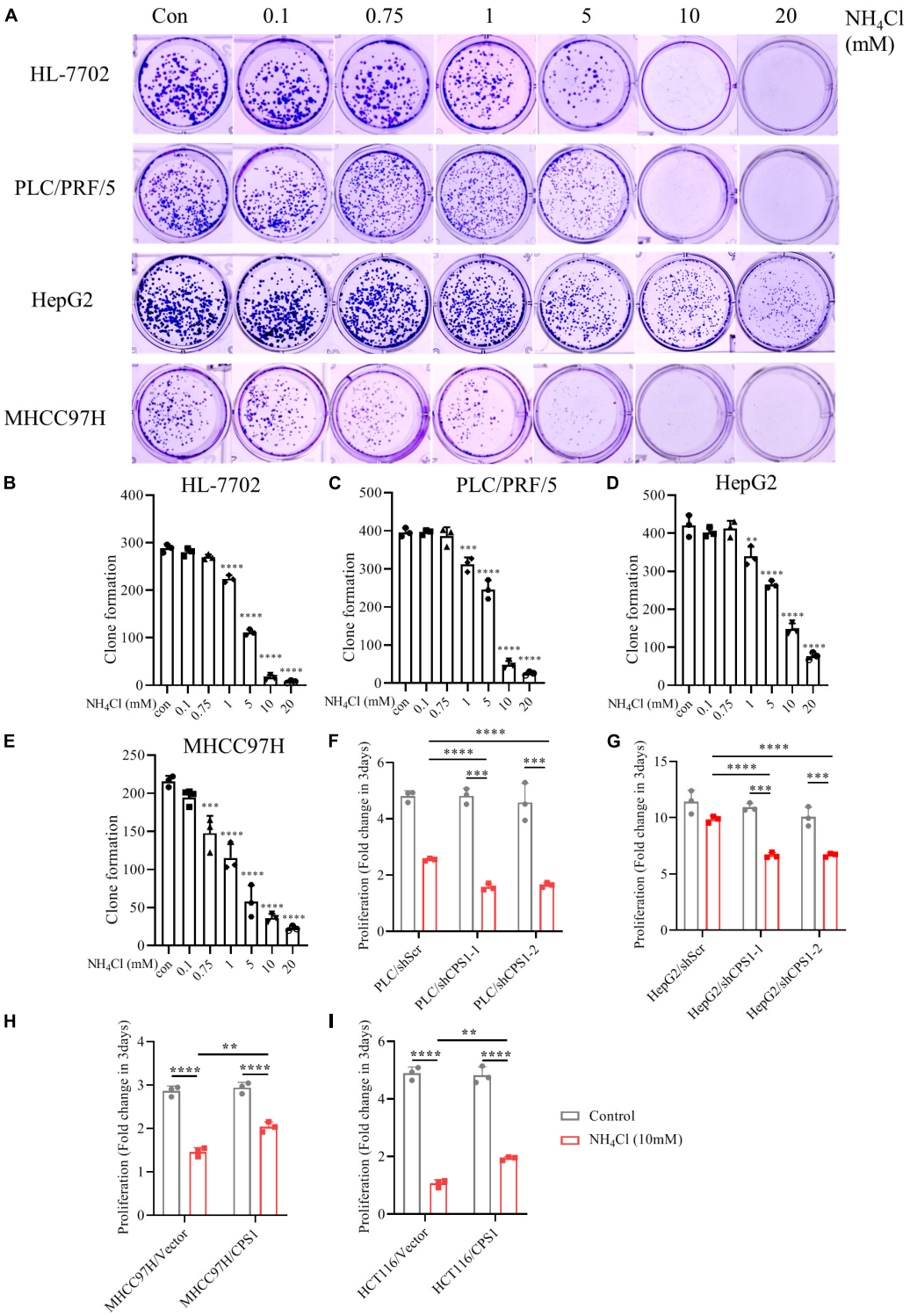

FIGURE 7 | Urea cycle protects cancer cells from high concentrations of ammonia. **(A)** Colony formation ability of HL-7702, PLC/PRF/5, HepG2 and MHCC97H under different concentrations of NH_4Cl. The culture time was 2 weeks. **(B–E)** Colony number quantification of HL-7702, PLC/PRF/5, HepG2 and MHCC97H under different concentrations of NH_4Cl by Image J. **(F)** Proliferation of PLC/PRF/5/shScr and PLC/PRF/5/shCPS1 cells cultured under control or 10 mM NH_4Cl for 3 days. **(G)** Proliferation of HepG2/shScr and HepG2/shCPS1 cells cultured under control or 10 mM NH_4Cl for 3 days. **(H)** Proliferation of MHCC97H/Vector, MHCC97H/CPS1 cells cultured under control or 10 mM NH_4Cl for 3 days. **(I)** Proliferation of HCT116/Vector, HCT116/CPS1 cells cultured under control or 10 mM NH_4Cl for 3 days. Values are the means ± SD of three independent experiments. $^*p < 0.05$; $^{**}p < 0.01$, $^{***}p < 0.001$, $^{****}p < 0.0001$.

HepG2 was much higher than HL-7702, HepG2 secreted less urea, indicating other metabolic fate of ammonia in HepG2. In addition to polyamine biosynthesis, it was also reported that concurrent occurrence of oncogenic KRAS and loss of LKB1 (KL) in cells the carbamoyl-phosphate catalyzed by CPS1 could be used for pyrimidine synthesis to maximize nitrogen utilization (Kim et al., 2017). Furthermore, we proved the underlying mechanism by direct contact cell model and co-culture cell models: normal liver cells can indeed metabolize the excess ammonia released by HCC cells, which may be the reason for the elevated serum urea in HCC patients. Moreover, the urea in HCC tissues was lower than that in adjacent tissues, while ammonia was higher, which further supports our speculation.

The ammonia-clearing system also includes GS and GDH1. However, the expression of CPS1, GS and GDH1 did not respond to high concentrations of NH_4Cl in normal liver cells and cancer cells, consistent with Jessica B. et al. observations (Spinelli et al., 2017). They revealed breast cancer cells can assimilate ammonia through reductive amination catalyzed by GDH, but its expression was not changed under high concentrations of NH_4Cl. CPS1 can be allosterically activated by N-acetyl-glutamate. We speculate that it may be high concentrations of ammonia accelerated the transamination reaction and cause the synthesis of N-acetyl-glutamate to enhance, thereby activating CPS1. Jessica B. et al. proved NH_4Cl was not toxic to breast cancer cells (Spinelli et al., 2017). We indeed found MCF-7 could even tolerate 1 mM NH_4Cl to proliferate. The cell lines with high expression of CPS1, including HL-7702, PLC/PRF/5, HepG2, and NCM460, could tolerate 0.75 mM NH_4Cl without colony number decrease, but the number of colonies formed in cell lines with low CPS1 expression, including MHCC97H and HCT116 had begun to decline significantly under 0.75 mM NH_4Cl. Knockdown of CPS1 did not inhibit the proliferation of PLC/PRF/5 and HepG2, which might be due to the compensation role of GS and/or GDH1. However, knockdown of CPS1 sensitizes PLC/PRF/5 and HepG2 to NH_4Cl, which significantly suppressed their proliferation and robustly inhibited their colony formation. Besides, over-expression of CPS1 could improve the ability of MHCC97H and HCT116 to tolerate ammonia. Taken together, our results revealed that the urea cycle can detoxify high concentration of ammonia to promote the rapid proliferation of cancer cells. The ammonia metabolism in cancer cells might be highly efficient, a part of ammonia in cancer cells may be used for biosynthesis, but a large amount or excess ammonia needs to be metabolized into non-toxic products by the cooperation of normal liver cells and cancer cells, and then secreted out of the cells. Winter M C et al. also reported that raised serum urea predicts for early death in small cell lung cancer (Winter et al., 2008). Next, we will investigate the effect of simultaneously inhibiting the three key enzymes in the ammonia-clearing system on cancer cell proliferation, and explore the possibility of them as targets for combination therapy.

In conclusion, the combination of metabolomics and routine testing can reveal the potential serum biomarkers of HCC, and quickly promote the application. Urea is a potential biomarker of HCC, and combining with AFP and CEA can improve the diagnostic efficiency of HCC. In addition to ammonia for biosynthesis, cancer cells also need to detoxify excess ammonia. Normal liver cells and cancer cells cooperate to metabolize ammonia into a non-toxic form, thereby promoting the proliferation of cancer cells.

DATA AVAILABILITY STATEMENT

The original contributions presented in the study are included in the article/**Supplementary Material**, further inquiries can be directed to the corresponding author/s.

ETHICS STATEMENT

The studies involving human participants were reviewed and approved by Ethics Committee of Tianjin Medical University Cancer Institute and Hospital. The patients/participants provided their written informed consent to participate in this study.

AUTHOR CONTRIBUTIONS

CB concepted and designed the study and wrote the manuscript. HW performed sample collection for metabolomics testing and analysis. DD, TL, ZY, DL, WZ, RY, and LW collected samples and conducted biochemical testing. JG and ZW performed bioinformatics analysis. CB and HW performed cell experiments. LR and YL provided insightful ideas and guided the experiment process. All authors have read and agreed to the published version of the manuscript.

FUNDING

This research was funded by Natural Science Foundation of China [Grants 81871719, 31900440, 81802080, and 81602213], Tianjin Natural Science Foundation [Grants 18JCQNJC80100, 20JCQNJC00510], and Tianjin Municipal Education Commission Foundation [Grants 2019KJ189]. The funders did not have any role in study design, data collection, data analysis, interpretation, or writing of the manuscript.

ACKNOWLEDGMENTS

We thank Professor Peng Jiang from Tsinghua University for donating the CPS1 plasmid, and also thank Dr. Lifang Li, Benfu Zhong and Miao Liu (Tianjin Medical University Cancer Institute and Hospital) for thoughtful discussion.

SUPPLEMENTARY MATERIAL

The Supplementary Material for this article can be found online at: https://www.frontiersin.org/articles/10.3389/fcell.2021.650748/full#supplementary-material

Supplementary Figure 1 | MetaboAnalyst analysis on altered metabolic pathways in HCC and HBV patients. **(A)** Results from MetaboAnalyst showing altered metabolic pathways in HCC patients versus healthy controls. Pathways are labeled: Arginine biosynthesis (1), Purine metabolism (2), Alanine, aspartate and glutamate metabolism (3), D-Glutamine and D-glutamate metabolism (4), Pyruvate metabolism (5), Citrate cycle (TCA cycle) (6), Cysteine and methionine metabolism (7), Arginine and proline metabolism (8). **(B)** Results from MetaboAnalyst showing altered metabolic pathways in HBV patients versus healthy controls. Pathways are labeled: Arginine biosynthesis (1), Citrate cycle (TCA cycle) (2), Pyruvate metabolism (3), Alanine, aspartate and glutamate metabolism (4), Phenylalanine, tyrosine and tryptophan biosynthesis (5), D-Glutamine and D-glutamate metabolism (6), Arginine and proline metabolism (7), Cysteine and methionine metabolism (8), Phenylalanine metabolism (9).

Supplementary Figure 2 | Expression and prognosis analysis of OTC in HCC patients. **(A)** UALCAN portal analysis of cancer samples from the TCGA database (http://ualcan.path.uab.edu/). A Comparison of OTC expression between normal and multiple cancer samples. Tumor tissues were shown in red, and normal tissues were shown in blue. **(B)** Expression of OTC of normal and HCC samples from proteinatlas (Human Protein Atlas available from http://www.proteinatlas.org). **(C)** UALCAN portal analysis of OTC expression between normal and different grade HCC samples from the TCGA database. **(D,E)** Survival probability between HCC patients with high and low OTC expression. The GEPIA database (http://gepia.cancer-pku.cn/) and Kaplan-Meier Plotter (http://kmplot.com/analysis/) were used to conduct survival analyses based on core gene expression. $^{*}p < 0.05$; $^{**}p < 0.01$, $^{***}p < 0.001$, $^{****}p < 0.0001$.

Supplementary Figure 3 | Expression and prognosis analysis of ARG1 in HCC patients. **(A)** UALCAN portal analysis of cancer samples from the TCGA database (http://ualcan.path.uab.edu/). A comparison of ARG1 expression between normal and multiple cancer samples. Tumor tissues were shown in red, and normal tissues were shown in blue. **(B)** Expression of ARG1 of normal and HCC samples from proteinatlas (Human Protein Atlas available from http://www.proteinatlas.org). **(C)** UALCAN portal analysis of ARG1 expression between normal and different grade HCC samples from the TCGA database. **(D,E)** Survival probability between HCC patients with high and low ARG1 expression. The GEPIA database (http://gepia.cancer-pku.cn/) and Kaplan-Meier Plotter (http://kmplot.com/analysis/) were used to conduct survival analyses based on core gene expression. $^{*}p < 0.05$; $^{**}p < 0.01$, $^{***}p < 0.001$, $^{****}p < 0.0001$.

Supplementary Figure 4 | Ammonia is metabolized by normal liver and cancer cells into urea. **(A)** The mRNA expression of CPS1, OTC and ARG1 of cancer cells from CCLE database (https://portals.broadinstitute.org/ccle/about). **(B)** Western blot to detect the expression of GDH1, GS, and a-tubulin from 14 pairs of cancer and adjacent tissues of HCC. **(C)** Schematic diagram of cell model. 200, 000 HL7702 or 100, 000 HL-7702 and 100, 000 MHCC97H were cultured separately. **(D)** Relative urea excretion of the cell lines as indicated. **(E)** Relative ammonia abundance in the upper medium of the cell lines as indicated. **(F)** Relative ammonia abundance in the lower medium of the cell lines as indicated. **(G)** Relative urea abundance in 10 pairs of fresh HCC and adjacent tissues. **(H)** Relative ammonia abundance in 10 pairs of fresh HCC and adjacent tissues.

Supplementary Figure 5 | The relationship of urea cycle with ammonia metabolism in cancer cells. **(A)** Western blot confirmed the knockdown of CPS1 in HepG2 cells. **(B)** Relative ammonia excretion in HepG2/Scramble, HepG2/shCPS1 for 8 h. **(C)** Relative urea excretion in HepG2/Scramble, HepG2/shCPS1 for 48 h. **(D)** Western blot confirmed the over-expression of CPS1 in HCT116 cells. **(E)** Relative ammonia excretion in HCT116/Vector, HCT116/CPS1 for 8 h. **(F)** Relative urea excretion in HCT116/Vector, HCT116/CPS1 for 48 h. Values are the means ± SD of three independent experiments. $^{*}p < 0.05$, $^{**}p < 0.01$, $^{***}p < 0.001$.

Supplementary Figure 6 | High concentrations of ammonia inhibits the proliferation of cancer cells. **(A)** Colony formation ability of NCM460, HCT116 and MCF-7 under different concentrations of NH_4Cl. **(B–D)** Colony number quantification of NCM460, HCT116, and MCF-7 under different concentrations of NH_4Cl by Image J. **(E,F)** Proliferation of PLC/PRF/5 and HepG2 cells cultured under 0, 5, 10 or 20 mM NH_4Cl for 3 days. Values are the means ± SD of three independent experiments. $^{*}p < 0.05$; $^{**}p < 0.01$, $^{***}p < 0.001$, $^{****}p < 0.0001$.

Supplementary Figure 7 | Urea cycle protect cancer cells from high concentrations of ammonia. **(A)** Colony formation ability of PLC/PRF/5/shScr and PLC/PRF/5/shCPS1-1, HepG2/shScr and HepG2/shCPS1-1 under control or 10 mM NH_4Cl. **(B,C)** Colony number quantification of PLC/PRF/5/shScr and PLC/PRF/5/shCPS1-1, HepG2/shScr and HepG2/shCPS1-1 under control or 10mM NH_4Cl by Image J. **(D)** Colony formation ability of MHCC97H/Vector and MHCC97H/CPS1, HCT116/Vector and HCT116/CPS1 under control or 10mM NH_4Cl. **(E,F)** Colony number quantification of MHCC97H/Vector and MHCC97H/CPS1, HCT116/Vector and HCT116/CPS1 under control or 10 mM NH_4Cl by Image J. Values are the means ± SD of three independent experiments. $^{*}p < 0.05$; $^{**}p < 0.01$, $^{***}p < 0.001$, $^{****}p < 0.0001$.

Supplementary Table 1 | Characteristics of serum samples from healthy controls, HBV, HBV positive cirrhosis, HCV, HBV positive HCC patients, and metastatic HCC patients.

Supplementary Table 2 | Characteristics of serum samples from lung cancer, breast cancer, colorectal cancer, HCC patients and healthy controls.

REFERENCES

Ahn, J. C., Teng, P. C., Chen, P. J., Posadas, E., Tseng, H. R., Lu, S. C., et al. (2020). Detection of circulating tumor cells and their implications as a novel biomarker for diagnosis, prognostication, and therapeutic monitoring in hepatocellular carcinoma. *Hepatology* 73, 422–436. doi: 10.1002/hep.31165

Banales, J. M., Iñarrairaegui, M., Arbelaiz, A., Milkiewicz, P., Muntané, J., Muñoz-Bellvis, L., et al. (2019). Serum metabolites as diagnostic biomarkers for cholangiocarcinoma. *Hepatocell. Carcinoma Prim. Scleros. Cholang.* 70, 547–562.

Biswas, S. K., Allavena, P., and Mantovani, A. (2013). Tumor-associated macrophages: functional diversity, clinical significance, and open questions. *Semin. Immunopathol.* 35, 585–600. doi: 10.1007/s00281-013-0367-7

Braissant, O. (2010). Ammonia toxicity to the brain: effects on creatine metabolism and transport and protective roles of creatine. *Mol. Genet. Metab.* 100(Suppl. 1), S53–S58.

Caldwell, R. W., Rodriguez, P. C., Toque, H. A., Narayanan, S. P., and Caldwell, R. B. (2018). Arginase: a multifaceted enzyme important in health and disease. *Physiol. Rev.* 98, 641–665. doi: 10.1152/physrev.00037.2016

Chandrashekar, D. S., Bashel, B., Balasubramanya, S. a. H., Creighton, C. J., Ponce-Rodriguez, I., Chakravarthi, B., et al. (2017). UALCAN: a portal for facilitating tumor subgroup gene expression and survival analyses. *Neoplasia.* 19, 649–658. doi: 10.1016/j.neo.2017.05.002

Cheong, C., Shin, J. S., and Suh, K. W. (2020). Prognostic value of changes in serum carcinoembryonic antigen levels for preoperative chemoradiotherapy response in locally advanced rectal cancer. *World J. Gastroenterol.* 26, 7022–7035. doi: 10.3748/wjg.v26.i44.7022

Chi, L., Xu, C., Li, S., Wang, X., Tang, D., and Xue, F. (2020). Thionine-doped nanometer-sized silica conjugated with phenylboronic acid: an innovative recognition/signal element for voltammetric aptasensing of colorectal cancer-related carcinoembryonic antigen. *Anal. Chim. Acta* 1136, 91–98. doi: 10.1016/j.aca.2020.08.029

Chong, J., Soufan, O., Li, C., Caraus, I., Li, S., Bourque, G., et al. (2018). MetaboAnalyst 4.0: towards more transparent and integrative metabolomics analysis. *Nucleic Acids Res.* 46, W486–W494.

Dasarathy, S., Mookerjee, R. P., Rackayova, V., Rangroo Thrane, V., Vairappan, B., Ott, P., et al. (2017). Ammonia toxicity: from head to toe? *Metab. Brain Dis.* 32, 529–538. doi: 10.1007/s11011-016-9938-3

De Matteis, S., Ragusa, A., Marisi, G., De Domenico, S., Casadei Gardini, A., Bonafè, M., et al. (2018). Aberrant metabolism in hepatocellular carcinoma provides diagnostic and therapeutic opportunities. *Oxid. Med. Cell. Longev.* 2018, 1–13. doi: 10.1155/2018/7512159

DeBerardinis, R. J., and Chandel, N. S. (2016). Fundamentals of cancer metabolism. *Sci. Adv.* 2:e1600200. doi: 10.1126/sciadv.1600200

DeBerardinis, R. J., Mancuso, A., Daikhin, E., Nissim, I., Yudkoff, M., Wehrli, S., et al. (2007). Beyond aerobic glycolysis: transformed cells can engage in

glutamine metabolism that exceeds the requirement for protein and nucleotide synthesis. *Proc. Natl. Acad. Sci. U.S.A.* 104, 19345–19350. doi: 10.1073/pnas.0709747104

DeLong, E. R., Delong, D. M., and Clarke-Pearson, D. L. (1988). Comparing the areas under two or more correlated receiver operating characteristic curves: a nonparametric approach. *Biometrics* 44, 837–845. doi: 10.2307/2531595

Forner, A., Reig, M., and Bruix, J. (2018). Hepatocellular carcinoma. *Lancet* 391, 1301–1314.

Fu, J., and Wang, H. (2018). Precision diagnosis and treatment of liver cancer in China. *Cancer Lett.* 412, 283–288. doi: 10.1016/j.canlet.2017.10.008

Fujiwara, N., Nakagawa, H., Enooku, K., Kudo, Y., Hayata, Y., Nakatsuka, T., et al. (2018). CPT2 downregulation adapts HCC to lipid-rich environment and promotes carcinogenesis via acylcarnitine accumulation in obesity. *Gut* 67, 1493–1504. doi: 10.1136/gutjnl-2017-315193

Galle, P. R., and Foerster, F. (2019). Biology and significance of alpha-fetoprotein in hepatocellular carcinoma. *Liver Int.* 39, 2214–2229.

Ghandi, M., Huang, F. W., Jané-Valbuena, J., Kryukov, G. V., Lo, C. C., Mcdonald, E. R., et al. (2019). Next-generation characterization of the cancer cell line encyclopedia. *Nature* 569, 503–508.

Hakvoort, T. B. M., He, Y., Kulik, W., Vermeulen, J. L. M., Duijst, S., Ruijter, J. M., et al. (2017). Pivotal role of glutamine synthetase in ammonia detoxification. *Hepatology* 65, 281–293. doi: 10.1002/hep.28852

Han, J., Han, M. U., Xing, H., Li, Z. I., and Yang, T. (2020). Tissue and serum metabolomic phenotyping for diagnosis and prognosis of hepatocellular carcinoma. *Int. J. Cancer* 146, 1741–1753. doi: 10.1002/ijc.32599

Hanahan, D., and Weinberg, R. A. (2011). Hallmarks of cancer: the next generation. *Cell* 144, 646–674. doi: 10.1016/j.cell.2011.02.013

Hernandez-Gea, V., Toffanin, S., Friedman, S. L., and Llovet, J. M. (2013). Role of the microenvironment in the pathogenesis and treatment of hepatocellular carcinoma. *Gastroenterology* 144, 512–527. doi: 10.1053/j.gastro.2013.01.002

Kappler, M., Pabst, U., Rot, S., Taubert, H., Wichmann, H., Schubert, J., et al. (2017). Normoxic accumulation of HIF1α is associated with glutaminolysis. *Clin. Oral Investig.* 21, 211–224. doi: 10.1007/s00784-016-1780-9

Khan, M., Li, W., Mao, S., Shah, S. N. A., and Lin, J.-M. (2019). Real-time imaging of ammonia release from single live cells via liquid crystal droplets immobilized on the cell membrane. *Adv. Sci.* 6:1900778. doi: 10.1002/advs.201900778

Kim, J., Hu, Z., Cai, L., Li, K., Choi, E., Faubert, B., et al. (2017). CPS1 maintains pyrimidine pools and DNA synthesis in KRAS/LKB1-mutant lung cancer cells. *Nature* 546, 168–172. doi: 10.1038/nature22359

Lee, J. S., Adler, L., Karathia, H., Carmel, N., Rabinovich, S., Auslander, N., et al. (2018). Urea cycle dysregulation generates clinically relevant genomic and biochemical signatures. *Cell* 174, 1559–1570.e1522.

Li, L., Mao, Y., Zhao, L., Li, L., Wu, J., Zhao, M., et al. (2019). p53 regulation of ammonia metabolism through urea cycle controls polyamine biosynthesis. *Nature* 567, 253–256. doi: 10.1038/s41586-019-0996-7

Luo, P., and Yin, P. (2018). A large-scale, multicenter serum metabolite biomarker identification study for the early detection of hepatocellular carcinoma. *Hepatology* 67, 662–675. doi: 10.1002/hep.29561

Menyhárt, O., Nagy, A., and Győrffy, B. (2018). Determining consistent prognostic biomarkers of overall survival and vascular invasion in hepatocellular carcinoma. *R. Soc. Open Sci.* 5:181006. doi: 10.1098/rsos.181006

Montal, R., Andreu-Oller, C., Bassaganyas, L., Esteban-Fabró, R., Moran, S., Montironi, C., et al. (2019). Molecular portrait of high alpha-fetoprotein in hepatocellular carcinoma: implications for biomarker-driven clinical trials. *Br. J. Cancer* 121, 340–343. doi: 10.1038/s41416-019-0513-7

Pavlova, N. N., and Thompson, C. B. (2016). The emerging hallmarks of cancer metabolism. *Cell Metab.* 23, 27–47. doi: 10.1016/j.cmet.2015.12.006

Robitaille, A. M., Christen, S., Shimobayashi, M., Cornu, M., Fava, L. L., Moes, S., et al. (2013). Quantitative phosphoproteomics reveal mTORC1 activates de novo pyrimidine synthesis. *Science* 339, 1320–1323. doi: 10.1126/science.1228771

Rom, K., Peter, S., Arkaitz, C., and Ayelet, E. (2018). Rewiring urea cycle metabolism in? Cancer to support anabolism. *Nat. Rev. Cancer* 18, 634–645. doi: 10.1038/s41568-018-0054-z

Schultz, V., and Lowenstein, J. M. (1978). The purine nucleotide cycle. Studies of ammonia production and interconversions of adenine and hypoxanthine nucleotides and nucleosides by rat brain in situ. *J. Biol. Chem.* 253, 1938–1943. doi: 10.1016/s0021-9258(19)62338-0

Soga, T., Sugimoto, M., Honma, M., Mori, M., Igarashi, K., Kashikura, K., et al. (2011). Serum metabolomics reveals γ-glutamyl dipeptides as biomarkers for discrimination among different forms of liver disease. *J. Hepatol.* 55, 896–905. doi: 10.1016/j.jhep.2011.01.031

Spinelli, J. B., and Yoon, H. (2017). Metabolic recycling of ammonia via glutamate dehydrogenase supports breast cancer biomass. *Science* 358, 941–946. doi: 10.1126/science.aam9305

Spinelli, J. B., Yoon, H., Ringel, A. E., Jeanfavre, S., Clish, C. B., and Haigis, M. C. (2017). Metabolic recycling of ammonia via glutamate dehydrogenase supports breast cancer biomass. *Science* 358, 941–946. doi: 10.1126/science.aam9305

Su, F., Weiss, N. S., Beste, L. A., Moon, A. M., Jin, G. Y., Green, P., et al. (2020). Screening is associated with a lower risk of hepatocellular carcinoma-related mortality in patients with chronic hepatitis B. *J. Hepatol.* 74, 850–859. doi: 10.1016/j.jhep.2020.11.023

Tang, Z., Li, C., Kang, B., Gao, G., Li, C., and Zhang, Z. (2017). GEPIA: a web server for cancer and normal gene expression profiling and interactive analyses. *Nucleic Acids Res.* 45, W98–W102.

Timo Alexander, A., Thomas, F., Garcia, S. R. M., Tobias, P., Ernst-Michael, J., Bernd, H., et al. (2020). Value of contrast-enhanced ultrasound (CEUS) in Focal Liver Lesions (FLL) with inconclusive findings on cross-sectional imaging. *Clin. Hemorheol. Microcirc.* 2020, 327–339. doi: 10.3233/ch-190718

Torre, L. A., Bray, F., Siegel, R. L., Ferlay, J., Lortet−Tieulent, J., and Jemal, A. (2015). Global cancer statistics, 2012. *CA Cancer J. Clin.* 65, 87–108. doi: 10.3322/caac.21262

Uhlén, M., Fagerberg, L., Hallström, B. M., Lindskog, C., Oksvold, P., Mardinoglu, A., et al. (2015). Proteomics. tissue-based map of the human proteome. *Science* 347:1260419. doi: 10.1126/science.1260419

Wang, Y., Bai, C., Ruan, Y., Liu, M., Chu, Q., Qiu, L., et al. (2019). Coordinative metabolism of glutamine carbon and nitrogen in proliferating cancer cells under hypoxia. *Nat. Commun.* 10:201.

Winter, M. C., Potter, V. A., and Woll, P. J. (2008). Raised serum urea predicts for early death in small cell lung cancer. *Clin. Oncol. (R. Coll. Radiol.)* 20, 745–750. doi: 10.1016/j.clon.2008.09.001

Wolpaw, A. J., and Chi, V. D. (2018). Exploiting metabolic vulnerabilities of cancer with precision and accuracy. *Trends Cell Biol.* 28, 201–212. doi: 10.1016/j.tcb.2017.11.006

Zech, C. J., Ba-Ssalamah, A., Berg, T., Chandarana, H., Chau, G. Y., Grazioli, L., et al. (2020). Consensus report from the 8th International forum for liver magnetic resonance imaging. *Eur. Radiol.* 30, 370–382. doi: 10.1007/s00330-019-06369-4

Conflict of Interest: The authors declare that the research was conducted in the absence of any commercial or financial relationships that could be construed as a potential conflict of interest.

frontiers in Cell and Developmental Biology

ORIGINAL RESEARCH
published: 09 April 2021
doi: 10.3389/fcell.2021.658856

SUMOylation Regulator-Related Molecules Can Be Used as Prognostic Biomarkers for Glioblastoma

Xiaozhi Li[1] *and Yutong Meng*[2]*

[1] *Department of Neurosurgery, Shengjing Hospital of China Medical University, Shenyang, China,* [2] *Department of Stomatology, Shengjing Hospital of China Medical University, Shenyang, China*

OPEN ACCESS

Edited by:
Bin Yuan,
George Washington University,
United States

Reviewed by:
Zhao Zhang,
The University of Texas Health Science Center at San Antonio,
United States
Bogang Wu,
George Washington University,
United States

***Correspondence:**
Yutong Meng
mengyt@vip.163.com

Specialty section:
This article was submitted to Molecular Medicine, a section of the journal Frontiers in Cell and Developmental Biology

Received: *26 January 2021*
Accepted: *08 March 2021*
Published: *09 April 2021*

Citation:
Li X and Meng Y (2021) SUMOylation Regulator-Related Molecules Can Be Used as Prognostic Biomarkers for Glioblastoma. Front. Cell Dev. Biol. 9:658856. doi: 10.3389/fcell.2021.658856

Introduction: SUMOylation is one of the post-translational modifications. The relationship between the expression of SUMOylation regulators and the prognosis of glioblastoma is not quite clear.

Materials and Methods: The single nucleotide variant data, the transcriptome data, and survival information were acquired from The Cancer Genome Atlas, Gene Expression Omnibus, and cBioportal database. Wilcoxon test was used to analyze differentially expressed genes between glioblastoma and normal brain tissues. Gene set enrichment analysis was conducted to find the possible functions. One risk scoring model was built by the least absolute shrinkage and selection operator Cox regression. Kaplain–Meier survival curves and receiver operating characteristic curves were applied to evaluate the effectiveness of the model in predicting the prognosis of glioblastoma.

Results: Single-nucleotide variant mutations were found in SENP7, SENP3, SENP5, PIAS3, RANBP2, USPL1, SENP1, PIAS2, SENP2, and PIAS1. Moreover, UBE2I, UBA2, PIAS3, and SENP1 were highly expressed in glioblastoma, whereas PIAS1, RANBP2, SENP5, and SENP2 were downregulated in glioblastoma. Functional enrichment analysis showed that the SUMOylation regulators of glioblastoma might involve cell cycle, DNA replication, and other functions. A prognostic model of glioblastoma was constructed based on SUMOylation regulator-related molecules (ATF7IP, CCNB1IP1, and LBH). Kaplain–Meier survival curves and receiver operating characteristic curves showed that the model had a strong ability to predict the overall survival of glioblastoma.

Conclusion: This study analyzed the expression of 15 SUMOylation regulators in glioblastoma. The risk assessment model was constructed based on the SUMOylation regulator-related genes, which had a strong predictive ability for the overall survival of patients with glioblastoma. It might provide targets for the study of the relationship between SUMOylation and glioblastoma.

Keywords: glioblastoma, prognosis, SUMOylation, post-translational modification, risk assessment model

INTRODUCTION

Glioblastoma is the most malignant intracranial tumor originating from glial cells. Common treatments for glioblastoma include microsurgery, the use of chemotherapy drugs, such as temozolomide, and radiotherapy. However, the prognosis of patients with glioblastoma is still very poor. Studies have shown that the 5-year survival rate is only approximately 5% (Stupp et al., 2009; Ostrom et al., 2017). Due to the high cost of treatment of glioblastoma and poor treatment effect, it has always been one of the difficulties in tumor treatment (Cloughesy et al., 2020; Faria et al., 2020; Reardon et al., 2020). Therefore, it is of great importance to find effective molecular targets and improve the prognosis of glioblastoma.

Epigenetic modification is a heritable change in gene expression without DNA change, which plays a very important

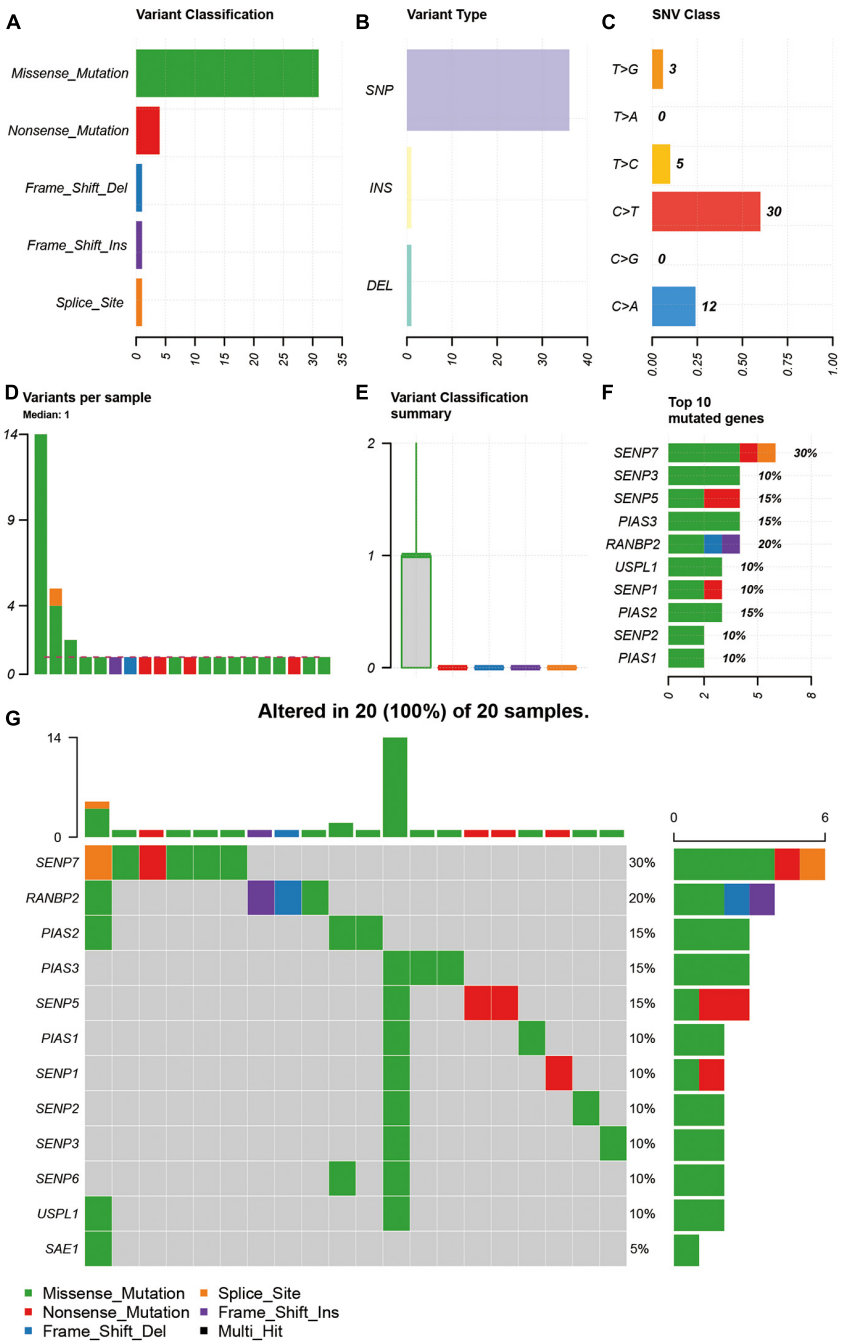

FIGURE 1 | Description of SNV of SUMOylation regulators in glioblastoma. **(A–C)** Missense mutation, SNP, and C > T were the main SNV types. **(D,E)** Most cases only have one single SNV of SUMOylation regulators. **(F)** SENP7 had the highest SNV frequency. **(G)** Relationship between the distribution of the SNV and the cases.

role in the development of glioblastoma (Kelly and Issa, 2017; Uddin et al., 2020). SUMOylation is one of the post-translational modifications. Through the catalysis of tertiary enzymes, the small ubiquitin-like modifier (SUMO) proteins bind to lysine residues (Rodriguez et al., 2001; Sampson et al., 2001), which can play various regulatory roles in tumor subcellular localization and transcription activities (Eifler and Vertegaal, 2015; Seeler and Dejean, 2017). The process of SUMOylation requires the activation of three kinds of enzymes (Johnson, 2004). SUMO-activating enzymes (E1, including SAE1, UBA2) can form heterodimers and transfers SUMO molecules to SUMO-conjugating enzyme (E2, including UBE2I). The SUMO-conjugating enzyme then transfers SUMO molecules to the lysine residue of the substrate. SUMO ligases (E3, including PIAS1, PIAS2, PIAS3, PIAS4, and RANBP2) make the substrate bind more closely to SUMO molecules. In addition, SUMOylation can be reversed by SUMO proteases (SENP1, SENP2, SENP3, SENP5, SENP6, SENP7, and USPL1), which is also called deSUMOylation. However, the relationship between the expression of SUMOylation regulators and the prognosis of glioblastoma is not quite clear.

This study aims to analyze the genome and transcriptome of glioblastoma and explore the expression characteristics and prognostic value of SUMOylation regulators and their related molecules in glioblastoma.

MATERIALS AND METHODS

Data Sources

The single-nucleotide variant (SNV) data of glioblastoma came from The Cancer Genome Atlas (TCGA) database[1]. The transcriptome data of glioblastoma was acquired from the TCGA database and the Gene Expression Omnibus (GEO) database (GSE13041 and GSE83300)[2]. The survival information of the TCGA dataset came from the cBioportal database[3].

Data Processing

Based on the data acquired, the SNV of SUMOylation regulators of glioblastoma was analyzed by the R language "maftools" package. The intersection genes of TCGA and GEO datasets were taken for subsequent expression and prognostic analysis. Wilcoxon test was used to analyze differentially expressed genes between glioblastoma and normal brain tissues. A heatmap was drawn for visualization. Because isocitrate dehydrogenase (IDH) mutations have a great impact on the prognosis of glioblastoma, we further analyzed the expression of SUMOylation regulators in different IDH mutation subgroups.

Functional Enrichment Analysis

To explore the biological functions that SUMOylation might regulate, the R language "clusterProfiler" package performed Kyoto Encyclopedia of Genes and Genomes (KEGG) enrichment analysis of glioblastoma genes.

Construction of a Prognostic Model

To find out the prognostic importance of SUMOylation regulator-related molecules, a prognostic model of glioblastoma was constructed. The TCGA dataset was used as the training group, whereas the GEO datasets (GSE13041 and GSE83300) were used as the validation group. In the training group, the differentially expressed genes between glioblastoma and

[1]https://cancergenome.nih.gov/

[2]https://www.ncbi.nlm.nih.gov/geo/

[3]https://www.cbioportal.org/

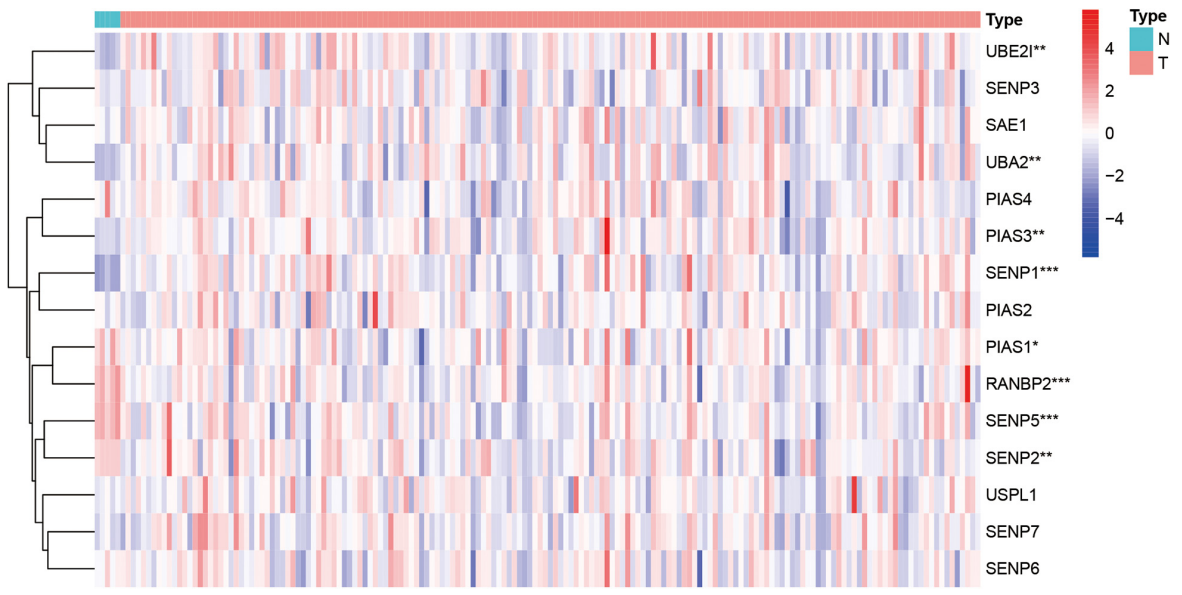

FIGURE 2 | Heatmap of all SUMOylation regulators in glioblastoma. *$p < 0.05$, **$p < 0.01$, and ***$p < 0.001$.

normal brain tissue were identified first. When the Pearson correlation coefficient was greater than 0.6, related molecules of the SUMOylation regulators were selected. Correlations between genes and overall survival of glioblastoma were performed by univariate Cox regression. Later, a risk-scoring model was built by the least absolute shrinkage and selection operator Cox regression. Kaplain–Meier survival curves and ROC curves were drawn in both the training group and the validation group to evaluate the effectiveness of the model in predicting the prognosis of glioblastoma. The nomogram was presented accordingly.

Statistical Analysis

R language (4.0.2) was used for data analysis and graphing. When $P < 0.05$, it was considered statistically significant.

RESULTS

Single-Nucleotide Variant Overview of SUMOylation Regulators in Glioblastoma

As SNV status was often associated with abnormal gene expression, we first checked the SNV status of SUMOylation regulators. From the perspective of SNV types, missense mutation, SNP, and C > T were the main mutation forms, as shown in **Figures 1A–C**. Most cases only have one single SNV of SUMOylation regulators (**Figures 1D,E**). SENP7, SENP3, SENP5, PIAS3, RANBP2, USPL1, SENP1, PIAS2, SENP2, and PIAS1 showed SNV, and SENP7 had the highest SNV frequency (**Figure 1F**). The relationship between the distribution of the SNV and the cases are

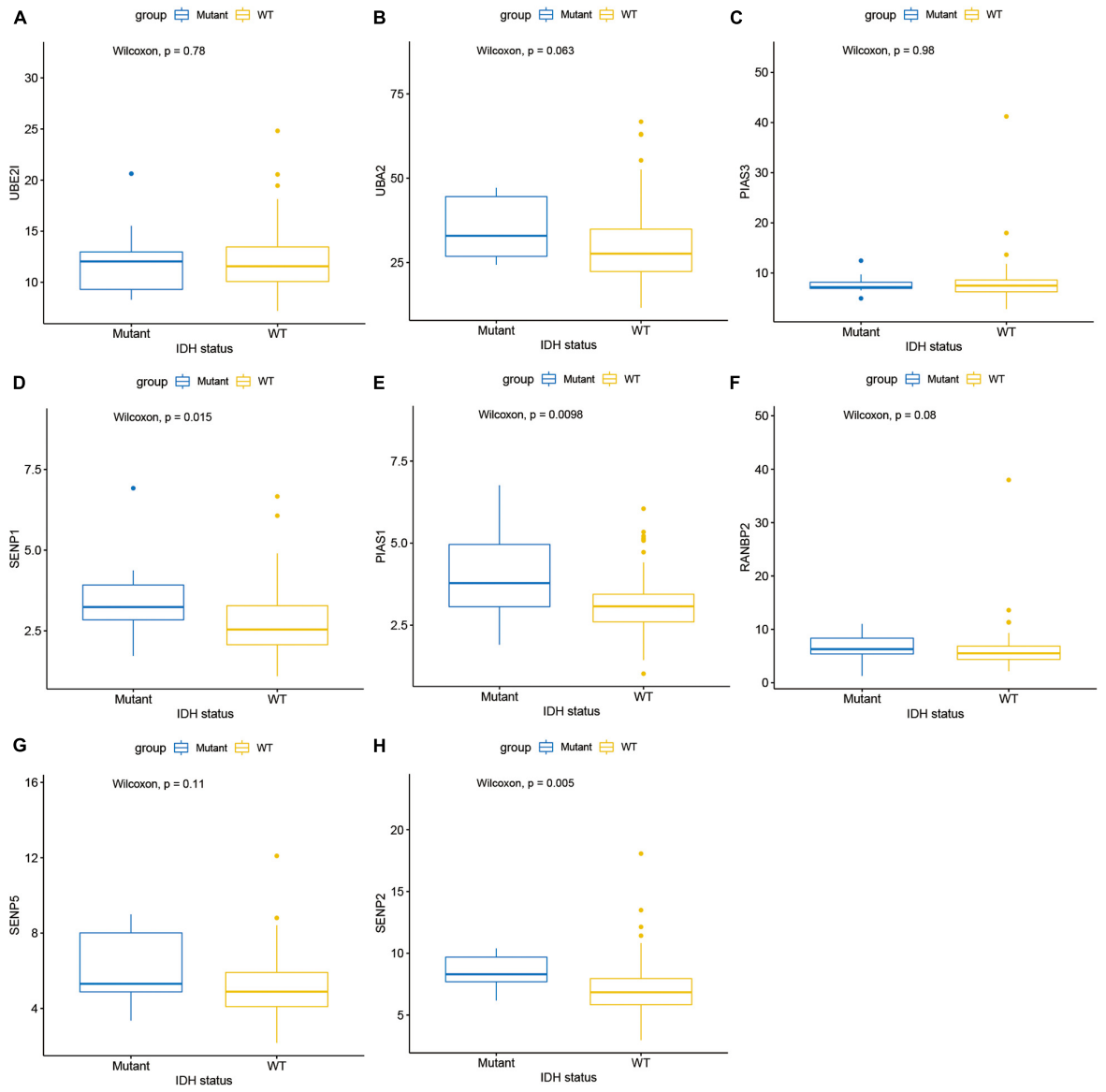

FIGURE 3 | Expression in different IDH mutation status subgroups of **(A)** UBE2I, **(B)** UBA2, **(C)** PIAS3, **(D)** SENP1, **(E)** PIAS1, **(F)** RANBP2, **(G)** SENP5, and **(H)** SENP2.

shown in **Figure 1G**. Because of the low SNV frequency of SUMOylation regulators (20/590), we could not accurately estimate the exact relationship between SNV and certain clinical characteristics, which required more sequencing studies by researchers.

Differentially Expressed SUMOylation Regulators

Next, this study investigated the expression difference of SUMOylation regulators between glioblastoma and normal brain tissue. The heatmap of the expression of all SUMOylation regulators in glioblastoma is shown in **Figure 2**. As can be seen from the figure, UBE2I, UBA2, PIAS3, and SENP1 were upregulated in glioblastoma, whereas PIAS1, RANBP2, SENP5, and SENP2 were downregulated in glioblastoma. Among the eight differentially expressed genes, SENP1, PIAS1, and SENP2 also had different expressions in different IDH mutation status subgroups. Compared with the IDH mutant type, these three genes were downregulated in the IDH wild type, as shown in **Figure 3**. Although many SUMOylation regulators were abnormally expressed in glioblastoma or in different glioblastoma IDH status, we did not find their significant predictive effect on overall survival. We presume this might be because SUMOylation was not the original driving factor of glioblastoma or might play a role at a certain stage of glioblastoma development. This phenomenon required further research into SUMOylation in the future.

Functional Enrichment Analysis

By calculating the correlation between genes, the upstream and downstream genes of the target gene can be found to gain a deeper understanding of the biological functions of the target gene. In this study, KEGG enrichment analysis was performed on genes whose correlation coefficients with SUMOylation regulators were greater than 0.6. The results are shown in **Figure 4**. SUMOylation regulators may be related to cell cycle, DNA replication, and other functions. These results suggested that SUMOylation might be involved in the regulation of glioblastoma cell proliferation.

Construction of a Glioblastoma Prognostic Model Based on SUMOylation Regulator-Related Molecules

Next, we used survival analysis to identify the SUMOylation-related prognostic signatures and test their prognostic values. Two hundred thirty-nine SUMOylation regulator-related molecules were differentially expressed in glioblastoma ($|\log 2\ FC| > 1$). Univariate Cox regression results suggested that KANK2, MYO15A, SEMA3F, ATF7IP, CCNB1IP1, HNRNPC, PTGIR, ZNF85, PXDN, ZNF432, and LBH were closely related to the prognosis of glioblastoma. The risk-scoring model for glioblastoma was constructed by the least absolute shrinkage and selection operator Cox regression (**Figures 5A,B**). The risk score was expressed by the following equation: Risk score = −0.138 × Expression ATF7IP-0.047 × Expression CCNB1IP1 + 0.054 × Expression LBH. The relationship between overall survival and risk score distribution is shown in **Figures 5C,D**.

In the training group, divided by the median risk score, the overall survival of patients with high-risk scores was significantly worse than that of patients with low-risk scores (**Figure 6A**, $P < 0.01$). The 1- and 3-year areas under the curve of ROC curves of the training group were 0.710 and 0.807, respectively (**Figure 6B**). In one validation group (GSE13041), the overall survival of patients with high-risk scores was also significantly worse than that of patients with low-risk scores (**Figure 6C**, $P < 0.01$). The 1- and 3-year areas under the curve of ROC curves in the GSE13041 group were 0.600 and 0.655, respectively (**Figure 6D**). In the other validation group (GSE83300), the survival curve and ROC plot also showed the predictive power of the model, as shown in **Figures 6E,F**. These results showed that the risk-scoring model based on SUMOylation-related signatures performed well in predicting the overall survival of glioblastoma

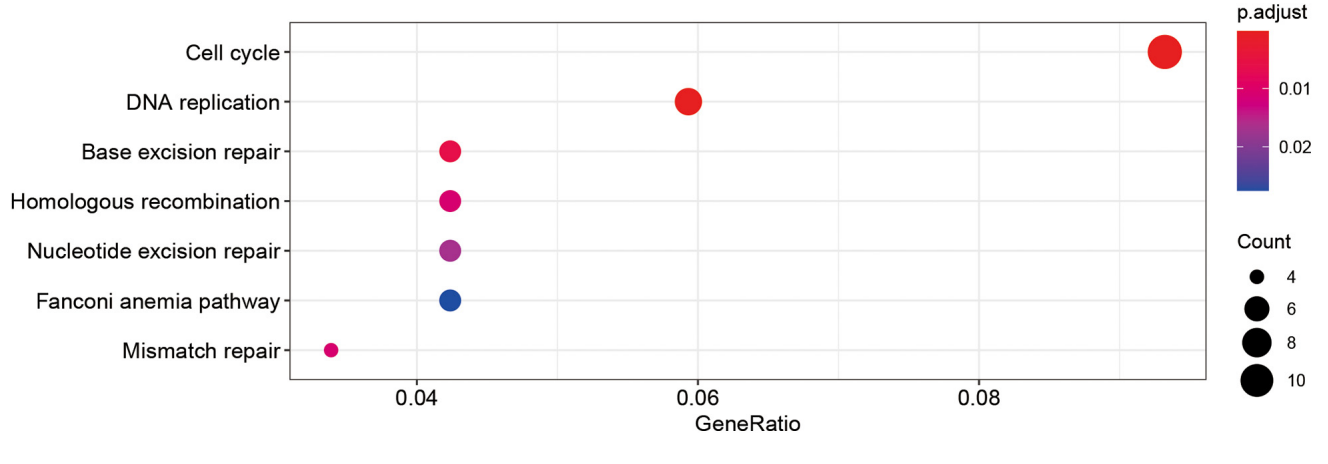

FIGURE 4 | Kegg analyses showed the SUMOylation regulators might be related to cell cycle, DNA replication, and other functions.

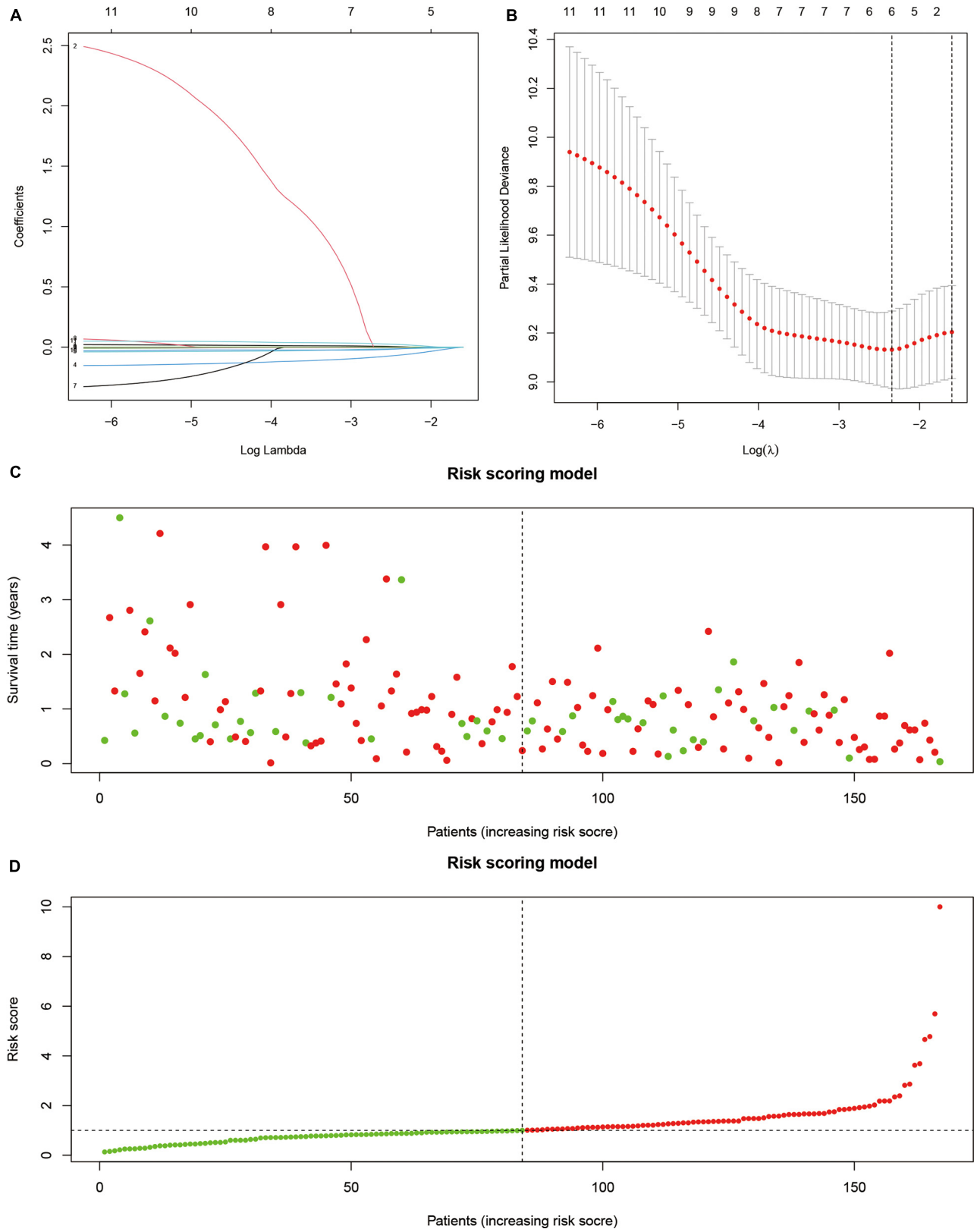

FIGURE 5 | Prognostic model based on SUMOylation regulator-related genes. **(A)** Lambda selection in the least absolute shrinkage and selection operator model. **(B)** Least absolute shrinkage and selection operator coefficient profiles of selected genes. **(C,D)** Relationship between overall survival and risk score distribution.

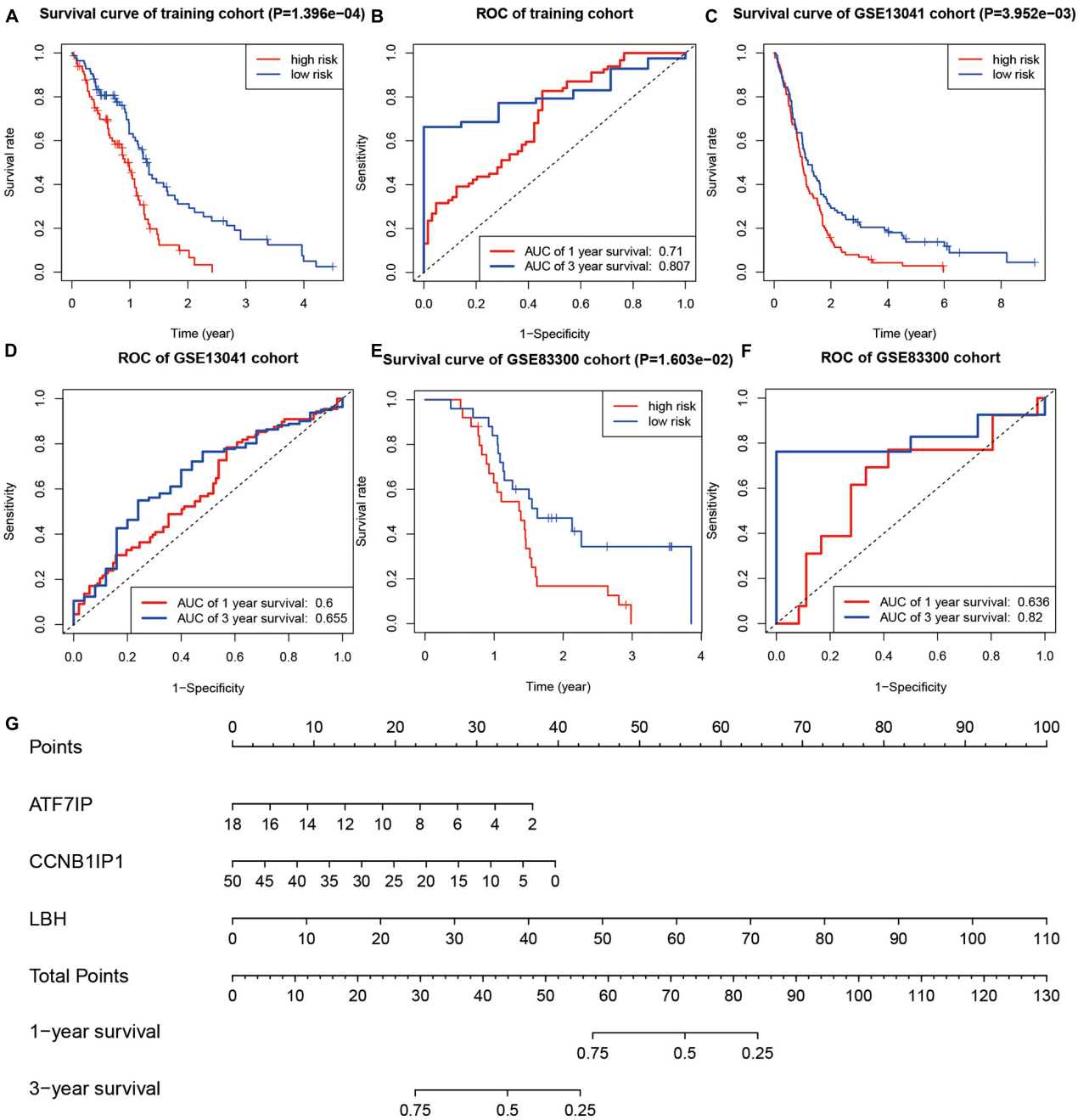

FIGURE 6 | Testing of the prognostic model. **(A,B)** Kaplan–Meier survival curve and ROC curve of the training group. **(C,D)** Kaplan–Meier survival curve and ROC curve of the GSE13041 group. **(E,F)** Kaplan–Meier survival curve and ROC curve of the GSE83300 group. **(G)** Nomogram for predicting the overall survival of glioblastoma patients.

patients. Finally, a nomogram based on the risk scoring model is drawn in **Figure 6G**.

DISCUSSION

This study explored the characteristics of SUMOylation in glioblastoma in terms of SNV, gene expression, functional enrichment, and prognostic values. In this study, we first analyzed the SNV of 15 SUMOylation regulators. SNV mutations were found in SENP7, SENP3, SENP5, PIAS3, RANBP2, USPL1, SENP1, PIAS2, SENP2, and PIAS1. Next, we analyzed the expression of all the SUMOylation regulators in glioblastoma. UBE2I, UBA2, PIAS3, and SENP1 were highly expressed in glioblastoma. PIAS1, RANBP2, SENP5, and SENP2 were downregulated in glioblastoma. However, the SNV frequency

of SUMOylation regulators in glioblastoma was relatively low compared with the well-known IDH. Then, KEGG enrichment analysis showed that the SUMOylation regulators of glioblastoma might involve cell cycle, DNA replication, and other functions. Finally, a prognostic model of glioblastoma was constructed based on SUMOylation regulator-related molecules (ATF7IP, CCNB1IP1, and LBH). Kaplain–Meier survival curves and ROC curves showed that the model had a strong ability to predict the overall survival of glioblastoma.

SUMOylation was first discovered in the 1990s (Matunis et al., 1996; Mahajan et al., 1997). It regulates the localization and activity of a variety of proteins (Yeh et al., 2000; Geiss-Friedlander and Melchior, 2007). The unbalanced regulation of SUMOylation and deSUMOylation is one of tumor pathogenesis (Wu et al., 2020, 2021; Samaržija, 2021). UBA2 is highly expressed in small cell lung cancer. Silencing UBA2 can reduce tumor cell migration and invasion ability and increase the sensitivity to etoposide and cisplatin (Liu et al., 2015). UBE2I is the only SUMO conjugating enzyme that is highly expressed in colon cancer and prostate cancer, whereas it is downregulated in breast, prostate, and lung cancers (Moschos et al., 2010). In breast cancer, overexpressed SENP2 enhances the deSUMOylation of NEMO and inhibits the activation of nuclear factor kappa-light-chain-enhancer of activated B cells (Gao et al., 2019). In addition, PIAS3 is upregulated in lung cancer, breast cancer, prostate cancer, colorectal cancer, and brain tumors (Wang and Banerjee, 2004). The SUMOylation pathway and drugs targeting SUMOylation are promising to provide new strategies for tumor treatment (He et al., 2017; Yang et al., 2018).

So far, there are limited treatment options for glioblastoma, and even with the existing standard treatment, the overall survival and quality of life of patients are still very poor. Therefore, the research on the pathogenesis of glioblastoma and the corresponding molecular targeted drugs are quite promising. Topotecan, a United States Food and Drug Administration-approved anti-glioblastoma drug, can reduce overall cell SUMOylation, CDK6, and HIF-1α levels and regulate the cell cycle, but the specific target is not clear (Zheng et al., 2020).

As one of the important results of this study, we found that UBE2I, UBA2, PIAS3, SENP1, PIAS1, RANBP2, SENP5, and SENP2 were differentially expressed in glioblastoma. A few studies were reported about these genes and consistent with our findings. For example, SENP1 is upregulated in glioblastoma. Knockdown of SENP1 can inhibit the phosphorylation of IκBα and Akt and inhibit the expression of Bcl-xL and cyclinD1, thereby promoting glioblastoma cell apoptosis (Xia et al., 2016). In addition, UBE2I promotes the SUMOylation of CDK6 in glioblastoma and promotes tumor cell development by regulating the cell cycle (Bellail et al., 2014). UBE2I is highly expressed in glioblastoma and promotes the SUMOylation of CRMP2, which in turn drives the proliferation of glioblastoma (Wang and Ji, 2019). Moreover, the upregulated UBE2I can promote the SUMOylation of PUM2 and ultimately promote glioma vasculogenic mimicry (Wang et al., 2020). However, other SUMOylation regulators are rarely reported in glioblastoma. The research on the SUMOylation regulator-related genes provides an important basis and direction for further exploring the research of SUMOylation in the pathogenesis of glioblastoma.

To further analyze the prognostic importance of SUMOylation-related genes, a risk-scoring model of glioblastoma was constructed based on the SUMOylation regulator-related genes. The results of Kaplain–Meier survival curves and ROC curves showed the effectiveness of the model's prediction. The nomogram based on the risk-scoring model provided a reference for molecular diagnosis, prognosis assessment, and possible targets for patients with glioblastoma.

This work also has some limitations. For example, the expression and function of SUMOylation regulators and their related genes need more basic experimental verification.

CONCLUSION

In conclusion, this study analyzed the expression of 15 SUMOylation regulators in glioblastoma. The risk assessment model was constructed based on the SUMOylation regulator-related genes, which had a strong predictive ability for the overall survival of patients with glioblastoma. It might provide targets for the study of the relationship between SUMOylation and glioblastoma.

DATA AVAILABILITY STATEMENT

Publicly available datasets were analyzed in this study. This data can be found here: Data was acquired from TCGA database (https://cancergenome.nih.gov/), GEO database (https://www.ncbi.nlm.nih.gov/geo/, GSE13041), and cBioportal database (https://www.cbioportal.org/).

AUTHOR CONTRIBUTIONS

YM contributed to the experiment design and final inspection. XL contributed to the data analysis and manuscript draft. Both authors have read and approved the final manuscript.

FUNDING

This study was supported by the 345 Talent Project.

REFERENCES

Bellail, A. C., Olson, J. J., and Hao, C. (2014). SUMO1 modification stabilizes CDK6 protein and drives the cell cycle and glioblastoma progression. *Nat. Commun.* 5:4234.

Cloughesy, T. F., Petrecca, K., Walbert, T., Butowski, N., Salacz, M., Perry, J., et al. (2020). Effect of vocimagene amiretrorepvec in combination with flucytosine vs standard of care on survival following tumor resection in patients with recurrent high-grade glioma: a randomized clinical trial. *JAMA Oncol.* 6, 1939–1946.

Eifler, K., and Vertegaal, A. C. O. (2015). SUMOylation-mediated regulation of cell cycle progression and cancer. *Trends Biochem. Sci.* 40, 779–793.

Faria, G. M., Soares, I. D. P., D'Alincourt Salazar, M., Amorim, M. R., Pessoa, B. L., da Fonseca, C. O., et al. (2020). Intranasal perillyl alcohol therapy improves survival of patients with recurrent glioblastoma harboring mutant variant for MTHFR rs1801133 polymorphism. *BMC Cancer* 20:294. doi: 10.1186/s12885-020-06802-8

Gao, X., Wu, Y., Qiao, L., and Feng, X. (2019). SENP2 suppresses NF-κB activation and sensitizes breast cancer cells to doxorubicin. *Eur. J. Pharmacol.* 854, 179–186. doi: 10.1016/j.ejphar.2019.03.051

Geiss-Friedlander, R., and Melchior, F. (2007). Concepts in sumoylation: a decade on. *Nat. Rev. Mol. Cell. Biol.* 8, 947–956. doi: 10.1038/nrm2293

He, X., Riceberg, J., Soucy, T., Koenig, E., Minissale, J., Gallery, M., et al. (2017). Probing the roles of SUMOylation in cancer cell biology by using a selective SAE inhibitor. *Nat. Chem. Biol.* 13, 1164–1171. doi: 10.1038/nchembio.2463

Johnson, E. S. (2004). Protein modification by SUMO. *Annu. Rev. Biochem.* 73, 355–382. doi: 10.1146/annurev.biochem.73.011303.074118

Kelly, A. D., and Issa, J. J. (2017). The promise of epigenetic therapy: reprogramming the cancer epigenome. *Curr. Opin. Genet. Dev.* 42, 68–77. doi: 10.1016/j.gde.2017.03.015

Liu, X., Xu, Y., Pang, Z., Guo, F., Qin, Q., Yin, T., et al. (2015). Knockdown of SUMO-activating enzyme subunit 2 (SAE2) suppresses cancer malignancy and enhances chemotherapy sensitivity in small cell lung cancer. *J. Hematol. Oncol.* 8:67.

Mahajan, R., Delphin, C., Guan, T., Gerace, L., and Melchior, F. (1997). A small ubiquitin-related polypeptide involved in targeting RanGAP1 to nuclear pore complex protein RanBP2. *Cell* 88, 97–107. doi: 10.1016/s0092-8674(00)81862-0

Matunis, M. J., Coutavas, E., and Blobel, G. (1996). A novel ubiquitin-like modification modulates the partitioning of the Ran-GTPase-activating protein RanGAP1 between the cytosol and the nuclear pore complex. *J. Cell. Biol.* 135, 1457–1470.

Moschos, S. J., Jukic, D. M., Athanassiou, C., Bhargava, R., Dacic, S., Wang, X., et al. (2010). Expression analysis of Ubc9, the single small ubiquitin-like modifier (SUMO) E2 conjugating enzyme, in normal and malignant tissues. *Hum. Pathol.* 41, 1286–1298. doi: 10.1016/j.humpath.2010.02.007

Ostrom, Q. T., Gittleman, H., Liao, P., Vecchione-Koval, T., Wolinsky, Y., Kruchko, C., et al. (2017). CBTRUS statistical report: primary brain and other central nervous system tumors diagnosed in the United States in 2010-2014. *Neuro. Oncol.* 19, v1–v88.

Reardon, D. A., Brandes, A. A., Omuro, A., Mulholland, P., Lim, M., Wick, A., et al. (2020). Effect of nivolumab vs bevacizumab in patients with recurrent glioblastoma: the checkmate 143 phase 3 randomized clinical trial. *JAMA Oncol.* 6, 1003–1010.

Rodriguez, M. S., Dargemont, C., and Hay, R. T. (2001). SUMO-1 conjugation in vivo requires both a consensus modification motif and nuclear targeting. *J. Biol. Chem.* 276, 12654–12659. doi: 10.1074/jbc.M009476200

Samaržija, I. (2021). Post-translational modifications that drive prostate cancer progression. *Biomolecules* 11:247.

Sampson, D. A., Wang, M., and Matunis, M. J. (2001). The small ubiquitin-like modifier-1 (SUMO-1) consensus sequence mediates Ubc9 binding and is essential for SUMO-1 modification. *J. Biol. Chem.* 276, 21664–21669. doi: 10.1074/jbc.M100006200

Seeler, J. S., and Dejean, A. (2017). SUMO and the robustness of cancer. *Nat. Rev. Cancer* 17, 184–197. doi: 10.1038/nrc.2016.143

Stupp, R., Hegi, M. E., Mason, W. P., van den Bent, M. J., Taphoorn, M. J., Janzer, R. C., et al. (2009). Effects of radiotherapy with concomitant and adjuvant temozolomide versus radiotherapy alone on survival in glioblastoma in a randomised phase III study: 5-year analysis of the EORTC-NCIC trial. *Lancet Oncol.* 10, 459–466. doi: 10.1016/s1470-2045(09)70025-7

Uddin, M. S., Mamun, A. A., Alghamdi, B. S., Tewari, D., Jeandet, P., Sarwar, M. S., et al. (2020). Epigenetics of glioblastoma multiforme: from molecular mechanisms to therapeutic approaches. *Semin. Cancer Biol.* [Epub ahead of print]. doi: 10.1016/j.semcancer.2020.12.015

Wang, D., Ruan, X., Liu, X., Xue, Y., Shao, L., Yang, C., et al. (2020). SUMOylation of PUM2 promotes the vasculogenic mimicry of glioma cells via regulating CEBPD. *Clin. Transl. Med.* 10:e168.

Wang, L., and Banerjee, S. (2004). Differential PIAS3 expression in human malignancy. *Oncol. Rep.* 11, 1319–1324.

Wang, L., and Ji, S. (2019). Inhibition of Ubc9-Induced CRMP2 SUMOylation disrupts glioblastoma cell proliferation. *J. Mol. Neurosci.* 69, 391–398. doi: 10.1007/s12031-019-01368-y

Wu, R., Fang, J., Liu, M. A. J., Liu, J., Chen, W., Li, J., et al. (2020). SUMOylation of the transcription factor ZFHX3 at Lys-2806 requires SAE1, UBC9, and PIAS2 and enhances its stability and function in cell proliferation. *J. Biol. Chem.* 295, 6741–6753.

Wu, Y., Yu, B., and Wang, M. (2021). SENP1 is required for the growth, migration, and survival of human adipose-derived stem cells. *Adipocyte* 10, 38–47.

Xia, W., Tian, H., Cai, X., Kong, H., Fu, W., Xing, W., et al. (2016). Inhibition of SUMO-specific protease 1 induces apoptosis of astroglioma cells by regulating NF-κB/Akt pathways. *Gene* 595, 175–179. doi: 10.1016/j.gene.2016.09.040

Yang, Y., Xia, Z., Wang, X., Zhao, X., Sheng, Z., Ye, Y., et al. (2018). Small-molecule inhibitors targeting protein SUMOylation as novel anticancer compounds. *Mol. Pharmacol.* 94, 885–894. doi: 10.1124/mol.118.112300

Yeh, E. T., Gong, L., and Kamitani, T. (2000). Ubiquitin-like proteins: new wines in new bottles. *Gene* 248, 1–14. doi: 10.1016/s0378-1119(00)00139-6

Zheng, Z., Mao, S., Zhang, W., Liu, J., Li, C., Wang, R., et al. (2020). Dysregulation of the immune microenvironment contributes to malignant progression and has prognostic value in bladder cancer. *Front. Oncol.* 10:542492. doi: 10.3389/fonc.2020.542492

Conflict of Interest: The authors declare that the research was conducted in the absence of any commercial or financial relationships that could be construed as a potential conflict of interest.

frontiers in Cell and Developmental Biology

BRIEF RESEARCH REPORT
published: 26 May 2021
doi: 10.3389/fcell.2021.666462

Identification of Precise Therapeutic Targets and Characteristic Prognostic Genes Based on Immune Gene Characteristics in Uveal Melanoma

Zhenxi Zhang, Jingyu Su, Li Li and Wenjing Du**

State Key Laboratory of Medical Molecular Biology, Department of Cell Biology, Institute of Basic Medical Sciences, Chinese Academy of Medical Sciences, School of Basic Medicine, Peking Union Medical College, Beijing, China

The tumor microenvironment is an important factor for the immunotherapy of tumor patients. The sequenced transcriptome data can be used to describe the tumor microenvironment and various immune subtypes. We exploited published data on patients with uveal melanoma (UVM) to identify immune subtypes. Based on the immune-related gene sets of 80 patients with UVM in the TCGA database, we used consensus clustering to identify two immune subgroups. In the two immune subtypes, we analyzed clinical characteristics and immune infiltration. Class1 has low immune infiltration, contains memory B cells, Th2 cells, Th17 cells, eosinophils, natural killer cells, and has a better prognosis. Class2 has higher immune infiltration. CD8+ T cells, Th1 cells, MDSCs, and Dendritic cells are enriched in class2, which has strong cytolytic activity, high expression of immune checkpoint genes, and poor outcome. Moreover, we have developed and verified an immune characteristic model that can predict the prognosis of patients well. Through this model, we screened prostaglandin-endoperoxide synthase 2 (*PTGS2*) as the therapeutic target of UVM. Treatment of choroidal melanoma cell line (OCM1) cells with celecoxib (an inhibitor of *PTGS2*) effectively inhibits cell growth, proliferation, and promotes apoptosis. Our results show the immunological heterogeneity of UVM patients and also provide an ideal therapeutic target for the future treatment design of patients.

Keywords: uveal melanoma, tumor microenvironment, immune classification, prognosis, precision therapy, PTGS2

OPEN ACCESS

Edited by:
Changliang Shan,
Nankai University, China

Reviewed by:
Bo Li,
Sun Yat-sen University, China
Liang Ge,
Tsinghua University, China

****Correspondence:***
Li Li
rene_ll@126.com
Wenjing Du
wenjingdu@ibms.pumc.edu.cn

Specialty section:
This article was submitted to Molecular Medicine, a section of the journal Frontiers in Cell and Developmental Biology

Received: *10 February 2021*
Accepted: *04 March 2021*
Published: *26 May 2021*

Citation:
Zhang Z, Su J, Li L and Du W (2021) Identification of Precise Therapeutic Targets and Characteristic Prognostic Genes Based on Immune Gene Characteristics in Uveal Melanoma. Front. Cell Dev. Biol. 9:666462. doi: 10.3389/fcell.2021.666462

INTRODUCTION

Uveal melanoma (UVM) is one of the most common primary intraocular malignant tumors, originating in the choroid, ciliary body, or iris (Willson et al., 2001; Chattopadhyay et al., 2016; Kaliki and Shields, 2017). It is estimated that there are about 7000 new cases of UVM every year worldwide, with an incidence rate of about 4.3 parts per million (Schank and Hassel, 2019). The 5-year survival rate of patients is 50–70%. However, UVM is very prone to metastasis. About 50% of patients will suffer from metastatic disease, which occurs more in the livers, lungs, and resulting

in higher mortality (Willson et al., 2001; Kaliki and Shields, 2017). Although the treatment of tumor has been improved continuously, there is still no standard treatment method for metastatic UVM.

Recently, clinical trials have shown that immunotherapy is a promising therapy for many kinds of malignant tumors, including immune checkpoint blockade, cell therapy, and cytokine therapy (Yang, 2015; Callahan et al., 2016; Castellanos and Horn, 2016). Among them, immune checkpoint inhibitor therapy has been applied to treat a broad range of cancer types, such as lung cancer, liver cancer, and skin melanoma (Snyder et al., 2014; Johnson et al., 2017; Sugie, 2018). In recent years, some immunotherapies have also begun to treat UVM, such as ipilimumab, pembrolizumab and nivolumab, and adoptive cell therapy, alone or in combination (Ji et al., 2012; Karivedu et al., 2019; Jansen et al., 2020; Pelster et al., 2020). Unfortunately, the treatment effect for UVM was not ideal. In an immunotherapy study of 96 patients with uveal melanin, nivolumab and pembrolizumab alone or in combination therapy were used to treat 32, 54, and 15 patients, respectively. Only two patients had a partial response (PR) on nivolumab and combination therapy, and only one patient had a partial response (PR) on pembrolizumab. None of the three treatments had a complete response (CR) (Heppt et al., 2017). Chandran et al. (2017) found that only 30% of patients achieved a partial response in adoptive cell therapy for UVM (Chandran et al., 2017). Taken together, these results indicate that UVM is resistant to immunotherapy, and it is necessary to further explore the immunological mechanism in this cancer.

To better understand the tumor immune microenvironment, in this study, we divided UVM into two immune subgroups, based on consensus clustering of immune gene sets. The two immune subtypes had unique molecules, immune cell characteristics, and clinical outcome. We used Cox proportional hazard regression model to predict the survival of patients, and screened prostaglandin-endoperoxide synthase 2 *(PTGS2)* gene as a therapeutic target for UVM. Identifying the immune subtypes of UVM may contribute to a precision treatment for immunotherapy.

METHODS

Patients and Datasets

The data for this study came from two databases (**Table 1**): The Cancer Genome Atlas (TCGA) and Gene Expression Omnibus (GEO). 80 UVM patients came from the TCGA database, containing RNA-seq data, somatic mutations, copy number variations (CNVs), DNA methylation and clinical sample data. 28 UVM patients came from GSE84976 containing RNA-seq data and clinical sample data (van Essen et al., 2016). 63 UVM patients came from GSE22138 containing RNA-seq data and clinical sample data (Laurent et al., 2011).

TABLE 1 | Clinical characteristics of patients in the study.

Characteristic		TCGA (*n* = 80)	GSE84976 (*n* = 28)	GSE22138 (*n* = 63)
Age	≤50	18	7	10
	>50	62	21	53
Sex	male	45	N/A	39
	female	35	N/A	24
Stage	IIA	4	N/A	N/A
	IIB	32	N/A	N/A
	IIIA	27	N/A	N/A
	IIIB	10	N/A	N/A
	IIIC	3	N/A	N/A
	IV	4	N/A	N/A

Identification of Immune Subtypes

Based on the previously reported expression of 782 immune-related genes, we used consensus clustering to identify the immune subtypes of UVM patients. The R package "ConsensusClusterPlus" was used for clustering. The following were some parameters, 80% items resampling, an evaluated K of 6, 50 resampling and others were the default values (Wilkerson and Hayes, 2010; Li et al., 2017). Cumulative distribution function (CDF) and consensus matrices were used to confirm the optimal number of subtypes.

The Immune Characteristics Comparison of Two Immune Subtypes

Estimation of stromal and immune cells in malignant tumor tissues using expression data (ESTIMATE) was carried out to estimate the level of immune cell infiltration and somatic tumor score (Yoshihara et al., 2013). When using ESTIMATE, the sample file needed to be converted into a GCT format file as an input file, and GeneSymbol was used as the basis for gene identification. We used immune genes to establish gene sets of immune cells, cytolytic activity, TIL, and immune checkpoints. Immune cell score and immune characteristic score were quantified by the single-sample gene set enrichment analysis (ssGSEA) using R package "GSVA" (Hanzelmann et al., 2013).

Differential Gene Analysis, Cox Proportional Hazard Regression Model

First, we used LIMMA to identify differential genes in count data of the two immune subtypes (Ritchie et al., 2015). The false discovery rate (FDR) < 0.05 was considered to be a differentially expressed gene. The R package "clusterProfiler" was used to analyze Gene Ontology (GO) (Yu et al., 2012).

A univariate Cox proportional hazard regression model was used to screen immune genes with prognostic value. We used the least absolute shrinkage and selection operator (LASSO) method for variable selection in the Cox regression model to determine meaningful prognostic genes and coefficient values. Using the linear combination of gene expression weighted regression coefficients, we got the risk score formula: risk score = (exp *PTGS2**3.88) + (exp *CCL24**0.32) + (exp *EPX**−1.25) + (exp *PAEP**0.03) + (exp *LY9**1.07) + (exp *PLXNB1**−0.007) + (exp *BDKRB2**0.4) + (exp *NKIRAS1**−0.19) + (exp *HLA-A**0.0003). The UVM patients were divided into low and high risk-score groups, and then the Kaplan–Meier method was used to analyze the relationship between risk scores and survival.

Cell Culture and Cell Activity Test

Choroidal melanoma cell line OCM1 was obtained from the American Type Culture Collection (ATCC, United States). Cells were cultured in Dulbecco's modified Eagle's medium (DMEM) supplemented with 10% FBS, 100 U/mL penicillin, and 100 mg/mL streptomycin, at 37°C and 5% CO2. For cell proliferation assay, cells were seeded in 6-well cell culture dishes at a density of 10,000 cells/well, and treated with celecoxib (Solarbio, China). Cells were collected and counted at a fixed time every day for 6 days. For cell viability assays, cells were seeded in 96-well cell culture dishes at a density of 1,000 cells/well, and treated with celecoxib. One day later, CCK8 (Pplygen, China) was added into culture dishes for 3 h. OD_{450nm} was measured using FlexStation 3. For cell clone experiment, cells were seeded in 6-well cell culture dishes at a density of 1,000 cells/well, and treated with celecoxib. After 10 days of culture, the cells were fixed with methanol for 30 min and stained with 0.1% crystal violet for 15 min. To detect apoptosis, cell culture media and cells were collected after 3 days. Apoptosis was detected by apoptosis kit (Keygentec, China).

Statistical Analysis

All calculations and statistics were done using R. Unpaired *t*-test was used to detect two sets of samples with normal distribution. The Kaplan–Meier method was used for survival analysis. $P < 0.05$ was considered statistically significant.

RESULTS

Immune Subtype Classification and Immune Cell Characteristics in UVM

In order to analyze the tumor microenvironment profile of UVM, we established an experimental diagram (**Supplementary Figure 1A**). Based on the consensus clustering analysis, TCGA UVM patients were divided into two immune types through immune gene expression profiles (**Supplementary Figures 1A,B**). Principal component analysis (PCA) was applied to further verify the difference in gene expression between these two immune types (**Figure 1B**). In these two immune subtypes, there were significant differences among the survival status of patients. Class2 patients had more deaths, higher rate of stage III and IV, higher risk of new tumor growth, in addition chromosome 3 loss and chromosome 8q gain (**Figures 1A,C**). While Class1 was associated with better survival rate (**Figure 1C**) and enriched in chromosome 6p gain (**Figure 1A**).

To analyze the immune characteristics of the two immune subtypes, we adopted two immune-related tools for analysis. We used the ESTIMATE method to compare the immune scores of these two subtypes. Class2 had higher stromal, immune and estimate scores but lower somatic cell purity (**Figure 1D**). Further, we applied the ssGSEA method to analyze the enrichment level of immune cells in immune subtypes. Class1 had higher amounts of memory B cells, Th2 cells, Eosinophils, natural killer (NK) cells, Th17 cells, CD56 bright natural killer cells, and Plasmacytoid dendritic cells (**Figure 1E**). Class2 was enriched in MDSCs, TH1 cells, activated dendritic cells, activated CD8 T cells and effector memory CD8 T cells (**Figure 1E**). Generally, human leukocyte antigen (HLA) and major histocompatibility complex (MHC) molecules activate CD8 T cells during antigen-specific immune responses (Garrido and Aptsiauri, 2019). Therefore, we further analyzed the changes of immune characteristics between these two subtypes. Higher expression levels of HLA and MHC molecules, more cytotoxicity, Tumor infiltrating lymphocytes (TIL) infiltration, and T cell costimulation were found in class 2 (**Supplementary Figure 2A**). Whereas in class1 there was a higher level of activated TNF-II molecule. In addition, immune checkpoint suppression therapy has become an effective tumor treatment method, so we compared the immune checkpoint gene expression between these two subgroups (Parry et al., 2005; Taggart et al., 2018). Tumor immune checkpoint genes such as *LAG3*, *IDO1*, *PDCD1* were highly expressed in class2 (**Supplementary Figure 2B**). Above all, these results indicate that class1 has a moderate immune microenvironment, while class2 has a high immune infiltration and the degree of immunosuppression.

Prognostic Associations of Tumor Immune Characteristics

Tumor infiltrating immune cells play an important role in many tumors for immunotherapy. Next, we detected the effect of immune cells in the prognosis of UVM. Among these immune characteristics, memory B cells, Th2 cells, NK cells, eosinophils and plasmacytoid dendritic cells, activated dendritic cells, activated CD8 T cells and MDSCs were related to prognosis (**Figure 2A**). Consistently with the Cox analysis, more activated dendritic cells, activated CD8 T cells and MDSCs were associated with a poor prognosis. High levels of Th17 cells, Th2 cells, and plasmacytoid dendritic cells linked with good prognosis (**Figure 2B**). In addition, we evaluated the prognosis of major immune checkpoints and found that high expression of *LAG3*, *PDCD1*, and *TIGIT* led to worse outcomes (**Figure 2C**). We further analyzed the correlation between immune cells and immune checkpoint genes. The data showed that immune checkpoint genes were positively correlated with these immune cells with poor prognosis, and negatively correlated with these immune cells with good prognosis (**Supplementary Figure 3A**). We analyzed the correlation of 28 immune cells. Activated CD8 T cells were positively correlated with effector memory CD8 T cells, MDSC cells, and negatively correlated with Plasmacytoid dendritic cells (**Supplementary Figure 3B**). These results suggest that infiltrating immune cells could affect the patient's outcome, and probably provide an idea for targeted immunotherapy of UVM.

Development and Validation of an Immune-Related Risk Model Using Cox Proportional Hazards Model

We next validated the survival model using the Cox proportional hazard model. We identified 2852 differentially expressed genes between class1 and class2 subtypes, of which 396 were immune genes by LIMMA (**Figure 3A**). We did GO analysis using

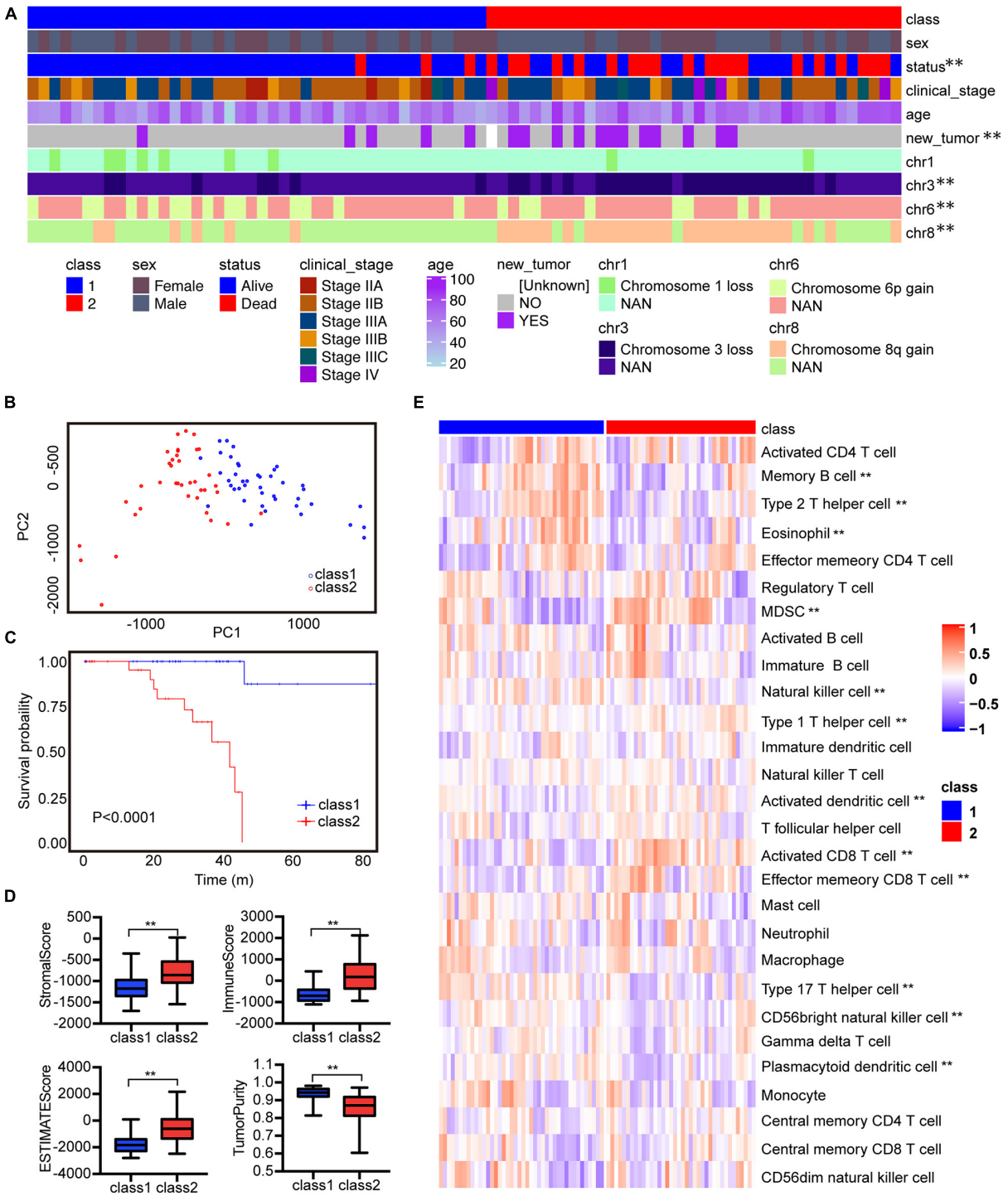

FIGURE 1 | The two immune subtypes show different clinical characteristics outcomes and tumor immune infiltrating characteristics in TCGA. **(A)** Clinical characteristics of two immune subtypes. **(B)** PCA of two immune subtypes using 782 genes in TCGA. **(C)** Kaplan–Meier analysis of two immune subtypes based on overall survival. **(D)** Comparison of stromal, immune, ESTIMATE scores, and tumor purity scores for different immune subtypes in TCGA using ESTIMATE R package. **(E)** Heatmap of GSVA signature scores in TCGA. $^{**}P < 0.05$.

differential genes. In Class2, the up-regulated genes were mainly enriched in receptor ligand activity, CCR chemokine receptor binding and MHC protein complex binding pathways (**Supplementary Figure 1E**). Using univariate Cox regression analysis, it was found that 306 genes were significantly related to the patient's prognosis. The best prognostic value model

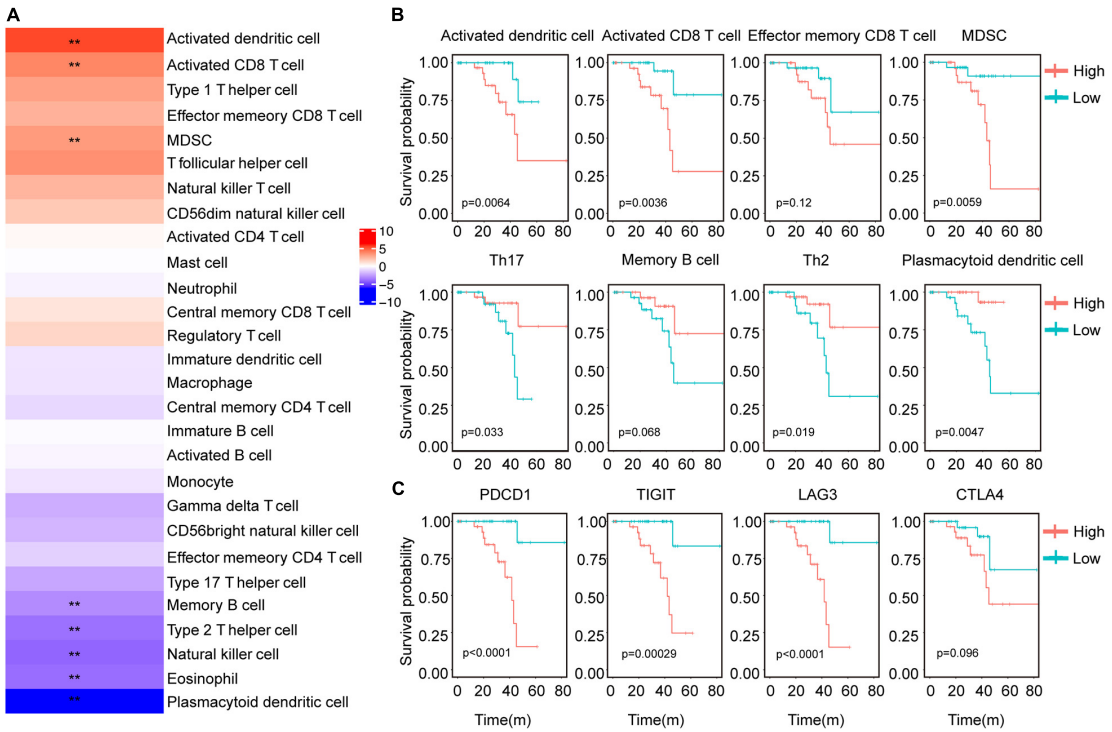

FIGURE 2 | Correlation between immune characteristics and clinical outcomes of UVM. **(A)** Heatmap showed the risk ratio of the immune cell characteristic score in the immune subtypes. **(B)** Kaplan–Meier analysis of the correlation between the scores of activated CD8 T cells, Th1 cells, Th2 cells, Th17 cells, NK cells, activated B cells, and OS. **(C)** Kaplan–Meier analysis of the correlation between gene expression of *LAG3*, *PDCD1*, *TIGIT*, and OS. The expression above the median is high and below the median is low. $^{**}P < 0.05$.

related to Cox was established via GLMNET (**Figure 3B**). The model obtained nine immune gene signals (**Figure 3C**), and we used this model to calculate the score of UVM patients. Compared to class1, class2 had a higher risk score (**Figure 3D**). In addition, we found that the risk score of UVM in the stage IV was higher than stage II (**Figure 3D**). Kaplan–Meier analysis showed that patients with high-risk risk scores had worse survival (**Figure 3E**). Similar result was obtained using GEO database data GSE84976 and GSE22138 (**Figure 3F** and **Supplementary Figure 4A**). However, in order to verify the adaptability of this prediction model, we verified three TCGA databases, Brain Lower Grade Glioma (TCGA-LGG), Skin Cutaneous Melanoma (TCGA-SKCM), and Liver Hepatocellular Carcinoma (TCGA-LIHC). This model can't effectively predict tumor models other than UVM (**Supplementary Figures 4B–D**). The area under the curve (AUC) validated that the immune risk model had a better predictive effect (AUC = 0.89) than age and sex predictions (**Figure 3G**). These results suggest that the immune gene prediction model has a good predictive effect in prognostic prediction.

PTGS2 Is a Potential Target for the Uveal Melanoma Therapy

In order to screen precision therapy targets for the treatment of uveal melanoma, we screened genes in the prediction model for verification. The previous risk prediction model showed that *PTGS2* (Cyclooxygenase-2, COX2) had the highest coefficient. Meanwhile, in UVM patients, high expression of *PTGS2* had a worse prognosis (**Figure 4A**). Therefore, *PTGS2* may be an effective therapeutic target. In order to explore the role of *PTGS2* in tumor cells, we used celecoxib, a selective inhibitor of *PTGS2*, to detect cell viability in OCM1 cells. Celecoxib effectively inhibited cell proliferation and cell viability in a dose-dependent way (**Figures 4B,C**). Colony formation experiment also showed celecoxib decreased cell growth (**Figure 4D**). Next, we examined the effect of celecoxib on cell apoptosis. As shown in **Figure 4E**, celecoxib treatment promoted late apoptosis dose-dependently. Taken together, these data indicate that *PTGS2* may be a potential therapeutic target for uveal melanoma treatment.

DISCUSSION

Clinical practice studies have shown that the effect of immunotherapy in the treatment of UVM is limited. A better understanding of the immune microenvironment of uveal tumors can help to improve the effectiveness of immunotherapy. Here we introduced the immunological features of UVM. Our results indicate that UVM can be divided into two immune subtypes (class1 and class2). Each immune subtype has unique immune cells and immune functions. Moreover, the clinical characteristics of these two immune subtypes

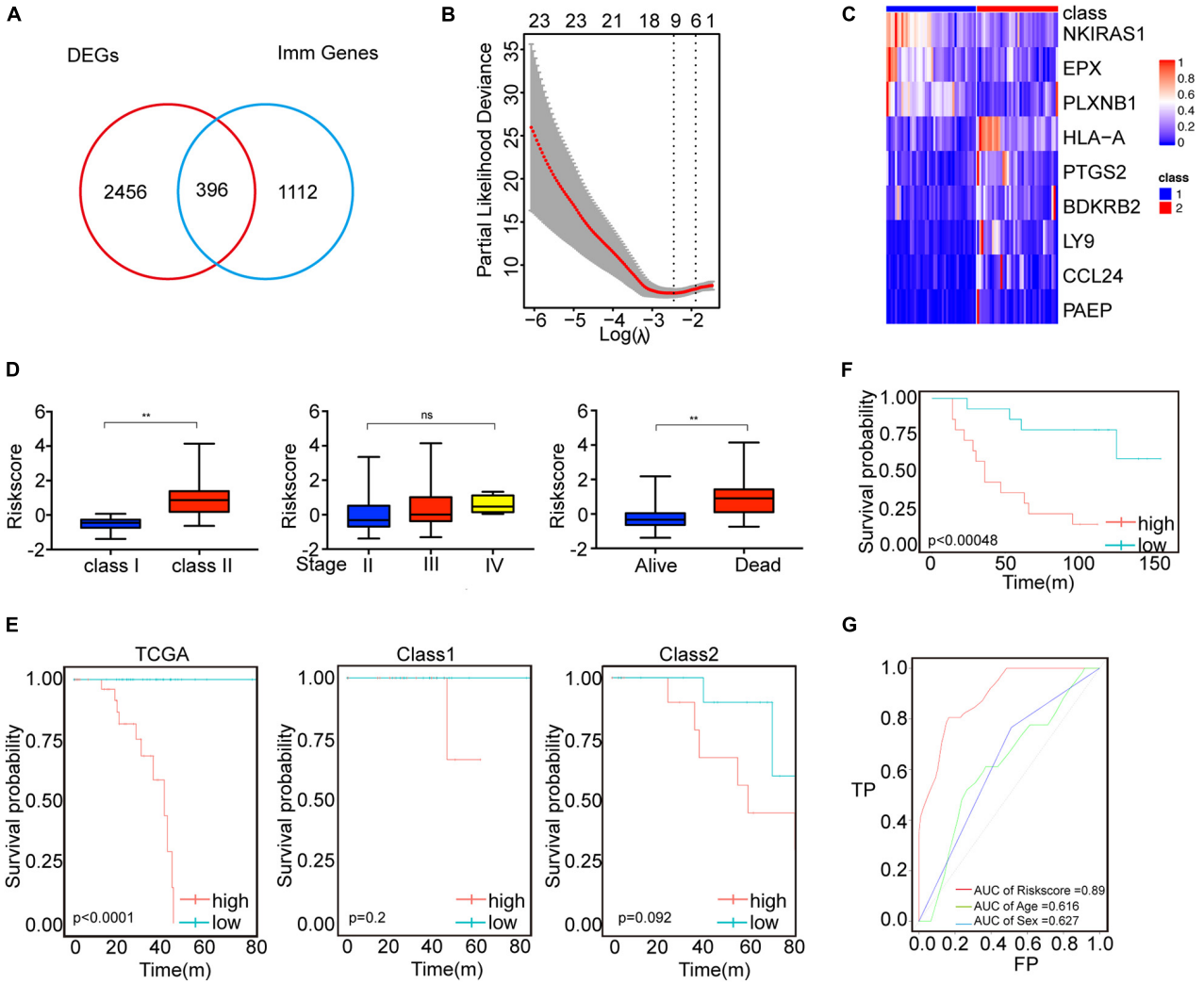

FIGURE 3 | Immune characteristics were identified by Cox proportional hazard model. **(A)** Venn diagram showed immune-related genes which are differentially expressed between the two immune subtypes. **(B)** Cross-validation for parameter selection in adjusted proportional hazard models. **(C)** Heatmap showed the expression level of characteristic genes. **(D)** Distribution of risk scores for immune subtypes, tumor stage, patient status. $^{**}P < 0.05$. **(E)** Survival analysis of risk scores in UVM immune subtypes. **(F)** Survival analysis of the risk score of GSE84976. **(G)** ROC curve analysis of age, sex, and immune score.

are significantly different. We used the risk model to predict the survival of patients, and screened *PTGS2* gene as a therapeutic target for UVM.

Class1 had a good prognosis, with higher Eosinophils, NK cells, Th17 cells, and Plasmacytoid dendritic cells infiltration. In some studies, these cells are beneficial to tumor infiltrating lymphocytes for killing tumor. The increase in Th17 cells significantly improves patient survival (Asadzadeh et al., 2017; Qian et al., 2017). Eosinophils promote immune response and there are more NK cells in the tumor, which can kill the tumor better (Malmberg et al., 2017; Moreira and Heinzerling, 2017; Cozar et al., 2020). Class2 had a worse outcome, with higher lymphocytes, MDSCs infiltration, immune checkpoint genes expression. These results indicate that class2 has a tumor microenvironment with high immune infiltration and high immunosuppression (Kumar et al., 2016; Sun et al., 2018). Therefore, for the patients in this subgroup of class 2, we can use immune checkpoint therapy to effectively improve the prognosis (Callahan et al., 2016). Moreover, the existing immunotherapy has no effect on some patients, which may be because these patients belong to class1. However, the gene expression profile data for immunotherapy needs to be further verified.

Considering the inability of single factor to predict prognosis, we used an elastic-net regression Cox model to screen out significant immune genes and constructed a prognostic prediction model. Among the differential genes of immune subtypes, there were 306 immune-related genes that were related to survival. Nine genes were screened out from 306 genes and used to construct a prediction model. In TCGA's UVM data, low risk-score and high risk-score show significant survival differences, and high risk-score patients have worse outcomes. This model has good predictive accuracy. At the same time, the

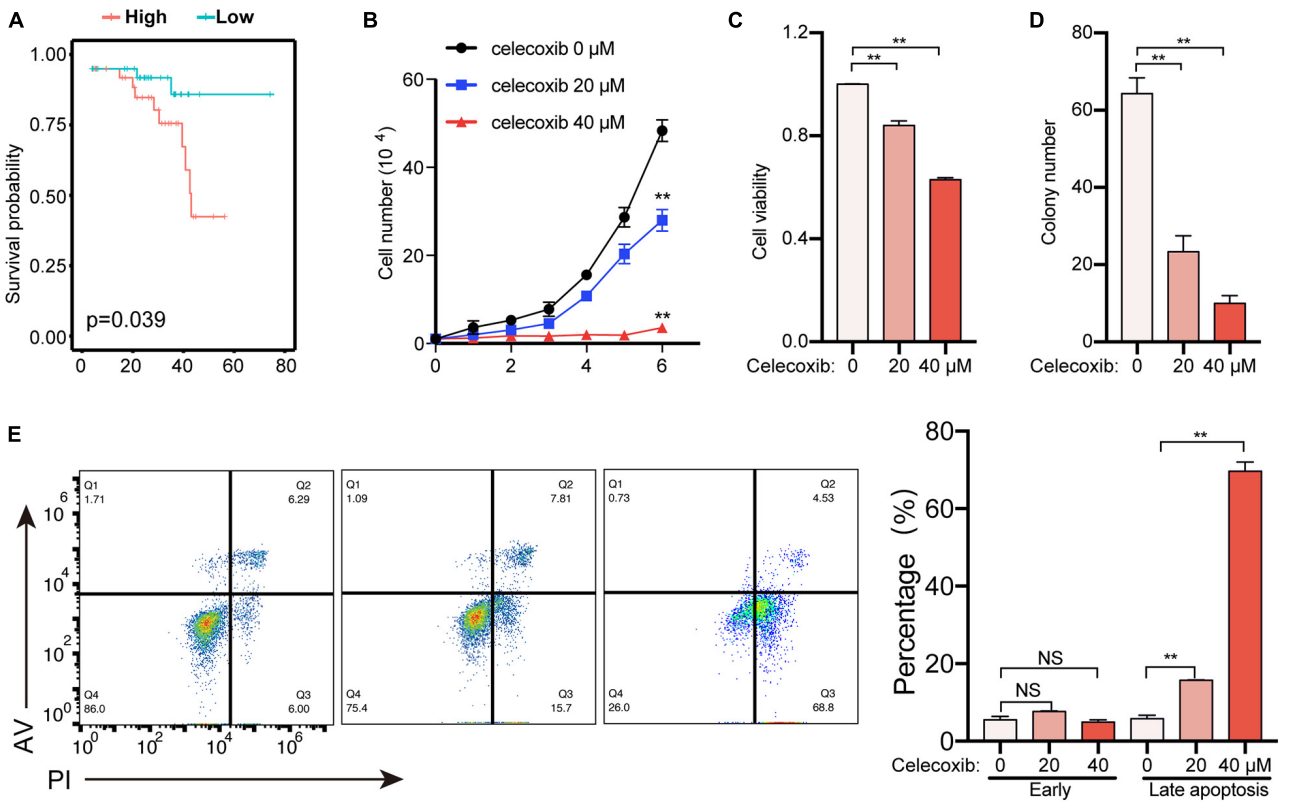

FIGURE 4 | PTGS2 is a potential therapeutic target to treat uveal melanoma. **(A)** Survival analysis of *PTGS2* expression in UVM. The *PTGS2* expression above the median is defined as high and below the median is defined as low. **(B)** OCM1 cells growth curve was detected for 6 days after celecoxib treatment. **(C)** OCM1 cells viability was detected using CCK8 after celecoxib treatment for 1 day. **(D)** OCM1 cells clone formation was detected. The number of cell clones was more than 2 mm in diameter. **(E)** OCM1 cells apoptosis was detected after celecoxib treatment for 3 days. $^{**}P < 0.05$.

applicability of the model was not only verified using GEO data, but also confirmed with TCGA data. Of course, this risk model needs more data and experiments to verify.

In order to screen therapeutic targets, we selected the key gene *PTGS2* from Cox model. *PTGS2* is expressed in many tumors and plays a role in tumorigenesis, tumor metastasis, and tumor treatment resistance (Ching et al., 2020). *PTGS2* plays a major role in promoting the proliferation, invasion, metastasis and anti-apoptosis of cancer cells through its metabolite prostaglandin E2. The PTGS2-PGE2-EP signaling pathway inhibits NK cells and T cells, and promotes tumor immune escape (Liu et al., 2015). In pancreatic cancer, knocking out PTGS2 or using its inhibitors can help the tumor to be sensitive to immunotherapy (Markosyan et al., 2019). *In vitro*, celecoxib treatment effectively inhibited OCM1 cells proliferation, cell viability, and promoted cell apoptosis. Whether Celecoxib treatment of OCM1 cells affects tumor immunotherapy remains to be verified. Celecoxib has been used for more than 20 years, mainly for the treatment of rheumatoid arthritis and other inflammatory diseases (Toloczko-Iwaniuk et al., 2019). In recent years, there are more and more researches on celecoxib for cancer treatment, such as breast cancer, colorectal cancer, and pancreatic cancer (Zuo et al., 2018; Toloczko-Iwaniuk et al., 2019). Although the clinical efficacy of celecoxib in the treatment of uveal melanoma needs further to be investigated, our data suggest celecoxib may be effective for treating uveal melanoma.

CONCLUSION

In our study, UVM can be divided into two immune subtypes. The identification of immune subtypes in UVM establishes a risk prediction model, which effectively predicts the prognosis of patients. Moreover, celecoxib treatment can effectively inhibit the proliferation of OCM1 cells and promote cell apoptosis. Thus, *PTGS2* is a potential target of precision therapy for UVM. Our work is conducive to the understanding of the tumor immune microenvironment of UVM, and also provides valuable information for patients' personalized immunotherapy.

DATA AVAILABILITY STATEMENT

All data supporting this study were openly available from TCGA database (http://cancergemome.nih.gov/) and GEO database (https://www.ncbi.nlm.nih.gov). The accession number(s) can be found in the article/**Supplementary Material**.

AUTHOR CONTRIBUTIONS

WD, LL, and ZZ conceived and designed the study. ZZ analyzed the data. LL, ZZ, and JS participated in the writing and revision of article. All authors contributed to the article and approved the submitted version.

FUNDING

This work was supported by the CAMS Innovation Fund for Medical Sciences (2016-I2M-4-002 to WD) and the National Natural Science Foundation of China (81672766 to WD).

ACKNOWLEDGMENTS

We would like to thank the participants for their important support for this study.

SUPPLEMENTARY MATERIAL

The Supplementary Material for this article can be found online at: https://www.frontiersin.org/articles/10.3389/fcell.2021.666462/full#supplementary-material

Supplementary Figure 1 | Consensus clustering based on immune gene expression of 80 UVM in TCGA. **(A)** Flow chart of the study. **(B)** Clustering matrix for $K = 2$. **(C)** CDF curve for $k = 2$ to $k = 6$. **(D)** Delta area for $k = 2$ to $k = 6$. **(E)** GO analysis of genes upregulated in class2.

Supplementary Figure 2 | (A) Heatmap of immune function score. **(B)** Heatmap of immune checkpoint related genes expression. $^{**}P < 0.05$.

Supplementary Figure 3 | (A) Heatmap of the correlation between immune cells and immune checkpoints. **(B)** Heatmap of the correlation between immune cells.

Supplementary Figure 4 | (A) Survival analysis of the risk score of GSE22138. **(B)** Survival analysis of the risk score of TCGA-LGG. **(C)** Survival analysis of the risk score of TCGA-SKCM. **(D)** Survival analysis of the risk score of TCGA-LIHC.

REFERENCES

Asadzadeh, Z., Mohammadi, H., Safarzadeh, E., Hemmatzadeh, M., Mahdian-Shakib, A., Jadidi-Niaragh, F., et al. (2017). The paradox of Th17 cell functions in tumor immunity. *Cell Immunol.* 322, 15–25. doi: 10.1016/j.cellimm.2017.10.015

Callahan, M. K., Postow, M. A., and Wolchok, J. D. (2016). Targeting T cell co-receptors for cancer therapy. *Immunity* 44, 1069–1078. doi: 10.1016/j.immuni.2016.04.023

Castellanos, E. H., and Horn, L. (2016). Immunotherapy in lung cancer. *Cancer Treat. Res.* 170, 203–223. doi: 10.1007/978-3-319-40389-2_10

Chandran, S. S., Somerville, R. P. T., Yang, J. C., Sherry, R. M., Klebanoff, C. A., Goff, S. L., et al. (2017). Treatment of metastatic uveal melanoma with adoptive transfer of tumour-infiltrating lymphocytes: a single-centre, two-stage, single-arm, phase 2 study. *Lancet Oncol.* 18, 792–802. doi: 10.1016/S1470-2045(17)30251-6

Chattopadhyay, C., Kim, D. W., Gombos, D. S., Oba, J., Qin, Y., Williams, M. D., et al. (2016). Uveal melanoma: from diagnosis to treatment and the science in between. *Cancer* 122, 2299–2312. doi: 10.1002/cncr.29727

Ching, M. M., Reader, J., and Fulton, A. M. (2020). Eicosanoids in cancer: prostaglandin E2 receptor 4 in cancer therapeutics and immunotherapy. *Front. Pharmacol.* 11:819. doi: 10.3389/fphar.2020.00819

Cozar, B., Greppi, M., Carpentier, S., Narni-Mancinelli, E., Chiossone, L., and Vivier, E. (2020). Tumor-Infiltrating natural killer cells. *Cancer Discov.* 11, 34–44. doi: 10.1158/2159-8290.CD-20-0655

Garrido, F., and Aptsiauri, N. (2019). Cancer immune escape: MHC expression in primary tumours versus metastases. *Immunology* 158, 255–266. doi: 10.1111/imm.13114

Hanzelmann, S., Castelo, R., and Guinney, J. (2013). GSVA: gene set variation analysis for microarray and RNA-Seq data. *BMC Bioinformatics* 14:7. doi: 10.1186/1471-2105-14-7

Heppt, M. V., Heinzerling, L., Kahler, K. C., Forschner, A., Kirchberger, M. C., Loquai, C., et al. (2017). Prognostic factors and outcomes in metastatic uveal melanoma treated with programmed cell death-1 or combined PD-1/cytotoxic T-lymphocyte antigen-4 inhibition. *Eur. J. Cancer* 82, 56–65. doi: 10.1016/j.ejca.2017.05.038

Jansen, Y. J. L., Seremet, T., and Neyns, B. (2020). Pembrolizumab for the treatment of uveal melanoma: a case series. *Rare Tumors* 12:2036361320971983. doi: 10.1177/2036361320971983

Ji, R. R., Chasalow, S. D., Wang, L. S., Hamid, O., Schmidt, H., Cogswell, J., et al. (2012). An immune-active tumor microenvironment favors clinical response to ipilimumab. *Cancer Immunol. Immunother.* 61, 1019–1031. doi: 10.1007/s00262-011-1172-6

Johnson, D. B., Sullivan, R. J., and Menzies, A. M. (2017). Immune checkpoint inhibitors in challenging populations. *Cancer* 123, 1904–1911. doi: 10.1002/cncr.30642

Kaliki, S., and Shields, C. L. (2017). Uveal melanoma: relatively rare but deadly cancer. *Eye (Lond)* 31, 241–257. doi: 10.1038/eye.2016.275

Karivedu, V., Eldessouki, I., Taftaf, A., Zhu, Z., Makramalla, A., and Karim, N. A. (2019). Nivolumab and ipilimumab in the treatment of metastatic uveal melanoma: a single-center experience. *Case Rep. Oncol. Med.* 2019:3560640. doi: 10.1155/2019/3560640

Kumar, V., Patel, S., Tcyganov, E., and Gabrilovich, D. I. (2016). The nature of myeloid-derived suppressor cells in the tumor microenvironment. *Trends Immunol.* 37, 208–220. doi: 10.1016/j.it.2016.01.004

Laurent, C., Valet, F., Planque, N., Silveri, L., Maacha, S., Anezo, O., et al. (2011). High PTP4A3 phosphatase expression correlates with metastatic risk in uveal melanoma patients. *Cancer Res.* 71, 666–674. doi: 10.1158/0008-5472.CAN-10-0605

Li, L., Cai, S., Liu, S., Feng, H., and Zhang, J. (2017). Bioinformatics analysis to screen the key prognostic genes in ovarian cancer. *J. Ovarian Res.* 10:27. doi: 10.1186/s13048-017-0323-6

Liu, B., Qu, L., and Yan, S. (2015). Cyclooxygenase-2 promotes tumor growth and suppresses tumor immunity. *Cancer Cell Int.* 15:106. doi: 10.1186/s12935-015-0260-7

Malmberg, K. J., Carlsten, M., Bjorklund, A., Sohlberg, E., Bryceson, Y. T., and Ljunggren, H. G. (2017). Natural killer cell-mediated immunosurveillance of human cancer. *Semin. Immunol.* 31, 20–29. doi: 10.1016/j.smim.2017.08.002

Markosyan, N., Li, J., Sun, Y. H., Richman, L. P., Lin, J. H., Yan, F., et al. (2019). Tumor cell-intrinsic EPHA2 suppresses anti-tumor immunity by regulating PTGS2 (COX-2). *J. Clin. Invest.* 129, 3594–3609. doi: 10.1172/JCI127755

Moreira, A., and Heinzerling, L. (2017). Eosinophilic count as a biomarker for prognosis of melanoma patients. *J. Dtsch. Dermatol. Ges.* 15, 14–15.

Parry, R. V., Chemnitz, J. M., Frauwirth, K. A., Lanfranco, A. R., Braunstein, I., Kobayashi, S. V., et al. (2005). CTLA-4 and PD-1 receptors inhibit T-cell activation by distinct mechanisms. *Mol. Cell. Biol.* 25, 9543–9553. doi: 10.1128/MCB.25.21.9543-9553.2005

Pelster, M. S., Gruschkus, S. K., Bassett, R., Gombos, D. S., Shephard, M., Posada, L., et al. (2020). Nivolumab and ipilimumab in metastatic uveal melanoma: results from a single-arm phase II study. *J. Clin. Oncol.* 39, 599–607. doi: 10.1200/JCO.20.00605

Qian, X., Chen, H. K., Wu, X. F., Hu, L., Huang, Q., and Jin, Y. (2017). Interleukin-17 acts as double-edged sword in anti-tumor immunity and tumorigenesis. *Cytokine* 89, 34–44. doi: 10.1016/j.cyto.2015.09.011

Ritchie, M. E., Phipson, B., Wu, D., Hu, Y., Law, C. W., Shi, W., et al. (2015). limma powers differential expression analyses for RNA-sequencing and microarray studies. *Nucleic Acids Res.* 43:e47. doi: 10.1093/nar/gkv007

Schank, T. E., and Hassel, J. C. (2019). Immunotherapies for the treatment of uveal melanoma-history and future. *Cancers* 11:1048. doi: 10.3390/cancers11081048

Snyder, A., Makarov, V., Merghoub, T., Yuan, J., Zaretsky, J. M., Desrichard, A., et al. (2014). Genetic basis for clinical response to CTLA-4 blockade in melanoma. *N. Engl. J. Med.* 371, 2189–2199. doi: 10.1056/NEJMoa1406498

Sugie, T. (2018). Immunotherapy for metastatic breast cancer. *Chin. Clin. Oncol.* 7:28. doi: 10.21037/cco.2018.05.05

Sun, C., Mezzadra, R., and Schumacher, T. N. (2018). Regulation and function of the PD-L1 checkpoint. *Immunity* 48, 434–452. doi: 10.1016/j.immuni.2018.03.014

Taggart, D., Andreou, T., Scott, K. J., Williams, J., Rippaus, N., Brownlie, R. J., et al. (2018). Anti-PD-1/anti-CTLA-4 efficacy in melanoma brain metastases depends on extracranial disease and augmentation of CD8(+) T cell trafficking. *Proc. Natl. Acad. Sci. U.S.A.* 115, E1540–E1549. doi: 10.1073/pnas.1714089115

Toloczko-Iwaniuk, N., Dziemianczyk-Pakiela, D., Nowaszewska, B. K., Celinska-Janowicz, K., and Miltyk, W. (2019). Celecoxib in cancer therapy and prevention - review. *Curr. Drug Targets* 20, 302–315. doi: 10.2174/1389450119666180803121737

van Essen, T. H., van Pelt, S. I., Bronkhorst, I. H., Versluis, M., Nemati, F., Laurent, C., et al. (2016). Upregulation of HLA expression in primary uveal melanoma by infiltrating leukocytes. *PLoS One* 11:e0164292. doi: 10.1371/journal.pone.0164292

Wilkerson, M. D., and Hayes, D. N. (2010). ConsensusClusterPlus: a class discovery tool with confidence assessments and item tracking. *Bioinformatics* 26, 1572–1573. doi: 10.1093/bioinformatics/btq170

Willson, J. K. V., Albert, D. M., Diener-West, M., McCaffrey, L., Moy, C. S., Scully, R. E., et al. (2001). Assessment of metastatic disease status at death in 435 patients with large choroidal melanoma in the Collaborative Ocular Melanoma Study (COMS). *Arch. Ophthalmol.* 119, 670–676.

Yang, Y. (2015). Cancer immunotherapy: harnessing the immune system to battle cancer. *J. Clin. Invest.* 125, 3335–3337. doi: 10.1172/JCI83871

Yoshihara, K., Shahmoradgoli, M., Martinez, E., Vegesna, R., Kim, H., Torres-Garcia, W., et al. (2013). Inferring tumour purity and stromal and immune cell admixture from expression data. *Nat. Commun.* 4:2612. doi: 10.1038/ncomms3612

Yu, G. C., Wang, L. G., Han, Y. Y., and He, Q. Y. (2012). clusterProfiler: an R package for comparing biological themes among gene clusters. *OMICS* 16, 284–287. doi: 10.1089/omi.2011.0118

Zuo, C., Hong, Y., Qiu, X., Yang, D., Liu, N., Sheng, X., et al. (2018). Celecoxib suppresses proliferation and metastasis of pancreatic cancer cells by down-regulating STAT3 / NF-kB and L1CAM activities. *Pancreatology* 18, 328–333. doi: 10.1016/j.pan.2018.02.006

Conflict of Interest: The authors declare that the research was conducted in the absence of any commercial or financial relationships that could be construed as a potential conflict of interest.

frontiers in Cell and Developmental Biology

BRIEF RESEARCH REPORT
published: 11 March 2021
doi: 10.3389/fcell.2021.655889

MYC Enhances Cholesterol Biosynthesis and Supports Cell Proliferation Through SQLE

*Fan Yang†, Junjie Kou†, Zizhao Liu, Wei Li and Wenjing Du**

State Key Laboratory of Medical Molecular Biology, Department of Cell Biology, Institute of Basic Medical Sciences Chinese Academy of Medical Sciences, School of Basic Medicine Peking Union Medical College, Beijing, China

Oncogene c-*Myc* (referred in this report as *MYC*) promotes tumorigenesis in multiple human cancers. MYC regulates numerous cellular programs involved in cell growth and cell metabolism. Tumor cells exhibit obligatory dependence on cholesterol metabolism, which provides essential membrane components and metabolites to support cell growth. To date, how cholesterol biosynthesis is delicately regulated to promote tumorigenesis remains unclear. Here, we show that MYC enhances cholesterol biosynthesis and promotes cell proliferation. Through transcriptional upregulation of SQLE, a rate-limiting enzyme in cholesterol synthesis pathway, MYC increases cholesterol production and promotes tumor cell growth. SQLE overexpression restores the cellular cholesterol levels in *MYC*-knockdown cells. More importantly, in *SQLE*-depleted cells, enforced expression of MYC has no effect on cholesterol levels. Therefore, our findings reveal that SQLE is critical for MYC-mediated cholesterol synthesis, and further demonstrate that SQLE may be a potential therapeutic target in MYC-amplified cancers.

Keywords: cholesterol synthesis, cell proliferation, cancer, SQLE, MYC

OPEN ACCESS

Edited by:
Binghui Li,
Capital Medical University, China

Reviewed by:
Changliang Shan,
Nankai University, China
Yide Mei,
University of Science and Technology of China, China

***Correspondence:**
Wenjing Du
wenjingdu@ibms.pumc.edu.cn;
wjdu123@hotmail.com

† These authors have contributed equally to this work

Specialty section:
This article was submitted to Molecular Medicine, a section of the journal Frontiers in Cell and Developmental Biology

Received: *19 January 2021*
Accepted: *19 February 2021*
Published: *11 March 2021*

Citation:
Yang F, Kou J, Liu Z, Li W and Du W (2021) MYC Enhances Cholesterol Biosynthesis and Supports Cell Proliferation Through SQLE. Front. Cell Dev. Biol. 9:655889. doi: 10.3389/fcell.2021.655889

INTRODUCTION

MYC is one of the most broadly deregulated oncogenes in human cancers (Dang, 2012). It is frequently translocated in multiple myelomas and is commonly found amplified among different human cancers (Shou et al., 2000; Zack et al., 2013; Annibali et al., 2014). MYC protein mediates its effects mainly through inappropriate regulation of transcriptional programs involved in a variety of biological processes, contributing to almost every aspect of tumorigenesis (Meyer and Penn, 2008). Indeed, *MYC* deletion inhibits cell growth such as T-cell leukemia (Sharma et al., 2006) and gastric cancer (Dong et al., 2019). MYC as a general transcription factor binds around 10–15% of all promoter regions (Li et al., 2003). Tumor cells require rapid biomass accumulation and high-fidelity DNA replication to sustain uncontrolled proliferation. MYC has been shown to activate metabolic genes involved in glucose and glutamine metabolism, as well as lipid and nucleotide biosynthesis, contributing to metabolic reprogramming (Ahuja et al., 2010; Morrish et al., 2010; Dang, 2013).

Cholesterol is vital for the survival and growth of tumor cells. It is produced via cholesterol biosynthesis pathway which involves two rate-limiting enzymes, 3-hydroxy-3-methylglutarylcoenzyme A reductase (HMGCR) and squalene monooxygenase (SQLE) (Luo et al., 2020). Cholesterol is an essential component of cell membrane to maintain its fluidity and impact intracellular signal transduction. In addition, cholesterol also serves as a precursor for steroid

hormone, bile acids, and specific vitamins (Riscal et al., 2019). Due to its importance, intracellular cholesterol homeostasis is delicately controlled. Indeed, imbalanced cholesterol levels have strong associations with the risk of cardiovascular diseases (Luo et al., 2019; Wong et al., 2019). Cancer cells require high levels of cholesterol for membrane biogenesis and other functional needs (Huang et al., 2020). Based on TCGA database, increased activity of the cholesterol synthesis pathway is correlated with poor patient survival in sarcoma, acute myeloid leukemia, and melanoma (Kuzu et al., 2016). Besides, at least one gene expression in the cholesterol synthesis was increased among approximately 60% melanomas (Kuzu et al., 2016). Conversely, inhibition of cholesterol metabolism hinders tumor growth and invasion in a variety of cancers (Li et al., 2017; Costa et al., 2018).

SQLE is recognized as one of the rate-limiting enzymes in cholesterol biosynthesis pathway, which catalyzes squalene oxidization (Gill et al., 2011). It is reported that SQLE promotes tumor development (Cirmena et al., 2018; Liu et al., 2018; Xu et al., 2020). Several drugs against SQLE have been evaluated in anti-tumor trials (Cirmena et al., 2018; Liu et al., 2018). Recent study has reported that SQLE can be regulated at transcriptional, translational, and post-translational levels (Chua et al., 2020). Here we report that MYC binds to and activates SQLE promoter. Through transcriptional upregulation of SQLE, MYC increases cellular cholesterol levels and promotes cell proliferation. We also provide evidence that SQLE is critical for MYC-regulated cholesterol biosynthesis. Thus, our findings suggest that SQLE may be a potential therapeutic target in MYC-driven cancers.

MATERIALS AND METHODS

Antibodies

Antibodies against β-Actin (#66009-1, dilution: 1/3000) and antibodies against SQLE (#12544-1-AP, dilution: 1/500) were purchased from Proteintech (United States). Antibodies against MYC (#ab32072, dilution: 1/1000) were purchased from Abcam (United States, dilution: 1/500).

Cell Culture and Transfection

Human osteosarcoma cell line U2OS, human hepatocellular carcinoma cell line HepG2, human lung cancer cell line H1299, human colorectal cancer cell line SW480, human clear cell carcinoma cell line Caki-1, and human renal epithelial cell line HEK293T were obtained from the American Type Culture Collection (ATCC, United States). U2OS, HepG2, SW480, Caki-1, and HEK293T cell lines were maintained in Dulbecco's modified Eagle's medium (DMEM), and H1299 cell line was cultured in RPMI 1640 medium. All mediums were supplemented with 10% fetal bovine serum (FBS) plus 1% penicillin and streptomycin (P/S). All cells were cultured at 37°C in a humidified incubator with 5%CO_2. All the growth mediums, FBS, and supplemental reagents were obtained from CELL technologies (United States).

The following siRNAs were purchased from GenPharma (China). siRNA sequences are listed below:

Control siRNA: 5′-UUCUCCGAACGUGUCACGUTT-3′;

hMYC siRNA#1: 5′-GCUCAUUUCUGAAGAGGACTT-3′;

hMYC siRNA#2: 5′-GGCGAACACACAACGUCUUTT-3′;

hSQLE siRNA#1: 5′-GCCUCUAAAUCUUUAGGUUTT-3′;

hSQLE siRNA#2: 5′-GCCCAGGUUGUAAAUGGUUTT-3′.

siRNAs were transfected into cells using Lipofectamine RNAiMAX transfection reagent (Invitrogen, United States) following the manufacturer's instruction.

Plasmids and Lentiviral Transduction

Two overexpression plasmids for MYC and SQLE were generated by cloning the ORF into the pRK5-Flag and pRK5-HA vectors separately. A lentiviral overexpression plasmid for MYC was generated by cloning the ORF into the pLV vector. Lentiviral particles were generated in HEK293T cells with cotransfection of the packaging vectors. Then, virus-containing supernatants were harvested and applied to infect the target cells with 8 μg/ml Polybrene (Santa Cruz Biotechnology, United States). Two days after the infection, the infected cells were cultured in the presence of 2 μg/ml puromycin (Sigma–Aldrich, United States) for 3 days. Finally, puromycin-resistant cells were pooled.

Semi-Quantitative PCR With Reverse Transcription and Quantitative Real-Time PCR

Total RNA was isolated from cells by Trizol reagent (TIANGEN, China), and 1 μg RNA of each sample was reversed to cDNA by the First-Strand cDNA Synthesis System (TIANGEN, China). cDNA (0.025 μg) of each sample was used as a template to perform PCR. The primer pairs for human genes were:

MYC-F: 5′-GGCTCCTGGCAAAAGGTCA-3′

MYC-R: 5′-CTGCGTAGTTGTGCTGATGT-3′;

SQLE-F: 5′-TGACAATTCTCATCTGAGGTCCA-3′

SQLE-R: 5′-CAGGGATACCCTTTAGCAGTTTT-3′;

β-Actin-F: 5′-GACCTGACTGACTACCTCATGAAGAT-3′

β-Actin-R5′-GTCACACTTCATGATGGAGTTGAAGGT-3′.

Chromatin Immunoprecipitation and Reporter Assays

For chromatin immunoprecipitation assays, HEK293T cells were crosslinked with 1% formaldehyde for 15 min at room temperature and crosslinking was stopped by the addition of 125 nM glycine (final concentration). Cell lysates were sonicated for 3 cycles to generate DNA fragments with an average size between 150 and 900 bp, and immunoprecipitated with IgG and MYC antibodies. Bound DNA fragments were eluted and amplified by PCR. Primer pairs were:

RE1-F: 5′-GCTATGCCGCGTTTGGCCAATC-3′ (−1079/−1058)

RE1-R: 5′-CCTGAGCCCCGCCCCCGGTCCC-3′ (−950/−929);

RE2-F: 5′-GGATCACTTAAGGTCAGGAGTT-3′ (+1271/+1292)

RE2-R: 5′-GAATGGAAGCAGGGCTATCAGGC-3′ (+1414/+1436);

β-Actin-F: 5′-GGGTCTGCGCTGTAAGAGTT-3′

β-Actin-R: 5′-GAACTCAGCCAAGGGGACTC-3′.

For reporter assay, the *SQLE* genomic fragments (C6849–C7006) containing either the wild-type RE1 (5′-GGGCAGCACGCGGGGCG-3′) or mutant [(5′-GGGAAGCAAATCTGGGCG-3′), with mutated nucleotides underlined] and the *SQLE* genomic fragments (C9190–C9364) containing the wild-type RE2 (5′-CCACGGCGCCTGGCCTG-3′) binding region were cloned into pGL3-basic vector. Luciferase reporter assays were performed as described. Briefly, the reporter plasmids were transfected into HEK293T cells together with a Renilla luciferase plasmid and a plasmid expressing MYC protein. Twenty-four hours after transfection, the luciferase activity was determined using a Dual Luciferase Assay System (Promega, United States). Transfection efficiency was normalized on the basis of the Renilla luciferase activity.

Cell Viability and Proliferation Assay

For cell viability assays, cells were transfected with siRNAs or plasmids for 48 h and seeded in 96-well cell culture dishes in triplicate at a density of 1000 cells per well. Two days later, CCK8 (Pplygen, China) was added into culture dishes for 3 h. $OD_{450\ nm}$ was measured to test cell viability by using microplate reader Flexstation 3 (Molecular Devices, United States). Relative $OD_{450\ nm}$ was calculated using the corrected sample reading.

Cell proliferation assays were performed as described. Briefly, cells were transfected with siRNAs or plasmids for48 h and seeded in six-well cell culture dishes in triplicate at a density of 40,000 cells per well. The medium was changed every day. Cell number at the indicated time points was counted using a Cell Counter (Countstar, China).

Western Blotting

Whole-cell lysates were made in modified RIPA lysis buffer(10 mM Tris–HCl at pH 7.5, 5 mM EDTA, 150 mM NaCl, 1% NP-40, 1% sodium deoxycholate, 0.025% SDS, and 5 mM protease inhibitors) for 30 min on ice, and boiled in 2× loading buffer. Protein samples were resolved by SDS–PAGE and transferred onto PVDF membrane, which was blocked in 5% BSA and probed with the indicated antibodies.

Statistical Analysis

Statistical significance was analyzed by two-tailed unpaired *t*-test and expressed as a *p*-value.

RESULTS

Myc Enhances Intracellular Cholesterol Levels and Promotes Cell Proliferation

Previous studies have revealed that MYC is required for the upregulation of mevalonate pathway in certain cancer cells (Wang et al., 2017). To further investigate the role of MYC in cholesterol biosynthesis, we knocked down *MYC* in human osteosarcoma U2OS cells and human hepatoma HepG2 cells. *MYC* depletion decreased intracellular cholesterol levels (**Figures 1A,B**). Conversely, MYC overexpression in U2OS and HepG2 cells led to a noticeable increase in cholesterol levels (**Figures 1C,D**). These results indicate that MYC enhances intracellular cholesterol levels. Furthermore, silencing of *MYC* inhibited cell viability and cell proliferation (**Figures 1E,F**), whereas overexpression of MYC promoted cell viability and proliferation in both U2OS and HepG2 cells (**Figures 1G,H**). We next knocked down MYC in U2OS and HepG2 cells and cultured cells in lipid-free medium in the presence or absence of cholesterol (**Figures 1I,J**). Cholesterol addition rescued the decreased cell viability and cell proliferation caused by MYC knockdown. These data indicated that MYC supports tumor cell growth through cholesterol. Taken together, these data indicate that MYC promotes cholesterol synthesis and cell proliferation.

MYC Transcriptionally Upregulates SQLE Expression

To investigate the mechanism by which MYC regulates the cholesterol biosynthesis, we analyzed the mRNA levels of several enzymes involved in cholesterol metabolism. *MYC*-knockdown decreased expression of genes in cholesterol synthesis, while SQLE expression was mostly reduced in *MYC*-depleted cells (**Figures 2A,B**). SQLE is a rate-limiting enzyme in cholesterol biosynthesis. We next examined how MYC regulates SQLE expression. We knocked down expression of MYC using two different sets of siRNAs in both U2OS and HepG2 cells. As shown in **Figures 2C,D,** both protein and mRNA levels of SQLE decreased in *MYC* knocking down cells compared to control cells (**Figures 2C,D**). Similar results were observed in the other three cell lines including H1299, SW480, and Caki-1 cells (**Supplementary Figures S1A–C**). Conversely, enforced expression of MYC promoted SQLE expression in both mRNA and protein levels (**Figures 2E,F** and **Supplementary Figures S1D–F**). These data suggest that MYC upregulates SQLE expression.

Next, to determine whether SQLE is a transcriptional target of MYC, we analyzed the human *SQLE* gene sequence for potential MYC protein response elements in JASPAR database. We identified two putative MYC response elements (RE1 and RE2) (**Figure 2G**). To investigate the binding of MYC to these two response elements, we performed ChIP-quantitative PCR (ChIP-qPCR) experiments. As shown in **Figure 2H**, MYC bound to the genomic region RE1 of *SQLE* gene, but not RE2 (**Figure 2H**). To evaluate whether the response element within *SQLE* confers MYC-dependent transcriptional activation, we cloned DNA fragments containing the wild-type response element (RE1) or a mutant response element (RE1-mut) into luciferase reporter plasmid. MYC was able to induce luciferase expression from the RE1 plasmid, but not from the RE1-mut plasmid (**Figure 2I**). These data suggest that SQLE is a transcriptional target of MYC and MYC activates SQLE expression in a transcriptional manner.

MYC Regulates Cellular Cholesterol Levels Through SQLE

We next determine the role of SQLE in MYC-mediated cholesterol synthesis. Inhibition of SQLE expression using two sets of siRNAs led to a decreased cholesterol level in both U2OS and HepG2 cells (**Figures 3A,B**). Conversely, SQLE

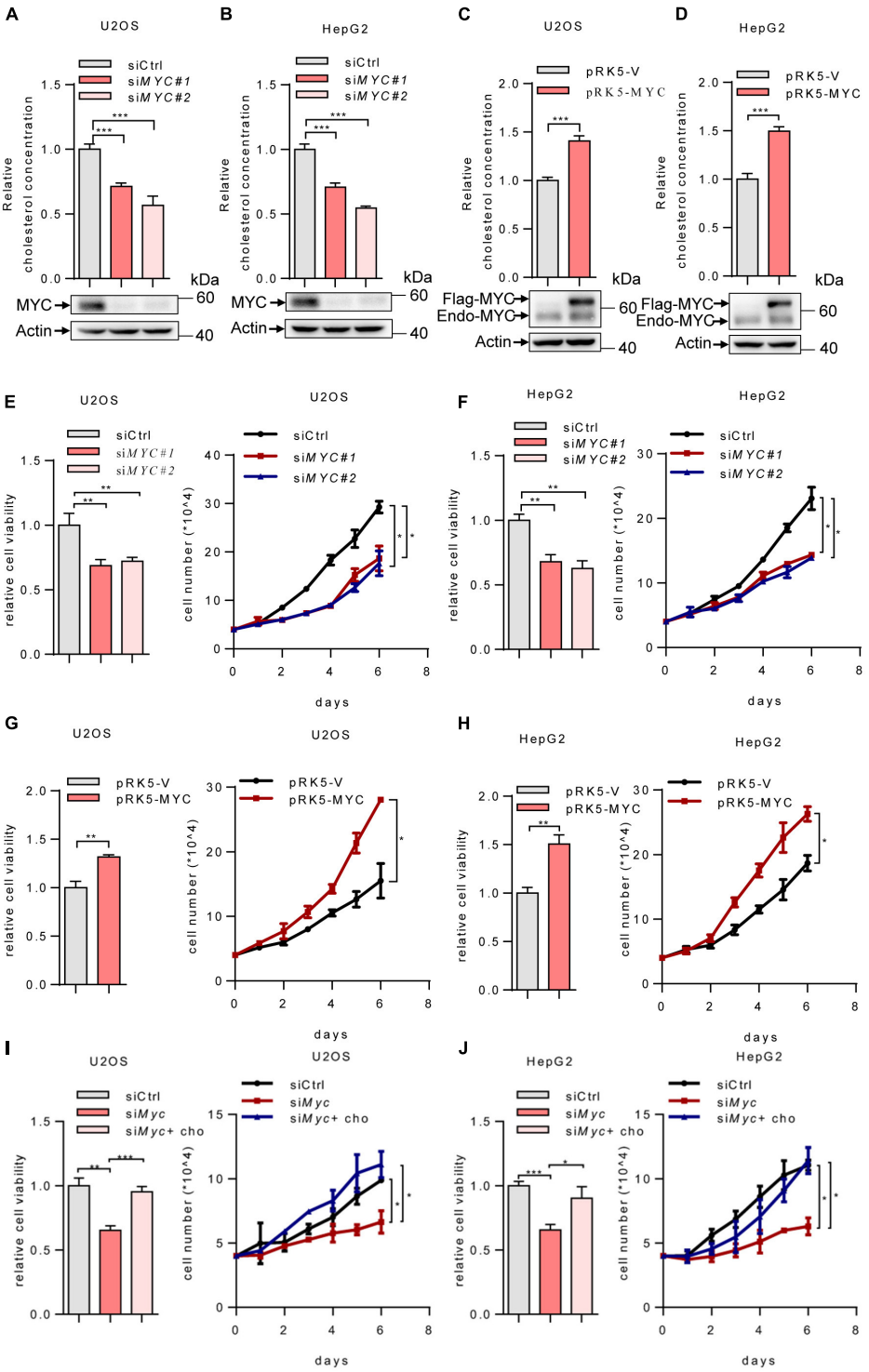

FIGURE 1 | MYC increases intracellular cholesterol levels and promotes cell proliferation. **(A,B)** U2OS and HepG2 cells were transfected with control or two different sets of *MYC* siRNAs. Cells were cultured in the lipoprotein-depleted fetal bovine serum (LPDS) medium. Intracellular cholesterol levels (top) and corresponding protein expression (bottom) were shown. **(C,D)** U2OS cells and HepG2 cells cultured in LPDS medium were transfected with plasmid expressing the MYC protein. Intracellular cholesterol levels (top) and corresponding protein expression (bottom) were shown. **(E,F)** Relative cell viability (left) and cell proliferation (right) in control and *MYC* knockdown U2OS cells and HepG2 cells. Relative cell viability was measured with CCK8. **(G,H)** Relative cell viability (left) and cell proliferation (right) in control and MYC overexpressing U2OS cells and HepG2 cells. Relative cell viability was measured with CCK8. **(I,J)** Relative cell viability (left) and cell proliferation (right) of U2OS and HepG2 *MYC*-knockdown cells cultured in LPDS medium with or without 20 μg/ml cholesterol. Relative cell viability was measured with CCK8. In **(A–H)**, $n = 3$ independent experiments. Data are means ± SD. Statistical significance was determined by two-tailed unpaired *t*-test. $^{*}P < 0.05$, $^{**}P < 0.01$, and $^{***}P < 0.001$.

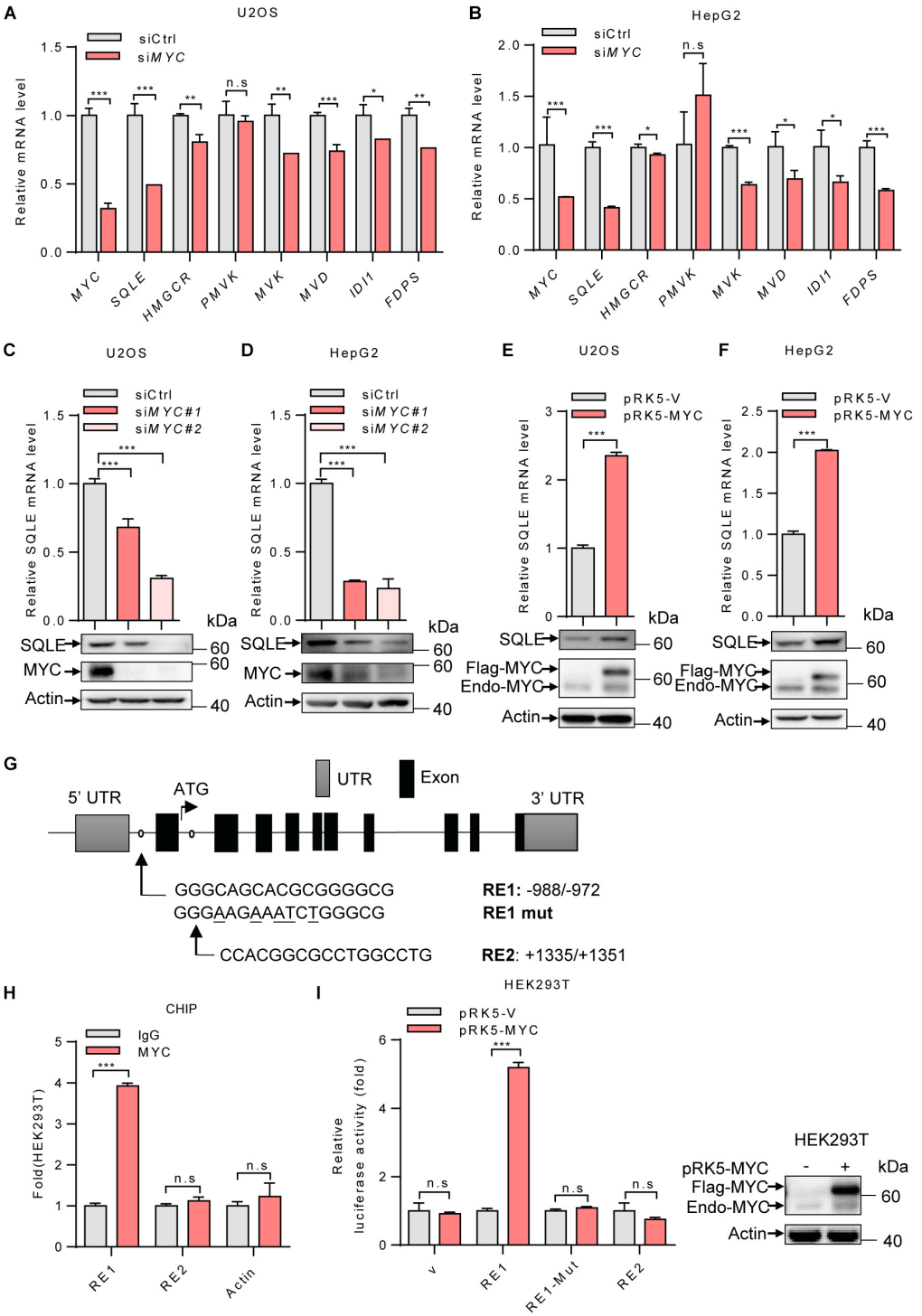

FIGURE 2 | MYC transcriptionally upregulates the expression of SQLE. **(A,B)** U2OS cells and HepG2 cells were transfected with control or *MYC* siRNA. The mRNA levels of seven metabolic enzymes in cholesterol synthesis pathway were detected by qPCR. **(C,D)** SQLE mRNA (top) and protein (bottom) expression in control and *MYC* knockdown U2OS and HepG2 cells. **(E,F)** *SQLE* mRNA (top) and protein (bottom) expression in U2OS and HepG2 cells expressing ectopic MYC or control protein. **(G)** Schematic representation of human SQLE genomic structure. Shown are the putative MYC response elements (RE1/RE2), and the mutant response element (RE1-mut, with mutated nucleotides underlined). Arrows mark the positions of the primers used for qPCR in the ChIP assay. UTR, untranslated region. **(H)** HEK293T cells were analyzed by ChIP assay using an anti-MYC antibody or rabbit IgG control. **(I)** Luciferase assays performed using reporter constructs containing the wild-type or mutant MYC response element were transfected into HEK293T cells, together with or without ectopically expressed MYC. Renilla vector was used as a transfection internal control. Relative levels of luciferase are shown (left). MYC expression in HEK293T cells was detected (right). In **(A–F,H,I)** $n = 3$ independent experiments. Data are means ± SD. Statistical significance was determined by two-tailed unpaired *t*-test. $^{*}P < 0.05$, $^{**}P < 0.01$, and $^{***}P < 0.001$.

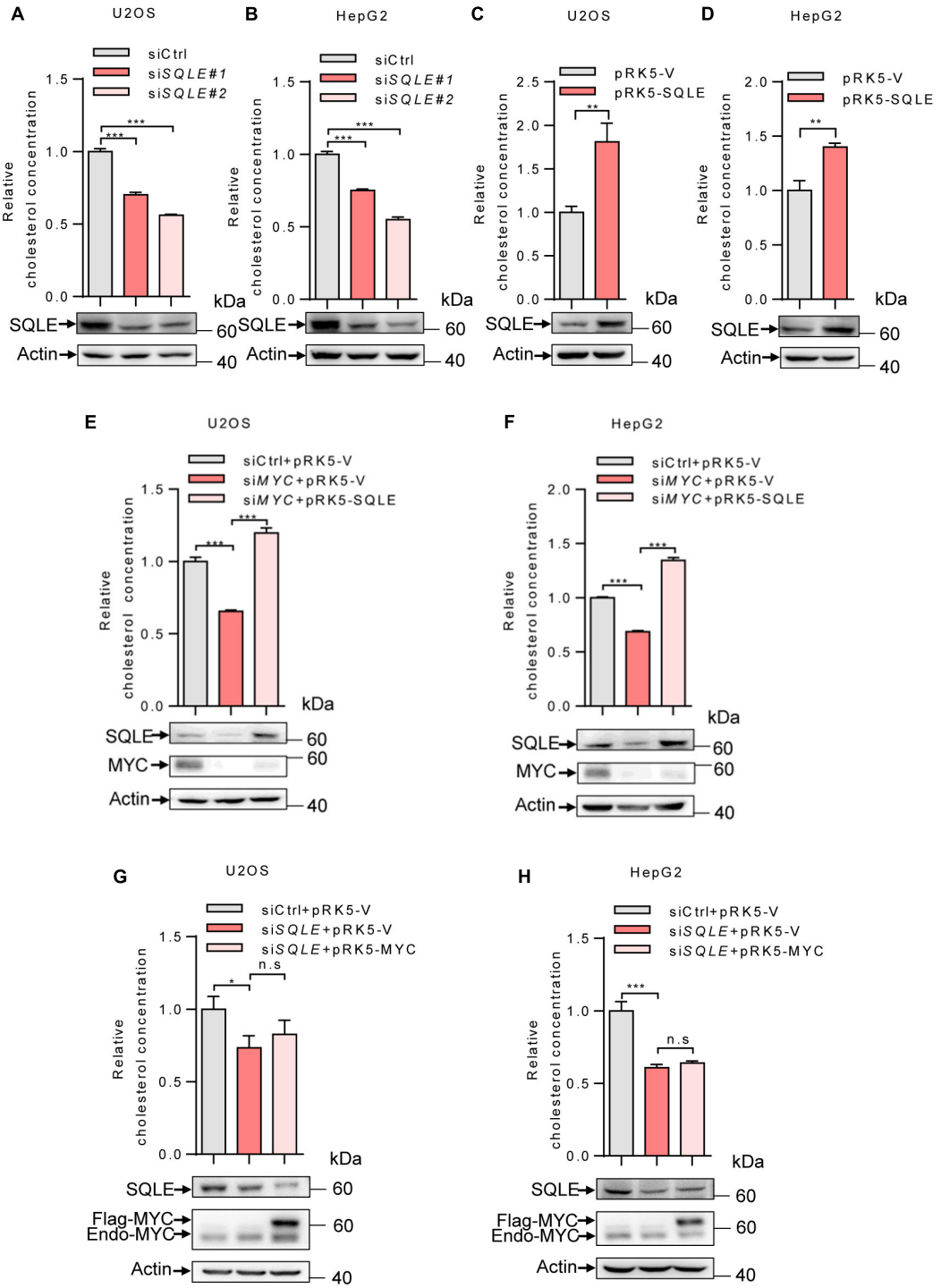

FIGURE 3 | MYC increases intracellular cholesterol levels through SQLE. **(A,B)** U2OS and HepG2 cells were transfected with control or different sets of *SQLE* siRNAs. Cells were cultured in the LPDS medium. Intracellular cholesterol levels (top) and corresponding protein expression (bottom) were detected. **(C,D)** U2OS cells and HepG2 cells cultured in LPDS medium were ectopically expressed the SQLE protein. Intracellular cholesterol levels (top) and corresponding protein expression (bottom) were shown. **(E,F)** Intracellular cholesterol levels (top) and protein expression (bottom) in U2OS and HepG2 cells transfected with control or *MYC* siRNA, with or without Flag-SQLE as indicated. **(G,H)** U2OS cells and HepG2 cells were transfected with control or *SQLE* siRNA, and then enforced expression of MYC into *SQLE* knockdown cells. Intracellular cholesterol levels (top) and protein expression (bottom) were examined, respectively. For cholesterol content detection, cells were cultured in the medium with LPDS. In **(A–H)** 2 μg plasmids and 1 μg siRNAs were used in all experiments. $n = 3$ independent experiments. Data are means ± SD. Western blots represent three independent experiments. Statistical significance was determined by two-tailed unpaired *t*-test. $^{*}P < 0.05$, $^{**}P < 0.01$, and $^{***}P < 0.001$.

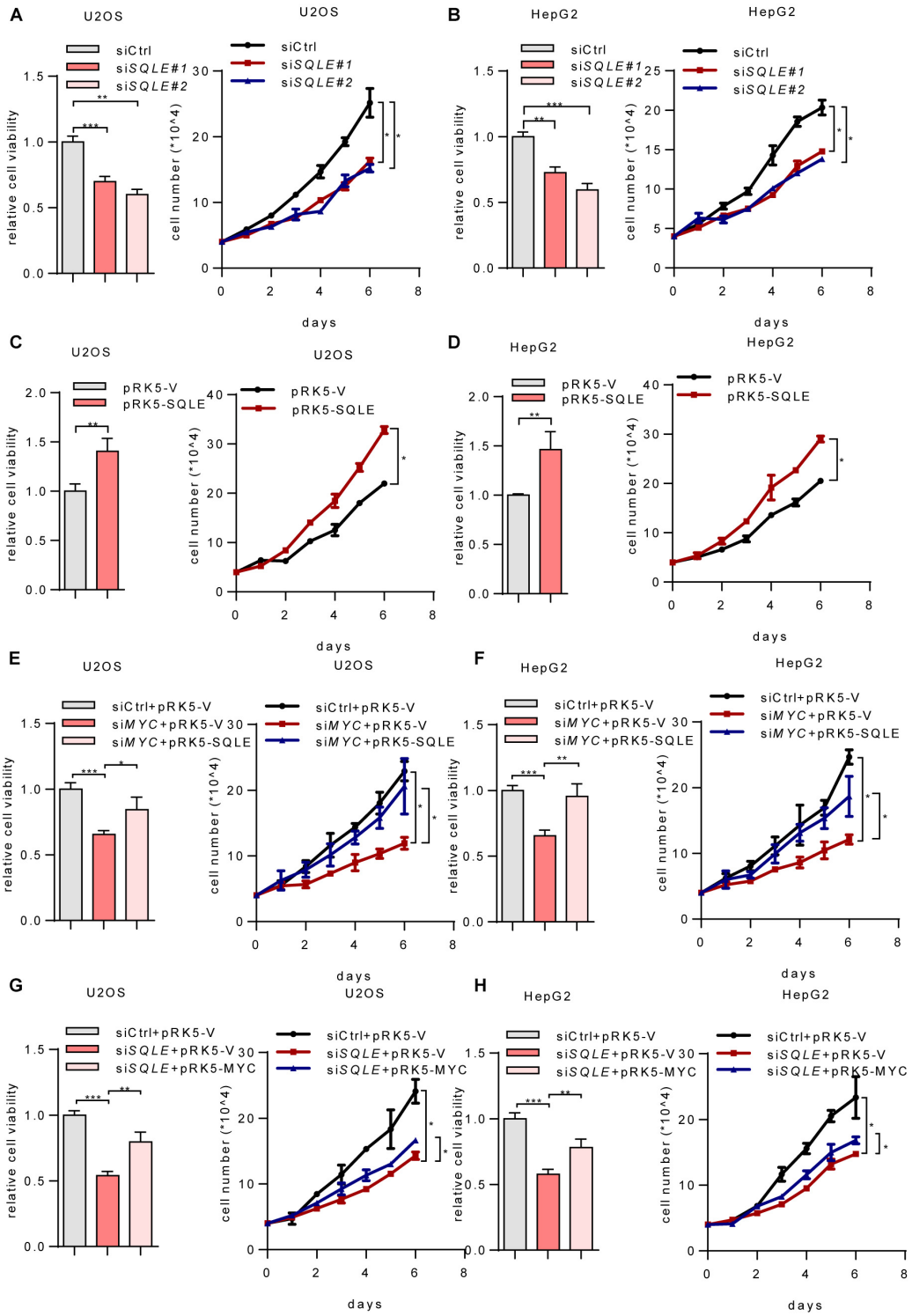

FIGURE 4 | MYC activates SQLE expression to support tumor growth. **(A,B)** Relative cell viability (left) and cell proliferation (right) in control and *SQLE* knockdown U2OS cells and HepG2 cells. Relative cell viability was measured with CCK8. **(C,D)** Relative cell viability (left) and cell proliferation (right) in control and SQLE overexpressing U2OS cells and HepG2 cells. Relative cell viability was measured with CCK8. **(E,F)** U2OS and HepG2 cells were transfected with control or *MYC* siRNA in the presence or absence of exogenous SQLE. Cell viability (left) and cell proliferation (right) were detected, respectively. Relative cell viability was measured with CCK8. **(G,H)** U2OS and HepG2 cells were transfected with control or *SQLE* siRNA in the presence or absence of exogenous MYC. Cell viability (left) and cell proliferation (right) were detected, respectively. Relative cell viability was measured with CCK8. In **(A–H)**, 2 μg plasmids and 1 μg siRNAs were used in all experiments. $n = 3$ independent experiments. Data are means ± SD. Statistical significance was determined by two-tailed unpaired *t*-test. $^{*}P < 0.05$, $^{**}P < 0.01$, and $^{***}P < 0.001$.

overexpression increased cholesterol levels (**Figures 3C,D**). Furthermore, we enforced expression of SQLE in *MYC*-knocking down cells. *MYC* depletion reduced cellular cholesterol levels, while SQLE overexpression reversed it in both U2OS and HepG2 cells (**Figures 3E,F**). Surprisingly, MYC overexpression failed to restore the cholesterol levels in *SQLE* deficient cells (**Figures 3G,H**). Together, these results suggest that MYC stimulates cholesterol biosynthesis through SQLE.

MYC Promotes Tumor Cell Growth Through SQLE

Cholesterol metabolism provides essential membrane components as well as metabolites with a variety of biological functions (Huang et al., 2020). To verify whether SQLE is involved in MYC-mediated cell growth, we depleted *SQLE* using two sets of siRNAs. Depletion of *SQLE* repressed cell proliferation and cell viability (**Figures 4A,B**). Conversely, ectopically expressing SQLE promoted cell growth (**Figures 4C,D**). More importantly, ectopically expressing SQLE almost completely rescued the decreased cell viability and cell proliferation caused by *MYC* knockdown (**Figures 4E,F**). On the contrary, overexpression of MYC partially increased cell viability and proliferation in *SQLE*-knockdown cells (**Figures 4G,H**). These data indicate that MYC promotes cell growth at least partially through SQLE. Then we analyzed TCGA cohort to identify the correlation between MYC and SQLE expression (**Supplementary Figure 2**). MYC was positively correlated with SQLE in several cancers such as cervical squamous cell carcinoma and endocervical adenocarcinoma (CESC), colon adenocarcinoma (COAD), head and neck squamous cell carcinoma (HNSC), and Sarcoma (SARC). Collectively, these data indicate that SQLE is critical for MYC-mediated tumor cell proliferation.

DISCUSSION

MYC promotes metabolic reprogramming in cancer and is involved in lipogenesis by pronouncedly activating acetyl-CoA carboxylase (ACACA), fatty acid synthetase (FASN), and stearoyl-CoA desaturase (SCD) (Zeller et al., 2003; Loven et al., 2012). In patient-derived brain-tumor-initiating cells, MYC is required for upregulation of the mevalonate pathway. And this upregulation further elevates miR-33b to increase MYC expression and thus establishes a positive feedback loop (Wang et al., 2017). In this study, we report that MYC stimulates cholesterol production and promotes tumor cell proliferation via transcriptionally upregulating SQLE.

SQLE is one of the rate-limiting enzymes in cholesterol biosynthesis, and is one of the most significantly upregulated genes in numerous tumors (Xu et al., 2020). A pan-cancer genomic and transcriptomic analysis also highlights SQLE as a key player in maintaining cell survival under hypoxia (Bai et al., 1992). Additionally, in hepatocellular carcinoma (Liu et al., 2018) and breast cancer (Cirmena et al., 2018), SQLE expression is correlated with cancer stage and identified as a prognostic marker. Here we explore the possible correlation between MYC and SQLE. Interestingly, enforced expression of SQLE in *MYC*-depleted cells completely rescues intracellular cholesterol contents, while overexpression of MYC fails to affect the cholesterol levels in *SQLE*-deficient cells. This means that SQLE is indispensable for MYC-regulated cholesterol levels. Of note, we cannot rule out the possibility that MYC may also simultaneously activate the upstream enzymes in the mevalonate pathway.

Recent studies show that SQLE and MYC are co-localized to the same amplicons (Brown et al., 2016; Wolpaw and Dang, 2018). And amplification of SQLE is thought to be associated with amplification of the oncogene MYC (Parris et al., 2014). Our work finds that MYC transcriptionally upregulates SQLE expression. Although a study shows that SQLE expression is independent of MYC in breast and ovarian cancers (Brown et al., 2016), indicating cell heterogeneity in different contexts.

Cholesterol metabolism is essential for tumor growth. Normal mammalian cells meet their need for cholesterol through uptake or *de novo* synthesis (Goldstein and Brown, 1990). Many cancer cell lines depend on exogenous cholesterol for their growth. For example, when incubated in lipoprotein-depleted serum, U-937 cells die after 4 days unless supplemented with cholesterol (Garcia-Bermudez et al., 2019). ALK^+ anaplastic large cell lymphoma (ALCL) cell lines and primary tumors which are less of SQLE expression are highly dependent on cholesterol uptake (Garcia-Bermudez et al., 2019). However, under lipid-free culture conditions, many cells still can proliferate suggesting that these cells may obtain sufficient cholesterol through *de novo* synthesis (Garcia-Bermudez et al., 2019). In addition, lower levels of LDLR but higher levels of SQLE are expressed in advanced-stage prostate cancer, revealing a greater dependence on cholesterol synthesis than uptake (Freudiger et al., 2008). As above, many tumor cells rely on cholesterol biosynthesis to support their growth. Because of its ubiquitous role in human tumors, MYC is an attractive therapeutic target. Cells with deregulated MYC expression often lose negative control and thus depend on a continual supply of nutrients, causing them to be nutrient addicted (Dang, 2012). Therefore, therapies targeting SQLE may be a promising strategy in the treatment of certain MYC-driven cancer.

DATA AVAILABILITY STATEMENT

The original contributions presented in the study are included in the article/**Supplementary Material**. Further inquiries can be directed to the corresponding author/s.

AUTHOR CONTRIBUTIONS

WD and FY designed the experiments and interpreted results. FY performed all experiments. ZL and WL provided technical assistance. WD supervised the research. WD and JK wrote the manuscript with the help of FY. All authors discussed the results and commented on the manuscript.

FUNDING

This work was supported by the National Natural Science Foundation of China (81672766 to WD) and CAMS Innovation Fund for Medical Sciences (2016-I2M-4-002 to WD).

SUPPLEMENTARY MATERIAL

The Supplementary Material for this article can be found online at: https://www.frontiersin.org/articles/10.3389/fcell.2021.655889/full#supplementary-material

Supplementary Figure 1 | MYC promotes the expression of SQLE. **(A–C)** SQLE mRNA (Top) and protein (Bottom) expression in control and *MYC* knockdown H1299 cells, SW480 cells, and Caki-1 cells. **(D–F)** SQLE mRNA (Top) and protein (Bottom) expression in H1299 cells, SW480 cells, and Caki-1 cells expressing ectopic MYC or control protein. In **(A–F)**, 2 μg plasmids and 1 μg siRNAs were used in all experiments. $n = 3$ independent experiments. Data are means ± SD. Statistical significance was determined by two-tailed unpaired *t*-test. $^{*}P < 0.05$, $^{**}P < 0.01$, and $^{***}P < 0.001$.

Supplementary Figure 2 | TCGA cohort identified a correlation between MYC and SQLE expression. **(A–D)** The correlation between MYC and SQLE expression in cervical squamous cell carcinoma and endocervical adenocarcinoma (CESC), colon adenocarcinoma (COAD), head and neck squamous cell carcinoma (HNSC), and Sarcoma (SARC) by analyzing TCGA cohort.

REFERENCES

Ahuja, P., Zhao, P., Angelis, E., Ruan, H., Korge, P., Olson, A., et al. (2010). Myc controls transcriptional regulation of cardiac metabolism and mitochondrial biogenesis in response to pathological stress in mice. *J. Clin. Invest.* 120, 1494–1505. doi: 10.1172/JCI38331

Annibali, D., Whitfield, J. R., Favuzzi, E., Jauset, T., Serrano, E., Cuartas, I., et al. (2014). Myc inhibition is effective against glioma and reveals a role for Myc in proficient mitosis. *Nat. Commun.* 5:4632. doi: 10.1038/ncomms5632

Bai, M., Xiao, X. Y., and Prestwich, G. D. (1992). Epoxidation of 2,3-oxidosqualene to 2,3;22,23-squalene dioxide by squalene epoxidase. *Biochem. Biophys. Res. Commun.* 185, 323–329. doi: 10.1016/s0006-291x(05)90003-x

Brown, D. N., Caffa, I., Cirmena, G., Piras, D., Garuti, A., Gallo, M., et al. (2016). Squalene epoxidase is a bona fide oncogene by amplification with clinical relevance in breast cancer. *Sci. Rep.* 6:19435. doi: 10.1038/srep19435

Chua, N. K., Coates, H. W., and Brown, A. J. (2020). Squalene monooxygenase: a journey to the heart of cholesterol synthesis. *Prog. Lipid Res.* 79:101033. doi: 10.1016/j.plipres.2020.101033

Cirmena, G., Franceschelli, P., Isnaldi, E., Ferrando, L., De Mariano, M., Ballestrero, A., et al. (2018). Squalene epoxidase as a promising metabolic target in cancer treatment. *Cancer Lett.* 425, 13–20. doi: 10.1016/j.canlet.2018.03.034

Costa, G. A., de Souza, S. B., da Silva Teixeira, L. R., Okorokov, L. A., Arnholdt, A. C. V., Okorokova-Facanha, A. L., et al. (2018). Tumor cell cholesterol depletion and V-ATPase inhibition as an inhibitory mechanism to prevent cell migration and invasiveness in melanoma. *Biochim. Biophys. Acta Gen. Subj.* 1862, 684–691. doi: 10.1016/j.bbagen.2017.12.006

Dang, C. V. (2012). MYC on the path to cancer. *Cell* 149, 22–35. doi: 10.1016/j.cell.2012.03.003

Dang, C. V. (2013). MYC, metabolism, cell growth, and tumorigenesis. *Cold Spring Harb. Perspect. Med.* 3:a014217. doi: 10.1101/cshperspect.a014217

Dong, Y., Li, X., Lin, Z., Zou, W., Liu, Y., Qian, H., et al. (2019). HOXC-AS1-MYC regulatory loop contributes to the growth and metastasis in gastric cancer. *J. Exp. Clin. Cancer Res.* 38:502. doi: 10.1186/s13046-019-1482-7

Freudiger, C. W., Min, W., Saar, B. G., Lu, S., Holtom, G. R., He, C., et al. (2008). Label-free biomedical imaging with high sensitivity by stimulated Raman scattering microscopy. *Science* 322, 1857–1861. doi: 10.1126/science.1165758

Garcia-Bermudez, J., Baudrier, L., Bayraktar, E. C., Shen, Y., La, K., Guarecuco, R., et al. (2019). Squalene accumulation in cholesterol auxotrophic lymphomas prevents oxidative cell death. *Nature* 567, 118–122. doi: 10.1038/s41586-019-0945-5

Gill, S., Stevenson, J., Kristiana, I., and Brown, A. J. (2011). Cholesterol-dependent degradation of squalene monooxygenase, a control point in cholesterol synthesis beyond HMG-CoA reductase. *Cell Metab.* 13, 260–273. doi: 10.1016/j.cmet.2011.01.015

Goldstein, J. L., and Brown, M. S. (1990). Regulation of the mevalonate pathway. *Nature* 343, 425–430. doi: 10.1038/343425a0

Huang, B., Song, B. L., and Xu, C. (2020). Cholesterol metabolism in cancer: mechanisms and therapeutic opportunities. *Nat. Metab.* 2, 132–141. doi: 10.1038/s42255-020-0174-0

Kuzu, O. F., Noory, M. A., and Robertson, G. P. (2016). The role of cholesterol in cancer. *Cancer Res.* 76, 2063–2070. doi: 10.1158/0008-5472.CAN-15-2613

Li, N., Zhou, Z. S., Shen, Y., Xu, J., Miao, H. H., Xiong, Y., et al. (2017). Inhibition of the sterol regulatory element-binding protein pathway suppresses hepatocellular carcinoma by repressing inflammation in mice. *Hepatology* 65, 1936–1947. doi: 10.1002/hep.29018

Li, Z., Van Calcar, S., Qu, C., Cavenee, W. K., Zhang, M. Q., and Ren, B. (2003). A global transcriptional regulatory role for c-Myc in Burkitt's lymphoma cells. *Proc. Natl. Acad. Sci. U. S. A.* 100, 8164–8169. doi: 10.1073/pnas.1332764100

Liu, D., Wong, C. C., Fu, L., Chen, H., Zhao, L., Li, C., et al. (2018). Squalene epoxidase drives NAFLD-induced hepatocellular carcinoma and is a pharmaceutical target. *Sci. Transl. Med.* 10:eaa9840. doi: 10.1126/scitranslmed.aap9840

Loven, J., Orlando, D. A., Sigova, A. A., Lin, C. Y., Rahl, P. B., Burge, C. B., et al. (2012). Revisiting global gene expression analysis. *Cell* 151, 476–482. doi: 10.1016/j.cell.2012.10.012

Luo, J., Jiang, L. Y., Yang, H., and Song, B. L. (2019). Intracellular cholesterol transport by sterol transfer proteins at membrane contact sites. *Trends Biochem. Sci.* 44, 273–292. doi: 10.1016/j.tibs.2018.10.001

Luo, J., Yang, H., and Song, B. L. (2020). Mechanisms and regulation of cholesterol homeostasis. *Nat. Rev. Mol. Cell Biol.* 21, 225–245. doi: 10.1038/s41580-019-0190-7

Meyer, N., and Penn, L. Z. (2008). Reflecting on 25 years with MYC. *Nat. Rev. Cancer* 8, 976–990. doi: 10.1038/nrc2231

Morrish, F., Noonan, J., Perez-Olsen, C., Gafken, P. R., Fitzgibbon, M., Kelleher, J., et al. (2010). Myc-dependent mitochondrial generation of acetyl-CoA contributes to fatty acid biosynthesis and histone acetylation during cell cycle entry. *J. Biol. Chem.* 285, 36267–36274. doi: 10.1074/jbc.M110.141606

Parris, T. Z., Kovacs, A., Hajizadeh, S., Nemes, S., Semaan, M., Levin, M., et al. (2014). Frequent MYC coamplification and DNA hypomethylation of multiple genes on 8q in 8p11-p12-amplified breast carcinomas. *Oncogenesis* 3:e95. doi: 10.1038/oncsis.2014.8

Riscal, R., Skuli, N., and Simon, M. C. (2019). Even cancer cells watch their cholesterol! *Mol. Cell* 76, 220–231. doi: 10.1016/j.molcel.2019.09.008

Sharma, V. M., Calvo, J. A., Draheim, K. M., Cunningham, L. A., Hermance, N., Beverly, L., et al. (2006). Notch1 contributes to mouse T-cell leukemia by directly inducing the expression of c-myc. *Mol. Cell. Biol.* 26, 8022–8031. doi: 10.1128/MCB.01091-06

Shou, Y., Martelli, M. L., Gabrea, A., Qi, Y., Brents, L. A., Roschke, A., et al. (2000). Diverse karyotypic abnormalities of the c-myc locus associated with c-myc dysregulation and tumor progression in multiple myeloma. *Proc. Natl. Acad. Sci. U.S.A.* 97, 228–233. doi: 10.1073/pnas.97.1.228

Wang, X., Huang, Z., Wu, Q., Prager, B. C., Mack, S. C., Yang, K., et al. (2017). MYC-regulated mevalonate metabolism maintains brain tumor-initiating cells. *Cancer Res.* 77, 4947–4960. doi: 10.1158/0008-5472.CAN-17-0114

Wolpaw, A. J., and Dang, C. V. (2018). MYC-induced metabolic stress and tumorigenesis. *Biochim. Biophys. Acta Rev. Cancer* 1870, 43–50. doi: 10.1016/j.bbcan.2018.05.003

Wong, L. H., Gatta, A. T., and Levine, T. P. (2019). Lipid transfer proteins: the lipid commute via shuttles, bridges and tubes. *Nat. Rev. Mol. Cell Biol.* 20, 85–101. doi: 10.1038/s41580-018-0071-5

Xu, H., Zhou, S., Tang, Q., Xia, H., and Bi, F. (2020). Cholesterol metabolism: new functions and therapeutic approaches in cancer. *Biochim. Biophys. Acta Rev. Cancer* 1874:188394. doi: 10.1016/j.bbcan.2020.188394

Zack, T. I., Schumacher, S. E., Carter, S. L., Cherniack, A. D., Saksena, G., Tabak, B., et al. (2013). Pan-cancer patterns of somatic copy number alteration. *Nat. Genet.* 45, 1134–1140. doi: 10.1038/ng.2760

Zeller, K. I., Jegga, A. G., Aronow, B. J., O'Donnell, K. A., and Dang, C. V. (2003). An integrated database of genes responsive to the Myc oncogenic transcription factor: identification of direct genomic targets. *Genome Biol.* 4:R69. doi: 10.1186/gb-2003-4-10-r69

Conflict of Interest: The authors declare that the research was conducted in the absence of any commercial or financial relationships that could be construed as a potential conflict of interest.

frontiers in Cell and Developmental Biology

CORRECTION
published: 09 June 2021
doi: 10.3389/fcell.2021.705769

Corrigendum: MYC Enhances Cholesterol Biosynthesis and Supports Cell Proliferation Through SQLE

*Fan Yang†, Junjie Kou†, Zizhao Liu, Wei Li and Wenjing Du**

State Key Laboratory of Medical Molecular Biology, Department of Cell Biology, Institute of Basic Medical Sciences Chinese Academy of Medical Sciences, School of Basic Medicine Peking Union Medical College, Beijing, China

Keywords: cholesterol synthesis, cell proliferation, cancer, SQLE, MYC

OPEN ACCESS

Edited and reviewed by:
Binghui Li,
Capital Medical University, China

***Correspondence:**
Wenjing Du
wenjingdu@ibms.pumc.edu.cn;
wjdu123@hotmail.com

†These authors have contributed equally to this work

Specialty section:
This article was submitted to Molecular Medicine, a section of the journal Frontiers in Cell and Developmental Biology

Received: *06 May 2021*
Accepted: *12 May 2021*
Published: *09 June 2021*

Citation:
Yang F, Kou J, Liu Z, Li W and Du W (2021) Corrigendum: MYC Enhances Cholesterol Biosynthesis and Supports Cell Proliferation Through SQLE. Front. Cell Dev. Biol. 9:705769. doi: 10.3389/fcell.2021.705769

A Corrigendum on

MYC Enhances Cholesterol Biosynthesis and Supports Cell Proliferation Through SQLE
by Yang, F., Kou, J., Liu, Z., Li, W., and Du, W. (2021). Front. Cell Dev. Biol. 9:655889. doi: 10.3389/fcell.2021.655889

In the original article, there was a mistake in **Figure 1I** and **Figure 1J** as published. The statistical significance was calculated between the siCtrl and siMYC+cho group. However, the correct comparison is between siMYC and siMYC+cho group. The corrected **Figure 1I** and **Figure 1J** appear below.

In the original article, there was a mistake in **Figure 3E** and **Figure 3F** as published. The statistical significance was calculated between the siCtrl+pRK5-V and siMYC+pRK5-SQLE group. However, the correct comparison is between siMYC+ pRK5-V and siMYC+pRK5-SQLE group. The corrected **Figure 3E** and **Figure 3F** appear below.

The authors apologize for these errors and state that this does not change the scientific conclusions of the article in any way. The original article has been updated.

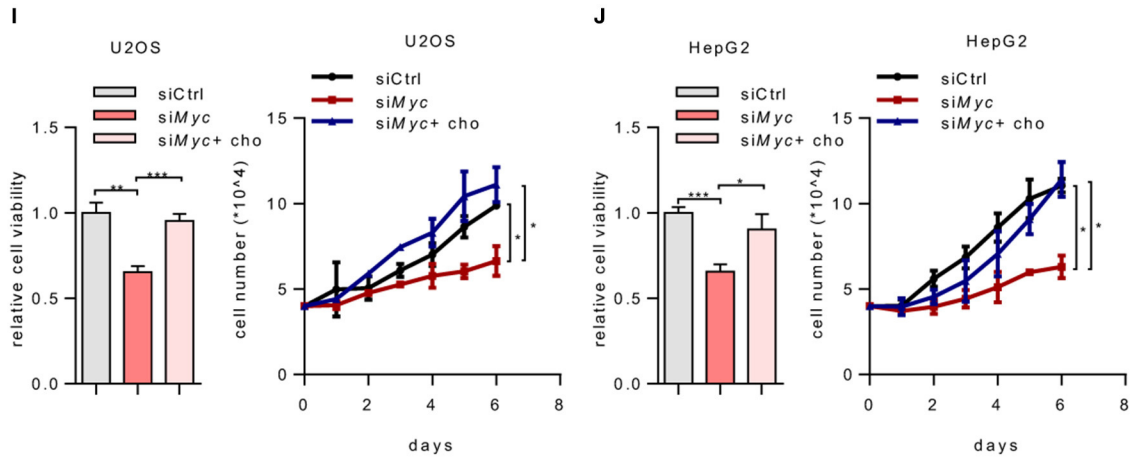

FIGURE 1 |

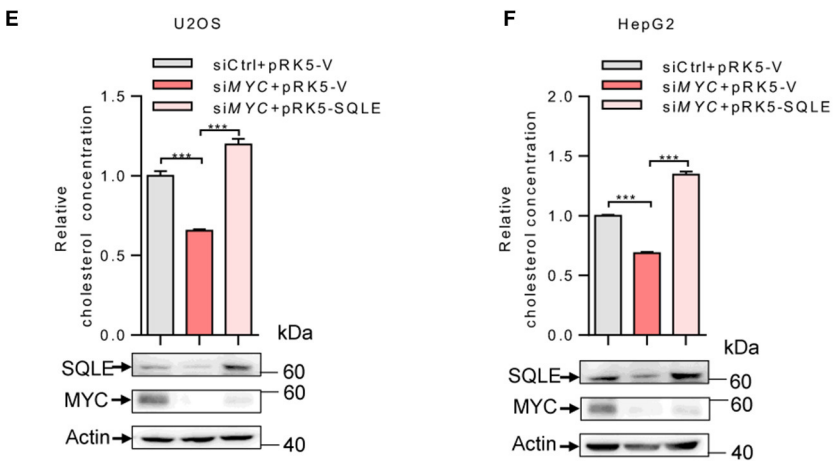

FIGURE 3 |

frontiers in Cell and Developmental Biology

BRIEF RESEARCH REPORT
published: 10 June 2021
doi: 10.3389/fcell.2021.698264

CREB1 and ATF1 Negatively Regulate Glutathione Biosynthesis Sensitizing Cells to Oxidative Stress

*Lina Zhao†, Wenjun Xia† and Peng Jiang**

School of Life Sciences, Tsinghua University, Beijing, China

The cAMP response element binding protein (CREB) family activating transcription factor 1 (ATF1) and cAMP response element binding protein 1 (CREB1) have been reported in a diverse group of tumors, however, the mechanistic basis for this remains unclear. Here we found that CREB1 and ATF1 unexpectedly regulate glutathione (GSH) biosynthesis by suppressing the expression of glutamate-cysteine ligase modifier subunit (GCLM) and glutathione synthase (GSS), two key enzymes of GSH biosynthesis pathway. Mechanistic studies reveal that GCLM and GSS are direct transcriptional targets of CREB1 and ATF1. Through repressing the expression of these two enzymes, CREB1 and ATF1 reduce the GSH biosynthesis and the capability of cells to detoxicate reactive oxygen species (ROS), thereby increasing cellular susceptibility to oxidative stress. Therefore, our findings link CREB1 family to cellular metabolism, and uncover a potential therapeutic approach by targeting GCLM or oxidative stress for the treatment of tumors with relatively high expression of CREB1 family proteins.

Keywords: CREB1, ATF1, GSH, ROS, survival, proliferation

OPEN ACCESS

Edited by:
Binghui Li,
Capital Medical University, China

Reviewed by:
Jun Fan,
Jinan University, China
Guoliang Qing,
Wuhan University, China

***Correspondence:**
Peng Jiang
pengjiang@tsinghua.edu.cn

†These authors have contributed equally to this work

Specialty section:
This article was submitted to Molecular Medicine, a section of the journal Frontiers in Cell and Developmental Biology

Received: *21 April 2021*
Accepted: *14 May 2021*
Published: *10 June 2021*

Citation:
Zhao L, Xia W and Jiang P (2021) CREB1 and ATF1 Negatively Regulate Glutathione Biosynthesis Sensitizing Cells to Oxidative Stress. Front. Cell Dev. Biol. 9:698264. doi: 10.3389/fcell.2021.698264

INTRODUCTION

Reactive oxygen species (ROS) is an important determinant of cancer cells metabolism phenotypes (Rodic and Vincent, 2018). The outcomes of ROS performance in tumor cells are dose-dependent. In general, low level of ROS facilities proliferation, growth, invasion and metastasis of tumor cells, while relatively high level of ROS leads to cell cycle arrest and even cell death. Therefore, it is essential for cancer cells to optimize cellular ROS level to maintain tumor progression (Ahmad et al., 2005; Aykin-Burns et al., 2009; Rodic and Vincent, 2018). To achieve this, tumors cells could increase their antioxidative capacity by upregulating relevant metabolic molecules and the expression of certain antioxidant enzymes. Glutathione (GSH) is thought to be a main small thiol-antioxidant derivative (Veeravalli et al., 2011; Quintana-Cabrera et al., 2012), consisting of L-glutamine, L-cysteine, and L-glycine, found in all mammalian tissues (Lu, 2009). GSH is generally synthesized exclusively in the cytoplasm in two consistently steps at the expenditure of ATP, the first step, which is also a rate-limiting step, catalyzes the generation of γ-glutamylcysteine by the GCL, and the glutathione synthase (GSS) catalyzes the second step to produce GSH. The GCL holoenzyme consists of two separate proteins, a catalytic subunit (GCLC) and a modifier subunit (GCLM) (Krejsa et al., 2010), which are encoded by different genes in humans. GCLC exhibits

catalytic activity (Seelig et al., 1984; Lu, 2009) and GCLM is enzymatically inactive but plays an important regulatory role by lowering the Km of GCL for glutamate and raising the Ki for GSH (Huang et al., 1993a,b). GSH synthesis pathway is severely activated by some stimuli including oxidative stress.

cAMP response element binding protein 1 (CREB1) belongs to the bZIP transcription factors. The other two members of CREB1 family are activating transcription factor 1 (ATF1) and cAMP response element modulator (CREM). CREB1 and ATF1 both express ubiquitously, whereas CREM mainly expresses in neuroendocrine tissues (Mayr and Montminy, 2001). Although CREB1 has been implicated in the physiology of nerve and most recently in some cancer cells by cooperating with some protein kinases or small molecules, including PKA, PKB (AKT), MAPK, cAMP, and Ca^{2+} to inhibit apoptosis and promote cell survival in unstressed situation (Bonni and Brunet, 1999; Shankar et al., 2005; Chhabra et al., 2007; Pigazzi et al., 2007; Aggarwal et al., 2008; Shukla et al., 2009), whether CREB families play a role in modulating tumor cellular metabolism remains unknown.

RESULTS

To determine if CREB1 regulates GSH synthesis, we examined the effect of CREB1 silencing on the expression of several major enzymes of the GSH synthetic pathways in multiple cell lines including U2OS and U87 cells (**Figure 1A**). Interestingly, while the mRNA level of most enzymes remained approximately the same (CTH and GCLC) or changed inconsistently (CBS, CDO1, and CSD), the mRNA levels of GCLM and GSS increased consistently and significantly when CREB1 was knocked down in U2OS, U87, and HepG2 cells (**Figures 1B,C** and **Supplementary Figure 1A**). Similar findings were found in A549, H1299, and H1975 cells. CREB1 ablation led to an increase in the expression of GCLM and GSS expression (**Supplementary Figures 1B–D**). Like CREB1, knocking down of ATF1 expression in U2OS and U87 cells resulted in strong increase in mRNA levels of both GCLM and GSS (**Figures 1D,E**). Moreover, upon ATF1 knockdown, GCLM and GSS mRNA levels augmented in multiple cell lines including HepG2, A549, H1299, and H1975 cells (**Supplementary Figures 1E–H**). Results from western blot analysis revealed that silencing of either of CREB1, ATF1 or both enhanced the protein levels of GCLM and GSS in U2OS and U87 cells, as well as in HepG2 and A549 cells (**Figure 1F** and **Supplementary Figures 1I,J**). Similarly, sgRNA-mediated knockout of CREB1 and ATF1 in U2OS cells strongly boosted the expression of GCLM and GSS (**Supplementary Figure 1K**). These findings were further confirmed by overexpression of CREB1 and ATF1. In line with the knockdown data, enforced expression of CREB1 and ATF1 led to strong reduction in protein levels of GCLM and GSS in U2OS cells (**Supplementary Figure 1L**). Collectively, these findings show that both CREB1 and ATF1 negatively regulate the expression of GCLM and GSS, two key enzymatic steps of GSH synthesis pathway.

To investigate whether CREB1 and ATF1 are the transcription factors for GCLM and GSS, we analyzed human *GCLM* and *GSS* gene sequences for potential response elements of CREB family proteins, which share the conservative sequence of 5′-TGACGTCA-3′. Potentially, we identified a response element (RE) for CREB1 and ATF1, respectively, in each of them (**Figure 2A**). Chromatin immunoprecipitation (ChIP) assays showed that CREB1 and ATF1 could bind to these REs (**Figures 2B,C**). Next, we cloned the fragments of *GCLM* and *GSS* genes containing the corresponding response elements into the promotor region of a luciferase reporter plasmid, and found that CREB1 and ATF1 repressed the luciferase activity driven by these REs, but not the mutant ones (**Figures 2D,E**). These results together indicate that GCLM and GSS may be the transcriptional targets for CREB1 and ATF1.

GCLM and GSS are essential for GSH synthesis (Li et al., 2016). Using small interfering RNA (siRNA) to simultaneously knock down the expression of CREB1 and ATF1, we observed that GSH production was substantially increased in U2OS cells (**Figures 3A,B**). GSH is considered to be one of the most important scavengers of reactive oxygen species (ROS). Consistent with this, ablation of CREB1 and ATF1 decreased the cellular level of ROS in both U2OS, U87, and HepG2 cells as determined by DCF staining (**Figure 3C** and **Supplementary Figures 2A,B**). The specificity of the assay was shown by an increase in the detected ROS upon G6PD silencing (**Supplementary Figure 2C**). G6PD is the first and rate-limiting enzyme of the PPP pathway, which is the main source of intracellular antioxygen NADPH (nicotinamide adenine dinucleotide phosphate, reduced) (Jiang et al., 2011). Conversely, overexpression of CREB1 and ATF1 led to increased intracellular ROS in U2OS cells (**Supplementary Figure 2D**). Consistent with previous study (Huang et al., 1993b; Chhabra et al., 2007), GSS depletion showed no effect on ROS level, which could be due to the complex GSH-independent action(s) of GSS (**Supplementary Figure 2E**). Nevertheless, silencing GCLM resulted in an increase in ROS level (**Supplementary Figure 2E**). Moreover, knockdown of GCLM alone elevated intracellular level of ROS, and reversed the suppressive effect of depletion of CREB1 and ATF1 on ROS in U2OS cells (**Figure 3D**). Collectively, these results indicate that CREB1 and ATF1 have a role in maintaining ROS though downregulation of GCLM and GSS expression.

The above findings that CREB1 and ATF1 unexpectedly reduce cell capability to scavenge ROS promoted us to investigate whether cells with ablation of CREB1 and ATF1 are resistant to oxidative stress. Indeed, deletion of CREB1 and ATF1 in U2OS cells resulted in a reduction in cell death as determined by FACS analysis when cells were cultured in medium containing 100 μM H_2O_2 (**Figure 4A**). To examine whether GCLM and GSS are involved in CREB1- and ATF1-mediated cell death under oxidative stress, we knocked down the expression of GCLM and GSS in U2OS cells expressing siRNAs against CREB1 and ATF1. Again, depletion of CREB1 and ATF1 led to increased cells viability, and this effect was reversed by GCLM and GSS silencing in the presence of 100 μM H_2O_2 (**Figures 4B,C**). We next confirmed these findings by an anchorage-independent growth in soft agar, an *in vitro* measurement of tumorigenicity. Depletion of CREB1 and ATF1 caused increased capacity of U87 cells to form colonies in soft agar supplied with 100 μM H_2O_2,

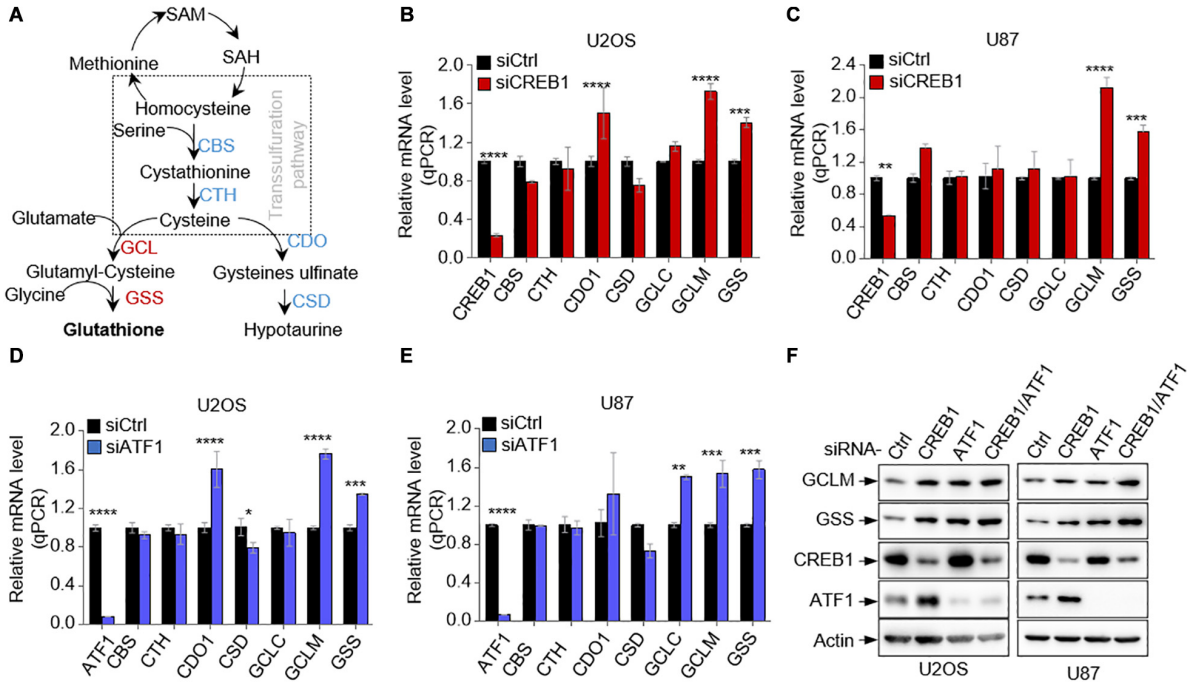

FIGURE 1 | CREB1 and ATF1 repress the expression of GCLM and GSS. **(A)** Schematic depicting the GSH synthesis pathway and its associated hypotaurine synthesis pathway. **(B,C)** Relative mRNA levels of enzymes of GSH synthesis pathway in U2OS cells **(B)** and U87 cells **(C)** transfected with CREB1 siRNA or control siRNA. **(D,E)** Relative mRNA levels of GSH synthesis enzymes in U2OS cells **(D)** and U87 cells **(E)** transfected with control siRNA or ATF1 siRNA as indicated. **(F)** U2OS and U87 cells expressing control siRNA, or siRNAs against CREB1, ATF1, or both (CREB1/ATF1) as indicated. Protein expression was analyzed by Western blot. Data are means ± SD. ($n = 3$), $^{*}p < 0.05$, $^{**}p < 0.01$, $^{***}p < 0.001$, $^{****}p < 0.00001$.

and knockdown of GCLM and GSS almost totally reduced the anchorage-independent growth regardless of CREB1 and ATF1 status (**Figures 4D,E** and **Supplementary Figure 3**).

CONCLUSION

In this work, we found a previously unappreciated role for CREB family proteins in controlling GSH synthesis. Through downregulation of the expression of GCLM and GSS, CREB1 and ATF1 unexpectedly reduce GSH generation and thereby dampen the cellular ability to scavenge ROS, leading to increased susceptibility of cells to oxidative stress. Intriguingly, GSS seems not to be essential for ROS detoxification, but still acts a key metabolic enzyme of the GSH *de novo* synthetic pathway. To elucidate the underlying mechanism(s) for these unexpected observations would be of great interest. One potential expectation is that GSS possess ROS-related but GSH synthesis-independent functions, which could comprise the effect of GSH production on ROS. Nevertheless, GCLM downregulation appears to be sufficient to abolish ROS reduction in cells depleted of CREB family proteins CREB1 and ATF1. CREB1 has been implicated in supporting tumor cell proliferation and survival in some types of tumor cells, indicating that CREB1 might be an oncogenic protein that can help tumor cell to proliferate in certain situations (Thway and Fisher, 2012). Here our findings reveal a metabolic mechanism for CREB1-mediated tumor cell survival, and also suggest that targeting GCLM or oxidative stress potentially could be a therapeutic approach for treatment of tumors with relatively high expression of CREB1 family proteins.

MATERIALS AND METHODS

Antibodies and Reagents

Antibodies against the following proteins/epitopes were used for immunoblot with the sources, catalog numbers, and dilutions indicated: Actin (Easy Bio, BE0037-10, 1:5000), Flag (Sigma-Aldrich, F3165, 1:5000), GCLM (Proteintech, 14241-1-AP, 1:1000), GSS (Santa Cruz Biotechnology, sc-166882, 1:1000), CREB1 (Proteintech, 12208-1-AP, 1:1000), and ATF1 (Proteintech, 11946-1-AP, 1:1000).

The ANNEXIN V-FITC/PI Apoptosis Detection Kit were purchased from Solarbio. The following regents were purchased from Sigma-Aldrich: crystal violet (CV), 0.4% trypan blue solution, 2′,7′-dichlorofluorescin diacetate (DCF), propidium iodide (PI), puromycin.

Cell Culture

Cells were maintained in standard culture conditions without any antibiotic. A549, H1299, HEPG2, H1975, and U87 were from ATCC (Manassas, VA, United States). All cells were cultured in a 5% CO_2 humidified incubator (Thermo Fisher Scientific, United States) at 37°C. A549 cell line was maintained in standard

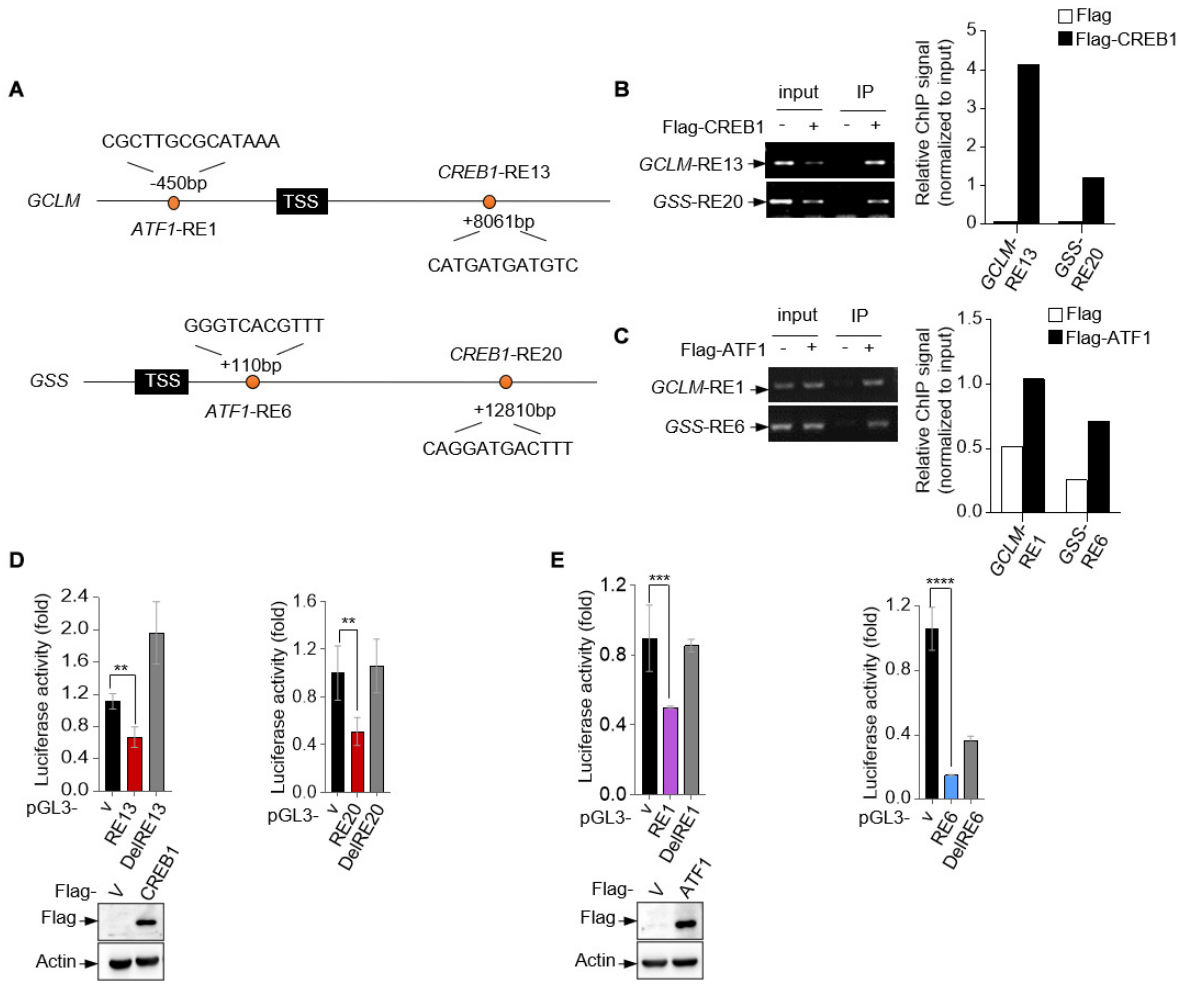

FIGURE 2 | GCLM and GSS are transcriptional targets of CREB1 and ATF1. **(A)** Schematic representation of human *GCLM* and *GSS* genomic structure. The sequences of potential CREB1 and ATF1 response elements *GCLM*-RE13, *GSS*-RE20, *GCLM*-RE1, and *GSS*-RE6 are shown. **(B,C)** 293T cells were transfected with Flag-CREB1 **(B)**, Flag-ATF1 **(C)** or vector control plasmid. Cell lysates were used for ChIP assay using anti-Flag antibody. Bound DNA was amplified by PCR. Results are representative of three independent experiments. **(D,E)** Luciferase constructs containing indicated responsive elements (REs) were transfected into 293T cells together with Flag-CREB1 **(D)**, Flag-ATF1 **(E)** and vector control, respectively. Renilla vector pRL-CMV was used as a transfection internal control. The relative luciferase activity was normalized to the co-transfected Renilla activity. Data are means ± SD. ($n = 3$), $^{**}p < 0.01$, $^{***}p < 0.001$, $^{****}p < 0.0001$.

Dulbecco's modified Eagle's medium (DMEM) (Thermo Fisher Scientific, C11995500BT) with 10% fetal bovine serum (FBS) (GEMINI, 100–106). U2OS cells were cultured in McCoy's 5 A Medium, U87 and HEPG2 cells in MEM supplemented with non-essential amino acid (Gibco,11140050). H1299 and H1975 cells were cultured in standard RPMI1640 medium (Thermo Fisher Scientific, 11875093) with 10% FBS. Unless indicated otherwise, all cells were cultured without the addition of penicillin-streptomycin and for no more than two consecutive months, and were routinely examined for mycoplasma contamination.

Genes Knock Down With siRNA

The flowing siRNAs were purchased from GenePharma. The sequences were: CREB1#1, 5′-AAA CAUUAACCAUGACCAATT-3′; CREB1#2, 5′-GGUGCCAA CUCCAAUUUACTT-3′; ATF1#1, 5′-AGGUACAACUAUUC UUCAGUA-3′; ATF1#2, 5′-GCUCAACAGGUAUCAUCUUUA-3′; GCLM; 5'-GCAAGUUUCCAAGAAGCUCTT-3′; GSS, 5′- CCAUCAAACAGGAUGACUUUATT -3′ G6PD, 5′-ACGAGCUGAUGAAGAGAGUGGGUUU-3′. siRNAs were transfected into cells using Lipo2000 Transfection Agent (Thermo Fisher Scientific, 12566014) following the manufacturer's instruction.

Plasmids

The coding sequences corresponding to the full-length human CREB1 and ATF1 were amplified by polymerase chain reaction (PCR) from cDNA library of 293T cells and then cloned into Prk5-flag empty vector as indicated. The cloning sequences are as follows: CREB1, 5′-CGCGGATCCGCGATGACCATGGAATCTGGAGCCG-3′ (forward) and 5′-CCCAAGCTTGGGTTAATCTGAT

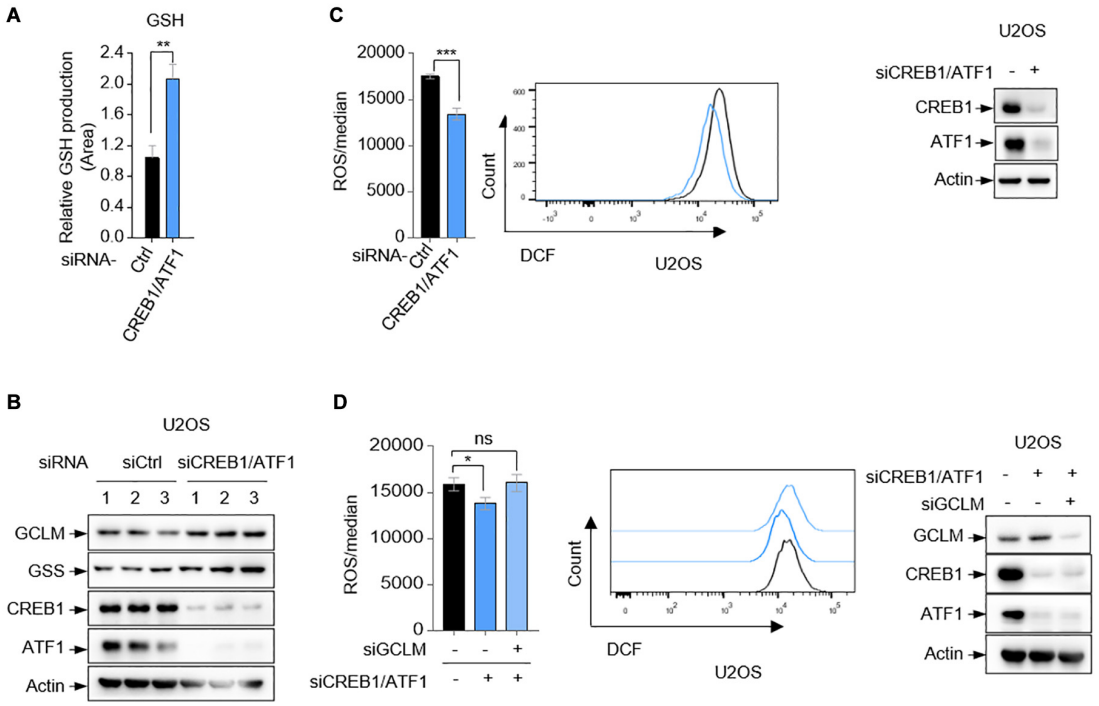

FIGURE 3 | CREB1 and ATF1 inhibit intracellular ROS. **(A,B)** U2OS cells transfected with control siRNA, or CREB1 siRNA together with ATF1 siRNA (siCREB1/ATF1) were assayed for intracellular GSH production by LC-MS. **(C)** Relative ROS level in U2OS cells transfected with CREB1 and ATF1 siRNAs (siCREB1/ATF1), or control siRNA was determined by flow cytometry analysis. Protein expression was analyzed by Western blot. **(D)** U2OS cells were transfected with control, CREB1, ATF1 and/or GCLM siRNA as indicated. Relative ROS level was analyzed by flow cytometry. Protein expression was analyzed by Western blot. Data are means ± SD. ($n = 3$), $^{*}p < 0.05$, $^{**}p < 0.01$, $^{***}p < 0.001$.

TTGTGGCAGTAAAGGTCCT-3′ (reverse); ATF1, 5′-TGC TCTAGAATGGAAGATTCCCACAAGAGTAC-3′ (forward) and 5′-CCCAAGCTTTCAAACACTTTTATTGGAATAAAGAT CC-3′ (reverse). sgRNAs were made in px330-GFP vector. The sequences were: CREB1:5′-CACCGGGGCAGACAGTTC AAGTCCA-3′(sense) and 5′-AAACTGGACTTGAACTGT CTGCCCC-3′ (antisense); ATF1: 5′-CACCGGAACGCTG ACGTCATCAACCCG-3′ (sense) and 5′-AAACGCACCGAC TCGGTGCCAC-3′ (antisense).

Semi-Quantitative RT-PCR and Quantitative RT-PCR

RNA was extracted by TRIzol (15596-018, Invitrogen) according to the manufacturer's instruction. 2 μg RNA of each sample was reversed to complementary DNA by First-strand cDNA Synthesis System (Thermo Fisher Scientific, catalog No. K1622), and 0.2 μg cDNA was used as a template to perform PCR. Quantitative PCR were performed on CFX96 Real-Time PCR System (Bio-Rad, United States) and the amplifications were done using the SYBR Green PCR Master Mix (Gene Star, China). The primer pairs were: CREB1, 5′-ATTCACAGGAGTCAGTGGATAGT-3′ (forward) and 5′-CACCGTTACAGTGGTGATGG-3′ (reverse); ATF1, 5′-AGGACTCATCCGACAGCATAG-3′ (forward) and 5′-TTCTGCCCCGTGTATCTTCAG-3′ (reverse); CBS, 5′-GTCA GACCAAGTTGGCAAAGT-3′ (forward) and 5′-CACCCCGA ACACCATCTGC-3′ (reverse); CTH, 5′-AAAGACGCCTCCT CACAAGG-3′ (forward) and 5′-AAGGCAATTCCTAGTG GGATTTC-3′ (reverse); CDO1, 5′-TCCATTGGCTTACATCG AGTAGA-3′ (forward) and 5′-CCCGAAGTTGCATTTGGAGT-3′ (reverse); CSD, 5′-AGAAGCGGGAAGGGTTTGAG-3′ (forward) and 5′-CCTTTCGTGGTAATCTGGACTC-3′ (re verse); GCLC, 5′-GGAGACCAGAGTATGGGAGTT-3′ (fo rward) and 5′-CCGGCGTTTTCGCATGTTG-3′ (reverse); GCLM, 5′-CATTTACAGCCTTACTGGGAGG-3′ (forward) and 5′-ATGCAGTCAAATCTGGTGGCA-3′ (reverse); GSS, 5′-GGGAGCCTCTTGCAGGATAAA-3′ (forward) and 5′-GAATGGGGCATAGCTCACCAC-3′ (reverse); β-actin, 5′GAC CTGACTGACTACCTCATGAAGAT-3′ (forward) and 5′-GTCACACTTCATGATGGAGTTGAAGG-3′ (reverse). The fold changes of gene expression are normalized to β-actin.

Western Blot Analysis

Whole-cell lysates were obtained using modified RIPA lysis buffer (10 mM Tris–HCl at pH 7.5, 5 mM EDTA, 150 mM NaCl, 1% NP-40, 1% sodium deoxycholate, 0.025% SDS, and added protease cocktail freshly). Cells were washed and incubated in lysis buffer for 30 min on ice, and boiled in 5x loading buffer. Protein samples were resolved by SDS-PAGE and transferred onto nitrocellulose membrane. The membrane was then blocked in 5% skimmed milk in TBST and probed with the indicated antibodies.

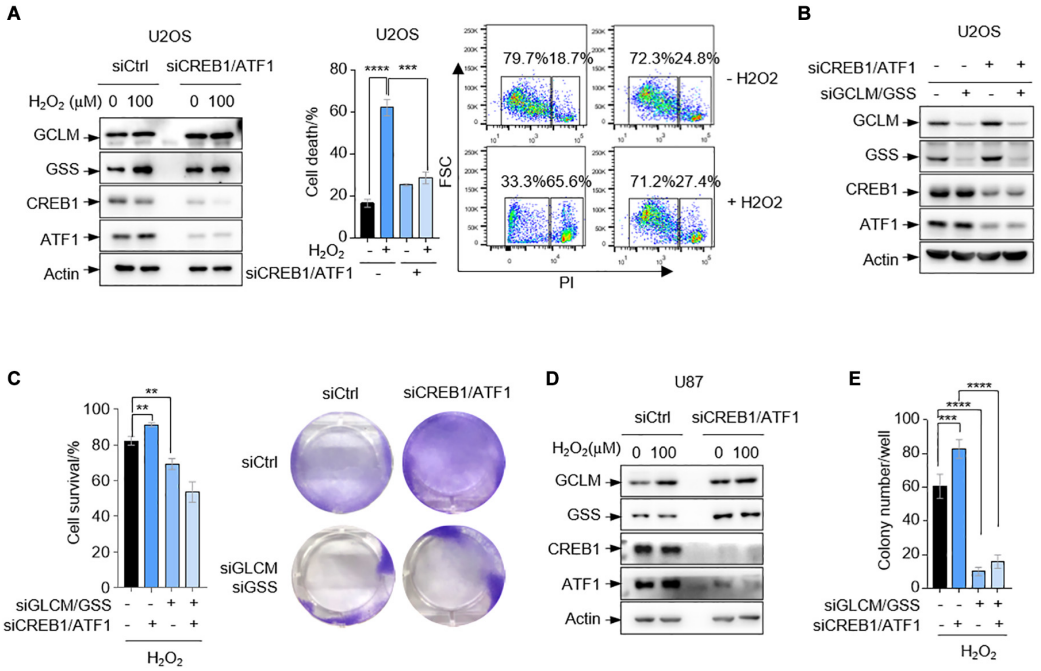

FIGURE 4 | CREB1 and ATF1 inhibit cell survival under oxidative stress. **(A)** U2OS cells transfected with control, or CREB1 and ATF1 siRNAs (siCREB1/ATF1) were treated with 100 μM H_2O_2 for 24 h. Protein expression was measured by Western blot analysis. Cell death was analyzed by flow cytometry after PI staining. **(B,C)** U2OS cells treated with control, CREB1, ATF1, GCLM, and/or GSS siRNAs as indicated. Protein expression was analyzed by Western blot **(B)**, and cell survival was assayed by crystal violet staining **(C)**. **(D)** U87 cells transfected with control siRNA, or siRNAs against CREB1 and ATF1 as indicated were treated with 100 μM H_2O_2 for 24 h. Protein expression was analyzed by Western blot. **(E)** U87 cells were transfected with control, CREB1, ATF1, GCLM, and/or GSS siRNAs for colony formation assay. Numbers of colonies with a diameter greater than 20 μm were quantified. Data are means ± SD. ($n = 3$), $^{**}p < 0.01$, $^{***}p < 0.001$, $^{****}p < 0.0001$.

Chromatin Immunoprecipitation (ChIP) and Reporter Assays

We used JASPAR[1] to identify the potential CREB1 and ATF1 response elements in *GCLM* and *GSS* genes. The ChIP analysis was performed with some modifications. The response elements were amplified by PCR. The primer pairs were: *GCLM* RE1, 5′-CCGCTCGAGGTCCTTGAAGGTAGCAAAGCGA-3′ (forward) and 5′-CCCAAGCTTCGGCCGCCCCAGG GTGGGCTTC-3′ (reverse); *GCLM* RE13, 5′-GAGTCAGAAT AGAACTTCAACTT-3′ (forward) and 5′-TCTCTTCATG TAACTTGCCCAG-3′ (reverse); *GSS* RE6, 5′-CCCT CGAGTCTGCCCCGCCTGCTCTTTAA-3′ (forward) and 5′-CCCAAGCTTCTAGACACTAGTTGCCCCGCTC-3′ (reverse); *GSS* RE20, 5′-GATTCAGGAGTCAATGACTGA-3′ (forward) and 5′-GACAGGTTACAGACTGGAGTAG-3′ (reverse).

For reporter assay, the sequences for CREB1 response elements in *GCLM* and *GSS* gene are: *GCLM*-RE13, 5′-CATGATGATGTC-3′, *GSS*-RE20, 5′-CAGGATGACTTT-3′. The sequences for ATF1 response elements in *GCLM* and *GSS* gene are: *GCLM*-RE1, 5′-CCGCTTGCGCATAAA-3′; *GSS*-RE6, 5′-GGGTCACGTTT-3′. These binding regions were cloned into pGL3-basic vector (Promega, Madison, WI, United States, catalog No: E1751). The luciferase activity was determined using a Dual Luciferase Assay System (Promega, catalog No: E1910). Transfection efficiency was normalized on the basis of the Renilla luciferase activity.

Measurements of GSH and ROS

Glutathione was determined using liquid chromatography-mass spectrometry (LC-MS). We used cold 80% methanol to extract metabolites analyzed by LC-MS. The measured mass isotopomer distributions were corrected by natural abundances.

Reactive oxygen species levels were determined as followed. Cells were incubated at 37°C for 30 min in PBS containing 10 μM 2′,7′-dichlorodihydrofluorescein diacetate (H2-DCFDA, Sigma). Afterward, the cells were washed twice in PBS, treated with trypsin, and resuspended in PBS. Fluorescence was immediately measured using a FACS Flow Cytometer (BD LSRFortessa SORP).

Cell Survival Assay

Cells were transfected with siRNA for 24 h then seeded in 6-well plates in triplicates at the density of 10^5 cells per well in 2 ml medium supplemented with 10% FBS. Cells were added with 100 μM H_2O_2 after fixing on the plate, then incubated for 24 h. For trypan blue staining, cells were harvested with trypsin, washed once and resuspended in PBS, then added 10 μl trypan blue into cell suspension at volume ratio 1:1. Live cell ratio was determined by counting using a hemocytometer. For CV staining, cells were fixed with 10% formalin for 5 min and

[1]http://jaspar.genereg.net

stained with 0.05% CV for 30 min. After washed with distilled water, cells were photographed.

Soft Agar and Colony Formation Assay

U87 cells were transfected with Luciferase siRNA or CREB1 and ATF1 siRNA for 24 h and then suspended in 1 ml MEM medium supplemented with or without 100 μM H_2O_2 plus 20% FBS containing 0.3% agarose and plated on the firm 0.6% agarose base in the 12-well plates (2,000 cells per well). Cells were then cultured in a 37°C with 5% CO_2 incubator. After 2–3 weeks, colonies were stained with 0.05% crystal violet in PBS for 1 h. Counted under a microscope and photoed after colonies turning into blue.

Statistical Analysis

All experiments in this work were performed at least three times independently. Multiple groups comparison was analyzed by two-way ANOVA with multiple comparison test by GraphPad Prism 7. For experiments with only two groups, a two-tailed Student's *t*-test was used to calculate the *P*-value. $P < 0.05$ was considered significant. $^{*}p < 0.05$, $^{**}p < 0.01$, $^{***}p < 0.001$, $^{****}p < 0.0001$, NS, not significant.

DATA AVAILABILITY STATEMENT

The raw data supporting the conclusions of this article will be made available by the authors, without undue reservation.

AUTHOR CONTRIBUTIONS

LZ, WX, and PJ designed the experiments. LZ and WX performed all the experiments. LZ and PJ wrote the manuscript. All authors reviewed and commented on the manuscript.

FUNDING

This research was supported by the National Key R&D Program of China (2019YFA0801701), Tsinghua-Peking Center for Life Sciences, and National Natural Science Foundation of China (81930082) to PJ.

ACKNOWLEDGMENTS

We thank Xiaohui Liu, Xueying Wang, and Lina Xu for the help with LC-MS analysis. We also thank all of the members of the Jiang laboratory for their technical assistance and/or discussions.

SUPPLEMENTARY MATERIAL

The Supplementary Material for this article can be found online at: https://www.frontiersin.org/articles/10.3389/fcell.2021.698264/full#supplementary-material

REFERENCES

Aggarwal, S., Kim, S. W., Ryu, S. H., Chung, W. C., and Koo, J. S. (2008). Growth suppression of lung cancer cells by targeting cyclic AMP response element-binding protein. *Cancer Res.* 68, 981–988. doi: 10.1158/0008-5472.can-06-0249

Ahmad, I. M., Aykin-Burns, N., Sim, J. E., Walsh, S. A., Higashikubo, R., Buettner, G. R., et al. (2005). Mitochondrial O2*- and H2O2 mediate glucose deprivation-induced stress in human cancer cells. *J. Biol. Chem.* 280, 4254–4263. doi: 10.1074/jbc.m411662200

Aykin-Burns, N., Ahmad, I. M., Zhu, Y., Oberley, L. W., and Spitz, D. R. (2009). Increased levels of superoxide and H2O2 mediate the differential susceptibility of cancer cells versus normal cells to glucose deprivation. *Biochem. J.* 418, 29–37. doi: 10.1042/bj20081258

Bonni, A., and Brunet, A. (1999). Cell survival promoted by the Ras-MAPK signaling pathway by transcription-dependent and -independent mechanisms. *Science* 286, 1358–1362. doi: 10.1126/science.286.5443.1358

Chhabra, A., Fernando, H., Watkins, G., Mansel, R. E., and Jiang, W. G. (2007). Expression of transcription factor CREB1 in human breast cancer and its correlation with prognosis. *Oncol. Rep.* 18, 953–958.

Huang, C. S., Anderson, M. E., and Meister, A. (1993a). Amino acid sequence and function of the light subunit of rat kidney gamma-glutamylcysteine synthetase. *J. Biol. Chem.* 268, 20578–20583. doi: 10.1016/s0021-9258(20)80764-9

Huang, C. S., Chang, L. S., Anderson, M. E., and Meister, A. (1993b). Catalytic and regulatory properties of the heavy subunit of rat kidney gamma-glutamylcysteine synthetase. *J. Biol. Chem.* 268, 19675–19680. doi: 10.1016/s0021-9258(19)36569-x

Jiang, P., Du, W., Wang, X., Mancuso, A., Gao, X., Wu, M., et al. (2011). p53 regulates biosynthesis through direct inactivation of glucose-6-phosphate dehydrogenase. *Nat. Cell Biol.* 13, 310–316. doi: 10.1038/ncb2172

Krejsa, C. M., Franklin, C. C., White, C. C., Ledbetter, J. A., Schieven, G. L., and Kavanagh, T. J. (2010). Rapid activation of glutamate cysteine ligase following oxidative stress. *J. Biol. Chem.* 285, 16116–16124. doi: 10.1074/jbc.m110.116210

Li, H., Stokes, W., Chater, E., Roy, R., de Bruin, E., Hu, Y., et al. (2016). Decreased glutathione biosynthesis contributes to EGFR T790M-driven erlotinib resistance in non-small cell lung cancer. *Cell Discov.* 2:16031.

Lu, S. C. (2009). Regulation of glutathione synthesis. *Mol. Aspects Med.* 30, 42–59. doi: 10.1016/j.mam.2008.05.005

Mayr, B., and Montminy, M. (2001). Transcriptional regulation by the phosphorylation-dependent factor CREB. *Nat. Rev. Mol. Cell Biol.* 2, 599–609. doi: 10.1038/35085068

Pigazzi, M., Ricotti, E., Germano, G., Faggian, D., Aricò, M., and Basso, G. (2007). cAMP response element binding protein (CREB) overexpression CREB has been described as critical for leukemia progression. *Haematologica* 92, 1435–1437. doi: 10.3324/haematol.11122

Quintana-Cabrera, R., Fernandez-Fernandez, S., Bobo-Jimenez, V., Escobar, J., Sastre, J., Almeida, A., et al. (2012). gamma-Glutamylcysteine detoxifies reactive oxygen species by acting as glutathione peroxidase-1 cofactor. *Nat. Commun.* 3:718.

Rodic, S., and Vincent, M. D. (2018). Reactive oxygen species (ROS) are a key determinant of cancer's metabolic phenotype. *Int. J. Cancer* 142, 440–448. doi: 10.1002/ijc.31069

Seelig, G. F., Simondsen, R. P., and Meister, A. (1984). Reversible dissociation of gamma-glutamylcysteine synthetase into two subunits. *J. Biol. Chem.* 259, 9345–9347. doi: 10.1016/s0021-9258(17)42703-7

Shankar, D. B., Cheng, J. C., Kinjo, K., Federman, N., Moore, T. B., Gill, A., et al. (2005). The role of CREB as a proto-oncogene in hematopoiesis and in acute myeloid leukemia. *Cancer Cell* 7, 351–362. doi: 10.1016/j.ccr.2005.02.018

Shukla, A., Bosenberg, M. W., MacPherson, M. B., Butnor, K. J., Heintz, N. H., Pass, H. I., et al. (2009). Activated cAMP response element binding protein is overexpressed in human mesotheliomas and inhibits apoptosis. *Am. J. Pathol.* 175, 2197–2206. doi: 10.2353/ajpath.2009.090400

Thway, K., and Fisher, C. (2012). Tumors with EWSR1-CREB1 and EWSR1-ATF1 fusions: the current status. *Am. J. Surg. Pathol.* 36, e1–e11.

Veeravalli, K., Boyd, D., Iverson, B. L., Beckwith, J., and Georgiou, G. (2011). Laboratory evolution of glutathione biosynthesis reveals natural compensatory pathways. *Nat. Chem. Biol.* 7, 101–105. doi: 10.1038/nchembio.499

Conflict of Interest: The authors declare that the research was conducted in the absence of any commercial or financial relationships that could be construed as a potential conflict of interest.

frontiers in Cell and Developmental Biology

ORIGINAL RESEARCH
published: 21 June 2021
doi: 10.3389/fcell.2021.694071

KRT6A Promotes Lung Cancer Cell Growth and Invasion Through MYC-Regulated Pentose Phosphate Pathway

Di Che[1†], Mingshuo Wang[2†], Juan Sun[2†], Bo Li[2], Tao Xu[2], Yuxiong Lu[1], Haiyan Pan[3], Zhaoliang Lu[3,4] and Xiaoqiong Gu[1*]*

[1] Clinical Biological Resource Bank, Guangzhou Institute of Pediatrics, Guangzhou Women and Children's Hospital, Zhongshan School of Medicine, Sun Yat-sen University, Guangzhou, China, [2] Zhongshan School of Medicine, Sun Yat-sen University, Guangzhou, China, [3] The School of Biomedical and Pharmaceutical Sciences, Guangdong University of Technology, Guangzhou, China, [4] Key Laboratory of Diagnosis and Treatment of Severe Hepato-Pancreatic Diseases of Zhejiang Province, The First Affiliated Hospital of Wenzhou Medical University, Wenzhou, China

OPEN ACCESS

Edited by:
Binghui Li,
Capital Medical University, China

Reviewed by:
Jun Fan,
Jinan University, China
Jing Li,
Nankai University, China

***Correspondence:**
Zhaoliang Lu
luzhaoliang8615@126.com
Xiaoqiong Gu
guxiaoqiong@gwcmc.org

[†]These authors have contributed equally to this work

Specialty section:
This article was submitted to Molecular Medicine, a section of the journal Frontiers in Cell and Developmental Biology

Received: *12 April 2021*
Accepted: *30 April 2021*
Published: *21 June 2021*

Citation:
Che D, Wang M, Sun J, Li B, Xu T, Lu Y, Pan H, Lu Z and Gu X (2021) KRT6A Promotes Lung Cancer Cell Growth and Invasion Through MYC-Regulated Pentose Phosphate Pathway. Front. Cell Dev. Biol. 9:694071. doi: 10.3389/fcell.2021.694071

Keratin 6A (KRT6A) belongs to the keratin protein family which is a critical component of cytoskeleton in mammalian cells. Although KRT6A upregulation in non-small cell lung cancer (NSCLC) has been reported, the regulatory mechanism and functional role of KRT6A in NSCLC development have been less well investigated. In this study, KRT6A was confirmed to be highly expressed in NSCLC tissue samples, and its high expression correlated with poor patient prognosis. Furthermore, overexpression of KRT6A promotes NSCLC cell proliferation and invasion. Mechanistically, KRT6A overexpression is sufficient to upregulate glucose-6-phosphate dehydrogenase (G6PD) levels and increase the pentose phosphate pathway flux, an essential metabolic pathway to support cancer cell growth and invasion. In addition, we discovered that lysine-specific demethylase 1A (LSD1) functions upstream to promote KRT6A gene expression. We also found that the MYC family members c-MYC/MYCN are involved in KRT6A-induced G6PD upregulation. Therefore, this study reveals an underappreciated mechanism that KRT6A acts downstream of LSD1 and functions as a pivotal driver for NSCLC progression by upregulating G6PD through the MYC signaling pathway. Together, KRT6A and LSD1 may serve as potential prognostic indictors and therapeutic targets for NSCLC.

Keywords: NSCLC, LSD1, G6PD, MYC, KRT6A

INTRODUCTION

Lung cancer is the most common cause of cancer related death in the world and China, especially among males (Torre et al., 2015; Feng et al., 2019). There are two main histological subtypes of lung cancer, known as small cell lung cancer (SCLC) and non-SCLC (NSCLC). Approximately 85% of lung cancer cases are attributed to NSCLC, and the most common subtypes of NSCLC are lung squamous cell carcinoma (LUSC) and lung adenocarcinoma (LUAD) (Molina et al., 2008). In the past few decades, the therapeutic treatments of NSCLC have made significant progress.

However,the overall cure and survival rate of NSCLC remain low (Herbst et al., 2018). Studies have shown that the 5-year survival rate for NSCLC from stage I to stage IIIA was about 14–49%, whereas the survival rate for stage IIIB/IV was less than 5% (Ko et al., 2018). The high mortality of lung cancer patients is primarily due to the fact that more than half of NSCLC patients already developed metastasis at diagnosis (Herbst et al., 2008; Scrima et al., 2017). Therefore, exploring the molecular mechanisms of NSCLC invasion and metastasis will help improve the therapeutic response and survival of NSCLC patients.

The keratin 6A (KRT6A) is a type II keratin protein involved in the epidermalization of squamous epithelium (Fujii et al., 2002; Chang et al., 2011). Recently, studies have found that KRT6A plays an important role in cell migration, particularly keratinocyte migration (Wang et al., 2018). Silencing KRT6A expression can inhibit cell invasion and metastasis of nasopharyngeal carcinoma (Chen and Shan, 2019). More importantly, high KRT6A levels in lung adenocarcinoma is associated with an unfavorable patient prognosis (Xiao et al., 2017), and KRT6A promotes the growth and metastasis of lung adenocarcinoma through inducing the epithelial-mesenchymal transition (Yang et al., 2020). Nevertheless, the functional mechanism of KRT6A in NSCLC warrants further investigation. Our study demonstrated the relationship between high KRT6A expression and pathological progression of NSCLC, and dissected the molecular mechanism underlying KRT6A regulated invasion of lung cancer cells. These results may assist to better understand the functional roles of KRT6A in NSCLC growth and metastasis, paving the way for developing new therapeutics against this common malignancy.

MATERIALS AND METHODS

Cell Lines and Clinical Tissue Sample

Two NSCLC cell lines (NCI-H1299 and A549) were purchased from Wuhan Procell Life Science and Technology Co. A549 cells were cultured in a Dulbecco Modified Eagle Medium (DMEM) with 10% fetal bovine serum (FBS) which purchased from ExCell Bio, China Co. H1299 cells were cultured in a RPMI 1640 medium with 10% FBS at 37°C and 5% CO_2. Tissue specimens (n = 30) obtained from patients diagnosed as stage I–IV NSCLC who underwent surgery at The First Affiliated Hospital of Wenzhou Medical University were used for immunohistochemical staining. This study was approved by the Ethics Committee of The First Affiliated Hospital of Wenzhou Medical University.

Reagents and Antibodies

Antibody against HA-Tag (1:1,000 times dilution) (Cat. 3724), β-actin (1:1,000 times dilution) (Cat. 3700), Flag-tag (1:1,000 times dilution) (Cat. 66008), KRT6A (1:1,000 times dilution) (Cat. ab93279) and E-cadherin (1:1,000 times dilution) (Cat. ab40772). Goat Anti-Mouse IgG H&L (HRP) (Cat. ab150113) and Goat Anti-Rabbit IgG H&L (HRP) (Cat. ab6721). LSD1 inhibitors ORY-1001 (Cat. S7795), SP2509 (Cat. S7680), GSK2879552 (Cat. S7796) were purchased from Selleck. shKRT6A was purchased from Shanghai Genesci Medical Technology Co., Ltd. G6PD promoter vector was a gift from Dr. Shuai Zhang (Tianjin University of Traditional Chinese Medicine, Tianjin, China). KRT6A promoter vector was obtained from Shandong Vigenebio Technology Co., Ltd.

Western Blot Analysis

Western Blot Analysis was performed using standard techniques: H1299 and A549 cells were harvested with RIPA lysis buffer (Thermo Fisher) on ice for 30 min and then centrifuged at 12,000 rpm for 15 min at 4°C. Total protein was quantified by the bicinchoninic acid assay (Thermo Fisher Scientific). Protein lysates were separated by 12% SDS-PAGE and transferred to PVDF membranes (Millipore). The membranes were blocked with 5% non-fat milk for 1 h, after three times TBST washes then incubated overnight at 4°C with primary antibodies. The membranes were washed and incubated 2 h at room temperature with secondary anti-IgG antibodies. Signals were detected using Luminol substrate solution.

Quantitative Real-Time PCR Analysis

H1299 and A549 cells were harvested for total RNA extraction with TRIzol reagent (Invitrogen). Purified RNA was converted to cDNA using PrimenScript^{TM} RT reagent Kit (Takara) according to the manufacturer's protocol. qRT-PCR was performed using SYBR Green (Biotool) on a Bio-rad CFX96 Real-time PCR System. All gene expression levels were normalized using housekeeping gene, β-actin and the relative fold change were calculated using the $2^{-\Delta\Delta Ct}$ method. KRT6A, G6PD, ACTIN, c-MYC, and MYCN primers for RT-qPCR are provided in **Table 1**.

Luciferase Reporter Assay

Luciferase reporter assay was according to the manufacturer's instructions of Dual-Luciferase Reporter Assay System (Promega). When H1299 cells were cultured to 70% confluence, they were seeded in 6-well plates and co-transfected with c-MYC/MYCN/LSD1 inhibitors with pGL3-G6PD-3'UTR, pGL3-KRT6A-promoter and Renilla luciferase plasmids using Lipo3000 (Sigma-Aldrich). Cells were lysed and each hundred microliters of protein extracts were analyzed in a luminometer for luciferase activity 48 h after transfection.

TABLE 1 | Primer sequences for RT-qPCR.

Gene	Primer sequence
Actin	F:5′-CATCGAGAAATTGAGACGGTG-3′ R: 5′-CCTTGGAAGATGGTCTTGAT-3′
G6PD	F: 5′-TGAGTCAGACAGGCTGGAAC-3′ R: 5′-CACGGAAAAGAGAGGAGATG-3′
KRT6A	F: 5′-AATCGATCCCACCATCCAGC-3′ R: 5′-CTCCAGGTTCTGCCTCACAG-3′
c-MYC	F: 5′-CGTCCTCGGATTCTCTGCTC-3′ R: 5′-GCTGCGTAGTTGTGCTGATG-3′
MYCN	F: 5′-ATGACTTCTACTTCGGCGGC-3′ R: 5′-CCACAGCTCGTTCTCAAGCA-3′

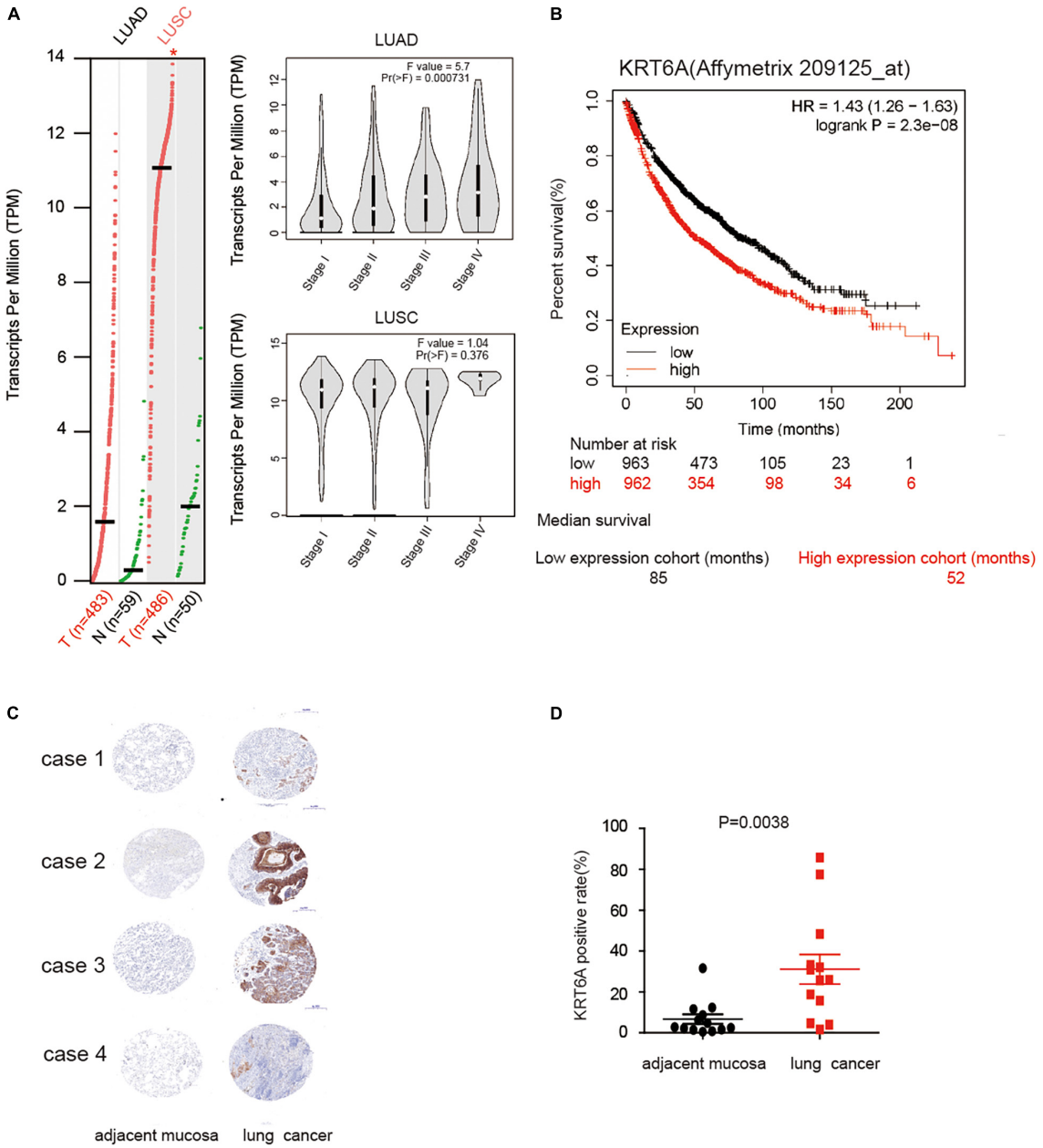

FIGURE 1 | KRT6A is upregulated in NSCLC and associated with patient prognosis. **(A)** The levels of KRT6A in 483 lung adenocarcinoma and 486 lung squamous carcinoma tissues, and its expression differed according to TNM stages as recorded in (http://gepia.cancer-pku.cn/). **(B)** Kaplan-Meiers survival analysis of KRT6A expression in lung cancer patients with low and high tumor expression of KRT6A, calculated from (http://kmplot.com/analysis/). The cutoff lines to divide into high and low group was median value. **(C)** IHC analysis of KRT6A in NSCLC tissues (×400). Note low staining of KRT6A in normal tissues and high staining of KRT6A in NSCLC tissues. **(D)** Quantification of IHC data revealed significantly increased KRT6A expression in NSCLC specimens compared with the adjacent tissues.

EdU Analysis of DNA Synthesis

EdU assay was carried out to determine DNA synthesis level as previously described (Shan et al., 2019). H1299 cells transiently expressed KRT6A were incubated with EdU for 2 h. After fixation and permeabilization, the incorporated EdU was incubated with 1 × Apollo (Ribobio) staining reaction solution for 30 min at room temperature (RT), visualized by means of click reaction. The nuclear DNA was stained with 1 × Hoechst33342 for 60 min at RT. The images were obtained by Leica inverted fluorescence microscope. The data were analyzed by image analysis software.

Cell Proliferation Assay

For cell proliferation assays, cells were seeded at the same number, 10 × 10 (Herbst et al., 2018) cells in six-well plates under the same conditions. Cell growth was

TABLE 2 | Association between KRT6A levels and clinicopathological parameters in NSCLC patients.

Variables	Low expression	High expression	χ^2	*P*
Average of month to birth	977.8	750	458.34	0.565
Pathological stage			25.96	0.001
I	195	70		
II	68	50		
III	40	41		
IV	12	14		

Statistically significant values are shown in red (P < 0.05)

TABLE 3 | Cox regression analysis of risk factors for cancer related death in NSCLC patients.

Element	Univariate		Multivariate	
	P	*HR*	*P*	*HR*
KRT6A (low vs. high)	5.736e-05	1.854	0.016	1.491
Average of month to birth	0.317	1.008	0.185	1.012
Pathological stage				
I	0.748	1.388	0.849	1.212
II	0.294	3.832	0.494	2.045
III	0.200	3.973	0.460	2.253
IV	0.119	5.061	0.216	3.683

Statistically significant values are shown in red (P < 0.05)

determined by counting cell numbers at 0, 1, 2, 3, and 4 days after seeding.

Transwell Assay

Transwell assay was carried out using transwell chambers (Corning) for detecting the invasiveness of H1299 cells and performed using 24 well transwell plates with polycarbonate membrane and 4.0 μM pores (Corning). After 24 h of LSD1 inhibitors treatment or 48 h of transfection, H1299 cells in serum-free RPMI 1640 medium were seeded in chambers with solidified matrigel (4.0 μg/μL, 60 μL) in advance for 3 h at RT. RPMI 1640 medium with 10% FBS was added to the lower chambers. H1299 cells in the upper chambers were at a density of 500 cells/per well. After 24 h, the medium from the lower chamber was removed and the upper chamber cells were wiped, then the migrated cells were fixed in 4% paraformaldehyde and stained with crystal violent for 30 min at RT. Migrating cell numbers were observed in four random fields under an inverted phase microscope (Leica) and cell numbers were enumerated using Image J.

Lentivirus Production and Generation of Stable Cell Lines

To produce lentivirus, psPAX2, pMD2.G and lentiviral vector were packaged with Lipofectamine2000 and transfected into HEK293T cells in 10 cm dishes according to a standard packaging system. The virus medium was collected and filtered two times at 24 and 48 h after transfection. To establish stable cell lines, cells were infected with virus-containing medium (filtered virus medium and fresh medium 1:1, and added 5 μg/mL polybrene). To screen the positively infected cells, 5 μg/mL puromycin was added 72 h after infection and selected for 7 days.

The target sequence of shKRT6A is: 1#: 5′-GCTCTCAAACT CTCTAACTTA-3′, 2#: 5′-TCGCTGTTTGCAATTGCTAAA-3′, 3#: 5′-CTCCAGCAGGAAGAGCTATAA-3′.

Bioinformatic Analysis

The public data set GSE19804 and the Gene Expression Profiling Interactive Analysis (GEPIA)[1] were used for bioinformatics analysis. Overall survival analysis was performed by Kaplan-Meier Plotter[2].

Statistical Analysis

All data were representative of three independent experiments and presented as the mean ± standard error. Statistical analyses were calculated from Student's *t*-test. $P < 0.05$ was considered to indicate a statistically significant difference.

RESULTS

KRT6A Expression Is Altered in Lung Cancer

To explore the role of KRT6A in lung cancer, we used expression data for KRT6A in lung cancer from The Cancer Genome Atlas (TCGA) database. KRT6A expression was significantly higher in lung adenocarcinoma (LUAD) and lung squamous cell carcinoma (LUSC) than normal tissues. Further analysis identified KRT6A expression also differed according to TNM stage. In LUAD, KRT6A were upregulated with increasing TNM stages, whereas KRT6A expression was

[1]http://gepia.cancer-pku.cn/
[2]http://kmplot.com/analysis

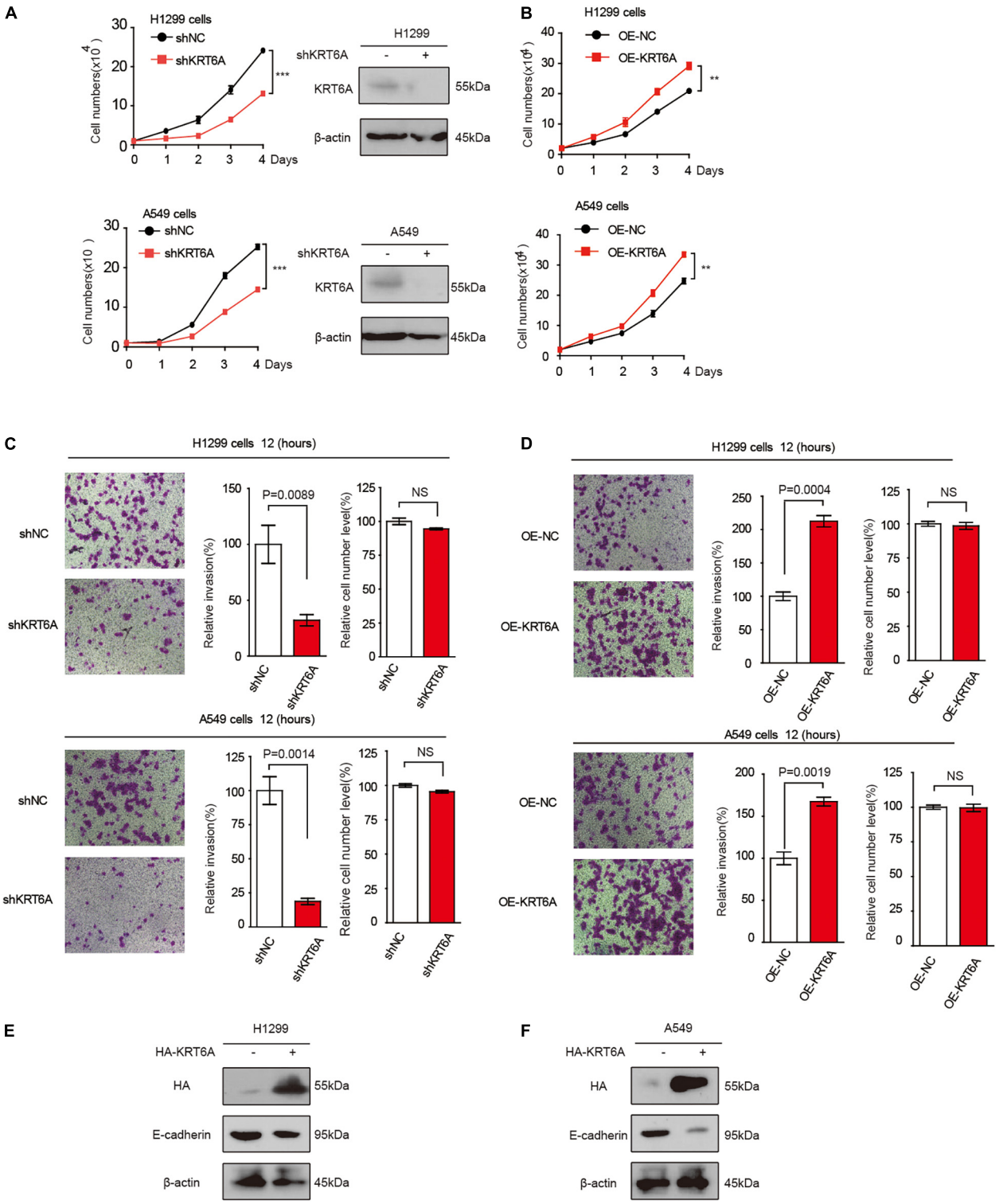

FIGURE 2 | KRT6A promotes lung cancer cell proliferation and invasion. **(A)** Cell proliferation rates of human lung cancer H1299 and A549 cells with stable knockdown of KRT6A. **(B)** Cell proliferation rates of human lung cancer H1299 and A549 cells with stable expression of KRT6A. **(C)** Transwell assay of cell invasion was performed in human lung cancer H1299 and A549 cells with stable knockdown of KRT6A. **(D)** Transwell assay of cell invasion was performed in human lung cancer H1299 and A549 cells with stable expression of KRT6A. **(E,F)** Overexpression of KRT6A significantly decreases E-cadherin levels in H1299 and A549 cells (**$0.001 < p < 0.01$; ***$p < 0.001$).

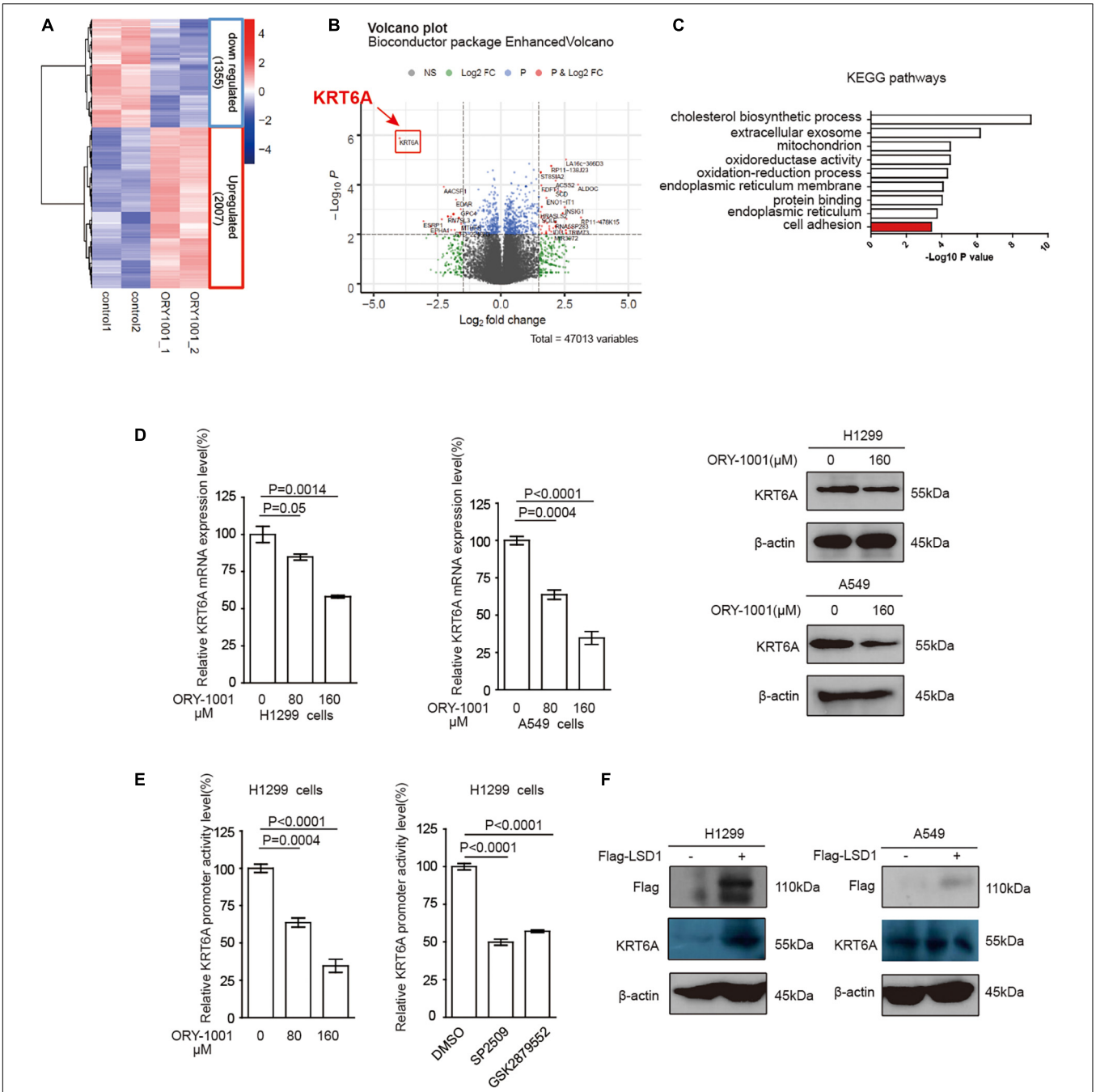

FIGURE 3 | LSD1 is involved in regulating KRT6A expression. **(A,B)** The transcripts in H1299 cells was determined by RNA-sequencing, showing that KRT6A was significantly reduced in H1299 cells treated with a LSD1 inhibitor ORY-1001. **(C)** KEGG pathways analysis of the RNA sequencing results revealed that 10 significantly altered pathways were identified and the cell adhesion pathway was highlighted in red. **(D)** The mRNA and protein expression of KRT6A after ORY-1001 treatments were significantly lower compared to control in H1299 and A549 cells. **(E)** The LSD1 inhibitors (ORY-1001, SP2509, and GSK2879552) led to significantly reduced KRT6A promoter activity. **(F)** Overexpression of LSD1 promotes KRT6A protein expression.

significantly increased in advanced LUSC tumors (**Figure 1A**). Kaplan-Meier analysis shows that high levels of KRT6A expression was associated with poor patient prognosis, based on calculations from http://kmplot.com/analysis/. The median survival of patients with low KRT6A expression was 85 months and high expression was 52 months (**Figure 1B**). Furthermore, immunohistochemical staining results showed significantly increased levels of KRT6A protein in tumor tissues than normal adjacent tissues (**Figures 1C,D**; $p < 0.05$). In summary, these data suggested that KRT6A expression is highly correlated with poor prognostic factors in NSCLC.

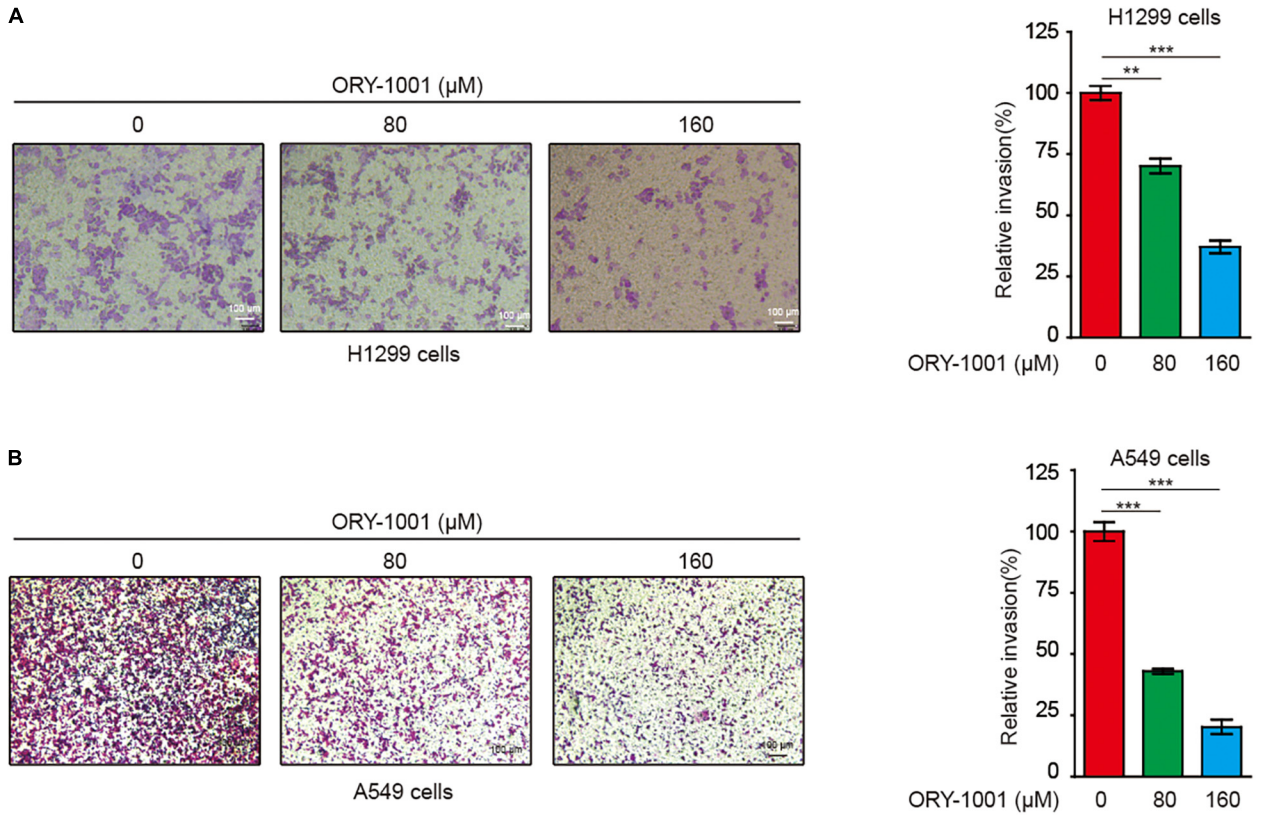

FIGURE 4 | ORY-1001 inhibits NSCLC cell invasion. **(A)** Transwell assay of cell invasion was performed in human lung cancer H1299 cells treated with or without ORY-1001. **(B)** Transwell assay of cell invasion was performed in human lung cancer A549 cells treated with or without ORY-1001 (**$0.001 < p < 0.01$; ***$p < 0.001$).

The Relationship Between KRT6A and Clinicopathological Characteristics in Patients With NSCLC

The clinicopathological characteristics of NSCLC patients are presented in **Table 2**, IHC analysis confirmed that high expression of KRT6A was associated with pathological stage ($p = 0.001$). Furthermore, Univariate and multivariate Cox regression analysis was performed in NSCLC patients. We found that patients with high KRT6A expression showed significantly high risk of death (univariate cox regression analysis: hazard ratio = 1.491, $p = 0.016$) (multivariate Cox regression analysis: hazard ratio = 1.854, $p = 5.736e\text{-}05$; **Table 3**). These results indicated that KRT6A could be used as a risk factor to predict the clinical outcome of NSCLC patients.

KRT6A Promotes Cell Proliferation and Invasion of NSCLC Cells

To address the functional consequence of KRT6A upregulation in lung cancer, we established H1299 and A549 cells with KRT6A knockdown or overexpression. Our results show that depleting KRT6A inhibited cell proliferation of lung cancer cells (**Figure 2A**), and KRT6A overexpression promoted cell proliferation (**Figure 2B**). Furthermore, overexpression of KRT6A significantly promoted cell invasion (>twofold promotion, $p < 0.01$) (**Figures 2C,D**). Consistent with this result, we found that the expression of E-cadherin was decreased by transient overexpression of KRT6A (**Figures 2E,F**). These data indicate that KRT6A promotes lung cancer cell proliferation and invasion.

LSD1 Promotes KRT6A Expression

LSD1 is an amine oxidase histone demethylase, and ORY-1001 is a potent and selective covalent inhibitor of LSD1 that suppresses the proliferation of acute leukemia cells (Fiskus et al., 2014). In this study, we investigated ORY-1001 treated and control H1299 cells with transcriptomic analysis via RNA-seq. After correction for multi-testing by controlling the false discovery rate at 0.05, we noticed that 2,007 genes were down-regulated, and 1,355 genes were up-regulated with ORY-1001 treatments (**Figure 3A**), with KRT6A being most significantly attenuated (**Figure 3B**). Pathway enrichment analysis revealed different pathways altered in ORY-1001 treated cells, including the cell adhesion pathway (**Figure 3C**). Quantitative real time-PCR and western blot analyses validated the suppression of KRT6A expression by multiple LSD1 inhibitors (ORY-1001, SP2509, and GSK879552) (**Figure 3D**). We also examined KRT6A promoter activity using a luciferase reporter, and found that LSD1 inhibitors significantly repressed KRT6A promoter activity (**Figure 3E**). Moreover, overexpression LSD1

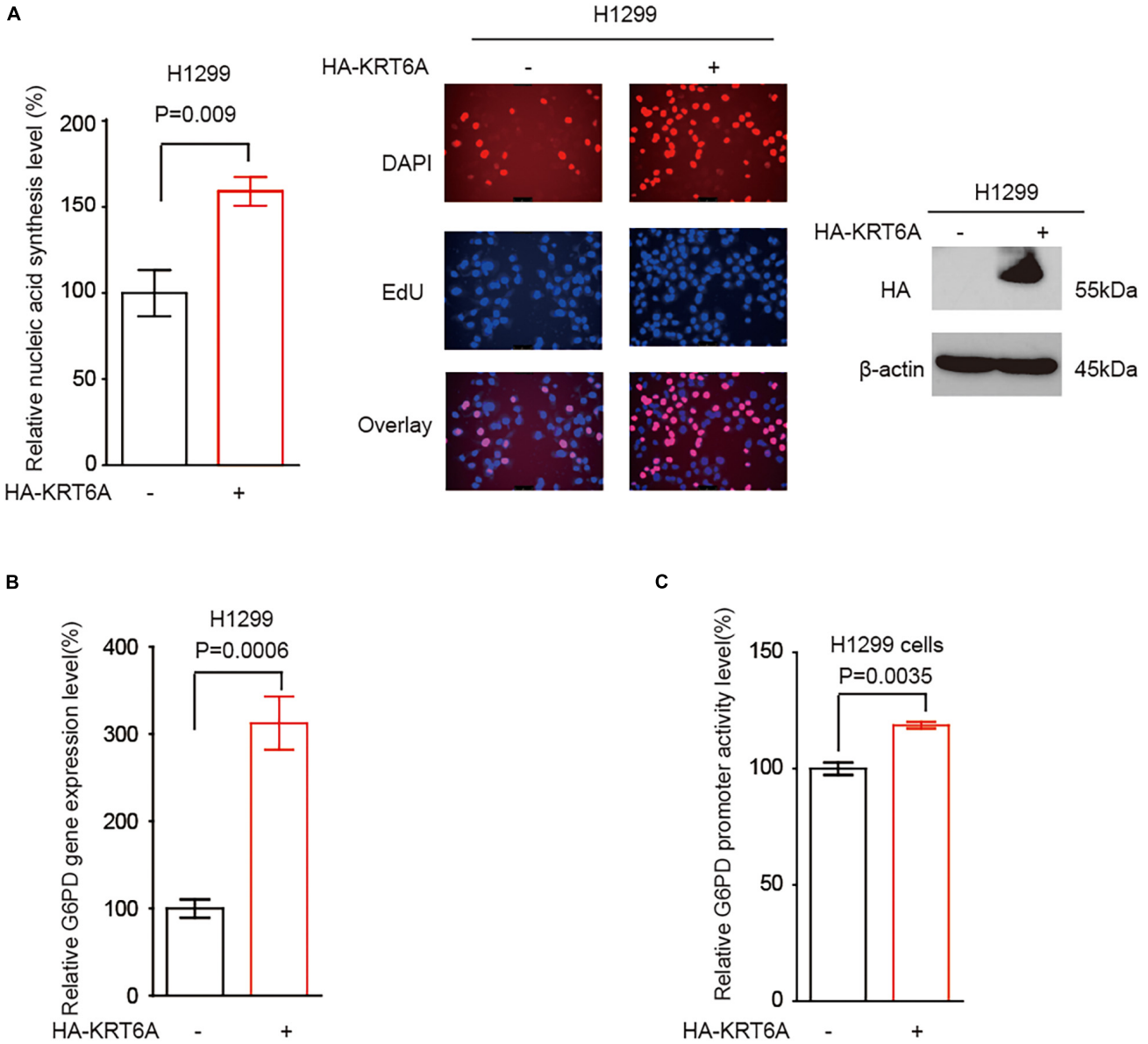

FIGURE 5 | KRT6A promotes G6PD expression. **(A)** DNA synthesis was quantified in H1299 cells overexpressing KRT6A or an empty vector. **(B)** Determination of G6PD expression levels by Real-time PCR in KRT6A overexpressing and control H1299 cells. **(C)** Determination of G6PD promoter activity in KRT6A overexpressing and control H1299 cells.

could promote KRT6A protein expression in H1299 and A549 cells (**Figure 3F**).

ORY-1001 Inhibits the Invasion of NSCLC Cells

Next, we conducted the transwell invasion assay to detect whether the LSD1 inhibitor could inhibit the invasion capability of lung cancer cells. As expected, ORY-1001 significantly inhibited the invasion of lung adenocarcinoma H1299 and A549 cells (**Figures 4A,B**).

KRT6A Promotes G6PD Expression

It has become noted that the pentose phosphate pathway (PPP) plays a critical role in cancer cell invasion, partially through upregulating DNA synthesis (Shan et al., 2019). However, the detailed signaling event regulating PPP to promote invasion is far from clear. G6PD is the rate-limiting enzyme of PPP flux, which may facilitate cancer cell invasion. Accordingly, we speculated that KRT6A may regulate G6PD expression and PPP flux to stimulate invasion. Indeed, overexpression of KRT6A could enhance DNA synthesis (**Figure 5A**), increase G6PD transcript level (**Figure 5B**), and strengthen G6PD promoter activity (**Figure 5C**).

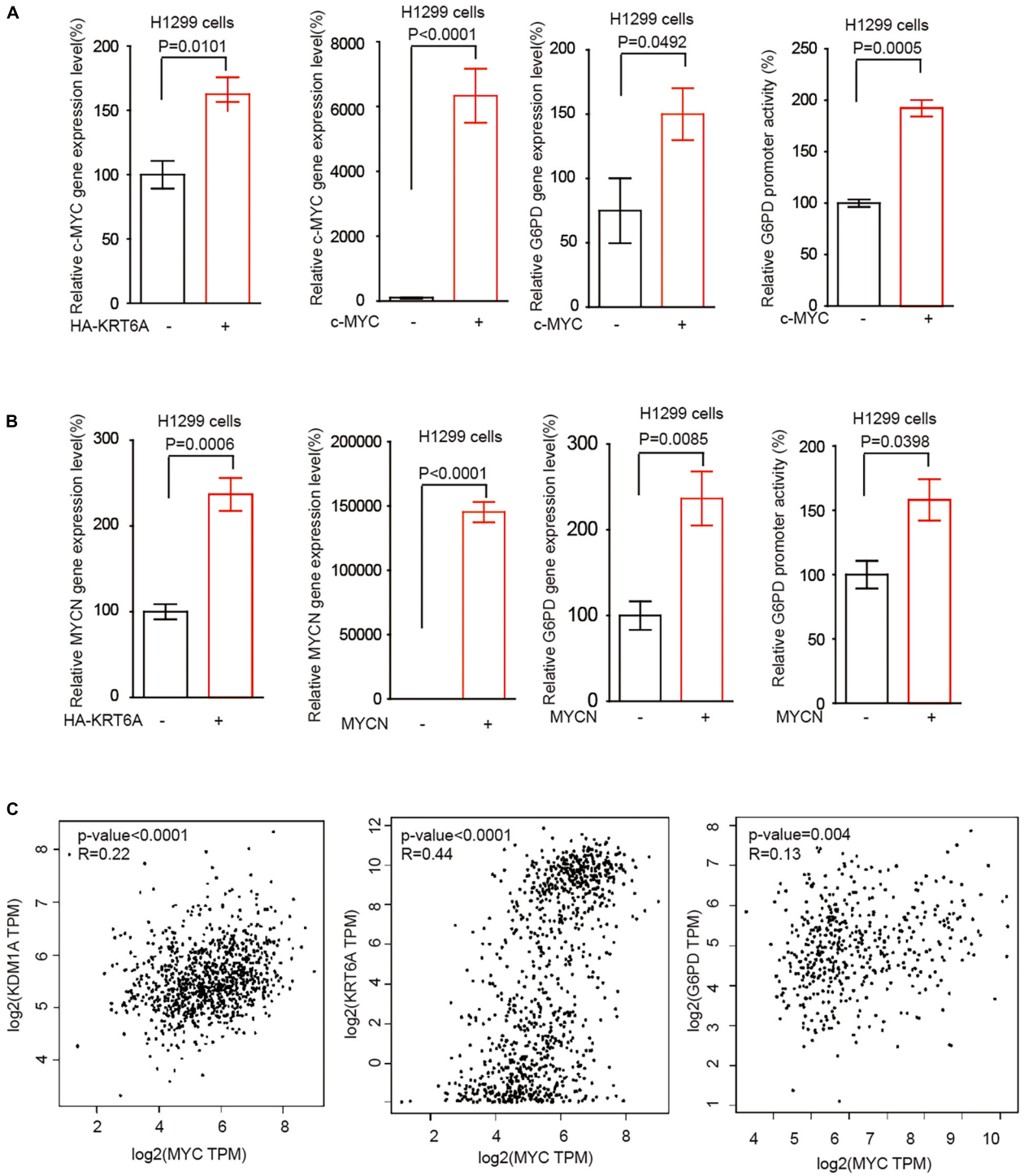

FIGURE 6 | KRT6A promotes G6PD expression through upregulation of c-MYC and MYCN. **(A)** Determination of c-MYC mRNA expression levels by Real-time PCR (left) in KRT6A overexpressing and control H1299 cells. The G6PD mRNA expression level and G6PD promoter activity (right) in c-MYC overexpressing and control H1299 cells. **(B)** The MYCN mRNA expression levels by Real-time PCR (left) in KRT6A overexpressing and control H1299 cells. The G6PD mRNA expression level and G6PD promoter activity (right) in MYCN overexpressing and control H1299 cells. **(C)** Correlation of c-MYC with LSD1 (KDM1A), KRT6A and G6PD expression in NSCLC tumor tissues, calculated from http://gepia.cancer-pku.cn/.

KRT6A Promotes G6PD Expression Through Upregulating c-MYC/MYCN

The MYC family member c-MYC and MYCN are the most frequently deregulated oncogenes in human cancer and promote tumor progression through multiple levels of mechanisms in particular reprogrammed metabolism (Yoshida, 2020). Interestingly, we found that KRT6A overexpression augmented c-MYC/MYCN gene expression. Furthermore, c-MYC/MYCN significantly upregulated the expression of G6PD and enhanced its promoter activity, phenocopying the effect of KRT6A (**Figures 6A,B**). Next, correlation analysis indicated that expression of c-MYC and KRT6A, LSD1, G6PD were positively correlated in NSCLC tumor tissues (**Figure 6C**). These data indicated that KRT6A might induce G6PD expression by upregulating c-MYC/MYCN.

DISCUSSION

Recent studies revealed that high expression of KRT6A is associated with unfavorable prognosis of lung cancer patients (Xiao et al., 2017). A study by Yang et al. (2020) suggested that KRT6A promotes the growth and metastasis of lung adenocarcinoma through inducing the epithelial-mesenchymal transition. Here, our study has yielded similar results, by showing that KRT6A is upregulated in NSCLC tumors and promotes lung cancer cell proliferation and invasion *in vitro*. Consistently, KRT6A significantly decreases E-cadherin levels in lung cancer cells. Through clinical analysis, we found that the elevated expression of KRT6A can be used as a risk factor for predicting the survival outcome of NSCLC patients. Interestingly, another study confirmed our finding by showing that KRT6A inhibits the proliferation and invasion of lung adenocarcinoma cells, and high expression of KRT6A protein may be a prognostic marker for patients with lung adenocarcinoma (Xiao et al., 2020). Therefore, deeper investigations are warranted to explore the function of KRT6A in lung cancer progression.

Histone lysine-specific demethylase 1 (LSD1/KDM1A) has been considered as an important and promising anti-cancer target (Fang et al., 2019; Dai et al., 2020). LSD1 is overexpressed in various tumor types, and may induce cancer cell proliferation, invasion, and migration (Dai et al., 2020). Importantly, studies have shown that LSD1 is a potential therapeutic target for NSCLC. High levels of LSD1 are correlated with poor prognosis of NSCLC patients and the proliferation, migration, and invasion capabilities of tumor cells (Lv et al., 2012). Moreover, it was reported that LSD1+8a is a LSD1 isoform contributing to neural differentiation in small cell lung cancer (Jotatsu et al., 2017). In addition, Takagi et al. (2017) found that the LSD1 inhibitor T-3775440 inhibits the proliferation of lung cancer cells by disrupting the LSD1 interaction with the SNAG domain proteins INSM1 and GFI1B. Our previous work suggested that another LSD1 inhibitor ORY-1001 inhibits lung cancer cell growth and induces cell apoptosis by triggering HK2-mediated cellular events (Lu et al., 2018). In this study, our data revealed that LSD1 promotes KRT6A expression. Moreover, we found that ORY-1001 inhibits the invasion of NSCLC cells in a dose-dependent manner, which is reminiscent of a recent finding that ORY-1001 induces tumor regression in small cell lung cancer patient-derived xenograft model by regulating NOTCH (Augert et al., 2019).

The molecular mechanism whereby KRT6A expression promotes tumor progression is incompletely understood. Notably, studies have found that the pentose phosphate pathway (PPP) is an essential glucose metabolic pathway promoting tumor growth and metastasis (such as in lung cancer). G6PD as a crucial rate-limiting enzyme of PPP, greatly facilitates tumor invasion (Mele et al., 2018; Jin and Zhou, 2019). Nagashio et al. (2019) reported that the survival rate of lung adenocarcinoma patients with G6PD upregulation in the invasive frontier was significantly lower than those without G6PD upregulation. Multivariate analysis further showed that G6PD expression is an independent factor for patient prognosis (Nagashio et al., 2019). Our study revealed that overexpression of KRT6A could promote DNA synthesis, increase G6PD expression level, and enhance G6PD promoter activity. These results suggested that KRT6A may promote lung cancer progression by regulating G6PD.

It has been reported that c-MYC and MYCN are amplified and/or overexpressed in lung cancer. c-MYC and MYCN may be used as therapeutic targets for treating lung cancer patients (Masso-Valles et al., 2020). There are also research findings showing that c-MYC is involved in the regulation of G6PD expression (Yang et al., 2018). In this study, we observed that KRT6A could promote c-MYC/MYCN expression. Furthermore, c-MYC/MYCN significantly upregulates the expression of G6PD by stimulating its promoter activity. Correlation analysis indicated that expressions of c-MYC and KRT6A, LSD1, G6PD were all positively correlated in NSCLC tumors. Together, our results indicated that KRT6A might induce G6PD expression through the c-MYC/MYCN axis.

In summary, we discovered that KRT6A expression is frequently upregulated in lung cancer. KRT6A regulates the expression of G6PD through c-MYC/MYCN to promote the proliferation and invasion of lung cancer cells. The elevated expression of KRT6A can be used as a risk factor for predicting the clinical outcome of NSCLC patients. Our data provide additional evidences to support KRT6A and LSD1 as potential therapeutic targets for treating NSCLC.

DATA AVAILABILITY STATEMENT

The datasets presented in this study can be found in online repositories. The names of the repository/repositories and accession number(s) can be found in the article/ **Supplementary Material**.

ETHICS STATEMENT

The studies involving human participants were reviewed and approved by Ethics Committee of Wenzhou Medical University. The patients/participants provided their written informed consent to participate in this study.

AUTHOR CONTRIBUTIONS

All authors contributed significantly to this work, gave final approval of the version to be published and agreed to be accountable for all aspects of the work, participated in drafting the article or revising it critically for important intellectual content, agreed to submit the manuscript to the current journal, made substantial contributions to the conception and design of the study as well as the acquisition, analysis and interpretation of data.

FUNDING

This study was supported by the pilot Grant from The First Affiliated Hospital of Wenzhou Medical University (7K0023), The Guangdong Natural Science Foundation (China, 2019A1515012061), The Guangzhou Institute of Pediatrics/Guangzhou Women and Children's Medical Center Fund (China, YIP-2018-019, GCP-2019-003, GCP-2019-006, and YIP-2019-050), and Guangzhou Science and Technology Program Key Projects (China, 20190401 0486).

SUPPLEMENTARY MATERIAL

The Supplementary Material for this article can be found online at: https://www.frontiersin.org/articles/10.3389/fcell.2021.694071/full#supplementary-material

REFERENCES

Augert, A., Eastwood, E., Ibrahim, A. H., Wu, N., Grunblatt, E., Basom, R., et al. (2019). Targeting NOTCH activation in small cell lung cancer through LSD1 inhibition. *Sci. Signal* 12:eaau2922.

Chang, H. H., Dreyfuss, J. M., and Ramoni, M. F. (2011). A transcriptional network signature characterizes lung cancer subtypes. *Cancer* 117, 353–360.

Chen, C., and Shan, H. (2019). Keratin 6A gene silencing suppresses cell invasion and metastasis of nasopharyngeal carcinoma via the betacatenin cascade. *Mol. Med. Rep.* 19, 3477–3484.

Dai, X. J., Liu, Y., Xiong, X. P., Xue, L. P., Zheng, Y. C., and Liu, H. M. (2020). Tranylcypromine Based Lysine-Specific Demethylase 1 inhibitor: summary and perspective. *J. Med. Chem.* 63, 14197–14215.

Fang, Y., Liao, G., and Yu, B. (2019). LSD1/KDM1A inhibitors in clinical trials: advances and prospects. *J. Hematol. Oncol.* 12:129.

Feng, R. M., Zong, Y. N., Cao, S. M., and Xu, R. H. (2019). Current cancer situation in China: good or bad news from the 2018 Global Cancer Statistics? *Cancer Commun. (Lond).* 39:22.

Fiskus, W., Sharma, S., Shah, B., Portier, B. P., Devaraj, S. G., Liu, K., et al. (2014). Highly effective combination of LSD1 (KDM1A) antagonist and pan-histone deacetylase inhibitor against human AML cells. *Leukemia* 28, 2155–2164.

Fujii, T., Dracheva, T., Player, A., Chacko, S., Clifford, R., Strausberg, R. L., et al. (2002). A preliminary transcriptome map of non-small cell lung cancer. *Cancer Res.* 62, 3340–3346.

Herbst, R. S., Heymach, J. V., and Lippman, S. M. (2008). Lung cancer. *N. Engl. J. Med.* 359, 1367–1380.

Herbst, R. S., Morgensztern, D., and Boshoff, C. (2018). The biology and management of non-small cell lung cancer. *Nature* 553, 446–454.

Jin, L., and Zhou, Y. (2019). Crucial role of the pentose phosphate pathway in malignant tumors. *Oncol. Lett.* 17, 4213–4221.

Jotatsu, T., Yagishita, S., Tajima, K., Takahashi, F., Mogushi, K., Hidayat, M., et al. (2017). LSD1/KDM1 isoform LSD1+8a contributes to neural differentiation in small cell lung cancer. *Biochem. Biophys. Rep.* 9, 86–94.

Ko, E. C., Raben, D., and Formenti, S. C. (2018). The integration of radiotherapy with immunotherapy for the treatment of non-small cell lung cancer. *Clin. Cancer Res.* 24, 5792–5806.

Lu, Z., Guo, Y., Zhang, X., Li, J., Li, L., Zhang, S., et al. (2018). ORY-1001 suppresses cell growth and induces apoptosis in lung cancer through triggering HK2 mediated warburg effect. *Front. Pharmacol.* 9:1411. doi: 10.3389/fphar.2018.01411

Lv, T., Yuan, D., Miao, X., Lv, Y., Zhan, P., Shen, X., et al. (2012). Over-expression of LSD1 promotes proliferation, migration and invasion in non-small cell lung cancer. *PLoS One* 7:e35065. doi: 10.1371/journal.pone.0035065

Masso-Valles, D., Beaulieu, M. E., and Soucek, L. M. Y. C. (2020). MYCL, and MYCN as therapeutic targets in lung cancer. *Expert. Opin. Ther. Targets* 24, 101–114.

Mele, L., Paino, F., Papaccio, F., Regad, T., Boocock, D., Stiuso, P., et al. (2018). A new inhibitor of glucose-6-phosphate dehydrogenase blocks pentose phosphate pathway and suppresses malignant proliferation and metastasis in vivo. *Cell Death Dis.* 9:572.

Molina, J. R., Yang, P., Cassivi, S. D., Schild, S. E., and Adjei, A. A. (2008). Non-small cell lung cancer: epidemiology, risk factors, treatment, and survivorship. *Mayo Clin. Proc.* 83, 584–594.

Nagashio, R., Oikawa, S., Yanagita, K., Hagiuda, D., Kuchitsu, Y., Igawa, S., et al. (2019). Prognostic significance of G6PD expression and localization in lung adenocarcinoma. *Biochim. Biophys. Acta Proteins Proteom.* 1867, 38–46.

Scrima, M., Zito Marino, F., Oliveira, D. M., Marinaro, C., La Mantia, E., Rocco, G., et al. (2017). Aberrant Signaling through the HER2-ERK1/2 pathway is predictive of reduced disease-free and overall survival in early stage non-small cell lung cancer (NSCLC) patients. *J. Cancer* 8, 227–239.

Shan, C. L., Lu, Z. L., Li, Z., Sheng, H., Fan, J., Qi, Q., et al. (2019). 4-hydroxyphenylpyruvate dioxygenase promotes lung cancer growth via pentose phosphate pathway (PPP) flux mediated by LKB1-AMPK/HDAC10/G6PD axis. *Cell Death Dis.* 10:13.

Takagi, S., Ishikawa, Y., Mizutani, A., Iwasaki, S., Matsumoto, S., Kamada, Y., et al. (2017). LSD1 inhibitor T-3775440 Inhibits SCLC Cell proliferation by disrupting LSD1 interactions with SNAG domain proteins INSM1 and GFI1B. *Cancer Res.* 77, 4652–4662.

Torre, L. A., Bray, F., Siegel, R. L., Ferlay, J., Lortet-Tieulent, J., and Jemal, A. (2015). Global cancer statistics, 2012. *CA Cancer J. Clin.* 65, 87–108.

Wang, F., Chen, S., Liu, H. B., Parent, C. A., and Coulombe, P. A. (2018). Keratin 6 regulates collective keratinocyte migration by altering cell-cell and cell-matrix adhesion. *J. Cell Biol.* 217, 4314–4330.

Xiao, J., Kuang, X., Dai, L., Zhang, L., and He, B. (2020). Anti-tumour effects of Keratin 6A in lung adenocarcinoma. *Clin. Respir. J.* 14, 667–674.

Xiao, J., Lu, X., Chen, X., Zou, Y., Liu, A., Li, W., et al. (2017). Eight potential biomarkers for distinguishing between lung adenocarcinoma and squamous cell carcinoma. *Oncotarget* 8, 71759–71771.

Yang, B., Zhang, W., Zhang, M., Wang, X., Peng, S., and Zhang, R. (2020). KRT6A Promotes EMT and cancer stem cell transformation in lung adenocarcinoma. *Technol. Cancer Res. Treat.* 19:1533033820921248.

Yang, X., Ye, H., He, M., Zhou, X., Sun, N., Guo, W., et al. (2018). LncRNA PDIA3P interacts with c-Myc to regulate cell proliferation via induction of pentose phosphate pathway in multiple myeloma. *Biochem. Biophys. Res. Commun.* 498, 207–213.

Yoshida, G. J. (2020). Beyond the Warburg Effect: N-Myc contributes to metabolic reprogramming in cancer cells. *Front. Oncol.* 10:791. doi: 10.3389/fonc.2020.00791

Conflict of Interest: The authors declare that the research was conducted in the absence of any commercial or financial relationships that could be construed as a potential conflict of interest.

frontiers in Cell and Developmental Biology

ORIGINAL RESEARCH
published: 12 July 2021
doi: 10.3389/fcell.2021.703338

Genome-Wide Analysis Identifies *Rag1* and *Rag2* as Novel Notch1 Transcriptional Targets in Thymocytes

Yang Dong[1,2†], Hao Guo[1,2†], Donghai Wang[2], Rongfu Tu[2], Guoliang Qing[2] and Hudan Liu[1,2*]*

[1] Department of Hematology, Zhongnan Hospital of Wuhan University, Wuhan, China, [2] Frontier Science Center for Immunology and Metabolism, Medical Research Institute, Wuhan University, Wuhan, China

OPEN ACCESS

Edited by:
Binghui Li,
Capital Medical University, China

Reviewed by:
Bo Li,
Sun Yat-sen University, China
Peng Li,
Guangzhou Institutes of Biomedicine and Health, Chinese Academy of Sciences (CAS), China

***Correspondence:**
Guoliang Qing
qingguoliang@whu.edu.cn
Hudan Liu
hudanliu@whu.edu.cn

† These authors have contributed equally to this work

Specialty section:
This article was submitted to Molecular Medicine, a section of the journal Frontiers in Cell and Developmental Biology

Received: 30 April 2021
Accepted: 15 June 2021
Published: 12 July 2021

Citation:
Dong Y, Guo H, Wang D, Tu R, Qing G and Liu H (2021) Genome-Wide Analysis Identifies Rag1 and Rag2 as Novel Notch1 Transcriptional Targets in Thymocytes. Front. Cell Dev. Biol. 9:703338. doi: 10.3389/fcell.2021.703338

Recombination activating genes 1 (*Rag1*) and *Rag2* are expressed in immature lymphocytes and essential for generating the vast repertoire of antigen receptors. Yet, the mechanisms governing the transcription of *Rag1* and *Rag2* remain to be fully determined, particularly in thymocytes. Combining cDNA microarray and ChIP-seq analysis, we identify *Rag1* and *Rag2* as novel Notch1 transcriptional targets in acute T-cell lymphoblastic leukemia (T-ALL) cells. We further demonstrate that Notch1 transcriptional complexes directly bind the *Rag1* and *Rag2* locus in not only T-ALL but also primary double negative (DN) T-cell progenitors. Specifically, dimeric Notch1 transcriptional complexes activate *Rag1* and *Rag2* through a novel *cis*-element bearing a sequence-paired site (SPS). In T-ALL and DN cells, dimerization-defective Notch1 causes compromised *Rag1* and *Rag2* expression; conversely, dimerization-competent Notch1 achieves optimal upregulation of both. Collectively, these results reveal Notch1 dimerization-mediated transcription as one of the mechanisms for activating *Rag1* and *Rag2* expression in both primary and transformed thymocytes. Our data suggest a new role of Notch1 dimerization in compelling efficient TCRβ rearrangements in DN progenitors during T-cell development.

Keywords: Notch1 dimerization, Recombination activating genes, T-cell acute lymphoblastic leukemia, Double negative thymocyte, T-cell development

INTRODUCTION

Notch receptors are a family of heterodimeric transmembrane proteins that determine cell fate decisions and growth control. A prime example is that Notch1, one of the four isoforms (Notch1–4), plays an essential role in T-cell development and homeostasis. From a surface protein to a nuclear transcription factor, Notch1 signaling becomes active upon interaction with the Delta and Serrate family of ligands (Delta-like 1, 3, and 4; and Jagged 1 and 2) on juxtaposed cells. This interaction triggers conformational changes of Notch1, allows stepwise proteolytic cleavages, and releases intracellular Notch1 (ICN1). ICN1 then rapidly translocates into the nucleus and forms a transcriptional activation complex with the DNA binding factor RBPJ (also known as CSL) and coactivator of the mastermind family (MAML) (Kopan and Ilagan, 2009). As previously reported, ICN1/RBPJ/MAML complexes dimerize in the nucleus through cooperatively assembling on a

specific sequence-paired site (SPS) in the promoter/enhancer of target genes, where the ANK domain within ICN1 mediates the dimer formation (Nam et al., 2007; Arnett et al., 2010).

Notch1 serves as a key regulator required at multiple stages for T-cell progenitor specification and maturation. Notch1 signaling determines T-cell lineage commitment and is essential to generate the early T-cell progenitors (ETP) from multipotent lymphoid progenitors (Sambandam et al., 2005; Tan et al., 2005). Inactivation of Notch1 signaling in hematopoietic progenitors results in a complete failure of T-cell generation, while it induces ectopic B-cell development in the thymus (Pui et al., 1999). Conversely, Notch1 overexpression causes extrathymic T-cell development in bone marrow at the expense of B cells (Radtke et al., 1999). Continuous Notch1 signaling is imperative in lymphocyte developmental progression through ETP, double negative 2 (DN2) and DN3 stages until completion of β-selection, a critical checkpoint where thymocytes successfully assemble pre-T-cell receptors (pre-TCRs) composed of a pre-T-cell antigen receptor α (pTα) chain and a functional TCRβ chain (Radtke et al., 2010). Notch1 expression drastically decreases after β-selection when thymocytes advance to double positive (DP) stage. During the progression, Notch1 provides essential differentiation, proliferation, survival, and metabolic signals, mainly *via* inducing the expression of downstream targets such as *Tcf1* (Weber et al., 2011), *Ptcra* (Reizis and Leder, 2002), *Myc* (Weng et al., 2006), *Il7r* (Gonzales-Garcia et al., 2009), and *Hes1* (Tomita et al., 1999; Kaneta et al., 2000). Notch1 dimerization appears essential in driving DN3 thymocytes through the β-selection, in part due to its ability to activate dimer-dependent target genes *Ptcra* and *Myc* (Liu et al., 2010).

When aberrantly activated, Notch acts as an oncogene driving acute T-cell lymphoblastic leukemia (T-ALL) (Aster et al., 2011; Liu et al., 2011; Paganin and Ferrando, 2011). Constitutive Notch1 expression in murine hematopoietic progenitors uniformly causes T-ALL (Pear et al., 1996). Moreover, the fact that more than half of the T-ALL patient samples bear gain-of-function Notch1 mutations suggests a central role of Notch1 in leukemogenesis (Weng et al., 2004). Consequently, enhanced Notch1 activity activates a spectrum of downstream targets that mediate leukemogenesis including *Myc* (Weng et al., 2006), *Hes1* (Real et al., 2009), *Lef1* (Spaulding et al., 2007), and *Deptor* (Hu et al., 2017). Unlike wild-type (WT) Notch1, dimer-disrupted allele failed to induce T-ALL in the mouse model, presumably due to the inactivation of dimer-responsive target *Myc* (Liu et al., 2010). It remains to be determined any additional Notch1 targets sensitive to dimeric Notch1 signaling.

Rag1 and *Rag2* encode site-specific endonucleases to create double-stranded breaks (DSB) in the process of V(D)J recombination to constitute the diverse repertoire of T-cell receptors and B-cell immunoglobulin (Ig) receptors in response to diverse exogenous pathogens (Helmink and Sleckman, 2012; Miyazaki et al., 2020). Mice deficient in either *Rag1* or *Rag2* expression are blocked in T- and B-cell differentiation and exhibit a severe combined immunodeficiency (SCID) phenotype (Mombaerts et al., 1992; Shinkai et al., 1992). Expression of *Rag1* and *Rag2* is tightly controlled through a variety of DNA *cis*-elements and *trans*-factors, frequently in a T- or B-cell-specific manner (Kuo and Schlissel, 2009). Aberrant *Rag1*/2 activity is linked to oncogenic translocations associated with immature human and mouse B and T leukemia/lymphoma (Zhang et al., 2010).

In the present study, we identified *Rag1* and *Rag2* as Notch1 downstream targets from the gene expression profiling analysis in murine T-ALL T6E cells. Further mechanistic analyses reveal that ICN1 directly binds the *Rag2* locus to activate transcription, where we uncover a novel *cis*-element specifically recognized by the dimeric ICN1/RBPJ/MAML1 complexes. The Notch1-dimer dependency is not only restricted to T-ALL cells but also observed in DN progenitors, suggesting a new role of Notch1 in the developmental stage prior to β-selection—advancing TCRβ rearrangement. We thereby present a novel mechanism of Notch1-mediated transcriptional activation of *Rag1* and *Rag2*, involved in both T-cell development and leukemia.

RESULTS

Recombination Activation Gene 1 and 2 Are Regulated by Dimeric Notch Signaling

Although the dimerization of Notch1 transcriptional complex is required for T-cell development and leukemogenesis (Liu et al., 2010; Severson et al., 2017), identities and the functional importance of Notch1 dimer-responsive targets remain largely unknown. To disclose novel dimeric Notch1 targets, we reanalyzed a genome-wide gene expression profiling (GSE97465) in a Notch1-dependent murine T-ALL cell line T6E (Severson et al., 2017). In this microarray data, T6E cells were infected with retroviruses expressing empty vector MigR1 with a surrogated GFP marker, MigR1 containing constitutive WT intracellular Notch1 (ICN1) or a dimerization-disrupted mutant ICN1 R1984A (R1984A) (Liu et al., 2010). Candidate genes which were efficiently induced by WT ICN1 but not ICN1 R1984A caught our attention. Filtered gene sets were aligned with fold changes to generate the heatmap of differential genes in response to Notch1 dimer and monomer (**Figure 1A**). While ICN1 R1984A upregulated many known Notch1 targets, including *Dtx1* and *Nrarp*, it failed to turn on a member of dimer-dependent genes, including previously reported *Myc*, *Hes1*, and *Deptor* (Liu et al., 2010; Hu et al., 2017). Of particular note, *Rag1* and *Rag2* rank at the top to be most differentially regulated by ICN1 and R1984A (**Figure 1A**).

Since ICN1 dramatically increased the expression of *Rag1* and *Rag2* as compared with the vector alone, we first confirmed whether their expression depends on Notch1 by analyzing the mRNA levels in various Notch1 inhibitory scenarios. γ-Secreatse inhibitor (GSI) JC-18 treatment, which suppresses Notch activation, in T6E cells resulted in decreased mRNA abundance of *Rag1* and *Rag2* (**Figure 1B**, left). Consistently, we detected lower *Rag1* and *Rag2* protein levels in T6E cells upon Notch inhibition (**Figure 1B**, right). As a further support, GSI treatment in human T-ALL KOPTK1 and CUTLL1 cells resulted in a significant decrease in mRNA and protein levels of *RAG1*

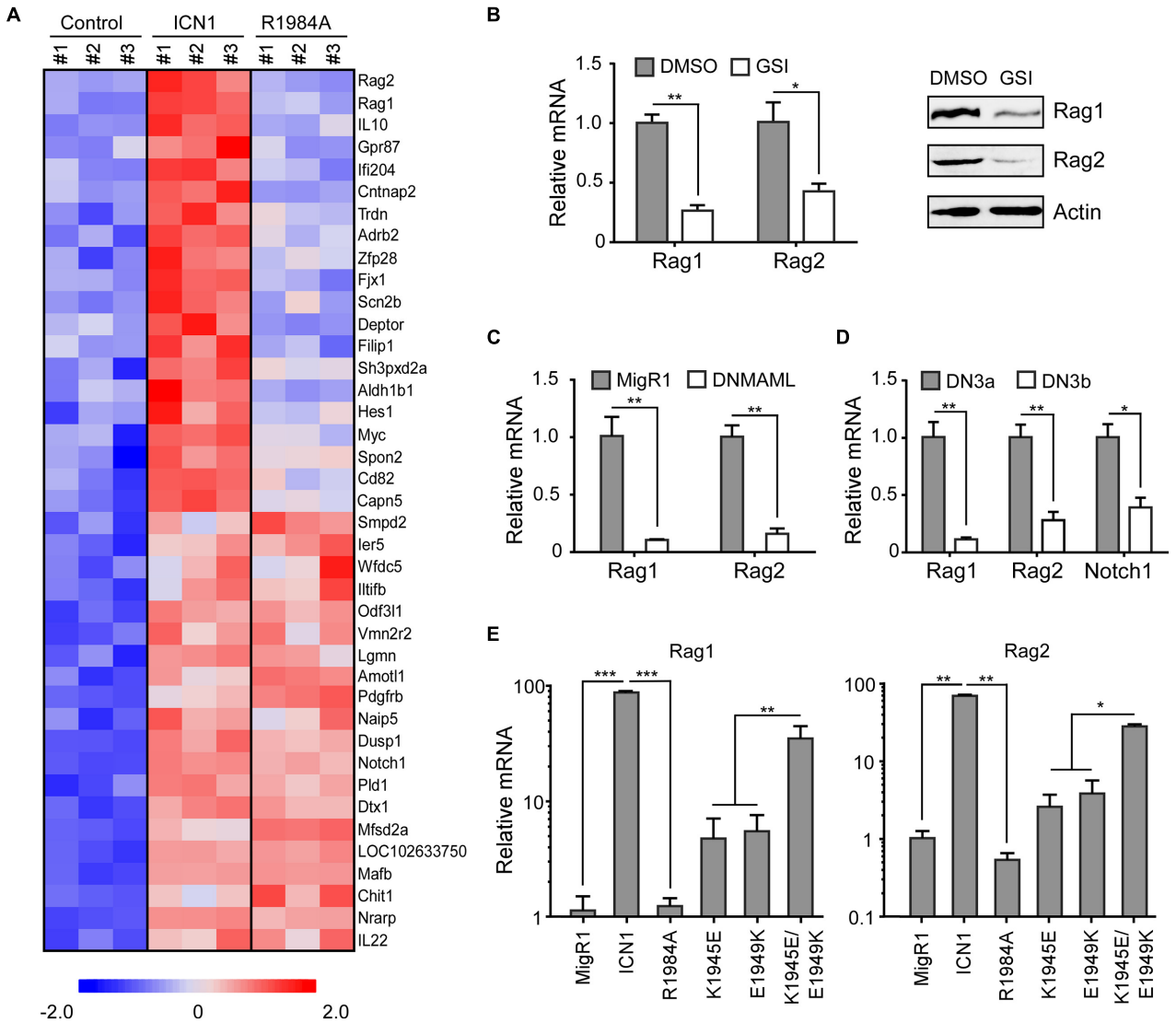

FIGURE 1 | Notch signaling induces *Rag1* and *Rag2* expression. **(A)** Identification of Notch1 dimer-dependent target genes. Notch1-dependent genes were determined from a microarray analysis in murine T-ALL T6E cells (GSE97465). Each gene expression is displayed with colored boxes which are scaled in the bottom. ICN1 expression means Notch1 monomer and dimer activation, and R1984A expression denotes only Notch1 monomer activation. Expression data from 20 genes most strictly dependent on the Notch1 dimer and 20 genes equally induced by both Notch1 dimer and monomer are depicted ($p < 0.05$). **(B)** T6E cells were treated with JC-18 (1 μM) or DMSO for 24 h. *Rag1* and *Rag2* mRNA and proteins were detected by real-time PCR (left) and immunoblots (right). **(C)** T6E cells were transduced with DNMAML1 or empty vector MigR1 surrogated with a GFP marker for 24 h. GFP^+ cells were sorted and subjected to mRNA analysis by real-time PCR. **(D)** DN3a and DN3b cells were isolated from C57BL/6 mice. *Rag1* and *Rag2* mRNA, along with positive control *Notch1* mRNA, were evaluated by real-time PCR. **(E)** T6E cells were infected by retroviruses expressing MigR1, WT ICN1, or designated dimerization mutants, then subjected to JC-18 treatment for 24 h. *Rag1* and *Rag2* mRNA levels were examined by real-time PCR. Above all, the expression of *Rag1* and *Rag2* relative to 18S RNA is shown as the mean of values from triplicate wells ± SD. Representative data from three independent experiments are shown. $^{***}p < 0.001$, $^{**}p < 0.01$, and $^{*}p < 0.05$.

and *RAG2* (**Supplementary Figures 1A,B**). We next expressed a dominant negative MAML1 (DNMAML1) to specifically repress the Notch1 pathway and observed sharp decreases of *Rag1* and *Rag2* as well (**Figure 1C**). Using primary murine thymocytes, we then investigated a physiological condition whereby Notch1 is downregulated. At the checkpoint of T-cell receptor β-selection, DN3a cells differentiate to DN3b cells, while Notch1 undergoes a dramatic decline upon the completion of TCRβ rearrangement. Correspondingly, *Rag1* and *Rag2* displayed similar reductions at the transition of DN3a to DN3b (**Figure 1D**).

The microarray data showed that both *Rag1* and *Rag2* were activated by ICN1 but not by dimerization-disrupted mutants R1984A (**Figure 1A**). To validate these data, we took advantage of various ICN1 mutants that are involved in the dimer formation of ICN1/RBPJ/MAML1 complexes on DNA, scoring their effects on *Rag1* and *Rag2* expression in

T6E cells (Liu et al., 2010). Retroviruses expressing empty vector MigR1, or MigR1-ICN1, R1984A, K1945E, E1949K, and K1945E/E1949K were infected to T6E cells, followed by 24 h JC-18 treatment to repress endogenous Notch1 activity. GFP^+ cells were sorted to analyze *Rag1* and *Rag2* mRNA abundance. Consistent with the microarray data, both *Rag1* and *Rag2* were activated by ICN1 but not by dimerization-disrupted mutant R1984A (**Figure 1E**). Expression of K1945E or E1949K alone, which breaks the intermolecular salt bridge between Notch1 dimer (Nam et al., 2007), induced moderate *Rag1* and *Rag2* expression. Notably, the double mutant K1945E/E1949K, which restores electrostatic complementarity and thereby the critical salt bridge essential for dimer formation (Nam et al., 2007), reconstituted the WT ICN1 activity to stimulate the *Rag1/2* mRNA expression (**Figure 1E**). Interestingly, we noticed that WT ICN1 but not dimerization-disrupted mutant R1984A was capable of activating the *RAG1/2* mRNA expression in human KOPTK1 and Jurkat cells (**Supplementary Figure 1B**). Collectively, these data argue that Notch1 dimerization-mediated transcriptional activation is a prominent and conserved mechanism underlying *Rag1* and *Rag2* regulation in T-ALL cells.

Notch1 Directly Binds the Transcriptional Regulatory Region of *Rag2* Gene

To determine if Notch1 transcriptional complex directly binds to and activates the gene expression, we first inspected the *Rag1/2* locus from the chromatin immunoprecipitation sequencing (ChIP-seq) data which provide comprehensive Notch1 and RBPJ binding sites in the genome of T6E cells (Wang et al., 2011). Within the *Rag* locus where *Rag1* and *Rag2* are juxtaposed with opposite orientation, we detected strong signals of Notch1 and RBPJ binding in the upstream 5′ region of the *Rag2* gene (**Figure 2A**). The tentative binding site locates at ∼2.8 kb from the transcription initiation site of the *Rag2* gene and contained a previously characterized *Rag2* P4 enhancer (Monroe et al., 1999; Wei et al., 2002). We reasoned that this enhancer region may include key *cis*-elements responsible for the *Rag2* transcription (**Figure 2A**).

ChIP assays were performed to validate Notch1 localization at the 5′ site upstream of *Rag2* in T-ALL cells. In T6E cells, Notch1 was found to bind to the *Rag2* -2.8 kb, like the well-characterized Notch1 binding site in the *Hes1* promoter. DNA regions without RBPJ binding site were included as a negative control (**Figure 2B**). By inhibiting γ-secretase-mediated proteolytic cleavage of membranous Notch1, GSI treatment decreased the nuclear ICN1 abundance, thus reducing global occupancy of Notch1/RBPJ binding sites in the genome, including that at the *Rag2* -2.8 kb site as well as the *Hes1* promoter. We further examined the Notch1 occupancy in primary T-ALL cells derived from the *Lck*-Cre $Kras^{G12D}$ transgenic mice (Chiang et al., 2008). *Ptcra*, a Notch1 direct target gene encoding the pre-T-cell antigen receptor α (Reizis and Leder, 2002; Liu et al., 2010), was bound by Notch1 at its enhancer region. Similarly, Notch1 bound the *Rag2* -2.8 kb site but not a non-specific region in the *Rag2* locus, nor a *Rag2* irrelevant DNA region bearing no RBPJ binding site shown as a negative control (**Figure 2C**).

When early T-cell progenitors migrate into the thymus, undergoing stepwise differentiation to mature T cells, *Rag1* and *Rag2* mRNA start to increase for TCRβ rearrangement. Their levels reach the peak at DN3a stage right prior to β-selection. Whether Notch1 plays a role to induce *Rag1* and *Rag2* at this developmental stage is not yet clarified. We examined the occupancy of Notch1 on the identified -2.8 kb site in the sorted DN2 and DN3a cells from C57BL/6 mice (**Figure 2D**). ChIP assays revealed the Notch1 binding at the *Rag2* -2.8 kb in both DN2 and DN3a cells, similar to the previously characterized target gene *Ptcra*. Besides Notch1, RBPJ also occupied the same region (data not shown). In contrast, DNA sequences without RBPJ binding site, as the negative control, were not bound by either Notch1 or RBPJ. Taken together, these results provide strong evidence that Notch1 directly and specifically binds to the regulatory region upstream of *Rag2*.

We also searched the tentative binding sites of Notch1 and RBPJ on the *RAG1/2* locus in human T-ALL cells from previously reported ChIP-seq data (Severson et al., 2017). It appears that the conserved binding sites around -2.8 kb of the *Rag2* gene are not present in CUTLL1 cells (**Supplementary Figure 2A**). Instead, a prominent distal Notch1 binding signal, which was associated with the RBPJ and H3K27ac binding peaks, was detected at 87 kb upstream of the transcription initiation site of the *RAG2*. Of note, GSI treatment reduced the binding signal intensity of Notch1 and RBPJ. This Notch1 and, mostly likely, *RAG2* distal enhancer interaction was validated by conventional ChIP assay (**Supplementary Figure 2B**). Our findings highly suggest that direct transcriptional activation of *RAG1/2* by Notch1 is well conserved between mouse and human, and *cis*-elements within the -87 kb distal site in human T-ALL cells are responsible for the transcriptional activation.

The *Rag2* Gene Locus Contains Paired Binding Sites in Response to Dimeric Notch1 Signaling

In the microarray analysis, *Rag1* and *Rag2* were shown specifically induced by WT ICN1 but not a dimerization-disrupted mutant R1984A (**Figure 1A**), suggesting they are Notch1 dimer dependent. Sequence search within the −2.8-kb region revealed a dimeric Notch1 recognizable sequence-paired site (SPS). The paired site consists of two RBPJ binding sites in the head-to-head orientation, separated by 16 nucleotides (**Figure 3A**). The canonical RBPJ binding site CATGGGAA was considered as a high affinity site, and the other non-canonical site CATGAGAA as a low affinity site based on the previous SPS definition (Arnett et al., 2010).

To functionally validate the putative SPS, we scored various dimerization mutants in a luciferase reporter assay. The putative *Rag2* SPS was constructed upstream of a luciferase reporter and co-expressed with WT ICN1 or mutants. As expected, WT ICN1 induced a robust activation of the *Rag2* reporter gene compared with the empty vector. In contrast, R1984A resulted in little reporter activity. The

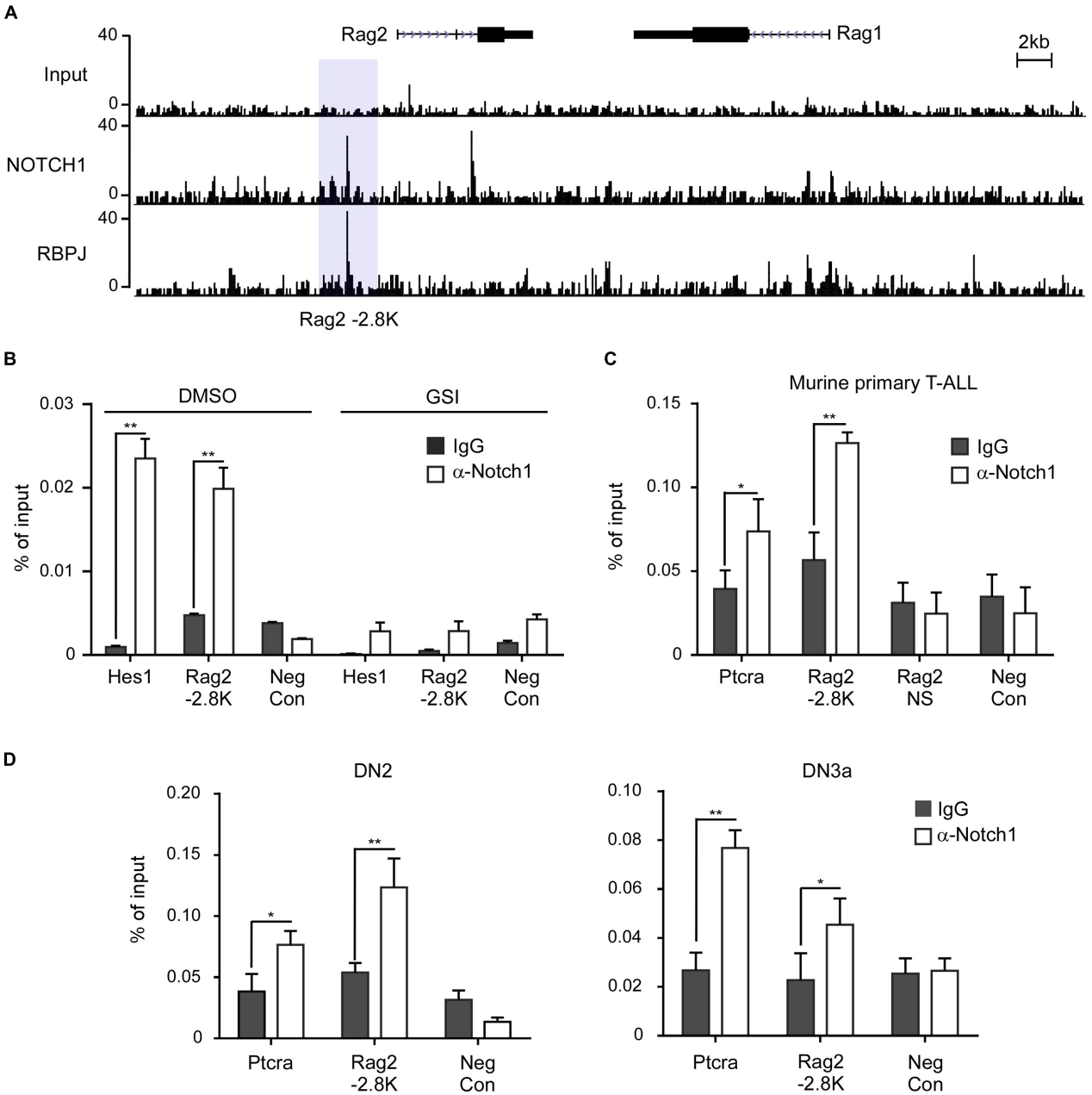

FIGURE 2 | Notch1 directly binds the *Rag*1/2 locus in T-ALL cells and T-cell progenitors. **(A)** Analysis of the *Rag2* locus in the ChIP-seq data (GSE 29600). The binding signals of Notch1 and RBPJ on the -2.8 kb site upstream of the *Rag2* gene are highlighted in light gray. **(B–D)** Chromatin immunoprecipitation (ChIP) was performed on cross-linked fragmented DNAs prepared from T6E cells treated with DMSO or 1 μM JC-18 for 24 h **(B)**, murine primary T-ALL samples **(C)**, or murine DN2 and DN3a cells **(D)**. Eluted DNAs were then analyzed by qPCR using primers flanking the -2.8 kb site. The amount of DNA amplified from immunoprecipitated DNAs was normalized to that amplified from input DNA. Each sample was prepared from at least two independent experiments and run in triplicates. *Rag2* NS, non-specific sequence in *Rag2* locus; Neg Con, non-specific sequence in the *Nanog* gene used as the negative control. $^{**}p < 0.01$ and $^{*}p < 0.05$.

other two dimerization-incompetent mutants K1945E and E1949K, impairing the intermolecular connection between Notch1 dimer, also resulted in a considerable decrease of the luciferase activity. As expected, the double mutant in *cis* K1945E/E1949K, capable of reconstituting dimeric ICN1, rescued the reporter expression (**Figure 3B**). These data together indicate that Notch1 dimerization is required to activate *Rag2* SPS-mediated transcription.

To directly confirm that *Rag2* SPS is a functional *cis*-element required for Notch1-mediated transcriptional activation, we mutated the high affinity binding site or the low affinity site individually to examine the *Rag2* SPS reporter gene

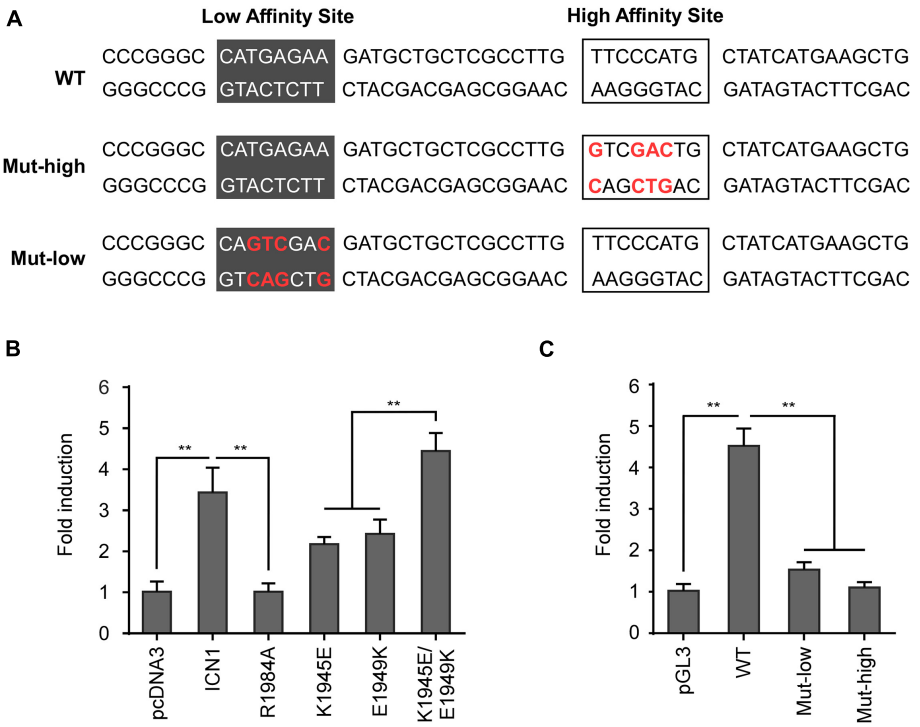

FIGURE 3 | Dimeric Notch1 directly regulates *Rag2* transcription. **(A)** Schematic presentation of the predicted mouse *Rag2* SPS. The SPS, within the *Rag2* enhancer, consists of a high affinity site (marked by frames) and a low affinity site (marked by dark gray). The high and low affinity sites were mutated as indicated (red), Mut-high and Mut-low, for the following luciferase assays. **(B)** The *Rag2* SPS was constructed to luciferase reporter vector pGL3, then co-transfected with WT ICN1 or indicated mutants. Reporter activities normalized to an empty vector were determined and presented as fold induction. **(C)** The WT *Rag2* SPS or indicated mutants were constructed to luciferase reporter vector pGL3, then co-transfected with WT ICN1. Reporter activities normalized to an empty vector were determined and presented as fold induction. All of the results were shown as the mean of values from triplicate wells ± SD. Data are representative of three independent experiments. $^{**}p < 0.01$.

activity. Previous reports suggest that both sites are required for cooperatively assembling dimeric complexes on DNA (Liu et al., 2010). Whereas ICN1 achieves full induction on WT SPS, mutations on either high affinity or low affinity site failed to induce the reporter gene expression (**Figure 3C**). Taken together, our results provide strong evidence that the identified murine *Rag2* SPS is a *bona fide* specific and functional *cis*-element, bound by Notch1 transcriptional complex and required for *Rag2* transcriptional activation. In human T-ALL cells, we noticed a highly conserved NOTCH1/RBPJ binding motif "GTGGGAA," a canonical high affinity site, within the distal *RAG2* regulatory DNA sequence, whereas a functional SPS site remained uncertain (**Supplementary Figure 2C**). It seems that *cis*-elements required for *RAG1/2* transcriptional activation are not well-conserved between human and mouse, despite the analogous mechanism of Notch1-mediated transcriptional activation.

Although no SPS was revealed yet on the *Rag1* transcriptional regulatory region, both endogenous *Rag1* and *Rag2* appeared to be regulated by Notch1 dimerization (**Figure 1E**), raising a question why *Rag1* is sensitive to Notch1 dimer. Given *Rag1* and *Rag2* are coordinately regulated at the transcriptional level and asymmetrically disposed elements are mostly found at the 5′ of *Rag2* gene (Kuo and Schlissel, 2009), the identified SPS is most likely one of the key *cis*-elements responsible for transcriptional activation of both recombination activating genes *in vivo*.

Enforced Dimeric Notch1 Expression in Hematopoietic Progenitors Induces Rapid *Rag1/2* Expression

Co-expression of *Rag1* and *Rag2* during thymocyte development is essential for the assembly of functional genes encoding the TCR by recognizing and cleaving conserved recombination signal sequences located adjacent to clusters of V, D, and J gene segments (Zhang et al., 2006; Bosticardo et al., 2021). The mechanisms responsible for the lymphoid-specific and developmental stage-specific regulation of *Rag1* and *Rag2* expression are poorly understood. To determine if *Rag1* and *Rag2* were regulated by Notch1 dimerization in thymocyte development, we exploited NG-BAC mice, a *Rag2* reporter strain in which a bacterial artificial chromosome (BAC) transgene expresses a GFP in place of *Rag2*, to investigate *Rag2* transcription (Yu et al., 1999). Hematopoietic progenitors ($Lin^{-}Sca^{+}c\text{-}Kit^{+}$, LSK cells) derived from NG-BAC mice were purified and transduced with retroviruses expressing the NGFR vector alone, ICN1, or the dimerization-disrupted mutant R1984A (**Figure 4A**). Transduced cells were subjected to *in vitro* co-culture with

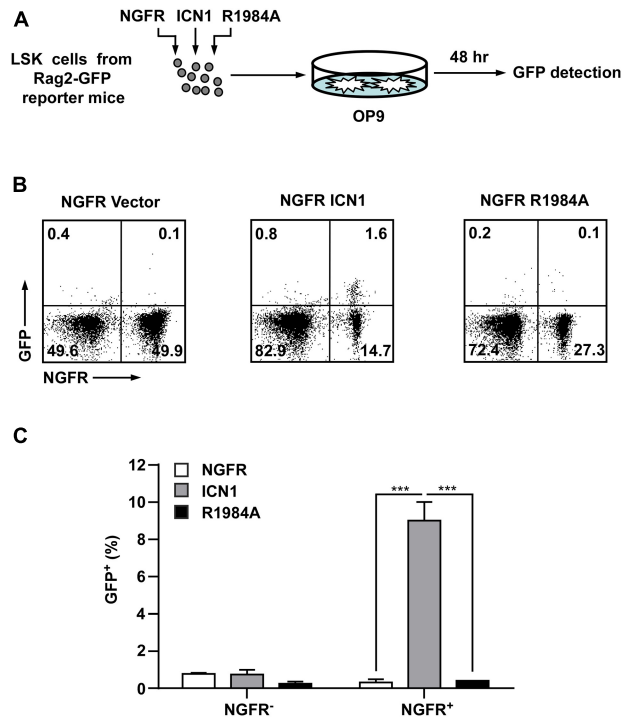

FIGURE 4 | Enforced expression of dimeric Notch1 activates the *Rag2* reporter expression in hematopoietic progenitors. **(A)** Schematic presentation of the experimental procedure. GFP$^-$ LSK (Lin$^-$Sca$^+$c-Kit$^+$) cells derived from *RAG2*-GFP reporter mice (NG-BAC) were transduced with viruses expressing ICN1 or R1984A with NGFR as surrogated marker. The infected cells were co-cultured with stromal cells OP9 for 48 h and then measured the GFP$^+$ percentage as an indication of *Rag2* expression. **(B)** Flow cytometry analysis of GFP and NGFR-PE expressions in hematopoietic cells recovered from OP9 culture. **(C)** A histogram presentation of GFP$^+$ cell percentages in NGFR-negative or NGFR-positive populations in panel **(B)**. ***$p < 0.001$.

murine OP9 stromal cells. The *Rag2* expression, reflected by GFP fluorescence, was analyzed. As early as 48 h post-transduction, *Rag2* expression was detected in approximately 10% in ICN1 expressing (NGFR$^+$) cells, whereas very few, if any, GFP$^+$ cells were seen in the vector control cells (**Figures 4B,C**). Again, R1984A-transduced cells failed to induce *Rag2* expression in this time frame, suggesting *Rag2* expression is much more sensitive to Notch1 dimerization during thymocyte development.

To further determine the role of Notch1 dimerization in the activation of *Rag1* and *Rag2* during T-cell fate specification, we purified hematopoietic stem and progenitor cells derived from C57BL/6 mice and transduced them with retroviruses expressing the MigR1 vector, ICN1, or the dimerization-disrupted mutant R1984A, then seeded them on murine OP9 stromal cells for 96 h. GFP$^+$ Thy1$^+$ T-lineage cells were then sorted to analyze the mRNA expression of *Rag1/2* and *Ptcra* (**Figure 5A**). As shown in **Figures 5B–D**, mRNA levels of *Rag1* and *Rag2* were markedly elevated in cells transduced with WT ICN1 as compared with empty vector control, while the expression of R1984A resulted in minimal induction of both genes (**Figures 5B,C**). As a well-characterized dimeric Notch1 target required for thymocyte development, *Ptcra* was selectively activated by WT ICN1 but not R1984A (**Figure 5D**). These data therefore argue the requirement of Notch1 dimerization in activating *Rag1/2* expression during T-cell specification.

DISCUSSION

The recombination activating genes 1 and 2 are crucial endonucleases to initiate V(D)J recombination in immature lymphocytes and, when overly activated, also implicated in lymphoid malignancies. Yet, transcriptional control of *Rag1* and *Rag2* is not completely understood. In this report, we demonstrate Notch1 activates *Rag1* and *Rag2* expression in both murine and human T cells. We identify a novel *cis*-element in murine T cells, which bears a dimeric Notch1 recognition site SPS and is required for Notch1-mediated transcriptional activation. Dimeric Notch1 enables the optimal expression of *Rag1* and *Rag2* in both T-ALL and T-cell progenitors. Hence, the present study manifests a prominent role of Notch1 in transcriptional activation of *Rag1* and *Rag2* in both T-cell development and leukemogenesis.

Notch1 transcriptional complex develops dimer in the nucleus on DNA sequence bearing SPS, such as the promoter of *Hes1*, a classical Notch1 target (Nam et al., 2007). Yet, the conventional SPS is not commonly detected in the genome. The hypothesis of SPS composition of one canonical site and one cryptic site was later confirmed in the enhancer of *Ptcra* and *Hes5* (Arnett et al., 2010; Liu et al., 2010). Using the matrix developed in the Blacklow Lab to predict the potential dimeric Notch1-responsive element (Arnett et al., 2010), we identified a tentative SPS proximal to the *Rag2* enhancer in murine thymocytes. Luciferase reporter assays with the site-specific mutagenesis demonstrate that the *cis*-element SPS is a *bona fide* dimeric Notch1-responsive site. Although residing on the *Rag2* transcription regulatory region, *Rag1* and *Rag2* appear dependent on dimeric Notch1 for full activation in T-ALL cells. Since inversely orientated *Rag1* and *Rag2* are coordinately regulated at the transcriptional level with major *cis*-elements identified on the *Rag2* side (Yu et al., 1999), our newly revealed SPS is most likely the DNA sequence essential for transcriptional activation of both *Rag1* and *Rag2* in murine T cells. Therefore, we not only give another example that one canonical site and one cryptic site constitute a functional SPS, but also provide a novel pair of *cis*-element (SPS) and *trans*-factor (dimeric Notch1) to dictate the transcription of *Rag1* and *Rag2*.

RAG2 has been shown as a functionally important downstream effector of Notch1 in mediating T-ALL development. T-ALL onsets were significantly delayed or impaired when ICN1 expression was enforced in the *Rag2*$^{-/-}$ bone marrow, which was reversed upon expression of the TCRβ transgene (Allman et al., 2001; Campese et al., 2006). The outcome suggests a critical synergistic effect of Notch1 and pre-TCR signaling to initiate T-ALL. In addition, it remains possible that Notch1-induced aberrant *RAG1/2* expression creates unnecessary DSBs, eliciting inappropriate translocations or inducing DNA damages that ordinate with Notch1 to amplify oncogenic signaling and drive further neoplastic progression.

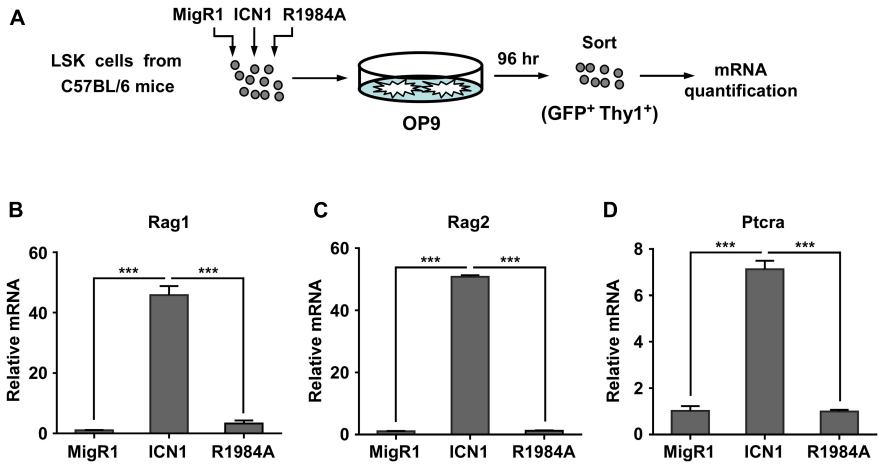

FIGURE 5 | Dimeric Notch1 activates *Rag1* and *Rag2* during thymocyte development. **(A)** Schematic presentation of the experimental procedure. LSK cells derived from C57BL/6 mice were transduced with retroviruses expressing the MigR1 vector, ICN1, or R1984A with GFP as a marker. After transduction, the infected cells were co-cultured with murine OP9 stromal cells for 96 h. GFP$^+$ Thy1$^+$ T-lineage cells were sorted for mRNA quantification. **(B–D)** qRT-PCR analysis showing the mRNA expression of *Rag1* **(B)**, *Rag2* **(C)**, and *Ptcra* **(D)** in sorted cells. ***$p < 0.001$.

For example, RAG endonuclease-elicited Notch1 truncations are revealed in almost all murine T-ALL (Tsuji et al., 2004; Ashworth et al., 2010). Likewise, in human T-ALL, there is a RAG-mediated SIL/SCL rearrangement in a Notch-dependent T-ALL line SIL-ALL, resulting in a remarkable increase of SCL (TAL1) expression (Aplan et al., 1992). We and others have shown that inhibition of Notch signaling results in *Rag1* and *Rag2* downregulation, manifesting an important correlation of Notch1 and *Rag1*/2 and also implying a role of *Rag1*/2 in Notch1-induced T-ALL (Riz et al., 2010; Kourtis et al., 2018). It is reasonable to speculate a new role of Notch1 in affecting genome instability *via* inducing *Rag1/2* expression. Another interesting finding is that depletion of *RAG1* or *RAG2* elicits T-ALL cell growth inhibition (data not shown), suggesting that these recombination activation genes may have other tumor-promoting roles in cells already transformed.

Our data also suggest that Notch1 activates *Rag2* in T-cell progenitors. Previous publications reported that inhibition of Notch1 impairs VDJβ rearrangement and TCRβ expression (Wolfer et al., 2002; Maillard et al., 2006). Although not yet demonstrated, the reduced TCRβ may result from the decreased *Rag2* expression in the absence of Notch1. Moreover, overexpression of ICN1 but not R1984A in hematopoietic progenitors led to rapid upregulation of *Rag1/2*, suggesting the role of dimeric Notch1 in upregulating *Rag1/2* in physiological conditions. However, whether Notch1 serves a primary role in activating *Rag1/2* expression prior to β-selection awaits further investigation. Since Notch1 expression decreases rapidly after β-selection, upregulation of *Rag1/2* for TCRα rearrangement is likely exerted by other transcriptional factors. Interestingly, when mice harboring Notch1 dimerization mutants were examined for the impacts of dimeric deficiency on multiorgan development, mature T-cell subsets appeared normal, despite the total number of thymocytes declined to some extent (Kobia et al., 2020). Functional validations of mature T cells in these Notch1 dimeric deficient mice are yet to be determined. Despite the paradoxical findings, we here provide compelling evidence that the transcriptional activation mediated by canonical Notch1 signaling pathway is one of the prominent mechanisms to orchestrate optimal *Rag1*/2 expression in T-cell progenitors during development and transformation.

MATERIALS AND METHODS

Mice

C57BL/6 mice were obtained from Beijing Vital River Laboratory Animal Technology Co., Ltd., Beijing, China. NG-BAC (*RAG2*-GFP) transgenic reporter mice were as described (Yu et al., 1999). All animal experiments were performed under animal ethical regulations, and the study protocol was approved by the Institutional Animal Care and Use Committee of Wuhan University.

Cell Culture

Murine T-ALL cell line T6E and human T-ALL cell lines KOPTK1, Jurkat, and CUTLL1 were kindly provided by Dr. Warren Pear (University of Pennsylvania, United States). The 293T cell line was purchased from the American Type Culture Collection (ATCC, Manassas, VA, United States). T-ALL cell lines were grown in complete RPMI-1640 (Gibco, Waltham, MA, United States) supplemented with 10% fetal bovine serum (FBS, Gemini Bio, West Sacramento, CA, United States), 1% penicillin/streptomycin (Hyclone, Logan, UT, United States), 1% non-essential amino acids (Gibco), 2 mM L-glutamine (Sigma, St. Louis, MO, United States), 1 mM sodium pyruvate (Sigma), and 100 μM β-mercaptoethanol (Sigma). The 293T cell was maintained in Dulbecco's modified Eagle's medium (DMEM, Gibco) containing 10% FBS (Gibco) and 1% penicillin/streptomycin (Hyclone). All cell lines were

authenticated using short tandem repeat (STR) analysis, cultured for fewer than 2 months after resuscitation, and tested for mycoplasma contamination once a month using PCR assay.

Reagents and Plasmids

γ-Secretase inhibitor JC-18 was a generous gift from Yue-Ming Li (Searfoss et al., 2003), and compound E was purchased from MedChemExpress (Monmouth Junction, NJ, United States). The retroviral constructs MigR1-ICN1 and MigR1-DNMAML1 (13–74)-GFP were as described (Weng et al., 2003), and MigR1-R1984A, NGFR-ICN1, and NGFR-R1984A were illustrated as previously reported (Liu et al., 2010). In the luciferase reporter assay, the murine DNA fragment containing SPS in *Rag2* transcriptional regulatory region was cloned into the pGL3 promoter vector. The forward primer is GCATATGGTACCTCGCATCCTTTTCTACTTCC and the reverse primer is ATATCTCGAGAGGAGGAGCACCACCA GTTT. The high and low affinity binding sites were subjected to mutation using QuickChange site-specific mutagenesis kit (Stratagene, San Diego, CA, United States). Primers to mutate the high affinity site are GATGCTGCTCGCCTTGGTCGACTGCTATCATGAAGCTG (forward) and CAGCTTCATGATAGCAGTCGACCAAGG CGAGCAGCATC (reverse); primers to mutate the low affinity site are GCCTATCCCCGGGCCAGTCGACGATGCTGC TCGCCTTG (forward) and CAAGGCGAGCAGCATC GTCGACTGGCCCGGGGATAGGC (reverse). All constructs were validated by DNA sequence.

qRT-PCR

Total RNA was prepared using TRIzol (Invitrogen, Waltham, MA, United States), followed by concentration and purity determination; 1 μg of random primed total RNAs was reverse-transcribed with SuperScript II (Invitrogen) according to the instructions of the manufacturer. Primer sequences for real-time PCR were as follows: murine *Rag1*—forward, CAACGAGCACTGAAACTCCA; reverse, CCCGTCACTCTTGAAACGAT; murine *Rag2*—forward, ATTCCTGCTACCTCCCACCT; reverse, CGGAAAGCTCAT TGTTTGGT; human *RAG1*—forward, GCAGATGAGT CTGACCACGA; reverse, CTTGAAAGTCCGGAGAATGC; and human *RAG2*—forward, CAAACCCGCCATGATCTACT; reverse, TTGCTTCCTGCTGACAGATG. Primers used for *Ptcra* and *18s* rRNA were as described (Liu et al., 2010). All the primers for SYBR green detection were used at a final concentration of 0.4 μM. Real-time amplification in FAST SYBR Green Master Mix (Bio-Rad, Hercules, CA, United States) was performed on CFX Connect Real-Time PCR System (Bio-Rad). Relative expression of the mRNA was calculated by the $2^{-\Delta\Delta Ct}$ method and normalized to *18s* rRNA.

Retroviral Transduction and OP9 Co-culture

High-titer retroviruses were produced as described (Chiang et al., 2008). For retroviral transduction of hematopoietic stem progenitor cells (HSPCs), LSK ($Lin^-Sca^+c\text{-}Kit^+$) cells were purified from 6- to 8-week-old C57BL/6 or NG-BAC mice. Retroviral supernatants were added into wells coated with 20 mg/ml RetroNectin (Takara, Tokyo, Japan) and incubated for 4–6 h at 37°C before washing with PBS. Purified LSK cells were suspended in the stimulation cocktails (DMEM, 1% penicillin–streptomycin, 15% FBS, 2 mM L-glutamate, 10 ng/ml mIL-3, 10 ng/ml mIL-6, 20 ng/ml mSCF, and 20 ng/ml mFlt3L) (Liu et al., 2010) and then added to virus-bound RetroNectin-coated plates. After transduction, the infected LSK cells were plated onto fresh OP9 monolayers at 10^6 cells/well in six-well plates. All co-cultures were performed in the presence of 1 ng/ml mIL-7 and 5 ng/ml hFlt3L within the OP9 culture medium (αMEM supplemented with 20% FBS and 1% penicillin–streptomycin) (Wong et al., 2012). For LSK cells derived from NG-BAC mice, transduced cells were analyzed by flow cytometry using PE anti-NGFR (BD Pharmingen, San Diego, CA, United States) and GFP fluorescence signals. For LSK cells derived from C57BL/6 mice, transduced T lineage cells (GFP^+ $Thy1^+$) were sorted for qRT-PCR analysis.

Chromatin Immunoprecipitation

The ChIP assay and the subsequent quantitative PCR were performed following the protocol as described (Weng et al., 2006). Briefly, T6E or CUTLL1 cells were treated with DMSO or GSI (1 μM compound E) for 24 h prior to fixation. After fixation for 10 min in 1% paraformaldehyde at room temperature, cells were washed, lysed, and sonicated to shear DNA between 200 and 600 bp in length. Antiserum specific for Notch1 TAD domain (Wu et al., 2000) or normal rabbit IgG was used for immunoprecipitating associated DNA, which was subjected to qPCR using the SYBR system on CFX Connect Real-Time PCR System (Bio-Rad). The primers used are specified as follows: *murine hes1* promoter—forward, CGTGTCTCTTCCTCCCAT; reverse, CCAGGACCAAGGAGAGAGGT; murine *Rag2* −2.8 kb enhancer—forward, AGCTCCCCACTACCCGAGTCA; reverse, GCTGGTCCACCTTTGTTCTCTAA; *Nanog* negative control—forward, GGCTGCCTCTCCTCGCCCT; reverse, GTGCACACAGCTGGGCCTGA; and human *RAG2* −87 kb enhancer—forward, TAACTGTCAGCTGGCCACAA; reverse, TGGTCTGTCTTGCTCACCTG. Each sample was independently prepared at least two times and run in triplicate. The input DNA was defined as an aliquot of sheared chromatin resulting from crude lysate and was used to normalize the sample to the amount of chromatin added to each ChIP reaction.

Purification of Double Negative Thymocytes

$CD4^-CD8^-$ DN thymocytes were negatively selected with anti-CD4 and anti-CD8 MACS beads according to the protocol of the manufacturer (Miltenyi Biotec, Auburn, CA, United States). After staining with antibodies against lineage (Lin) markers B220, CD19, CD11b, Gr1, CD11c, NK1.1, Ter119, CD3ε, CD8α, CD8β, TCRβ, and TCRγδ (BD Pharmingen), DN2 thymocytes ($c\text{-}Kit^{hi}CD25^{hi}Lin^-$) were purified based on staining with anti-c-Kit and anti-CD25 antibodies (BD Pharmingen) by cell sorting

on FACSAria (BD Biosciences) and analyzed on the LSR-II (BD Biosciences). DN3a (c-Kit$^{-/lo}$CD25^{hi}Lin^{-}CD27^{lo}) cells were purified by sorting after staining with anti-CD27 antibody (eBioscience, San Diego, CA, United States).

Luciferase Reporter Gene Assays

Empty pcDNA3 or pcDNA3 expressing ICN1 (or indicated mutants) was transiently co-transfected in triplicate into human 293T cells with firefly luciferase pGL3-promoter vector pGL3 or driven by elements containing the *Rag2* SPS (or mutants). Cells were transfected using FuGENE 6 Transfection Reagent (Promega, Madison, WI, United States) with 0.8 μg of firefly luciferase reporter constructs, 0.1 μg of expression vectors, and 0.1 μg of Renilla luciferase expression vector. Luciferase activities were measured 24 h later using the Promega Dual Luciferase kit (Promega). Firefly luciferase activities were normalized with Renilla luciferase control values. Relative activity from the empty vector lysate was set arbitrarily to a value of 1.

Flow Cytometry

Cells transduced with NGFR or NGFR-ICN1 and NGFR-R1984A were stained with the PE anti-NGFR (BD Pharmingen) in FACS buffer [1 × DPBS, 10 mM HEPES, 0.02% NaN_3, 0.2% BSA (w/v)] on ice in the presence of rat and mouse IgG (Sigma-Aldrich, St. Louis, MO, United States) for 20 min, then washed and resuspended in FACS buffer. Acquisition was performed on LSRII (BD Biosciences). Dead cells and doublets were excluded based on FSC and SSC characteristics. Data were analyzed with FlowJo software (Tree Star, Ashland, OR, United States).

DATA AVAILABILITY STATEMENT

The raw data supporting the conclusions of this article will be made available by the authors, without undue reservation.

ETHICS STATEMENT

The animal study was reviewed and approved by Institutional Animal Care and Use Committee of Wuhan University.

AUTHOR CONTRIBUTIONS

All authors listed have made a substantial, direct and intellectual contribution to the work, and approved it for publication.

FUNDING

This work was supported by the National Natural Science Foundation of China (81770177 and 81970152 to HL and 81830084 to GQ) and the Fundamental Research Funds for the Central Universities (2042020kf0208 to HL).

ACKNOWLEDGMENTS

We would like to thank Warren Pear (University of Pennsylvania, United States) and Avinash Bhandoola (National Institute of Health, United States) for conceptual contribution and technique support.

SUPPLEMENTARY MATERIAL

The Supplementary Material for this article can be found online at: https://www.frontiersin.org/articles/10.3389/fcell.2021.703338/full#supplementary-material

REFERENCES

Allman, D., Karnell, F. G., Punt, J. A., Bakkour, S., Xu, L., Myung, P., et al. (2001). Separation of Notch1 promoted lineage commitment and expansion/transformation in developing T cells. *J. Exp. Med.* 194, 99–106. doi: 10.1084/jem.194.1.99

Aplan, P. D., Lombardi, D. P., Reaman, G. H., Sather, H. N., Hammond, G. D., and Kirsch, I. R. (1992). Involvement of the putative hematopoietic transcription factor SCL in T-cell acute lymphoblastic leukemia. *Blood* 79, 1327–1333. doi: 10.1182/blood.v79.5.1327.bloodjournal7951327

Arnett, K. L., Hass, M., McArthur, D. G., Ilagan, M. X., Aster, J. C., Kopan, R., et al. (2010). Structural and mechanistic insights into cooperative assembly of dimeric Notch transcription complexes. *Nat. Struct. Mol. Biol.* 17, 1312–1317. doi: 10.1038/nsmb.1938

Ashworth, T. D., Pear, W. S., Chiang, M. Y., Blacklow, S. C., Mastio, J., Xu, L., et al. (2010). Deletion-based mechanisms of Notch1 activation in T-ALL: key roles for RAG recombinase and a conserved internal translational start site in Notch1. *Blood* 116, 5455–5464. doi: 10.1182/blood-2010-05-286328

Aster, J. C., Blacklow, S. C., and Pear, W. S. (2011). Notch signalling in T-cell lymphoblastic leukaemia/lymphoma and other haematological malignancies. *J. Pathol.* 223, 262–273.

Bosticardo, M., Pala, F., and Notarangelo, L. D. (2021). RAG deficiencies: recent advances in disease pathogenesis and novel therapeutic approaches. *Eur. J. Immunol.* 51, 1028–1038. doi: 10.1002/eji.202048880

Campese, A. F., Garbe, A. I., Zhang, F., Grassi, F., Screpanti, I., and von Boehmer, H. (2006). Notch1-dependent lymphomagenesis is assisted by but does not essentially require pre-TCR signaling. *Blood* 108, 305–310. doi: 10.1182/blood-2006-01-0143

Chiang, M. Y., Xu, L., Shestova, O., Histen, G., L'heureux, S., Romany, C., et al. (2008). Leukemia-associated NOTCH1 alleles are weak tumor initiators but accelerate K-ras-initiated leukemia. *J. Clin. Invest.* 118, 3181–3194. doi: 10.1172/jci35090

Gonzales-Garcia, S., García-Peydró, M., Martin-Gayo, E., Ballestar, E., Esteller, M., Bornstein, R., et al. (2009). CSL-MAML-dependent Notch1 signaling controls T lineage-specific IL-7Ralpha gene expression in early human thymopoiesis and leukemia. *J. Exp. Med.* 206, 779–791. doi: 10.1084/jem.20081922

Helmink, B. A., and Sleckman, B. P. (2012). The response to and repair of RAG-mediated DNA double-strand breaks. *Annu. Rev. Immunol.* 30, 175–202. doi: 10.1146/annurev-immunol-030409-101320

Hu, Y., Su, H., Liu, C., Wang, Z., Huang, L., Wang, Q., et al. (2017). DEPTOR is a direct NOTCH1 target that promotes cell proliferation and

survival in T-cell leukemia. *Oncogene* 36, 1038–1047. doi: 10.1038/onc.2016.275

Kaneta, M., Osawa, M., Sudo, K., Nakauchi, H., Farr, A. G., and Takahama, Y. (2000). A role for pref-1 and HES-1 in thymocyte development. *J. Immunol.* 164, 256–264. doi: 10.4049/jimmunol.164.1.256

Kobia, F. M., Preusse, K., Dai, Q., Weaver, N., Hass, M. R., Chaturvedi, P., et al. (2020). Notch dimerization and gene dosage are important for normal heart development, intestinal stem cell maintenance, and splenic marginal zone B-cell homeostasis during mite infestation. *PLoS Biol.* 18:e3000850. doi: 10.1371/journal.pbio.3000850

Kopan, R., and Ilagan, M. X. (2009). The canonical Notch signaling pathway: unfolding the activation mechanism. *Cell* 137, 216–233. doi: 10.1016/j.cell.2009.03.045

Kourtis, N., Lazaris, C., Hockemeyer, K., Balandrán, J. C., Jimenez, A. R., Mullenders, J., et al. (2018). Oncogenic hijacking of the stress response machinery in T cell acute lymphoblastic leukemia. *Nat. Med.* 24, 1157–1166. doi: 10.1038/s41591-018-0105-8

Kuo, T. C., and Schlissel, M. S. (2009). Mechanisms controlling expression of the RAG locus during lymphocyte development. *Curr. Opin. Immunol.* 21, 173–178. doi: 10.1016/j.coi.2009.03.008

Liu, H., Chi, A. W., Arnett, K. L., Chiang, M. Y., Xu, L., Shestova, O., et al. (2010). Notch dimerization is required for leukemogenesis and T-cell development. *Genes Dev.* 24, 2395–2407. doi: 10.1101/gad.1975210

Liu, H., Chiang, M. Y., and Pear, W. S. (2011). Critical roles of NOTCH1 in acute T-cell lymphoblastic leukemia. *Int. J. Hematol.* 94, 118–125. doi: 10.1007/s12185-011-0899-3

Maillard, I., Tu, L., Sambandam, A., Yashiro-Ohtani, Y., Millholland, J., Keeshan, K., et al. (2006). The requirement for Notch signaling at the beta-selection checkpoint in vivo is absolute and independent of the pre-T cell receptor. *J. Exp. Med.* 203, 2239–2245. doi: 10.1084/jem.20061020

Miyazaki, K., Watanabe, H., Yoshikawa, G., Chen, K., Hidaka, R., Aitani, Y., et al. (2020). The transcription factor E2A activates multiple enhancers that drive Rag expression in developing T and B cells. *Sci. Immunol.* 5:eabb1455. doi: 10.1126/sciimmunol.abb1455

Mombaerts, P., Iacomini, J., Johnson, R. S., Herrup, K., Tonegawa, S., and Papaioannou, V. E. (1992). RAG-1-deficient mice have no mature B and T lymphocytes. *Cell* 68, 869–877. doi: 10.1016/0092-8674(92)90030-g

Monroe, R. J., Chen, F., Ferrini, R., Davidson, L., and Alt, F. W. (1999). RAG2 is regulated differentially in B and T cells by elements 5' of the promoter. *Proc. Natl. Acad. Sci. U.S.A.* 96, 12713–12718. doi: 10.1073/pnas.96.22.12713

Nam, Y., Sliz, P., Pear, W. S., Aster, J. C., and Blacklow, S. C. (2007). Cooperative assembly of higher-order Notch complexes functions as a switch to induce transcription. *Proc. Natl. Acad. Sci. U.S.A.* 104, 2103–2108. doi: 10.1073/pnas.0611092104

Paganin, M., and Ferrando, A. (2011). Molecular pathogenesis and targeted therapies for NOTCH1-induced T-cell acute lymphoblastic leukemia. *Blood Rev.* 25, 83–90. doi: 10.1016/j.blre.2010.09.004

Pear, W. S., Aster, J. C., Scott, M. L., Hasserjian, R. P., Soffer, B., Sklar, J., et al. (1996). Exclusive development of T cell neoplasms in mice transplanted with bone marrow expressing activated Notch alleles. *J. Exp. Med.* 183, 2283–2291. doi: 10.1084/jem.183.5.2283

Pui, J. C., Allman, D., Xu, L., DeRocco, S., Karnell, F. G., Bakkour, S., et al. (1999). Notch1 expression in early lymphopoiesis influences B versus T lineage determination. *Immunity* 11, 299–308. doi: 10.1016/s1074-7613(00)80105-3

Radtke, F., Fasnacht, N., and Macdonald, H. R. (2010). Notch signaling in the immune system. *Immunity* 32, 14–27. doi: 10.1016/j.immuni.2010.01.004

Radtke, F., Wilson, A., Stark, G., Bauer, M., van Meerwijk, J., MacDonald, H. R., et al. (1999). Deficient T cell fate specification in mice with an induced inactivation of Notch1. *Immunity* 10, 547–558. doi: 10.1016/s1074-7613(00)80054-0

Real, P. J., Tosello, V., Palomero, T., Castillo, M., Hernando, E., de Stanchina, E., et al. (2009). Gamma-secretase inhibitors reverse glucocorticoid resistance in T cell acute lymphoblastic leukemia. *Nat. Med.* 15, 50–58. doi: 10.1038/nm.1900

Reizis, B., and Leder, P. (2002). Direct induction of T lymphocyte-specific gene expression by the mammalian Notch signaling pathway. *Genes Dev.* 16, 295–300. doi: 10.1101/gad.960702

Riz, I., Hawley, T. S., Luu, T. V., Lee, N. H., and Hawley, R. G. (2010). TLX1 and NOTCH coregulate transcription in T cell acute lymphoblastic leukemia cells. *Mol. Cancer* 9:181. doi: 10.1186/1476-4598-9-181

Sambandam, A., Maillard, I., Zediak, V. P., Xu, L., Gerstein, R. M., Aster, J. C., et al. (2005). Notch signaling controls the generation and differentiation of early T lineage progenitors. *Nat. Immunol.* 6, 663–670. doi: 10.1038/ni1216

Searfoss, G. H., Jordan, W. H., Calligaro, D. O., Galbreath, E. J., Schirtzinger, L. M., Berridge, B. R., et al. (2003). Adipsin, a biomarker of gastrointestinal toxicity mediated by a functional gamma-secretase inhibitor. *J. Biol. Chem.* 278, 46107–46116. doi: 10.1074/jbc.m307757200

Severson, E., Arnett, K. L., Wang, H. F., Zang, C., Taing, L., Liu, H., et al. (2017). Genome-wide identification and characterization of Notch transcription complex-binding sequence-paired sites in leukemia cells. *Sci. Signal.* 10:eaag1598. doi: 10.1126/scisignal.aag1598

Shinkai, Y., Rathbun, G., Lam, K. P., Oltz, E. M., Stewart, V., Mendelsohn, M., et al. (1992). RAG-2-deficient mice lack mature lymphocytes owing to inability to initiate V(D)J rearrangement. *Cell* 68, 855–867. doi: 10.1016/0092-8674(92)90029-c

Spaulding, C., Reschly, E. J., Zagort, D. E., Yashiro-Ohtani, Y., Beverly, L. J., Capobianco, A., et al. (2007). Notch1 co-opts lymphoid enhancer factor 1 for survival of murine T-cell lymphomas. *Blood* 110, 2650–2658. doi: 10.1182/blood-2007-04-084202

Tan, J. B., Visan, I., Yuan, J. S., and Guidos, C. J. (2005). Requirement for Notch1 signals at sequential early stages of intrathymic T cell development. *Nat. Immunol.* 6, 671–679. doi: 10.1038/ni1217

Tomita, K., Hattori, M., Nakamura, E., Nakanishi, S., Minato, N., and Kageyama, R. (1999). The bHLH gene Hes1 is essential for expansion of early T cell precursors. *Genes Dev.* 13, 1203–1210. doi: 10.1101/gad.13.9.1203

Tsuji, H., Ishii-Ohba, H., Katsube, T., Ukai, H., Aizawa, S., Doi, M., et al. (2004). Involvement of illegitimate V(D)J recombination or microhomology-mediated nonhomologous end-joining in the formation of intragenic deletions of the Notch1 gene in mouse thymic lymphomas. *Cancer Res.* 64, 8882–8890. doi: 10.1158/0008-5472.can-03-1163

Wang, H., Zou, J., Zhao, B., Johannsen, E., Ashworth, T., Wong, H., et al. (2011). Genome-wide analysis reveals conserved and divergent features of Notch1/RBPJ binding in human and murine T-lymphoblastic leukemia cells. *Proc. Natl. Acad. Sci. U.S.A.* 108, 14908–14913. doi: 10.1073/pnas.1109023108

Weber, B. N., Chi, A. W., Chavez, A., Yashiro-Ohtani, Y., Yang, Q., Shestova, O., et al. (2011). A critical role for TCF-1 in T-lineage specification and differentiation. *Nature* 476, 63–68. doi: 10.1038/nature10279

Wei, X. C., Kishi, H., Jin, Z. X., Zhao, W. P., Kondo, S., Matsuda, T., et al. (2002). Characterization of chromatin structure and enhancer elements for murine recombination activating gene-2. *J. Immunol.* 169, 873–881. doi: 10.4049/jimmunol.169.2.873

Weng, A. P., Ferrando, A. A., Lee, W., Morris, J. P. IV, Silverman, L. B., Sanchez-Irizarry, C., et al. (2004). Activating mutations of NOTCH1 in human T cell acute lymphoblastic leukemia. *Science* 306, 269–271. doi: 10.1126/science.1102160

Weng, A. P., Millholland, J. M., Yashiro-Ohtani, Y., Arcangeli, M. L., Lau, A., Wai, C., et al. (2006). c-Myc is an important direct target of Notch1 in T-cell acute lymphoblastic leukemia/lymphoma. *Genes Dev.* 20, 2096–2109. doi: 10.1101/gad.1450406

Weng, A. P., Nam, Y., Wolfe, M. S., Pear, W. S., Griffin, J. D., Blacklow, S. C., et al. (2003). Growth suppression of pre-T acute lymphoblastic leukemia cells by inhibition of notch signaling. *Mol. Cell Biol.* 23, 655–664. doi: 10.1128/mcb.23.2.655-664.2003

Wolfer, A., Wilson, A., Nemir, M., MacDonald, H. R., and Radtke, F. (2002). Inactivation of Notch1 impairs VDJbeta rearrangement and allows pre-TCR-independent survival of early alpha beta Lineage Thymocytes. *Immunity* 16, 869–879. doi: 10.1016/s1074-7613(02)00330-8

Wong, G. W., Knowles, G. C., Mak, T. W., Ferrando, A. A., and Zuniga-Pflucker, J. C. (2012). HES1 opposes a PTEN-dependent check on survival, differentiation, and proliferation of TCRbeta-selected mouse thymocytes. *Blood* 120, 1439–1448. doi: 10.1182/blood-2011-12-395319

Wu, L., Aster, J. C., Blacklow, S. C., Lake, R., Artavanis-Tsakonas, S., and Griffin, J. D. (2000). MAML1, a human homologue of Drosophila mastermind, is a transcriptional co-activator for NOTCH receptors. *Nat. Genet.* 26, 484–489. doi: 10.1038/82644

Yu, W., Misulovin, Z., Suh, H., Hardy, R. R., Jankovic, M., Yannoutsos, N., et al. (1999). Coordinate regulation of RAG1 and RAG2 by cell type-specific DNA elements 5' of RAG2. *Science* 285, 1080–1084. doi: 10.1126/science.285.5430.1080

Zhang, F., Thomas, L. R., Oltz, E. M., and Aune, T. M. (2006). Control of thymocyte development and recombination-activating gene expression by the zinc finger protein Zfp608. *Nat. Immunol.* 7, 1309–1316. doi: 10.1038/ni1397

Zhang, Y., Gostissa, M., Hildebrand, D. G., Becker, M. S., Boboila, C., Chiarle, R., et al. (2010). The role of mechanistic factors in promoting chromosomal translocations found in lymphoid and other cancers. *Adv. Immunol.* 106, 93–133. doi: 10.1016/s0065-2776(10)06004-9

Conflict of Interest: The authors declare that the research was conducted in the absence of any commercial or financial relationships that could be construed as a potential conflict of interest.

frontiers in Cell and Developmental Biology

ORIGINAL RESEARCH
published: 15 July 2021
doi: 10.3389/fcell.2021.686737

JFK Is a Hypoxia-Inducible Gene That Functions to Promote Breast Carcinogenesis

Ziran Yang[1†], Xuehong Zhou[1†], Enrun Zheng[1], Yizhou Wang[1], Xinhua Liu[2], Yue Wang[1,2], Yanpu Wang[3], Zhaofei Liu[3], Fei Pei[4], Yue Zhang[1], Jie Ren[1], Yunchao Huang[1], Lu Xia[1], Sudun Guan[1], Sen Qin[1], Feiya Suo[1], Jie Shi[5], Lijing Wang[6], Lin He[1,5] and Luyang Sun[1,7]**

[1] Department of Biochemistry and Molecular Biology, School of Basic Medical Sciences, Key Laboratory of Carcinogenesis and Translational Research (Ministry of Education), Peking University Health Science Center, Beijing, China, [2] Department of Biochemistry and Molecular Biology, School of Basic Medical Sciences, Hangzhou Normal University, Hangzhou, China, [3] Medical Isotopes Research Center and Department of Radiation Medicine, School of Basic Medical Sciences, Peking University Health Science Center, Beijing, China, [4] Department of Pathology, Peking University Third Hospital, School of Basic Medical Sciences, Peking University Health Science Center, Beijing, China, [5] National Institute on Drug Dependence, Peking University, Beijing, China, [6] Vascular Biology Research Institute, Guangdong Pharmaceutical University, Guangzhou, China, [7] Department of Integration of Chinese and Western Medicine, School of Basic Medical Sciences, Peking University Health Science Center, Beijing, China

Many carcinomas feature hypoxia, a condition has long been associated with tumor progression and poor prognosis, as well as resistance to chemoradiotherapy. Here, we report that the F-box protein JFK promotes mammary tumor initiation and progression in MMTV-PyMT murine model of spontaneous breast cancer. We find that *JFK* is inducible under hypoxic conditions, in which hypoxia-inducible factor HIF-1α binds to and transcriptionally activates *JFK* in breast cancer cells. Consistently, analysis of public clinical datasets reveals that the mRNA level of JFK is positively correlated with that of HIF-1α in breast cancer. We show that JFK deficiency leads to a decrease in HIF-1α-induced glycolysis in breast cancer and sensitizes hypoxic breast cancer cells to ionizing radiation and chemotherapeutic treatment. These results indicate that JFK is an important player in hypoxic response, supporting the pursuit of JFK as a potential therapeutic target for breast cancer intervention.

Keywords: breast carcinogenesis, transcriptional regulation, cancer metabolism, hypoxia, JFK

OPEN ACCESS

Edited by:
Qinong Ye,
Institute of Biotechnology (CAAS), China

Reviewed by:
Binghui Li,
Capital Medical University, China
Shan Gao,
Suzhou Institute of Biomedical Engineering and Technology (CAS), China

***Correspondence:**
Lin He
linhe@bjmu.edu.cn
Luyang Sun
luyang_sun@hsc.pku.edu.cn

[†] These authors have contributed equally to this work

Specialty section:
This article was submitted to Molecular Medicine, a section of the journal Frontiers in Cell and Developmental Biology

Received: *27 March 2021*
Accepted: *21 June 2021*
Published: *15 July 2021*

Citation:
Yang Z, Zhou X, Zheng E, Wang Y, Liu X, Wang Y, Wang Y, Liu Z, Pei F, Zhang Y, Ren J, Huang Y, Xia L, Guan S, Qin S, Suo F, Shi J, Wang L, He L and Sun L (2021) JFK Is a Hypoxia-Inducible Gene That Functions to Promote Breast Carcinogenesis. Front. Cell Dev. Biol. 9:686737. doi: 10.3389/fcell.2021.686737

INTRODUCTION

Among females, breast cancer is the most commonly diagnosed cancer and the leading cause of cancer death (Bray et al., 2018). Although the development of comprehensive breast cancer treatment strategies has supported a downward trend in breast cancer mortality, there are still no means of definitively identifying patients who will be resistance to radiotherapy and chemotherapy and relapse (Akram et al., 2017). Evidence is mounting that the oxygen (O_2) content of tumor tissue is an important determinant of metastasis, and tumor hypoxia has been associated with increased malignancy, poor prognosis, and resistance to both radiotherapy and chemotherapy (Keith et al., 2011). Thus, particular interest has been focused on the mechanisms by which hypoxic tumor

cells alter their transcriptional profiles to modulate processes including initiation, progression, and metastasis to persist under conditions of hypoxic stress.

Aerobic glycolysis, also termed the Warburg effect, is a general feature of glucose metabolism in tumor cells (Hanahan and Weinberg, 2011; Chen et al., 2019). Tumor cells predominantly utilize glycolysis for energy production mechanisms and have higher rates of glycolysis, which increases biosynthesis, inhibits apoptosis, and generates signaling metabolites to enhance tumor cell survival under difficult conditions including hypoxia (Pavlova and Thompson, 2016; Wu et al., 2020). It is well established that hypoxia can lead to high rates of glycolysis through stabilization of hypoxia-inducible factors (HIFs) (Wu et al., 2020). HIFs are heterodimeric complexes composed of basic helix-loop-helix/PAS (bHLH-PAS) proteins including an O_2-labile alpha subunit (HIF-1α, HIF-2α, or HIF-3α) and a stable beta subunit (HIF-1β) (Iommarini et al., 2017). HIF transcription factors are master regulators of the cellular response to hypoxia and coordinate a transcriptional program that ensures optimal functional, metabolic, and vascular adaptation to oxygen shortages (Jurikova et al., 2016). In breast cancer, HIF-1α transcriptionally activates the expression of genes with known functions in cell survival, angiogenesis, metabolic reprogramming, invasion, and metastasis, through binding to hypoxia response elements (HREs) in the promoters of its target genes (Masoud and Li, 2015). However, it remains to be investigated the mechanism(s) underlying how cancer cells response to hypoxic conditions through HIF-1α-mediated transcriptional regulation.

To date, the best-characterized mammalian multi-subunit RING-finger type of E3 ligases is the SCF (SKP1-CUL1-F-box) complex, comprising SKP1, RBX1, CUL1, and a flexible F-box protein (FBP) that acts as a receptor for substrate recognition (Jia and Sun, 2011). In previous studies, we reported that JFK is the only Kelch domain-containing F-box protein in humans, and targets p53 and ING4 for degradation through the assembly of a SCF complex (Sun et al., 2009, 2011; Yan et al., 2015). We showed that JFK destabilizes p53, contributing to reduced cell apoptosis and sensitizing cells to ionizing radiation-induced cell death. Additionally, JFK-mediated ING4 proteasomal degradation promotes angiogenesis and metastasis of breast cancer. JFK is highly expressed in breast cancer, supporting that it could be used as a target molecule for the design of new breast cancer therapies. However, the upstream activators (and cellular contexts) which drive elevated JFK levels in breast cancers are currently unknown.

In the present study, using MMTV-PyMT model of spontaneous breast cancer, we report that JFK promotes mammary tumorigenesis. HIF-1α binds to and transcriptionally activates *JFK* in hypoxic breast cancer cells, and analyses of public clinical datasets support the positive correlation between mRNA expression of JFK and HIF-1α in breast cancer. We showed that JFK knockdown leads to a decrease in hypoxia-enhanced glycolysis and overcomes chemo-radiotherapeutic resistance in hypoxic breast cancer cells. We demonstrated that *JFK* is a hypoxia-induced oncogene, and explored the clinicopathological significance of the HIF-1α-JFK axis in breast cancer progression and intervention.

MATERIALS AND METHODS

Antibodies

The antibodies used were αTubulin from Sigma; αHIF-1α from Abcam; αp53, αING4, αKi-67, αPCNA, αE2F1, αFOXP3, and αMYC from Santa Cruz. Polyclonal antibodies against JFK were raised against the C-terminal epitope of the JFK protein (CYPKTNALYFVRAKR) in rabbits.

JFK Transgenic Mice

JFK transgenic mice were generated by Cyagen Biosciences on the C57BL/6 background. ORF of human *JFK* with a FLAG tag was cloned into the mammalian expression vector pRP (Exp)-EF1A. After digestion, linearized DNA was used for microinjection into the pro-nuclei of fertilized oocytes from hormonally superovulated C57BL/6 female mice under a microscope. The injected fertilized eggs were transplanted into the oviducts of pseudo-pregnant mice. The genomic DNA were extracted from mouse tail tips for molecular genotyping. The primers specific for the transgene *JFK* (forward: 5′-GCTTTTGGAGTACGTCGTCT-3′; reverse: 5′-GGCTCCTCATCTTGATCCAT-3′) were used to amplify a 334 bp fragment, and the primers for internal control (forward: 5′-CAACCACTTACAAGAGACCCGTA-3′; reverse: 5′-GAGCCCTTAGAAATAACGTTCACC-3′) were used to amplify a 632 bp fragment.

MMTV-PyMT Mouse Model

FVB/N-Tg (MMTV-PyMT) mice were crossed with wild-type mice (C57BL/6 strain) for six generations to backcross into the C57BL/6 strain. Genotyping analyses were performed by PCR with genomic DNA extracted from tail tips. The primers specific for the transgene *PyMT* (forward: 5′-GGAAGCAAGTACTTCACAAGGG-3′; reverse: 5′-GGAAAGTCACTAGGAGCAGGG-3′) were used to amplify a 556 bp fragment. Animal handling and procedures were approved by the Institutional Animal Care of Peking University Health Center.

Small-Animal SPECT/CT Imaging of ^{99m}Tc-3PRGD2

The integrin αvβ3-targeting radiotracer ^{99m}Tc-3PRGD2 was synthesized by labeling the precursor HYNIC-3PRGD2 with $Na^{99m}TcO_4$ as previously described (Jia et al., 2011). ^{99m}Tc-3PRGD2 was prepared with the radiochemical purity of >98% and was then used for *in vivo* imaging studies. For small-animal SPECT/CT, MMTV-PyMT mice were intravenously injected with 37 MBq of ^{99m}Tc-3PRGD2. At 30 min postinjection, SPECT/CT scanning was performed using a NanoScan SPECT/CT Imaging System (Mediso, Budapest, Hungary) as previously described (Liu et al., 2012, 2014).

Cell Culture and Transfection

MCF-7 and T47D cells were maintained according to the ATCC's recommendation. Transfections of expression plasmids were carried out using polyethyleneimine (PEI, Polysciences), and siRNA oligonucleotides (GeneChem Inc.) were transfected into cells using RNAiMAX (Invitrogen) according to the manufacturer's instructions. The sequences of siRNAs were: HIF-1α siRNA, 5′-UUCAAGUUGGAAUUGGUAG-3′; JFK siRNA, 5′-GGUGUAGCCCAUCAGUGUU-3′; and control siRNA, 5′-UUCUCCGAACGUGUCACGU-3′.

Western Blotting

Cellular lysates were prepared by incubating the cells in lysis buffer (50 mM Tris–HCl, pH 7.5, 150 mM NaCl, 0.5% NP-40, and 2 mM EDTA) containing protease inhibitor cocktail and phosphatase inhibitor for 20 min at 4°C, followed by centrifugation at 14,000 *g* for 15 min at 4°C. The protein concentration of the lysates was determined using the BCA protein assay kit (Pierce) according to the manufacturer's protocol. For western blotting, the samples were resolved on SDS-PAGE gels and transferred onto nitrocellulose membranes. The membranes were incubated with appropriate antibodies overnight at 4°C followed by incubation with a secondary antibody. Immunoreactive bands were visualized using western blotting Luminol reagent (Santa Cruz) according to the manufacturer's recommendation. The dilutions of primary antibodies were: 1: 1000 with αJFK, αING4, αKi-67, αPCNA, or αHIF-1α; 1: 2000 with αp53 or α Tubulin.

Real-Time Reverse Transcription PCR

Total mRNAs were isolated with Trizol reagents (Invitrogen) for cDNA synthesis. Real-time reverse transcriptase PCR was performed using the ABI PRISM 7500 system (Applied Biosystems) that measures real-time SYBR green fluorescence and then calculated by means of the comparative Ct method (2-ΔΔCt) with the expression of GAPDH as an internal control. The primers used were: *JFK*: 5′-AGCCCCACCCAGTATTGGA-3′ (forward) and 5′-CCTGATACGGTGAGAGAAAGGA-3′ (reverse); *GAPDH:* 5′-GAAGGTGAAGGTCGGAGTC-3′ (forward) and 5′-GAAGATGGTGATGGGATTTC-3′ (reverse).

ChIP and qChIP

MCF-7 or T47D cells treated with hypoxia (1% O_2) for 24 h were crosslinked with 1% formaldehyde for 10 min at room temperature and quenched by the addition of glycine to a final concentration of 125 mM for 5 min. The fixed cells were resuspended in lysis buffer (1% SDS, 5 mM EDTA, and 50 mM Tris–HCl, pH 8.1) containing protease inhibitors, then subjected to 30 cycles (30 s on and off) of sonication (Bioruptor, Diagenode) to generate chromatin fragments of ∼300 bp in length. Lysates were diluted in buffer (1% Triton X-100, 2 mM EDTA, 150 mM NaCl, and 20 mM Tris–HCl, pH 8.1) containing protease inhibitors. For immunoprecipitation, the diluted chromatin was incubated with normal IgG (control) or HIF-1α antibodies overnight at 4°C with constant rotation, followed by incubation with 50 μl of 50% (v/v) protein A/G Sepharose beads for an additional 2 h. Beads were successively washed with the following buffers: TSE I (0.1% SDS, 1% Triton X-100, 2 mM EDTA, 150 mM NaCl, and 20 mM Tris–HCl, pH 8.0); TSE II (0.1% SDS, 1% Triton X-100, 2 mM EDTA, 500 mM NaCl, and 20 mM Tris–HCl, pH 8.0); TSE III (0.25 M LiCl, 1% Nonidet P-40, 1% sodium deoxycholate, 1 mM EDTA, and 10 mM Tris–HCl, pH 8.0). The pulled-down chromatin complex eluted by TE (1 mM EDTA and 10 mM Tris–HCl, pH 8.0) and input were de-crosslinked at 55°C for 12 h in elution buffer (1% SDS and 0.1 M $NaHCO_3$) (Li et al., 2016). The DNA was purified with the QIAquick PCR Purification Kit (QIAGEN). qChIPs were performed using Power SYBR Green PCR Master Mix and an ABI PRISM 7500 system (Applied Biosystems, Foster City, CA, United States). The primers used were: *JFK*: 5′-TGAGCACATTTGTGTGCCG-3′ (forward) and 5′-TGGACACTACTAGGCGGTCA-3′ (reverse).

Luciferase Reporter Assay

MCF-7 or T47D cells in 24-well plates were infected with lentiviruses carrying luciferase reporter, renilla, and indicated expression constructs. The amount of DNA in each transfection was kept constant by addition of empty vector. Twenty-four hours after transfection, the firefly and renilla luciferase were assayed according to the manufacturer's protocol (Promega), and the firefly luciferase activity was normalized to that of renilla luciferase. Each experiment was performed in triplicate and repeated at last three times.

Measurement of Glucose Uptake and Lactate Production

The extracellular lactate was measured using the cell culture medium with Lactate Colorimetric Assay Kit (BioVision) according to the manufacturer's instruction. Intracellular glucose was measured using cell lysates with Glucose Colorimetric/Fluorometric Assay Kit (BioVision) according to the manufacturer's instruction.

Histologic Analysis

Mammary tumors or livers of female mice were excised, fixed with 10% neutral buffered formalin for 24 h. After paraffin embedding and sectioning (5 μm), tissues were stained with hematoxylin and eosin (H&E). In tissue immunohistochemical staining, the antigen was retrieved by high pressure and incubation in 0.01 M sodium citrate buffer. Then the samples were blocked in 10% normal goat serum in PBS, and incubated with primary antibodies at 4°C overnight in primary antibody solution. After being washed with PBS buffer, the samples were incubated with polymer HRP goat anti-rabbit (DAKO, Agilent) for 30 min at room temperature, developed with DAB (3,3′-diaminobenzidine tetrahydrochloride), and counterstained with hematoxylin (Zhongshan Golden Bridge Biotechnology Company). All specimens were evaluated by two pathologists without knowledge of the experimental group.

Cell Viability Assay

MCF-7 cells with control or JFK-depleted were cultured in normoxia or hypoxia for 48 h, and were subsequently treated

with X-ray irradiation, tamoxifen, or fulvestrant before growing for 5 days. The cell viability rate of MCF-7 cells was evaluated using Cell Counting Kit (CCK, TransGen Biotech) according to the manufacturer's instruction.

Statistical Analysis

Results are reported as mean ± SD for triplicate experiments or mean ± SEM unless otherwise noted. SPSS V.19.0 was used for statistical analysis. Comparisons between two groups were performed using two-tailed paired Student's *t* test. Comparisons among three groups were performed using one-way ANOVA followed by Tukey's honestly significant difference (HSD) *post hoc* test.

RESULTS

JFK Promotes Mammary Tumor Initiation and Metastasis in Mice

It has been reported that JFK is highly expressed in tumor tissues including breast, kidney, and pancreatic cancer, with the highest JFK expression level reported in breast cancer (Yan et al., 2015). To further investigate the potential function of JFK in breast cancer development, we first generated *JFK* transgenic (JFK^{TG}) mice by nuclear transplantation. Briefly, the open reading frame (ORF) of human *JFK* (with a FLAG tag) was cloned into the mammalian expression vector pRP(Exp)-EF1A. After digestion, linearized DNA was micro-injected into the pronuclei of fertilized zygotes derived from C57BL/6 female mice, and the embryos were transplanted onto pseudo-pregnant mice to breed JFK^{TG} founders.

The expression of mRNA and protein of JFK in JFK^{TG} mice was verified by real-time reverse transcriptase PCR (qPCR) and western blotting, and these both indicated that JFK transgenic mice were obtained successfully (**Figure 1A**). We then crossed the JFK^{TG} mice with mouse mammary tumor virus-polyoma virus middle T-antigen (MMTV-PyMT) transgenic mice (Murai, 2015) – a widely utilized preclinical mouse model that recapitulates human breast cancer progression from early hyperplasia to malignant breast carcinoma – to obtain female $JFK^{WT}/PyMT^{TG}$ and $JFK^{TG}/PyMT^{TG}$ mice. We observed that $JFK^{TG}/PyMT^{TG}$ mice developed palpable tumors at the average age of 12-week-old, 2 weeks earlier than $JFK^{WT}/PyMT^{TG}$ mice. Moreover, the number of subcutaneous tumors was significantly greater, and the volume of subcutaneous tumors was significantly larger in $JFK^{TG}/PyMT^{TG}$ mice compared with $JFK^{WT}/PyMT^{TG}$ mice (**Figure 1B**).

Previous studies reported that integrin $\alpha_v\beta_3$ is expressed at high levels on the surface of a variety of solid tumor cells and on the tumor vasculature (Liu et al., 2011). To further explore the effect of JFK on breast carcinogenesis, we used an integrin $\alpha_v\beta_3$-targeting radiotracer, ^{99m}Tc-3PRGD2 (Zhu et al., 2012), to conduct single photon emission computed tomography (SPECT)/computed tomography (CT) *in vivo* imaging. To this end, ^{99m}Tc-3PRGD2 was injected into the 14-week-old $JFK^{WT}/PyMT^{TG}$ and $JFK^{TG}/PyMT^{TG}$ mice via the tail vein. SPECT/CT of $JFK^{WT}/PyMT^{TG}$ and $JFK^{TG}/PyMT^{TG}$ mice at 30 min after injection showed that there was remarkable accumulation of ^{99m}Tc-3PRGD2 in mammary tumors at 30 min post-injection, and $JFK^{TG}/PyMT^{TG}$ mice developed more multifocal palpable tumors compared with $JFK^{WT}/PyMT^{TG}$ mice (**Figure 1C** and **Supplementary Movies 1**, **2**). The quantification analysis of total tumor volumes revealed that $JFK^{TG}/PyMT^{TG}$ mice exhibited increased tumorigenesis compared with $JFK^{WT}/PyMT^{TG}$ mice (**Figure 1C**). Hematoxylin-eosin (H&E) staining analysis of liver tissues also revealed that the $JFK^{TG}/PyMT^{TG}$ mice had significantly elevated numbers of liver metastases compared to $JFK^{WT}/PyMT^{TG}$ mice (**Figure 1D**). Collectively, these *in vivo* results support that JFK overexpression somehow promotes mammary tumor initiation and metastasis.

To further explore the role of JFK in promoting breast cancer, we collected breast tumors from 14-week-old $JFK^{WT}/PyMT^{TG}$ and $JFK^{TG}/PyMT^{TG}$ mice and performed histological analysis. H&E staining of tumor sections showed that abnormal mitoses in mammary tumor tissue of $JFK^{TG}/PyMT^{TG}$ mice are about 3-fold greater in number than in $JFK^{WT}/PyMT^{TG}$ mice (**Figure 1E**), clearly suggesting that JFK overexpression somehow promotes cell division of breast cancer cells *in vivo*. Pursuing this, we performed immunohistochemical analysis of breast tumor tissues of $JFK^{WT}/PyMT^{TG}$ and $JFK^{TG}/PyMT^{TG}$ mice for expression of Ki-67 and Pcna, two well-documented markers for cellular proliferation (Jurikova et al., 2016). $JFK^{TG}/PyMT^{TG}$ mice exhibited substantially more Ki-67-positive and Pcna-positive nuclei than $JFK^{WT}/PyMT^{TG}$ mice (**Figure 1F**), indicating that JFK promotes cell proliferation *in vivo*. Western blotting analysis showed that overexpression of JFK was accompanied by increased accumulation of the Ki-67 and Pcna proteins but reduced levels of the p53 and Ing4 proteins, findings consistent with previous studies showing that JFK targets p53 and ING4 proteins for ubiquitination and degradation (Sun et al., 2009; Yan et al., 2015; **Figure 1G**) and supporting the aforementioned hypothesis that JFK impacts tumor progression through its function in SCF^{JFK} in destabilizing tumor suppressor genes. Together, these *in vivo* results show that *JFK* functions in mammary tumorigenesis in the MMTV-PyMT mouse model by promoting cell proliferation.

Genome-Wide Identification of Transcriptional Targets of HIF-1α

Given that JFK is expressed at aberrantly high levels in breast cancer at both the mRNA and protein levels, we next explored mechanism(s) underlying JFK dysregulation in diverse samples by adopting a phenolyzer approach (Yang H. et al., 2015). Specifically, to predict any transcription factors likely to bind at the *JFK* promoter in breast cancer, we analyzed data from PROMO[1] using tools for the phenotype-based gene analyzer[2]. We initially focused on transcription factors with reported links to breast cancer, and found that 16 transcription factors including HIF-1α, MYC, FOXP3, and E2F1 were predicted to target the *JFK* locus (**Figure 2A**). Soluble chromatin from MCF-7 cells was prepared for ChIP assays, and the results showed that

[1]http://alggen.lsi.upc.es/cgi-bin/promo_v3/promo/promoinit.cgi?dirDB=TF_8.3
[2]http://phenolyzer.wglab.org/

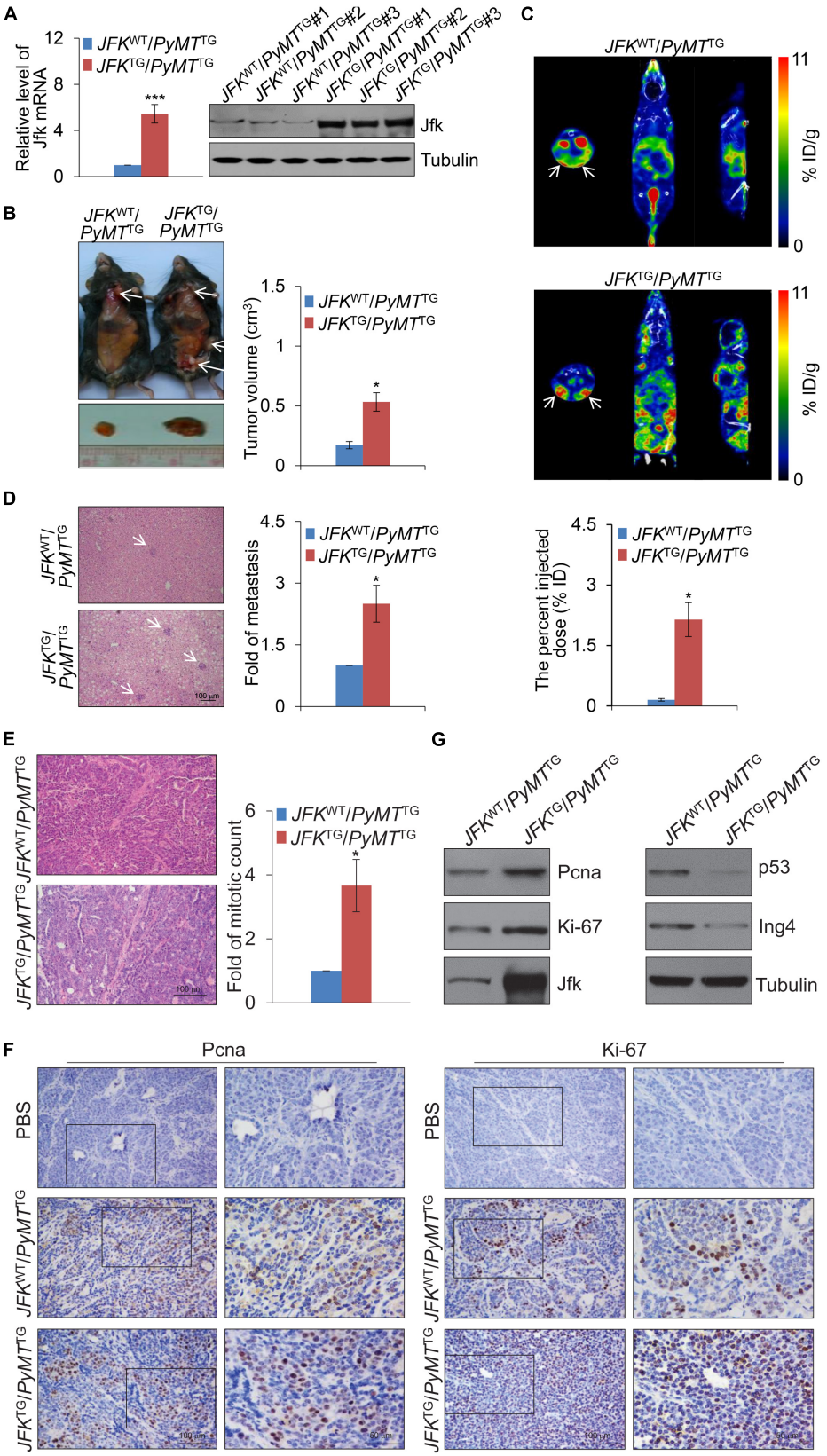

FIGURE 1 | Continued

FIGURE 1 | JFK promotes mammary tumor initiation and metastasis in mice. **(A)** Total RNAs or proteins from the tail tip of $JFK^{WT}/PyMT^{TG}$ or $JFK^{TG}/PyMT^{TG}$ mice were extracted, and respectively, analyzed for Jfk expression by qPCR or western blotting with the indicated antibodies. Error bars represent the mean ± SD for triplicate experiments (***$p < 0.001$). **(B)** Representative images of tumors resected from 14-week-old $JFK^{WT}/PyMT^{TG}$ or $JFK^{TG}/PyMT^{TG}$ mice on autopsy. Arrows indicate the subcutaneous breast tumors, and tumor size was measured using digital calipers. Error bars represent the mean ± SEM ($n = 6$, *$p < 0.05$). **(C)** Representative SPECT/CT images of $JFK^{WT}/PyMT^{TG}$ or $JFK^{TG}/PyMT^{TG}$ mice at 30 min after injection of ^{99}mTc-3PRGD2 (37 MBq) via the tail vein. Error bars represent the mean ± SEM ($n = 6$, *$p < 0.05$). **(D)** Representative images of liver sections from $JFK^{WT}/PyMT^{TG}$ or $JFK^{TG}/PyMT^{TG}$ mice stained with hematoxylin and eosin (H&E) are shown. Bar, 100 μm. Error bars represent the mean ± SEM ($n = 6$, *$p < 0.05$). **(E)** Representative images of tumor sections from 14-week-old $JFK^{WT}/PyMT^{TG}$ and $JFK^{TG}/PyMT^{TG}$ mice stained with H&E. Bar, 100 μm. Error bars represent the mean ± SEM ($n = 6$, *$p < 0.05$). **(F)** Immunohistochemical staining of mammary tumors with from 14-week-old $JFK^{WT}/PyMT^{TG}$ and $JFK^{TG}/PyMT^{TG}$ mice for the expression of Ki-67 and Pcna. **(G)** Total protein extracts were prepared from mammary tumor tissues from 14-week-old $JFK^{WT}/PyMT^{TG}$ and $JFK^{TG}/PyMT^{TG}$ mice and analyzed via western blotting with the indicated antibodies.

HIF-1α, FOXP3, and E2F1 were enriched at *JFK* promoter (**Figure 2B**). Briefly, HIF-1α overexpression, but not FOXP3 nor E2F1, has been reported to be closely related to high histological grade, lymph node metastasis, large tumor size, and increased angiogenesis in breast cancer (Qin et al., 2006; Yamamoto et al., 2008; Li et al., 2018), which is consistent with the function of JFK. In light of the common view that tumor microenvironment is often hypoxic and HIF-1α is a hypoxia-inducible factor (Barker et al., 2015), we focused on the effect of HIF-1α on transcriptional regulation of *JFK*.

We further analyzed published chromatin immunoprecipitation-coupled massive parallel DNA sequencing (ChIP-seq) data for the genome-wide transcriptional profile of HIF-1α and to identify candidate direct transcriptional activation targets of HIF-1α in breast cancer (GSE59935) (Zhang et al., 2015). In these experiments, ChIP was performed in hypoxia-treated T47D cells using antibodies against HIF-1α (Zhang et al., 2015). After processing with the alignment to the unmasked human reference genome (GRCh37, hg19) using Bowtie2, we performed MACS2 (Model-based Analysis for ChIP-Seq) analysis using a cutoff of $q < 1e\text{-}2$. After filtering, a total of 99,681 HIF-1α-specific binding peaks were called, with the majority of the peaks located at promoter sequences (23.92%) and the remainder at intronic (32.71%) or intergenic (34.75%) regions (**Figure 2C**).

The genomic landscape of HIF-1α binding peaks at promoter sequences (≤3 K) were analyzed by deepTools (**Figure 2D**). Using R and Bioconductor, further GO enrichment analysis of the promoter regions (≤500 bp) with enriched HIF-1α occupancy revealed enrichment for functional annotations including mitotic cytokinesis, glycolytic process, cell cycle, and fatty acid β-oxidation, which were related to cell proliferation and metabolism (**Figure 2E**). Consistent with above prediction, tracks visualizing the ChIP signal analysis indicated that HIF-1α binds at the *JFK* promoter (**Figure 2F**). Quantitative ChIP (qChIP) analysis with antibodies against HIF-1α and *JFK*-specific primers of MCF-7 cells or T47D cells cultured in hypoxia (1% O_2) conditions validated that the HIF-1α protein is highly enriched at *JFK* promoter (**Figure 2G**). Together, these observations suggest that *JFK* is a potential target gene of HIF-1α .

JFK Is Transcriptionally Activated by HIF-1α

To further investigate the expression regulation of *JFK*, we next cloned a 600 bp fragment from the *JFK* promoter (Chr 1: 16,679,286–16,679,886) and constructed a *JFK* promoter-driven luciferase reporter (*JFK*-Luc). In these experiments, MCF-7 or T47D cells were co-transfected with HIF-1α expression plasmids together with the wild-type *JFK*-Luc promoter or a mutant *JFK*-Luc promoter lacking the predicted HIF-1α binding motif. The results showed that HIF-1α was able to activate transcription from the *JFK* promoter, but only when the CACGTG motif was present (**Figure 3A**), demonstrating that the HIF-1α protein can directly bind to the *JFK* promoter.

Both qPCR and western blotting were then performed in MCF-7 or T47D cells treated with control or HIF-1α siRNAs, under normoxia or hypoxia treatment for 24 h. The results showed that hypoxic conditions led to significantly increased expression of *JFK* (**Figures 3B,C**). No such increase in JFK mRNA or protein accumulation was observed upon HIF-1α knockdown in hypoxic condition (**Figures 3B,C**). These results demonstrate a direct functional impact of HIF-1α in the observed hypoxia-induced transcriptional activation of *JFK* in breast cancer cells.

Extending our investigation to the MMTV-PyMT mouse model, we harvested tumors from 14-week-old or 16-week-old $JFK^{WT}/PyMT^{TG}$ mice. Immunohistochemical staining showed that, compared to 14-week-old $JFK^{WT}/PyMT^{TG}$ mice, the Hif-1α and Jfk protein levels were clearly up-regulated in the mammary tumors of the 16-week-old $JFK^{WT}/PyMT^{TG}$ mice (**Figure 3D**). Collectively, these results support that the hypoxia-mediated induction of JFK is mediated by HIF-1α binding and transcriptional activation and, further, defines an HIF-1α-JFK axis which apparently functions in promoting breast carcinogenesis.

JFK Promotes HIF-1α-Induced Glycolysis

It is known that HIF-1α is a metabolic regulator that plays an important role in glycolysis metabolism (Wu et al., 2020), we further investigated whether JFK functions in hypoxia-induced glycolysis of breast cancer cells. To this end, MCF-7 cells treated with control or JFK siRNAs were cultured in normoxia or hypoxia conditions, or co-transfected with vector or HIF-1α, and we performed glucose colorimetric/fluorometric or lactate colorimetric assay to detect glucose uptake or lactate production. The results showed that JFK knockdown significantly dampened hypoxia or HIF-1α-induced glycolysis in breast cancer cells (**Figures 4A,B**).

To further extend our investigation to the MMTV-PyMT mouse model, we digested tumor tissues from $JFK^{WT}/PyMT^{TG}$

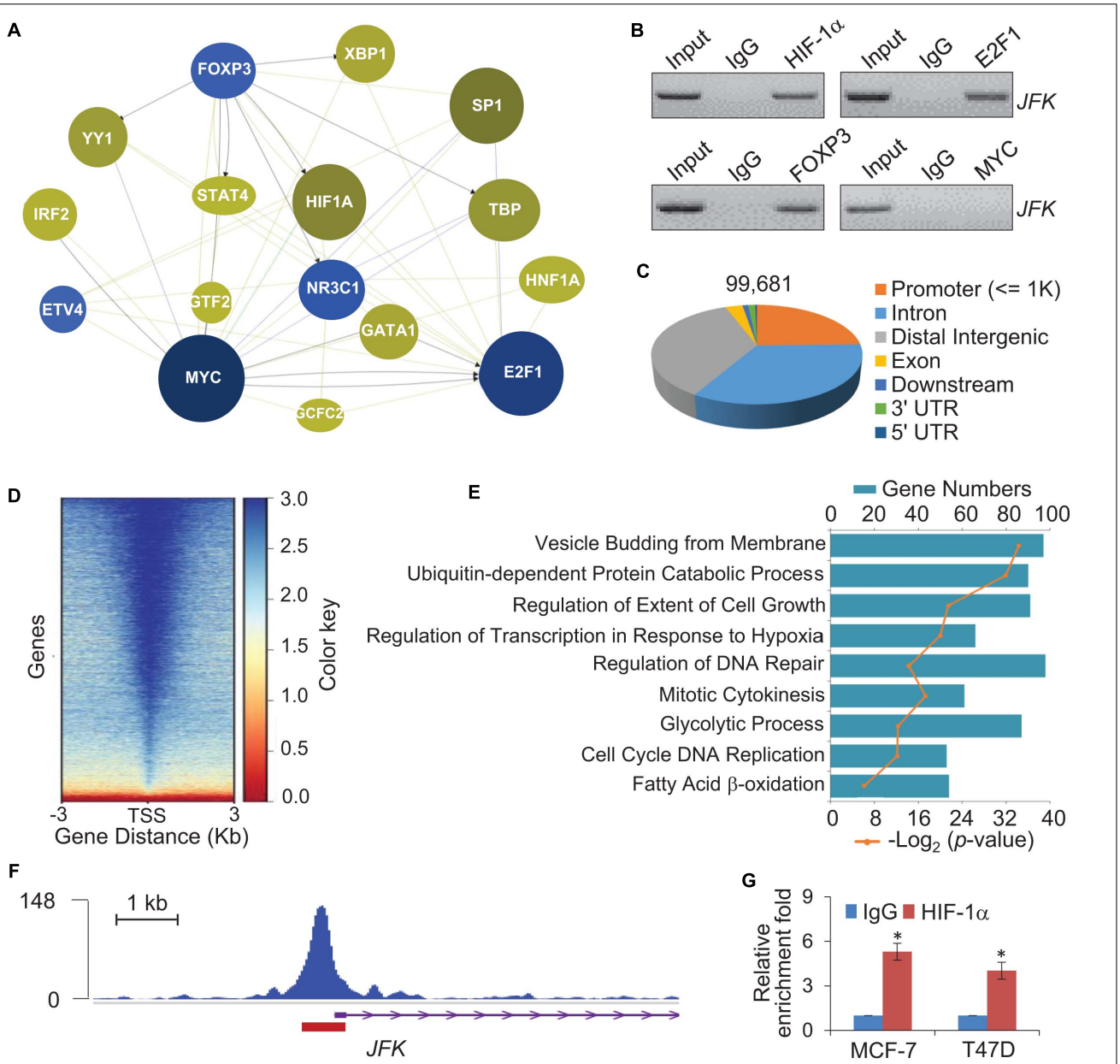

FIGURE 2 | Genome-wide identification of transcriptional targets for HIF-1α. **(A)** Breast cancer associated transcription factors which bind at the promoter of *JFK* were assessed using a Phenolyzer approach. The size and shade of each circle represent the strength of correlation between a given transcription factor that was predicted to bind at the promoter of *JFK* and breast cancer. **(B)** Soluble chromatin from MCF-7 cells was prepared for ChIP assays with antibodies against the indicated proteins. **(C)** Genomic distribution of HIF-1α determined by ChIP-seq analysis. ChIP was performed in hypoxia-treated T47D cells with antibodies against HIF-1α, followed by deep sequencing. The raw data were analyzed by MACS2 with a cutoff *q* value < 1e-2. **(D)** Binding density of HIF-1α across its specific binding sites, visualized by deepTools. The heatmap shows the normalized ChIP-seq tag counts ordered by signal strength. **(E)** GO enrichment (biological processes) analysis of potential target genes. **(F)** Tracks visualizing the ChIP signal for HIF-1α binding at representative locus. The red rectangle indicates the peak region/binding site of HIF-1α at the *JFK* promoter. **(G)** qChIP-based verification of HIF-1α binding at the *JFK* locus under hypoxia. Soluble chromatin from MCF-7 or T47D cells exposed with hypoxia (1% O_2) for 24 h was prepared, and qChIP analysis was performed for the *JFK* promoter using the antibody against HIF-1α. Error bars represent the mean ± SD for triplicate experiments. Statistical significance of differences is indicated as $^*p < 0.05$.

or $JFK^{TG}/PyMT^{TG}$ mice, and the isolated cells were put into primary culture. Isolated cells cultured in normoxia or hypoxia conditions were performed glucose colorimetric/fluorometric or lactate colorimetric assay to detect glucose uptake or lactate production. The results revealed that JFK overexpression significantly strengthened hypoxia-induced glycolysis in breast cancer (**Figure 4C**). Furthermore, primary tumor cells were cultured in normoxia or hypoxia conditions for 72 h, and cell viability analysis showed that the JFK overexpression significantly weakened the decreased cell viability under hypoxia (**Figure 4D**).

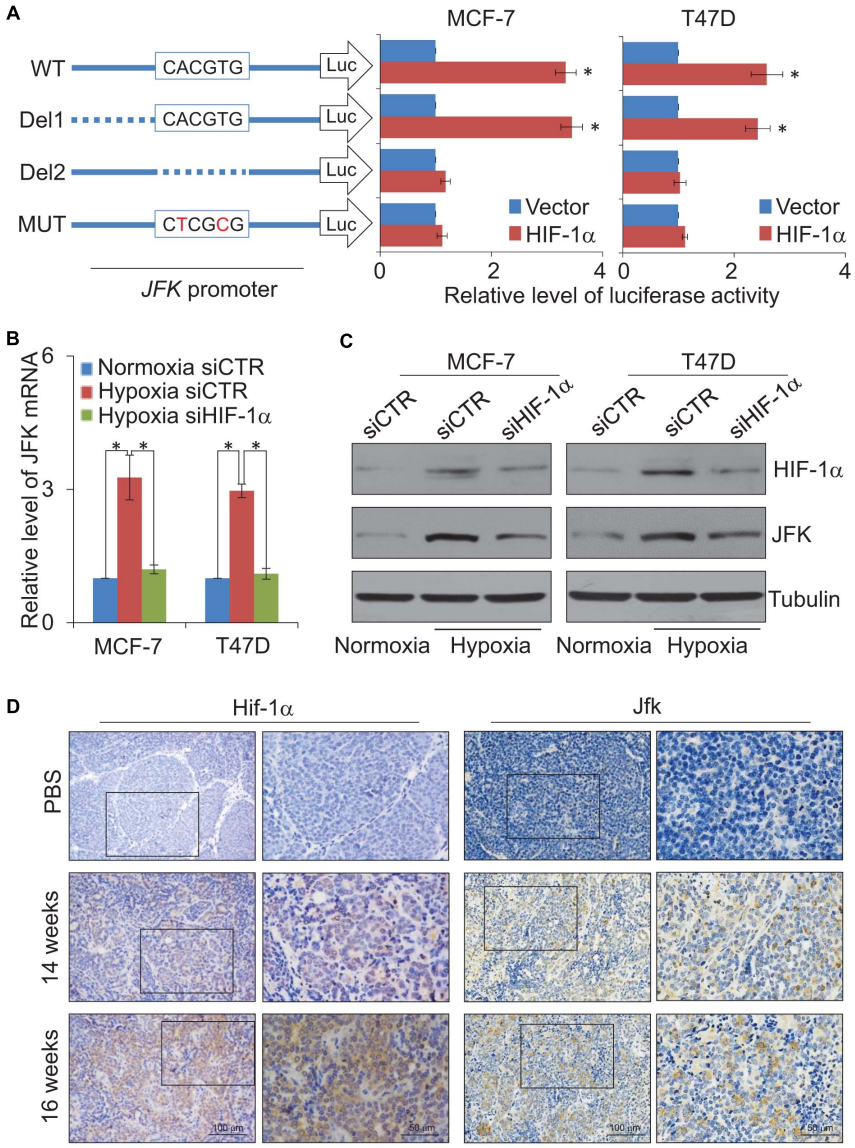

FIGURE 3 | JFK is transcriptionally activated by HIF-1α. **(A)** MCF-7 or T47D cells infected with lentiviruses carrying *JFK*-Luc wild-type, deletion, or mutant variants, as well as control vector or HIF-1α expression constructs, were harvested, lysed, and assayed for firefly and Renilla luciferase activity using the dual-luciferase reporter assay system. Error bars represent the mean ± SD for triplicate experiments. **(B)** qPCR measurement of the *JFK* expression in MCF-7 or T47D cells treated with control or HIF-1α siRNAs, under normoxia or hypoxia (1% O_2) for 24 h. Error bars represent the mean ± SD for triplicate experiments. **(C)** Western blotting analysis of cellular extracts from MCF-7 or T47D cells treated with control or HIF-1α siRNAs, under normoxia or hypoxia (1% O_2) for 24 h. **(D)** Immunohistochemical staining of breast tumors from 14-week-old or 16-week-old $JFK^{WT}/PyMT^{TG}$ mice to assess the expression of Hif-1α and Jfk. Statistical significance of differences is indicated as $^*p < 0.05$.

Together, these results suggest that *JFK* promotes HIF-1α-induced glycolysis thus elevating cellular tolerance to hypoxia in breast cancer.

JFK Deficiency Sensitizes Hypoxic Breast Cancer Cells to Chemo-Radiotherapeutic Treatment

Considering that the high expression of HIF-1α has been related to resistance to radiotherapy and chemotherapy in breast cancer (Yang J. et al., 2015), we next investigated the role of JFK in breast cancer cell sensitivity to ionizing radiation (IR) and chemotherapeutic agents under hypoxia. To this end, MCF-7 cells treated with control or JFK siRNAs under normoxia or hypoxia were exposed to X-ray irradiation or treated with chemotherapeutic agents (tamoxifen or fulvestrant). Cell viability analysis showed that JFK deficiency significantly weakened the increased cell viability in response to hypoxia-induced resistance to IR or chemotherapeutic agents of MCF-7 cells (**Figures 5A,B**). These observations suggest

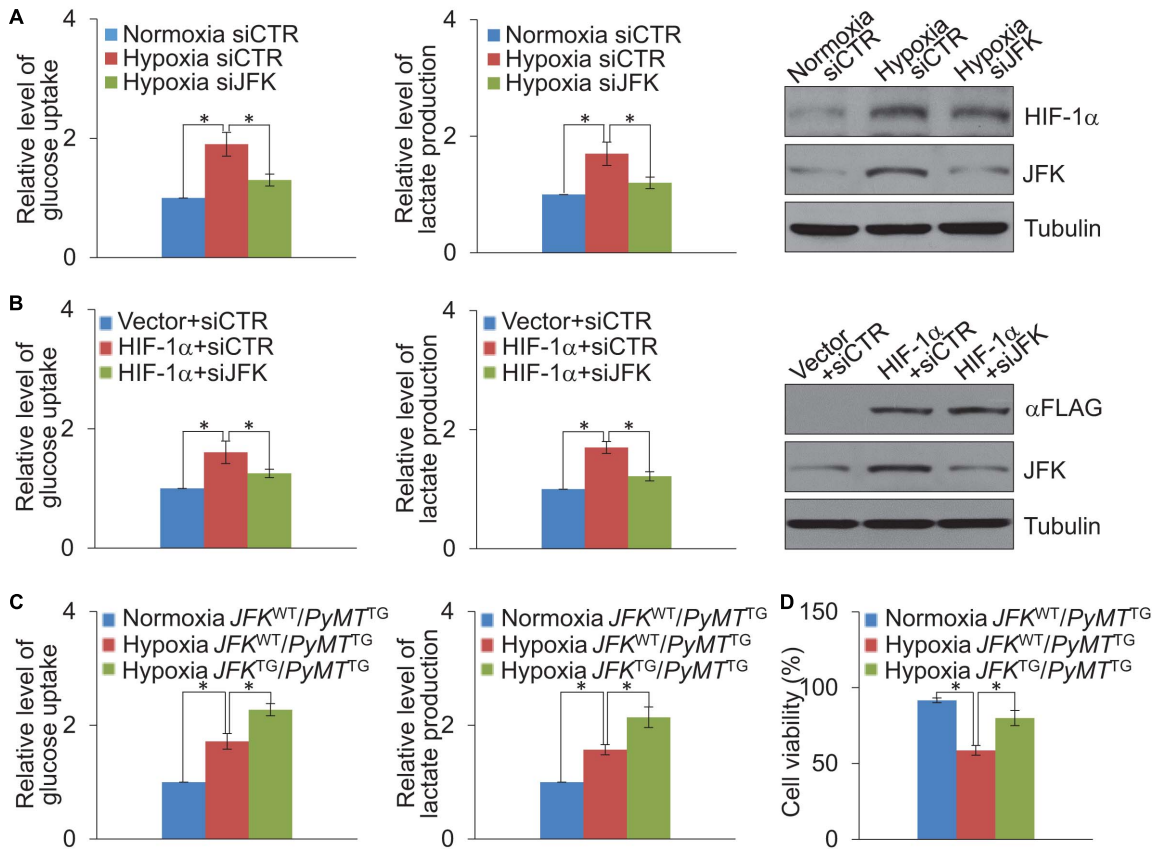

FIGURE 4 | JFK promotes HIF-1α-induced glycolysis. **(A)** Cellular extracts or cell culture medium of MCF-7 cells treated with control or JFK siRNAs and cultured in hypoxia (1% O_2) conditions for 24 h were prepared for measurement of intracellular glucose or extracellular lactate. Error bars represent the mean ± SD for triplicate experiments. Cellular extracts were prepared for western blotting analysis with the indicated antibodies. **(B)** Cellular extracts or cell culture medium of MCF-7 cells treated with control or JFK siRNAs and transfected with vector or HIF-1α were prepared for measurement of intracellular glucose or extracellular lactate. Error bars represent the mean ± SD for triplicate experiments. Cellular extracts were prepared for western blotting analysis with the indicated antibodies. **(C)** Cellular extracts or cell culture medium of primary tumor cells from $JFK^{WT}/PyMT^{TG}$ or $JFK^{TG}/PyMT^{TG}$ mice cultured in normoxia or hypoxia (1% O_2) conditions for 24 h were prepared for measurement of intracellular glucose or extracellular lactate. Error bars represent the mean ± SD for triplicate experiments. **(D)** Primary tumor cells from $JFK^{WT}/PyMT^{TG}$ or $JFK^{TG}/PyMT^{TG}$ mice cultured in normoxia or hypoxia (0.2% O_2) conditions for 72 h, followed by cell viability assessment. Error bars represent the mean ± SD for three independent experiments. Statistical significance of differences is indicated as $^*p < 0.05$.

that JFK protected cells from toxic insults and promoted cell survival under hypoxia.

To gain further support for the impacts of this HIF-1α-JFK axis on breast cancer, and seeking to add clinicopathologically relevant data to our observations, we collected samples from resected breast carcinomas – paired with adjacent normal mammary tissues – from 14 breast cancer patients. Western blotting analysis showed that both HIF-1α and JFK protein levels were significantly upregulated in the cancer tissue compared to the normal tissue (**Figure 5C**). Additionally, and consistent with HIF-1α as a transcription activator of *JFK*, quantitation and statistical analysis revealed that the relative level of JFK protein was significantly and positively correlated with that of HIF-1α (Spearman's rank correlation coefficient, 0.690; $p < 0.001$) (**Figure 5C**).

We also analyzed public data to evaluate the *HIF-1α* and *JFK* mRNA expression levels in breast cancers. Analysis of published clinical datasets (GSE31192, GSE32646, and GSE21653) revealed a positive correlation between *HIF-1α* and *JFK* mRNA expression detected for all of the examined datasets (**Figure 5D**). At minimum, these analyses of previously published breast cancer datasets and our own analysis of tissues from 14 breast cancer patients support our identification of the HIF-1α-JFK axis. Collectively, these findings support a notion that HIF-1α-JFK axis is an important regulator that acts to elevate cellular tolerance to hypoxia and contribute to cell survival in promoting breast carcinogenesis.

DISCUSSION

Elevated accumulation of the HIF-1α protein has been observed in a broad array of human cancer cell types including breast cancer cells, in which elevated levels of HIF-1α are associated with poor prognosis (Jun et al., 2017). Specifically, knockout of *HIF-1α* in the MMTV-PyMT mouse model was reported

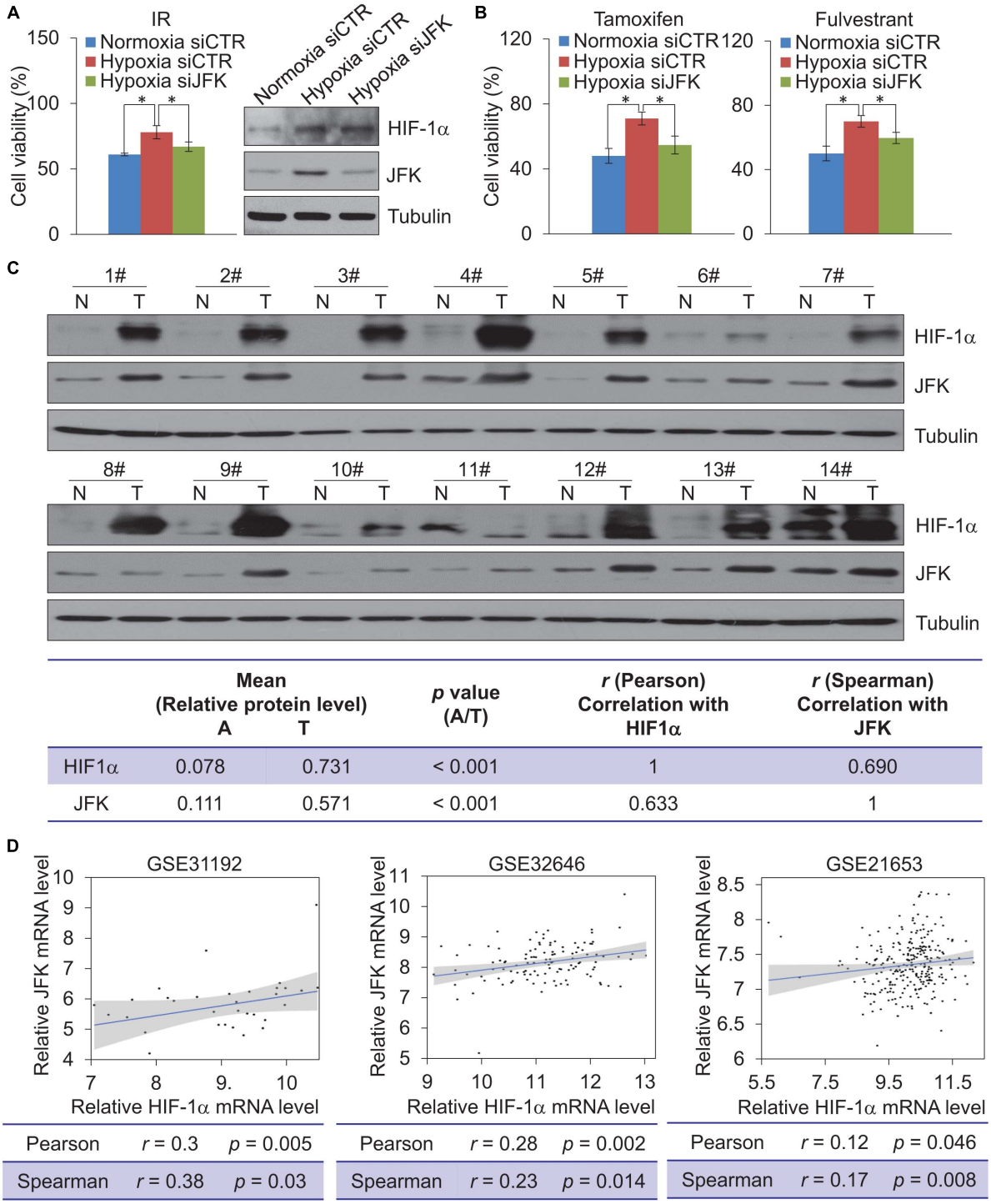

	Mean (Relative protein level) A	T	*p* value (A/T)	*r* (Pearson) Correlation with HIF1α	*r* (Spearman) Correlation with JFK
HIF1α	0.078	0.731	< 0.001	1	0.690
JFK	0.111	0.571	< 0.001	0.633	1

Pearson	*r* = 0.3	*p* = 0.005	Pearson	*r* = 0.28	*p* = 0.002	Pearson	*r* = 0.12	*p* = 0.046
Spearman	*r* = 0.38	*p* = 0.03	Spearman	*r* = 0.23	*p* = 0.014	Spearman	*r* = 0.17	*p* = 0.008

FIGURE 5 | JFK deficiency sensitizes hypoxic breast cancer cells to chemo-radiotherapeutic treatment. **(A)** MCF-7 cells treated with control or JFK siRNAs were cultured in normoxia or hypoxia (1% O_2) conditions, and treated with IR (5 Gy) and subjected to cell viability assessment. Error bars represent the mean ± SD for triplicate experiments. Cellular extracts were prepared for western blotting analysis with the indicated antibodies. **(B)** MCF-7 cells treated with control or JFK siRNAs were cultured in normoxia or hypoxia (1% O_2) conditions, and treated with tamoxifen (0.5 μM) or fulvestrant (0.5 μM) and subjected to cell viability assessment. Error bars represent the mean ± SD for triplicate experiments. **(C)** Western blotting analysis in 14 breast tumors (T) paired with adjacent normal tissues (N) from breast carcinoma patients for the expression of HIF-1α and JFK. Quantitation was performed based on densitometry using Image J, and the values are expressed after normalization to the level of tubulin. The results from correlation analysis between HIF-1α and JFK expression are shown. **(D)** The level of *JFK* mRNA expression was plotted against the level of *HIF-1α* mRNA expression in published clinical datasets (GSE31992, GSE32646, and GSE21653); the line presents a fitted linear model, and the shading represents the 95% confidence interval. Statistical significance of differences is indicated as $^*p < 0.05$.

to suppress both primary tumor growth and lung metastasis (Schwab et al., 2012), which is consistent with our observation that *JFK* overexpression promotes mammary tumor initiation and metastasis in the MMTV-PyMT mouse model. Together these findings support our hypothesis that the HIF-1α-JFK axis contributes to breast cancer cell survival. Our observation of selective (i.e., hypoxia-specific) transcriptional activation of *JFK* by HIF-1α is notable because JFK dysregulation/overexpression has been reported to be a frequent event in breast cancer and has been associated with especially aggressive clinical features and worse survival in breast cancer patients (Yan et al., 2015).

The HREs bound by HIF-1α and HIF-2α have both been shown to contain a conserved RCGTG core sequence, and there are reports that they share transcription target genes including *IL-6*, *FILAG*, and *GLUT1*, which are involved in the adaptation of tumor cells to hypoxia (Keith et al., 2011); thus, it is possible that HIF-2α may also bind to the HRE in the *JFK* promoter. A previous study reported that the HIF-2α protein is stabilized under 5% O_2 (resembling end capillary oxygen conditions) and – in contrast to the low transcription activation activity of HIF-1α at this oxygen level – HIF-2α strongly promotes the transcription of genes such as *VEGF* (Holmquist-Mengelbier et al., 2006). It is known that untreated breast cancer tumors can be hypoxic (∼1.3% oxygen); this level is >5 times lower than oxygen levels found in the normal breast tissues (Wang et al., 2015; Rankin and Giaccia, 2016). Given that O_2 levels vary widely across sub-domains of solid tumors [owing, for example, to rapid cell division and aberrant tumor angiogenesis and blood flow (Bertout et al., 2008)], it will be interesting to explore whether *JFK* is a co-target of both HIF-1α and HIF-2α, perhaps under different severities of hypoxia, in different tumor sub-domains, or at different stages of breast cancer development. Clarifying these points should deepen our understanding of the roles of hypoxia generally, and JFK and HIF-1α/HIF-2α specifically, in breast cancer.

Among breast cancer tumors, basal-like tumors are the most aggressive and are associated with the highest rates of metastasis and recurrence (Alluri and Newman, 2014). Clinical dataset analyses in our previous study revealed that higher *JFK* expression levels were associated with worse overall survival in basal-like breast cancer patients (Yan et al., 2015), so it will be interesting to further investigate whether *JFK* levels in, for example, diagnostic tumor biopsies may be useful for identifying basal-like breast cancers in patients, which are at increased risk of developing metastasis. Consistently, HIF-1α has been identified as one of five signature markers predictive of disease outcomes among node-negative breast cancer patients (Charpin et al., 2012). In addition, it is known that basal-like tumors frequently show morphologic evidence of hypoxia (central fibrosis and necrosis) (Livasy et al., 2006); conventional chemotherapy is not always effective on these tumors and a systemic relapse is often observed, potentially due to the development of drug resistance (Boichuk et al., 2017). Our study revealed that JFK deficiency sensitizes breast cancer cells to chemo-radiotherapeutic treatment under hypoxia, indicating that hypoxia-induced JFK upregulation in basal-like tumors might contribute to drug resistance.

Obesity has been proposed to be a highly significant risk factor for breast carcinogenesis and aggressiveness (Perez-Hernandez et al., 2014), as excessive adipose tissue in obese patients not only alters the local microenvironment by remodeling the extracellular matrix but also provides both energy and niches for cancer cell proliferation and invasion (Seo et al., 2015; Gao et al., 2020). In this regard, drugs (e.g., metformin) targeting signaling pathways that are deregulated in obesity might help to prevent carcinogenesis in obese women (Oppong et al., 2014; Gao et al., 2020). Intriguingly, our recent study demonstrated that JFK suppresses hepatic lipid catabolism and exacerbates the development of obesity and non-alcoholic fatty liver disease (NAFLD) by destabilizing ING5. Moreover, *JFK* is up-regulated in liver tissues from NAFLD patients ($n = 206$) as compared with healthy controls ($n = 10$) according to a recently published public dataset (GSE135251) (Govaere et al., 2020). In the present study, we show that JFK promotes mammary progression in mice, and that the protein level of JFK is up-regulated in resected breast tumors compared with the adjacent normal tissues from breast cancer patients. Although the molecular mechanisms underlying the strong association between obesity and poor breast cancer outcomes are not well understood, it seems plausible that JFK acts as a regulatory hub that coordinates obesity and breast carcinogenesis. Considering that HIF-1α controls oxygen delivery into tumors via angiogenesis and metabolic adaptation of tumors to hypoxia via glycolysis (Semenza, 2002), the HIF-1α-JFK axis we identified in the present study may regulate processes (including glycolysis and fatty-acid β-oxidation) with broad impacts on tumor initiation and metastasis. Moreover, further exploratory screens for interaction partners or degradation substrates of JFK under several conditions including hypoxia, dysregulated energy metabolism, and lipid abnormalities to characterize how JFK functions in apparently diverse cellular processes would likely be scientifically informative.

Our previous studies also revealed that JFK depletion suppresses proliferation and angiogenesis of breast cancer cells through accumulation of tumor suppressors p53 and ING4 (Sun et al., 2009, 2011; Yan et al., 2015). In this study, we showed that JFK depletion reduces cellular tolerance to hypoxia by suppressing glycolysis, and thus contributes to cell survival in breast cancer, which deepens the mechanistic understanding of cancer cell responses to normoxic versus hypoxic conditions. The fact that cancer cells can become addicted to specific metabolic pathways has led to the recent development of novel drugs that target these metabolic vulnerabilities (Tennant et al., 2010). Beyond defining the hypoxia-sensitive HIF-1α-SCF^{JFK} axis, which promotes breast carcinogenesis, we extended these molecular and cell-context specific insights into clinical relevance when targeting HIF-1α is not effective, supporting the hypothesis that JFK is a vulnerable target for the development of innovative therapeutic interventions against breast cancer.

DATA AVAILABILITY STATEMENT

The datasets presented in this study can be found in online repositories. The names of the repository/repositories and

accession number(s) can be found in the article/**Supplementary Material**.

ETHICS STATEMENT

The animal study was reviewed and approved by the Institutional Animal Care and Use Committee at Peking University.

AUTHOR CONTRIBUTIONS

ZY, LH, and LS designed the research. ZY, XZ, and LH conducted the experiments. ZY, XZ, LH, YpW, EZ, and YZ performed the animal experiments and analyzed the data. YzW, XL, YW, ZL, FP, JR, YH, LX, SG, SQ, FS, JS, and LW provided technical assistance. ZY, XZ, LH, and LS wrote the manuscript. All authors contributed to the article and approved the submitted version.

FUNDING

This work was supported by a grant (2016YFC1302304 to LS) from the Ministry of Science and Technology of China, and grants (81874158 to LS and 82002992 to LH) from the National Natural Science Foundation of China, a grant (QNBJ2020-2 to LS) from National Program for Support of Top-notch Young Professionals, a grant (Z200020 to LS) from Beijing Natural Science Foundation of China, and a grant (2019M650385 to LH) from China Postdoctoral Science Foundation.

ACKNOWLEDGMENTS

We thank the National Center for Protein Sciences at Peking University (Beijing, China) for providing technical support.

SUPPLEMENTARY MATERIAL

The Supplementary Material for this article can be found online at: https://www.frontiersin.org/articles/10.3389/fcell.2021.686737/full#supplementary-material

Supplementary Movie 1 | Three-dimensional SPECT/CT image of $JFK^{WT}/PyMT^{TG}$ at 30 min after intravenous injection of ^{99}mTc-3PRGD2.

Supplementary Movie 2 | Three-dimensional SPECT/CT image of $JFK^{TG}/PyMT^{TG}$ at 30 min after intravenous injection of ^{99}mTc-3PRGD2.

REFERENCES

Akram, M., Iqbal, M., Daniyal, M., and Khan, A. U. (2017). Awareness and current knowledge of breast cancer. *Biol. Res.* 50:33. doi: 10.1186/s40659-017-0140-9

Alluri, P., and Newman, L. A. (2014). Basal-like and triple-negative breast cancers: searching for positives among many negatives. *Surg. Oncol. Clin. N. Am.* 23, 567–577. doi: 10.1016/j.soc.2014.03.003

Barker, H. E., Paget, J. T., Khan, A. A., and Harrington, K. J. (2015). The tumour microenvironment after radiotherapy: mechanisms of resistance and recurrence. *Nat. Rev. Cancer* 15, 409–425. doi: 10.1038/nrc3958

Bertout, J. A., Patel, S. A., and Simon, M. C. (2008). The impact of O2 availability on human cancer. *Nat. Rev. Cancer* 8, 967–975. doi: 10.1038/nrc2540

Boichuk, S., Galembikova, A., Sitenkov, A., Khusnutdinov, R., Dunaev, P., Valeeva, E., et al. (2017). Establishment and characterization of a triple negative basal-like breast cancer cell line with multi-drug resistance. *Oncol. Lett.* 14, 5039–5045. doi: 10.3892/ol.2017.6795

Bray, F., Ferlay, J., Soerjomataram, I., Siegel, R. L., Torre, L. A., and Jemal, A. (2018). Global cancer statistics 2018: GLOBOCAN estimates of incidence and mortality worldwide for 36 cancers in 185 countries. *CA Cancer J. Clin.* 68, 394–424. doi: 10.3322/caac.21492

Charpin, C., Tavassoli, F., Secq, V., Giusiano, S., Villeret, J., Garcia, S., et al. (2012). Validation of an immunohistochemical signature predictive of 8-year outcome for patients with breast carcinoma. *Int. J. Cancer* 131, E236–E243. doi: 10.1002/ijc.27371

Chen, F., Chen, J., Yang, L., Liu, J., Zhang, X., Zhang, Y., et al. (2019). Extracellular vesicle-packaged HIF-1alpha-stabilizing lncRNA from tumour-associated macrophages regulates aerobic glycolysis of breast cancer cells. *Nat. Cell Biol.* 21, 498–510. doi: 10.1038/s41556-019-0299-0

Gao, Y., Chen, X., He, Q., Gimple, R. C., Liao, Y., Wang, L., et al. (2020). Adipocytes promote breast tumorigenesis through TAZ-dependent secretion of Resistin. *Proc. Natl. Acad. Sci. U.S.A.* 117, 33295–33304. doi: 10.1073/pnas.2005950117

Govaere, O., Cockell, S., Tiniakos, D., Queen, R., Younes, R., Vacca, M., et al. (2020). Transcriptomic profiling across the nonalcoholic fatty liver disease spectrum reveals gene signatures for steatohepatitis and fibrosis. *Sci. Transl. Med.* 12:eaba4448. doi: 10.1126/scitranslmed.aba4448

Hanahan, D., and Weinberg, R. A. (2011). Hallmarks of cancer: the next generation. *Cell* 144, 646–674. doi: 10.1016/j.cell.2011.02.013

Holmquist-Mengelbier, L., Fredlund, E., Lofstedt, T., Noguera, R., Navarro, S., Nilsson, H., et al. (2006). Recruitment of HIF-1alpha and HIF-2alpha to common target genes is differentially regulated in neuroblastoma: HIF-2alpha promotes an aggressive phenotype. *Cancer Cell* 10, 413–423. doi: 10.1016/j.ccr.2006.08.026

Iommarini, L., Porcelli, A. M., Gasparre, G., and Kurelac, I. (2017). Non-canonical mechanisms regulating hypoxia-inducible factor 1 Alpha in Cancer. *Front. Oncol.* 7:286. doi: 10.3389/fonc.2017.00286

Jia, B., Liu, Z., Zhu, Z., Shi, J., Jin, X., Zhao, H., et al. (2011). Blood clearance kinetics, biodistribution, and radiation dosimetry of a kit-formulated integrin alphavbeta3-selective radiotracer 99mTc-3PRGD 2 in non-human primates. *Mol. Imaging Biol.* 13, 730–736. doi: 10.1007/s11307-010-0385-y

Jia, L., and Sun, Y. (2011). SCF E3 ubiquitin ligases as anticancer targets. *Curr. Cancer Drug Targets* 11, 347–356. doi: 10.2174/156800911794519734

Jun, J. C., Rathore, A., Younas, H., Gilkes, D., and Polotsky, V. Y. (2017). Hypoxia-inducible factors and Cancer. *Curr. Sleep Med. Rep.* 3, 1–10. doi: 10.1007/s40675-017-0062-7

Jurikova, M., Danihel, L., Polak, S., and Varga, I. (2016). Ki67, PCNA, and MCM proteins: markers of proliferation in the diagnosis of breast cancer. *Acta Histochem.* 118, 544–552. doi: 10.1016/j.acthis.2016.05.002

Keith, B., Johnson, R. S., and Simon, M. C. (2011). HIF1alpha and HIF2alpha: sibling rivalry in hypoxic tumour growth and progression. *Nat. Rev. Cancer* 12, 9–22. doi: 10.1038/nrc3183

Li, L., Shi, L., Yang, S., Yan, R., Zhang, D., Yang, J., et al. (2016). SIRT7 is a histone desuccinylase that functionally links to chromatin compaction and genome stability. *Nat. Commun.* 7:12235. doi: 10.1038/ncomms12235

Li, X., Gao, Y., Li, J., Zhang, K., Han, J., Li, W., et al. (2018). FOXP3 inhibits angiogenesis by downregulating VEGF in breast cancer. *Cell Death Dis.* 9:744. doi: 10.1038/s41419-018-0790-8

Liu, Z., Huang, J., Dong, C., Cui, L., Jin, X., Jia, B., et al. (2012). 99mTc-labeled RGD-BBN peptide for small-animal SPECT/CT of lung carcinoma. *Mol. Pharm.* 9, 1409–1417. doi: 10.1021/mp200661t

Liu, Z., Liu, H., Ma, T., Sun, X., Shi, J., Jia, B., et al. (2014). Integrin alphavbeta(6)-Targeted SPECT imaging for pancreatic cancer detection. *J. Nucl Med.* 55, 989–994. doi: 10.2967/jnumed.113.132969

Liu, Z., Wang, F., and Chen, X. (2011). Integrin targeted delivery of radiotherapeutics. *Theranostics* 1, 201–210. doi: 10.7150/thno/v01p0201

Livasy, C. A., Karaca, G., Nanda, R., Tretiakova, M. S., Olopade, O. I., Moore, D. T., et al. (2006). Phenotypic evaluation of the basal-like subtype of invasive breast carcinoma. *Mod. Pathol.* 19, 264–271. doi: 10.1038/modpathol.3800528

Masoud, G. N., and Li, W. (2015). HIF-1alpha pathway: role, regulation and intervention for cancer therapy. *Acta Pharm. Sin. B* 5, 378–389. doi: 10.1016/j.apsb.2015.05.007

Murai, T. (2015). Cholesterol lowering: role in cancer prevention and treatment. *Biol. Chem.* 396, 1–11. doi: 10.1515/hsz-2014-0194

Oppong, B. A., Pharmer, L. A., Oskar, S., Eaton, A., Stempel, M., Patil, S., et al. (2014). The effect of metformin on breast cancer outcomes in patients with type 2 diabetes. *Cancer Med.* 3, 1025–1034. doi: 10.1002/cam4.259

Pavlova, N. N., and Thompson, C. B. (2016). The emerging hallmarks of cancer metabolism. *Cell Metab.* 23, 27–47. doi: 10.1016/j.cmet.2015.12.006

Perez-Hernandez, A. I., Catalan, V., Gomez-Ambrosi, J., Rodriguez, A., and Fruhbeck, G. (2014). Mechanisms linking excess adiposity and carcinogenesis promotion. *Front. Endocrinol.* 5:65. doi: 10.3389/fendo.2014.00065

Qin, G., Kishore, R., Dolan, C. M., Silver, M., Wecker, A., Luedemann, C. N., et al. (2006). Cell cycle regulator E2F1 modulates angiogenesis via p53-dependent transcriptional control of VEGF. *Proc. Natl. Acad. Sci. U.S.A.* 103, 11015–11020. doi: 10.1073/pnas.0509533103

Rankin, E. B., and Giaccia, A. J. (2016). Hypoxic control of metastasis. *Science* 352, 175–180. doi: 10.1126/science.aaf4405

Schwab, L. P., Peacock, D. L., Majumdar, D., Ingels, J. F., Jensen, L. C., Smith, K. D., et al. (2012). Hypoxia-inducible factor 1alpha promotes primary tumor growth and tumor-initiating cell activity in breast cancer. *Breast Cancer Res.* 14:R6. doi: 10.1186/bcr3087

Semenza, G. L. (2002). HIF-1 and tumor progression: pathophysiology and therapeutics. *Trends Mol. Med.* 8(4 Suppl.), S62–S67. doi: 10.1016/s1471-4914(02)02317-1

Seo, B. R., Bhardwaj, P., Choi, S., Gonzalez, J., Andresen Eguiluz, R. C., Wang, K., et al. (2015). Obesity-dependent changes in interstitial ECM mechanics promote breast tumorigenesis. *Sci. Transl. Med.* 7:301ra130. doi: 10.1126/scitranslmed.3010467

Sun, L., Shi, L., Li, W., Yu, W., Liang, J., Zhang, H., et al. (2009). JFK, a Kelch domain-containing F-box protein, links the SCF complex to p53 regulation. *Proc. Natl. Acad. Sci. U.S.A.* 106, 10195–10200. doi: 10.1073/pnas.0901864106

Sun, L., Shi, L., Wang, F., Huangyang, P., Si, W., Yang, J., et al. (2011). Substrate phosphorylation and feedback regulation in JFK-promoted p53 destabilization. *J. Biol. Chem.* 286, 4226–4235. doi: 10.1074/jbc.M110.195115

Tennant, D. A., Duran, R. V., and Gottlieb, E. (2010). Targeting metabolic transformation for cancer therapy. *Nat. Rev. Cancer* 10, 267–277. doi: 10.1038/nrc2817

Wang, Z., Dabrosin, C., Yin, X., Fuster, M. M., Arreola, A., Rathmell, W. K., et al. (2015). Broad targeting of angiogenesis for cancer prevention and therapy. *Semin. Cancer Biol.* 35(Suppl.), S224–S243. doi: 10.1016/j.semcancer.2015.01.001

Wu, Z., Wu, J., Zhao, Q., Fu, S., and Jin, J. (2020). Emerging roles of aerobic glycolysis in breast cancer. *Clin. Transl. Oncol.* 22, 631–646. doi: 10.1007/s12094-019-02187-8

Yamamoto, Y., Ibusuki, M., Okumura, Y., Kawasoe, T., Kai, K., Iyama, K., et al. (2008). Hypoxia-inducible factor 1alpha is closely linked to an aggressive phenotype in breast cancer. *Breast Cancer Res. Treat.* 110, 465–475. doi: 10.1007/s10549-007-9742-1

Yan, R., He, L., Li, Z., Han, X., Liang, J., Si, W., et al. (2015). SCF(JFK) is a bona fide E3 ligase for ING4 and a potent promoter of the angiogenesis and metastasis of breast cancer. *Genes Dev.* 29, 672–685. doi: 10.1101/gad.254292.114

Yang, H., Robinson, P. N., and Wang, K. (2015). Phenolyzer: phenotype-based prioritization of candidate genes for human diseases. *Nat. Methods* 12, 841–843. doi: 10.1038/nmeth.3484

Yang, J., AlTahan, A., Jones, D. T., Buffa, F. M., Bridges, E., Interiano, R. B., et al. (2015). Estrogen receptor-alpha directly regulates the hypoxia-inducible factor 1 pathway associated with antiestrogen response in breast cancer. *Proc. Natl. Acad. Sci. U.S.A.* 112, 15172–15177. doi: 10.1073/pnas.1422015112

Zhang, J., Wang, C., Chen, X., Takada, M., Fan, C., Zheng, X., et al. (2015). EglN2 associates with the NRF1-PGC1alpha complex and controls mitochondrial function in breast cancer. *EMBO J.* 34, 2953–2970. doi: 10.15252/embj.201591437

Zhu, Z., Miao, W., Li, Q., Dai, H., Ma, Q., Wang, F., et al. (2012). 99mTc-3PRGD2 for integrin receptor imaging of lung cancer: a multicenter study. *J. Nucl. Med.* 53, 716–722. doi: 10.2967/jnumed.111.098988

Conflict of Interest: The authors declare that the research was conducted in the absence of any commercial or financial relationships that could be construed as a potential conflict of interest.

Advantages of publishing in Frontiers

OPEN ACCESS
Articles are free to read for greatest visibility and readership

FAST PUBLICATION
Around 90 days from submission to decision

HIGH QUALITY PEER-REVIEW
Rigorous, collaborative, and constructive peer-review

TRANSPARENT PEER-REVIEW
Editors and reviewers acknowledged by name on published articles

Frontiers
Avenue du Tribunal-Fédéral 34
1005 Lausanne | Switzerland

Visit us: www.frontiersin.org
Contact us: frontiersin.org/about/contact

REPRODUCIBILITY OF RESEARCH
Support open data and methods to enhance research reproducibility

DIGITAL PUBLISHING
Articles designed for optimal readership across devices

FOLLOW US
@frontiersin

IMPACT METRICS
Advanced article metrics track visibility across digital media

EXTENSIVE PROMOTION
Marketing and promotion of impactful research

LOOP RESEARCH NETWORK
Our network increases your article's readership